TROPICAL HEAT SOURCES AND THEIR ASSOCIATED LARGE-SCALE

ATMOSPHERIC CIRCULATION

by

CARLOS A. NOBRE

B.S., Instituto Tecnológico de Aeronáutica
São José Dos Campos, Brazil
(1974)

SUBMITTED IN PARTIAL FULFILLMENT
OF THE REQUIREMENTS FOR THE
DEGREE OF

DOCTOR OF PHILOSOPHY

at the

MASSACHUSETTS INSTITUTE OF TECHNOLOGY

January 1983

© Massachusetts Institute of Technology 1983

Signature of Author _____
Department of Meteorology and Physical Oceanography
January 1983

Certified by _____
Jagadish Shukla
Thesis Supervisor

_____
Peter H. Stone
Thesis Supervisor

Accepted by _____
Ronald Prinn
Chairman, Departmental Graduate Committee

TROPICAL HEAT SOURCES AND THEIR ASSOCIATED LARGE-SCALE ATMOSPHERIC CIRCULATION

by

CARLOS A. NOBRE

ABSTRACT

The forcing of large-scale, stationary, zonally asymmetric motions by tropical diabatic heating is examined using idealized models. An equatorial β-p ane, five-layer primitive equation model is used to study the nonlinear tropical response to time-mean, zonally asymmetric forcing. Idealized simple forms of diabatic heating are prescribed, and a time-marching approach is used to obtain steady-state solutions. Linear and nonlinear solutions are compared, and the sensitivity of the response to the intensity and scale of the heat source and to its latitudinal position is discussed. For the linear model, dissipative effects near the equator are important. Nonlinear balances are dominant close to the equator for the nonlinear model. In the case of heating centered at the equator, the maximum upper-level winds are found to the east and to the west of the heating for the linear case. For the nonlinear case, the response is strongly dependent on the heating intensity. Linear and nonlinear solutions are very similar for small heating but differ substantially for moderate to strong heating. Maximum upper-level response for the nonlinear case is found in the subtropics to the east and polewards of the heat source, and there is a considerable degree of east-west asymmetry at equatorial latitudes. For the lower levels the region of westerlies to the west of the heat source becomes longitudinally more confined. Nonlinearities are important in the zonal momentum equation, and the zonal wind is approximately in geostrophic balance even near the equator. In the thermodynamic equation, diabatic heating is balanced primarily by adiabatic ascent or descent. Possible relations between some aspects of the nonlinear model response and observed features of the tropical circulations and of the upper level subtropical jet stream of the winter hemisphere are discussed.

An observational part is also included. The horizontal structure of the planetary-scale circulation in the Goddard Laboratory for Atmospheric Sciences analyses of data from the First GARP Global Experiment is presented. Streamfunction and velocity potential are calculated. The divergent component of the flow is not much smaller than the rotational part for the tropics. East-west (Walker-type) and localized north-south (Hadley-type) circulations are observed to have comparable intensities. Two east-west planetary mass overturnings are evident, one with rising motion over South America and the other with rising motion over a broad area extending from the eastern Indian Ocean to the western Pacific Ocean. Subsidence occurs over the subtropical oceans and northern Africa.

Thesis Supervisor: Jagadish Shukla
Title: Research Affiliate

Thesis Supervisor: Peter H. Stone
Title: Professor of Meteorology

DEDICATION

To the memory of Professor Charney,

a great scientist whose vision

illuminated this work.

TABLE OF CONTENTS

My stay at M.I.T. was made more pleasant by the solicitous help of Jane McNabb, Virginia Mills and Diana Spiegel.

Lastly, I want to express my deep gratitude to my family in Brazil who although distant, gave all the moral support that I needed to continue my work.

Many people have helped me throughout my graduate work. Unfortunately I cannot mention all of them by name, although I am grateful for all the help that I have received.

CHAPTER 1

INTRODUCTION

A traditional and fruitful approach in meteorology has been to divide the particular phenomenon being studied into its climatological (time-mean) and fluctuating (departures from climatology) components and to examine these two components separately. For the large-scale motions in the atmosphere, a suitable time-averaging period is a season or a year, so that the climatological flow is given by the long-term seasonal or annual averages. Generally, the climatological flow changes slowly in response to external forcing and to boundary conditions, and superimposed on this time mean flow are fluctuations of shorter time-scales. For the study of the faster-changing fluctuations (perturbations), the climatological flow (basic-state) is customarily assumed to be time-independent and known; this approach has been historically the backbone of stability analysis.

In a great number of cases, the perturbations owe their existence to the hydrodynamic instability of the climatological flow, and the dynamic behavior of the perturbations is closely related to the general properties of this time-mean basic state. The baroclinic waves of midlatitudes, for example, "are due to the instability of the mean, axially-symmetric, circumpolar vortex whose gravity and Coriolis forces balance the pressure forces associated with the radiatively induced pole to equator temperature gradient" (Charney, 1971).

The detailed vertical and horizontal structure of the circumpolar vortex of midlatitudes has been reasonably explained. Its longitudinal variations, i.e., the standing wave pattern in midlatitudes, have been associated with the atmosphere's response to large-scale orographic and

thermal forcing (Charney and Eliassen, 1949; Smagorinsky, 1953; Derome and Wiin-Nielsen, 1971; Egger, 1976a,b; 1977).

The state of knowledge of the mechanisms responsible for the maintenance of the tridimensional, time-mean planetary-scale flow in the tropics is not nearly as complete as it is for its midlatitude counterpart. Just a few decades ago, motions in the tropics were thought to be forced essentially by midlatitude disturbances through lateral coupling in the subtropics. Currently, it is widely recognized that tropical circulations are forced mostly by diabatic heating sources and sinks within the tropics primarily by the latent heating of condensation due to cumulus convection. Therefore, it is of considerable interest to find out what kind of circulation results from the observed time-mean distribution of latent heating sources.

A first attempt in that direction was to study models of the axially symmetric steady-state circulation forced by the release of latent heat of condensation in the tropical rain belt, radiation, and transient and stationary eddy flux divergences (Dickinson, 1971a,b; Pushistov, 1973; Schneider and Lindzen, 1977; Schneider, 1977; Held and Hou, 1980; Crawford and Sasamori, 1981). These axially symmetric models were successful in simulating and explaining several aspects of the zonally averaged circulation, such as the scale and intensity of the Hadley and Ferrel circulations, the latitudinal position and the magnitude of the winds in the subtropical jet stream, the easterlies in the tropics and westerlies throughout the middle and high latitudes, and the slack temperature gradients in the tropics. The main tropical forcing for these axially symmetric models, i.e., the condensational heating, is assumed to be zonally symmetric and concentrated in a narrow equatorial strip in the

Intertropical Convergence Zone (ITCZ). Some models attempt to take into account zonal asymmetries by incorporating the observed zonally averaged stationary eddies as forcing terms of the mean meridional circulation, as in Dickinson (1971a,b), and Crawford and Sasamory (1981).

It is a valid question to ask whether the time-mean tropical circulations can be accurately represented as being axially symmetric, in which case zonal asymmetries in the forcing and in the circulation are unimportant when compared to the symmetric part, or whether they present longitudinal variations of such magnitude as to render the axially symmetric representation incomplete. For example, on an ocean-covered earth the ITCZ would be axially symmetric and the time-mean, large-scale circulation in the tropics would be nothing but a north-south mass overturning forced by this deep heat source at equatorial latitudes and by radiative cooling at subtropical latitudes. A north-south overturning would also be forced by a latitudinal surface temperature gradient only, but several calculations have shown that such a circulation would be shallow, weak, and have little resemblance to the observed Hadley cell.

However, there are extensive, noncontiguous land masses throughout the equatorial area: South America, Africa and the Indonesian "maritime continent." Land surfaces, unlike oceans, do not store much of the absorbed solar radiation due to their considerably smaller heat capacity. Over the tropical continents, a large fraction of the absorbed solar radiation is used for evapotranspiration. Vertical motions due to convective instabilities transport the water vapor upward which, upon condensation during cumulus convection, heats up the large-scale environment.

Unlike the oceans, tropical land masses act as a quick transfer mechanism for solar radiation to heat up the atmosphere. For the oceans, solar radiation is absorbed mostly at the top few meters, and the heat is well-distributed throughout the mixed layer (20 to 100m). This and the large heat capacity of water make diurnal and seasonal temperature fluctuations small for the oceans. For land surfaces the scenario is different. Absorbed solar radiation quickly raises the surface temperature, and if there is availability of moisture, a large fraction of the absorbed solar radiation is used for evapotranspiration. This rapid diurnal warming of the land surface by solar radiation makes the atmosphere column gravitationally unstable so that the water vapor, when available, is carried upward and the conditional instability can be released.

The regions of maximum precipitation over the tropical oceans seem to lie over warm waters, and the mechanisms to release the conditional instability are related to large-scale convergence patterns. It is quite likely that these large-scale convergence regions are at least initiated by sea surface temperature (SST) gradients.

The ITCZ over the oceans is narrow ($\simeq 10°$ of latitude), and its latitudinal migration is not very large, being approximately $10°$ of latitude from its southernmost to its northernmost position, and these lag behind the sun by two to three months. This lag can be understood in term of typical oceanic response time to external thermal forcing. Unlike the oceanic ITCZ, the region of convective rainfall over land extends much further poleward. For instance, over South America and Africa, this region extends as far as $30°S$ during the southern summer. Also, because the response time to solar heating for land surfaces is short, there is almost

no lag between the location of the band of maximum precipitation and the sun's position.

Therefore, it seems that due to the existence of land masses in the tropical regions of the globe and of longitudinal asymmetries of SST's, the distribution of precipitation (and thus, the condensational heating of the atmosphere) for that region is far from being axially symmetric. In fact, the distribution of precipitation in the tropics presents local maxima over continents, and these are relatively confined in relation to the large expanses of the tropical and subtropical oceans where (except for the narrow oceanic ITCZ) rainfall has very low values. To illustrate the zonally asymmetric character of tropical precipitation we show in Figure 1.1 the zonally averaged precipitation as a function of latitude and the corresponding standard deviation for the seasons and in Figure 1.2, for the year. Note the high values of the standard deviation for the tropics during southern summer and the lower but still significant values during northern summer.

By and large the presence of zonal asymmetries in tropical rainfall can be attributed to the existence of continents. The extensive area of precipitation in the western Pacific Ocean would appear to be an exception to this rule. Perhaps that is not so. Western Pacific SST's are among the highest observed anywhere for the oceans, and this probably contributes to the large precipitation through the mechanism of large-scale convergence induced by SST gradients (and perhaps also by increased evaporation, although Cornejo-Garrido and Stone (1977) have suggested that this effect is less important). There has been a suggestion (M. Cane and E. Sarachik, personal communication) that those warm SST's are a result of the existence of a western boundary "wall" provided by the Indonesian Archipelago. The

JAEGER ZONAL RAIN FOR WINTER
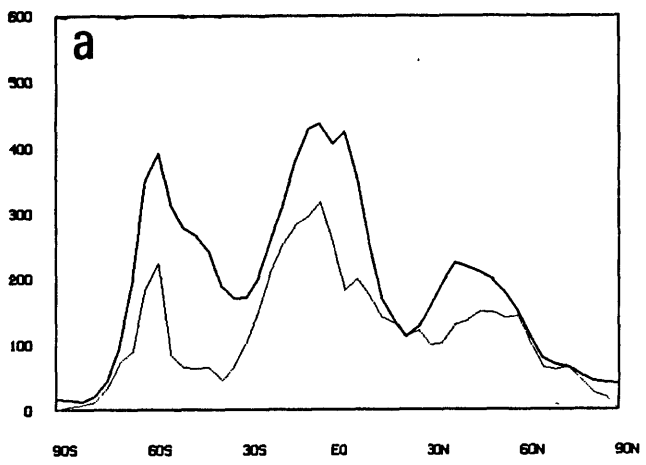
JAEGER ZONAL RAIN FOR SPRING
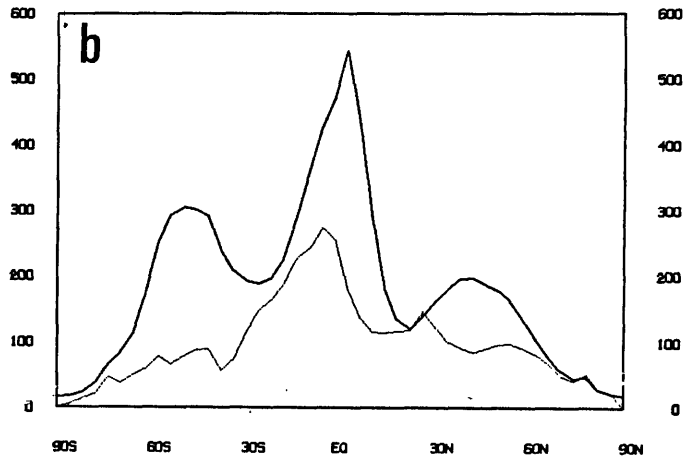
JAEGER ZONAL RAIN FOR SUMMER
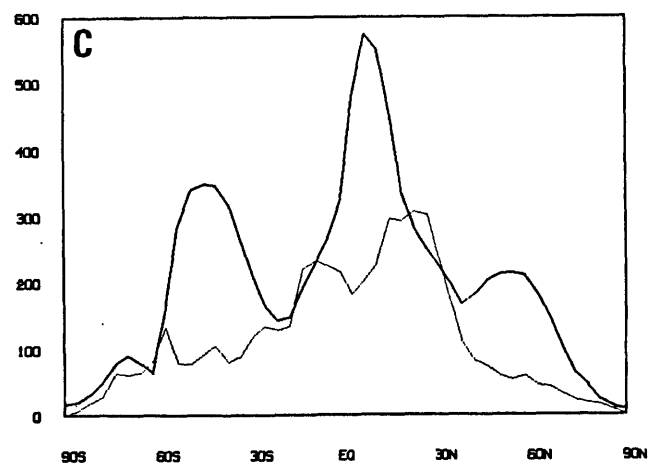
JAEGER ZONAL RAIN FOR FALL
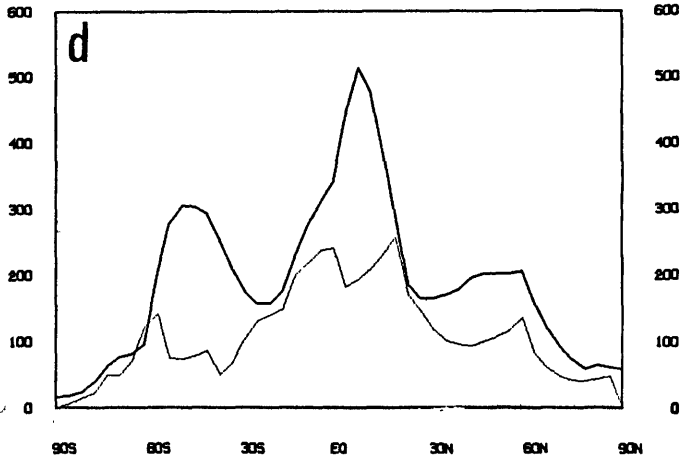
Figure 1.1 Zonally averaged rainfall (thick lines) and corresponding
standard deviation (thin lines) as a function of latitude for
a) DJF, b) MAM, c) JJA, and d) SON; units in mm/day (map pre-
pared at GLAS based on data from Jaeger, 1976).

JAEGER ZONAL RAIN FOR ANNUAL
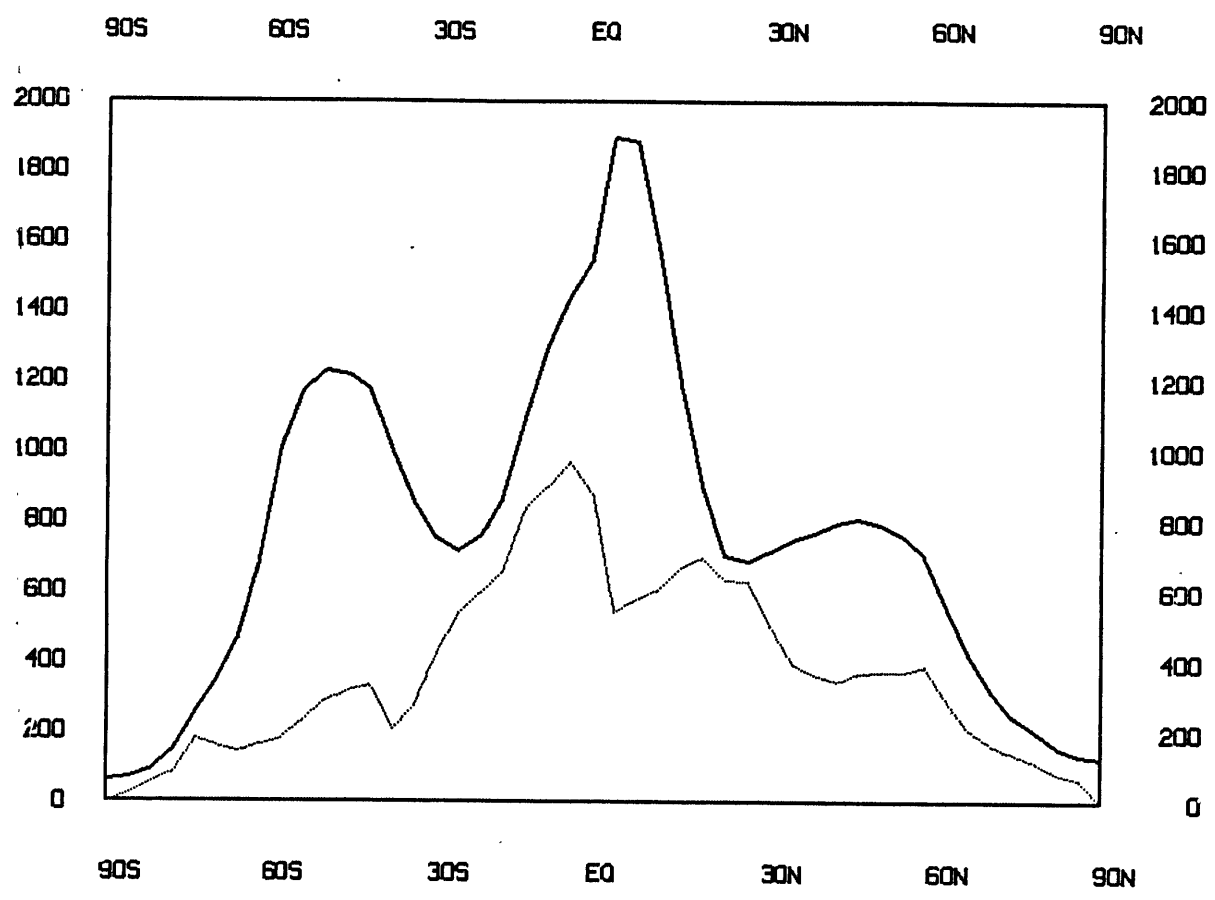
Figure 1.2 Same as Figure 1.1 but for the annual
rainfall.

argument goes as follows: easterly trade winds over the equatorial Pacific transfer momentum to the ocean, which would tend to pile water up against the western boundary. This piling up of water would create an east-west sea level slope, thus deepening the thermocline in the western part of the oceanic basin and causing the surface temperature to be warmer. Therefore, it is likely that even the broad area of high rainfall in the western Pacific Ocean is indirectly linked to the Indonesian land masses through the above-mentioned mechanism of warmer SST's.

In addition to tropical land-sea contrasts in the zonal direction, there are not-less-important land-sea contrasts in the latitudinal direction as well. Because of the uneven distribution of land between the tropical regions of both hemispheres (majority of the land in the northern hemisphere), there are regions where a tropical or subtropical continent lies just north of an equatorial ocean. These land masses would be preferred regions for convection during the northern summer by the same type of argument as suggested above for the equatorial continents, i.e., sustained convection caused, or at least initiated, by strong solar heating of the ground. Here, however, it is likely that the transports of moisture from the warm equatorial ocean would constitute a major source of water vapor and the intense land heating would act as a mechanism for establishing large-scale moisture convergence. The conspicuous examples of such circulations are the West African and the vigorous Indian-Southeast Asian monsoons during northern summer. Albeit these monsoonal circulations are primarily initiated by the meridional land-sea contrast, the land masses where they occur are longitudinally confined; therefore, they add to the zonal asymmetries of the tropical thermal sources.

If zonal asymmetries in precipitation are indeed important, and we believe they are, then we would expect to see thermally direct mass overturnings established in the zonal plane with the rising branch located where the release of convective heating is maximum, i.e., over the tropical continents, and the sinking branch located where precipitation is at a minimum, over the eastern part of the subtropical oceans.

There are a number of observational studies supporting this view and demonstrating the importance of zonal asymmetries in the forcing of tropical circulations. Ramage (1968) analyzed two distinct January circulations for the eastern hemisphere and linked the differences to anomalous precipitation over the maritime continent of Indonesia. Krishnamurti (1971) and Krishnamurti et al. (1973) computed upper level velocity potential fields for a summer and a winter season and detailed the structure of thermally direct east-west circulations with intensities comparable to that of the Hadley-type circulations and tied to zonal asymmetries of heating. Krueger and Winston (1974) analyzed the tropical circulation for two contrasting circulation regimes (February 1969 and February 1971) and attributed the differences to precipitation changes over the three continental regions. Cornejo-Garrido and Stone (1977) studied the heat budget of the Walker circulation and found that the primary drive for that circulation is the heating due to zonal variations in condensation. Johnson and Townsend (1981), and Otto-Bliesner and Johnson (1982) computed the thermally forced mean mass circulation in isentropic coordinates for the northern hemisphere and concluded that zonal asymmetries in the heating lead to longitudinal variations of the meridional circulation and to pronounced east-west overturnings. Paegle and Baker (1982) analyzed the First GARP Global Experiment (FGGE) data set

and indicated the importance of longitudinal heating gradients to the forcing of ultra-long waves. Additionally, there have been studies of the effects of interannual variability of tropical heating gradients (Bjerknes, 1966; 1969; Julian and Chervin, 1978; Horel and Wallace, 1981; and many others).

A number of theoretical and modeling studies have attempted to explain the atmosphere's <u>linear</u> response to planetary-scale tropical heat sources and sinks. Matsuno (1966), in his classical paper on equatorial waves, calculated the linear response of an equatorial β-plane, shallow water model to the imposition of stationary, periodic mass sources and mass sinks along the east-west direction. Webster (1972) used a two-layer numerical model on a sphere, including dissipation and realistic basic currents, to calculate the large-scale, stationary, zonally asymmetric motions that result from heating and the orographic effect in the tropical atmosphere. Gill (1980) used a simple analytic equatorial β-plane model to elucidate some basic features of the response of the tropical atmosphere to diabatic heating concentrated in an area of finite extent. He found east-west asymmetry which was explained in terms of the propagation properties of equatorial waves (Kelvin waves to the east of the heat source and Rossby waves to the west). Webster (1981 and 1982), Hoskins and Karoly (1981), and Simmons (1982) studied the local and remote (teleconnection) response of the atmosphere to thermal forcing (usually thought of as resulting from SST anomalies) located at various latitudes. They used linearized, steady-state, multi-layer baroclinic models on a sphere containing a zonally symmetric basic state with horizontal and vertical shear. Geisler (1981) introduced momentum mixing by cumulus clouds (cumulus friction) in a study of the Walker circulation. Lau and Lim (1982) utilized a

shallow-water, equatorial β-plane model to study the heat-induced monsoon circulations during Southeast Asian northeasterly cold surges. Webster and Holton (1982) used a nonlinear shallow water model containing a longitudinally varying, time-mean, basic-state zonal wind field to investigate the cross-equatorial propagation of forced waves. They found the interesting result that "...if the longitudinally-asymmetric basic state includes a 'duct' in which the zonal winds are westerly, waves of zonal scale less than the zonal scale of the westerly duct may propagate from one hemisphere to the other even though the zonally-symmetric mean zonal wind remains easterly in the equatorial region."

A common characteristic shared by most of the above-mentioned modeling studies is that, by virtue of their linear character, they are actually dealing with heating perturbations which are departures from the time-mean diabatic heating field. The validity of these models' results is dependent on the assumption that heating perturbations are small, so as to make nonlinearities unimportant. However, there is considerable observational evidence suggesting that when the heating perturbation results from SST anomalies (for example, large anomalous precipitation over the central Pacific Ocean in El Niño years), the magnitude of the perturbation is as large as the mean heating field. If that is the case, nonlinear behavior is likely to become important, primarily when we recall that anomalous precipitation rates can be higher than 10 mm/day, hence nonlinearities should not be excluded a priori.

Another assumption common to this class of modeling studies is to prescribe a time-mean, basic state zonal wind. This zonal wind distribution is variously taken as zero (resting atmosphere) or longitudinally independent, and only in Simmons (1982), and Webster and

Holton (1982), was a more realistic, longitudinally varying, basic-state zonal wind considered. It is an observational fact, however, that time-mean circulations present a significant degree of zonal asymmetry in the tropics, i.e., easterly and westerly winds are observed at different longitudes for both lower and upper levels.

This study is a theoretical attempt to investigate the nonlinear response of the tropical atmosphere to large-scale, stationary, zonally asymmetric diabatic heating forcing and to gain some understanding about the influence of this forcing on the time-mean circulation. We hypothesize that the observed zonal asymmetries of the time-mean tropical circulation are related to the stationary diabatic heating asymmetries, i.e., the localized character of tropical precipitation over land masses. Given that seasonal precipitation rates can be as high as 15 mm/day (or roughly 3.5°K/day heating for the tropospheric column) and that near the equator the flow is likely to become increasingly ageostrophic (large Rossby number), we also hypothesize that nonlinearities may play an important role in the dynamical balances of stationary motions forced by zonally asymmetric diabatic heating sources. To this end we develop an idealized, five-layer, primitive, steady-state nonlinear model on an equatorial β-plane and calculate the response to a variety of prescribed, equatorial, zonally asymmetric heat sources. Topographic forcing and transports of heat and momentum by large-scale transient eddies such as those associated with baroclinic-barotropic instabilities and short-term fluctuations in the latent heating sources are not considered.

In Chapter 2 we review observations and observational studies pertaining to zonal asymmetries in the tropics; we also analyze a subset of the FGGE data set attempting to demonstrate the importance of divergent

tropical circulations (Hadley-type and Walker-type circulations). A simple, linearized analytic model is developed in Chapter 3, and linear solutions are described. In Chapter 4 we develop the nonlinear model and describe the numerical integration procedure. The presentation of the results of this model for a number of idealized heat source distributions and comparison of linear and nonlinear solutions is made in Chapter 5. In the concluding section, Chapter 6, we discuss the results and some of the limitations of the model.

CHAPTER 2: <u>REVIEW OF OBSERVATIONS AND FGGE DATA ANALYSIS</u>

2.1 <u>INTRODUCTION</u>

Before we introduce the more theoretical aspects of this study, it will prove to be of utility to review the observational work more directly related to the existence of zonal asymmetries in the tropical forcing fields. This Chapter is divided into two sections: in the first we examine a selected set of observations and observational studies, and in the second we analyze in detail a subset of FGGE data.

The usefulness of the review is threefold: First, it will provide observational evidence to demonstrate the importance of zonal asymmetries in the various meteorological fields and also to show that the planetary-scale zonal circulations are comparable in strength to the meridional circulations. Second, it will form the basis for prescribing the structure and intensity of the diabatic heating forcing to be used in the models described in subsequent chapters. And lastly, it will provide the framework for discussing the results of the models developed in Chapters 3 and 4.

Here we will not be concerned with describing in detail the general circulation of the tropical atmosphere; for that the reader is referred to elsewhere in the literature [Newell <u>et al</u>., 1972, Riehl, 1979]. We will attempt to emphasize the non-zonally symmetric nature of the planetary-scale tropical circulations and also try, from an observational point of view, to link zonal asymmetries to the isolated regions of strong convective activity over the tropical land masses.

2.2 REVIEW OF OBSERVATIONS

We selected maps of cloudiness, precipitation, pressure, winds and streamlines, and velocity potential to study departures from zonal symmetry in the tropics.

2.2.1 CLOUDINESS AND PRECIPITATION

Diabatic heating is not a directly measured quantity in the atmosphere. For the tropics the regions of strong convective activity and thus of latent heating of the atmosphere can be identified through the analysis of cloudiness and precipitation maps. Precipitation distributions are well-known for continental areas but less reliable for oceanic ones. They can give a quantitative idea of the total heating of the atmospheric column by the condensation of water vapor in precipitating clouds but do not say anything about the vertical distribution of this heating.

After the advent of satellites, the areal distribution of cloudiness became well-established. Cloudiness is not a quantitative measure of latent heating; however, its study provides important information about geographical and seasonal distribution of regions of strong convection, primarily over the oceans, due to the sparcity of reliable precipitation measurements for those regions.

CLOUDINESS

Figure 2.1 shows the satellite-derived tropical cloudiness map for
each season averaged for the period 1967-1970 adapted from U.S.
Department of Commerce and U.S. Air Force (1971).*

For the northern winter season (DJF), we note the following
features:

> a) the brightest areas occur over South America, southern
> Africa and the maritime continent of Indonesia,

> b) the mean latitude of the ITCZ cloudiness band of
> Atlantic and Pacific Oceans is 5°-6°N; forking of the
> cloudiness occurs over Western Pacific approximately at
> the date line with the southern Pacific convergence
> zone (SPCZ) cloudiness band running approximately NW-SE
> and joining the southern hemisphere midlatitude
> cloudiness belt,

> c) over South America and southern Atlantic, cloudiness
> also takes a NW-SE orientation.

---

* Deserts such as Sahara and Saudi Arabia appear as bright areas. Also,
bright areas off the west coasts of South and North America, South and
North Africa represent non-precipitating stratus clouds over cold waters.

DECEMBER JANUARY FEBRUARY
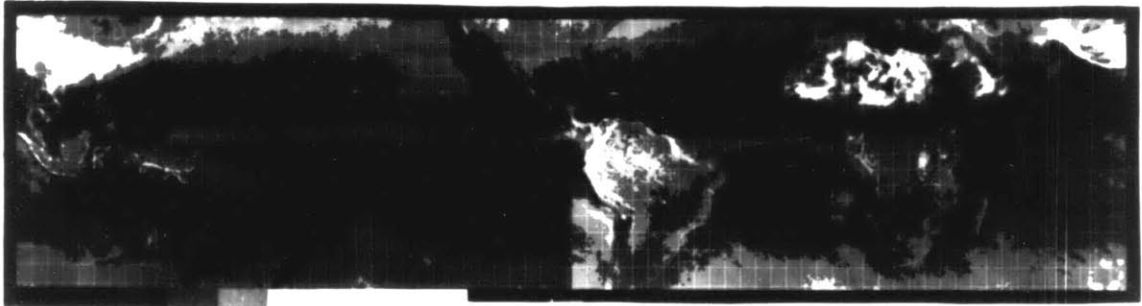
MARCH APRIL MAY

JUNE JULY AUGUST
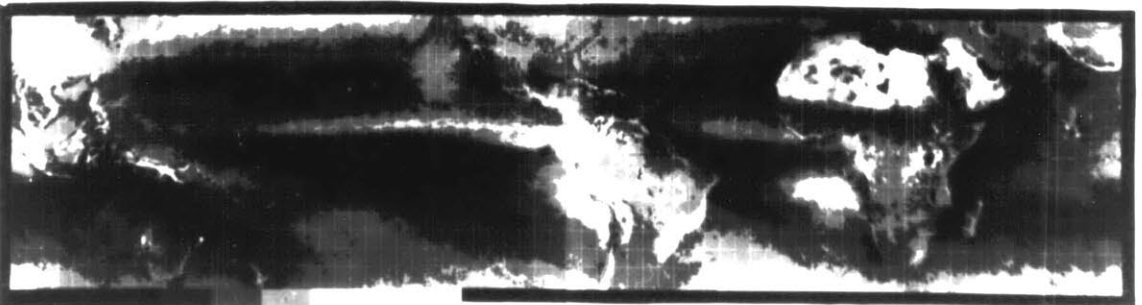
SEPTEMBER OCTOBER NOVEMBER

Figure 2.1 Satellite-derived tropical cloudiness for each season (adapted from U. S. Department of Commerce and U. S. Air Force, 1971).

For the northern summer season (JJA):

a) brightest areas are found over an extensive
region comprising India, Southeast Asia and the
maritime continent, over eastern equatorial Pacific and
northwest South America, and over West Africa,

b) the mean position of the ITCZ cloudiness band over
the Atlantic and Pacific Oceans is 7°-8°N,

c) the width of the ITCZ is larger over the eastern
part of the ocean basins (Pacific and Atlantic) than
over the western part.

We point out that the oceanic ITCZ cloudiness band lags behind the
continental band of cloudiness in its latitudinal migration following the
sun's motion. The oceanic ITCZ's southernmost (northernmost) position
happens during the MAM (SON) season, whereas the continental cloudiness
responds more quickly to the solar forcing, i.e., its southernmost
(northernmost) displacement occurs in the DJF (JJA) season.

PRECIPITATION

Fig. 2.2 depicts the total annual precipitation, and Fig. 2.3, the
seasonal precipitation. These maps were prepared at GLAS using data from
Jaeger (1976). Some features of interest from the annual precipitation
map are:

a) highest precipitation rates are found over the
Amazon, West Africa and the maritime continent of
Indonesia,

SMØØTHED   MINTZ/JAEGER MØNTHLY MEAN PRECIPITATIØN SMØØTHED

MEAN RAIN (MM/DAY) FOR ANNUAL
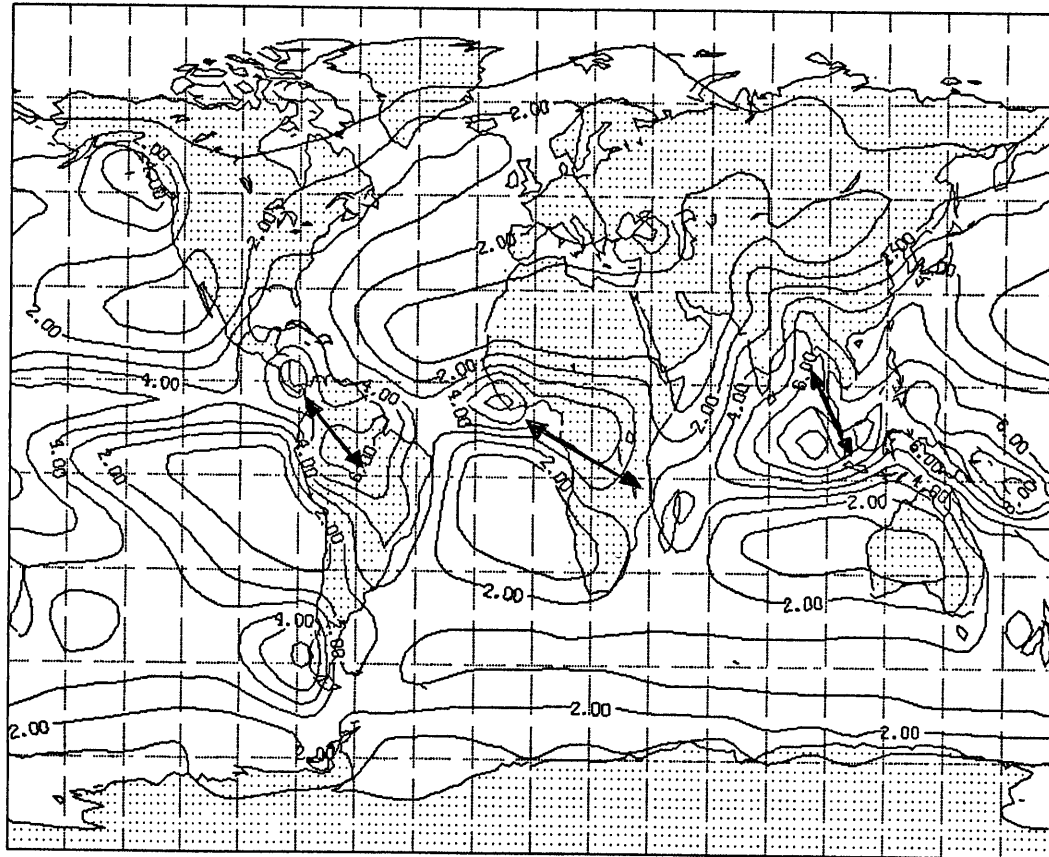
CØNTØUR FRØM 0.0   TØ 0.90000E+01 CØNTØUR INTERVAL ØF 0.10000E+01

Figure 2.2   Global annual precipitation in mm/day (map
             prepared at GLAS based on data from Jaeger,
             1976).Arrows indicate direction of displacement
             of centers of maximum precipitation between
             summer and winter.

b) lowest precipitation is seen over the eastern part
of oceans (South and North Atlantic, South and North
Pacific and Indian Oceans) and adjoining continents at
the latitude of the subtropical deserts,

c) subtropical belt of low precipitation is broken over
India and southeast Asia,

d) both in terms of intensities and areal extent,
precipitation over the Indonesian maritime continent and
western Pacific is the largest.

For the DJF season:

a) highest precipitation rates are found over South
America and the Indonesian maritime continent-western
Pacific region with maximum $\geqslant 10$ mm/day,

b) over southern Africa precipitation is less intense,
and maximum of 6 mm/day occurs over Madagascar,

c) most of the precipitation and therefore latent heating
is concentrated in the Southern Hemisphere,

d) heating over the Amazon is quite isolated both
longitudinally and latitudinally with x and y
dimensions of the order of 4×10^3 km and 2×10^3 km,
respectively, and centered at about 10°S,

e) latent heating over Indonesian-western Pacific region
is more zonal with an NW-SE orientation from the

MEAN RAIN (MM/DAY) FOR WINTER
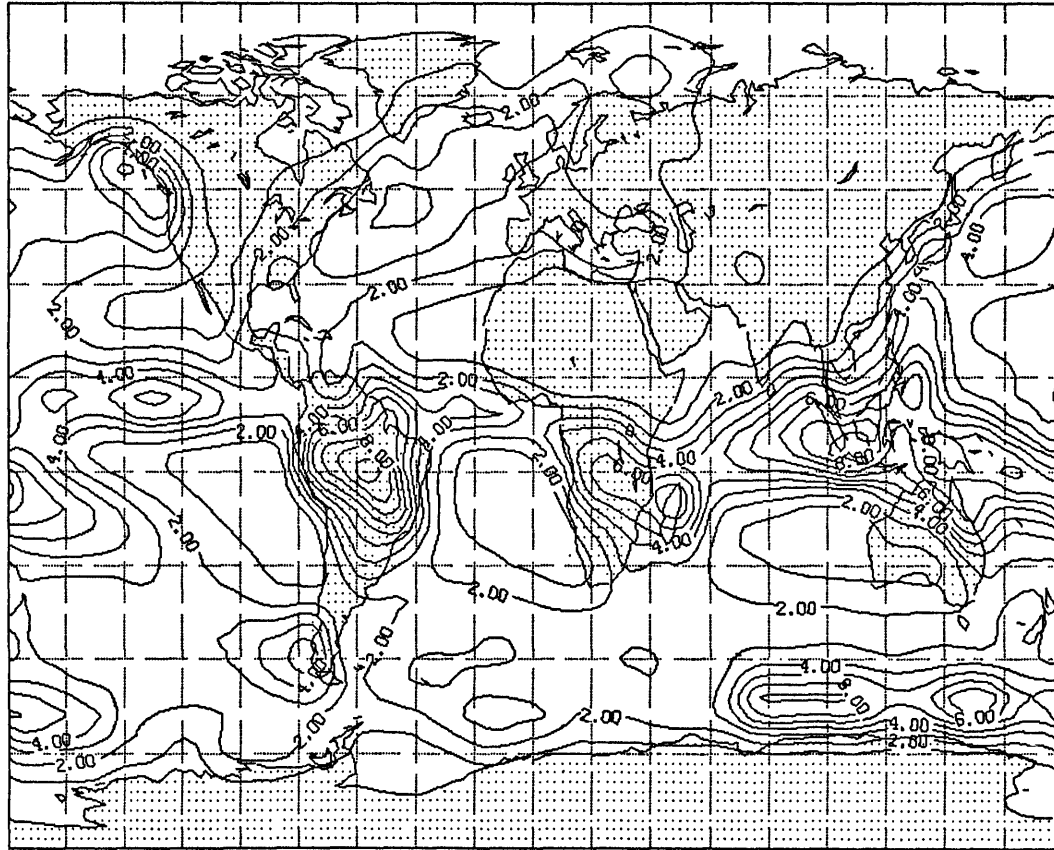
CØNTØUR FRØM 0.0   TØ 0.10000E+02 CØNTØUR INTERVAL ØF 0.10000E+01

Figure 2.3a   Same as Figure 2.2 but for DJF season.

eastern Indian Ocean towards the South Pacific; scales in the x and y direction are approximately 10^4 km and 2×10^3 km, respectively, and centered at about 5°-6°S,

f) latent heating over southern Africa also presents an NW-SE orientation from the Atlantic coast towards Madagascar; it is centered at about 15°S, and its eastern flank joins with the western part of the Indonesian-Western Pacific heating,

g) in general, precipitation over the oceanic ITCZ is less than the maximum over land areas; for instance, 4 to 6 mm/day over equatorial oceans as opposed to 10 mm/day or more over South America and Indonesia, which stresses the nature of alternating, isolated heat sources over land masses,

h) minimum of precipitation over the subtropical oceans,

i) regions of low precipitation are oriented NW-SE over southern Atlantic and southern Pacific,

j) over the Indian Ocean and Australia, the area of low precipitation is more zonally oriented, perhaps reflecting the more zonal distribution of precipitation to the north over the Indonesian maritime continent.

MEAN RAIN (MM/DAY) FOR SPRING

CØNTØUR FRØM 0.0   TØ 0.1000OE+02 CØNTØUR INTERVRL ØF 0.10000E+01

Figure 2.3b   Same as Figure 2.2 but for MAM season.

For the JJA season:

a) maximum rainfall rates are over northwestern South
America-Central America-eastern equatorial Pacific
region, West Africa-eastern equatorial Atlantic region
and the extensive precipitation area of the Southeast
Asian monsoon-Indonesia-western Pacific region,

b) the maximum over South America is centered at 10°N
with a NW-SE orientation following the orientation
of land in Central America,

c) over Africa it is remarkably zonal with a conspi-
cuous maximum of up to 10 mm/day over West Africa, the
band being centered at about 7°N,

d) the most striking feature of any season in terms of
precipitation is the huge area of intense rainfall over
India, Southeast Asia, Indonesian maritime continent, and
western Pacific during northern summer where precipi-
tation rates are up to 12 mm/day over Southeast Asia,
and the areal extent of this active precipitation
region is several times greater than those over Africa
and South America-Central America,

e) this area is slanted in a NW-SE direction from India
towards the South Pacific and presents very sharp
rainfall gradients at its western, northern, and southern
boundaries; it is to be expected that this area will

MEAN RAIN (MM/DAY) FOR SUMMER

CONTOUR FROM 0.0   TO 0.13000E+02 CONTOUR INTERVAL OF 0.10000E+01

Figure 2.3c Same as Figure 2.2 but for JJA season.

exert a major role for the northern summer tropical
circulation given its intensity and extent,

f) most of the heat sources are located in the northern
hemisphere,

g) subtropical areas of low precipitation now cover
most of the southern hemisphere subtropics and have
a zonal orientation,

h) precipitation gradients are mostly meridional except
over the Arabian Sea, where they are strongly zonal,

i) precipitation over the oceanic ITCZ is lower than
over land and over the Southeast Asian monsoon region
with the exception of the oceanic monsoon areas of
South America and West Africa where the precipitation
rate is higher.

COMPARISON OF DJF AND JJA SEASONS:

If the continents were perfectly symmetric about the equator, one
would expect that there would be precipitation maxima at the longitudes
of the continents due to their existence and that these maxima would move
north-south with the sun's motion and perhaps not vary much in their
position within the continents. In reality the distribution of land is
far from being symmetric about the equator, and most of the land masses
are found in the northern hemisphere. In the cases of India and
Southeast Asia, West Africa, and to a lesser extent Central America,
tropical land masses are found just north of an equatorial ocean. This

latitudinally asymmetric distribution of land is bound to cause the tropical rainfall maximum to vary longitudinally as well as latitudinally with the seasons, and that is exactly what is observed. During southern summer, rainfall maxima are located in the southern hemisphere and tilted NW-SE; whereas during northern summer they are found in the northern hemisphere, still tilted NW-SE though not at all at the same longitudes but west of their southern summer position. The general SE-NW movement of the centers of rainfall maximum is indicated in Fig. 2.2. Also it is worth mentioning that the rainfall distribution is less zonally asymmetric for the northern summer season than for that of the southern summer.

MAM AND SON SEASONS:

The MAM season resembles more closely the DJF season in that most of the rainfall is to be found in the southern hemisphere; whereas the SON SON season is closer to the JJA season with most of the precipitation concentrated in the northern hemisphere. The transition from one regime to the other (i.e., mostly southern hemisphere latent heating to mostly northern hemisphere latent heating and vice-versa) generally does not proceed slowly throughout spring and autumn seasons, but the change in regimes takes place rather abruptly by the time the monsoon circulations of the northern hemisphere are established or cease to exist, approximately in June and November, respectively.

Rainfall rates over the oceanic ITCZ are still weaker than over land for spring and autumn. Annual precipitation totals over the oceanic ITCZ can be almost as high as annual totals over land, primarily because the

MEAN RAIN (MM/DAY) FOR FALL
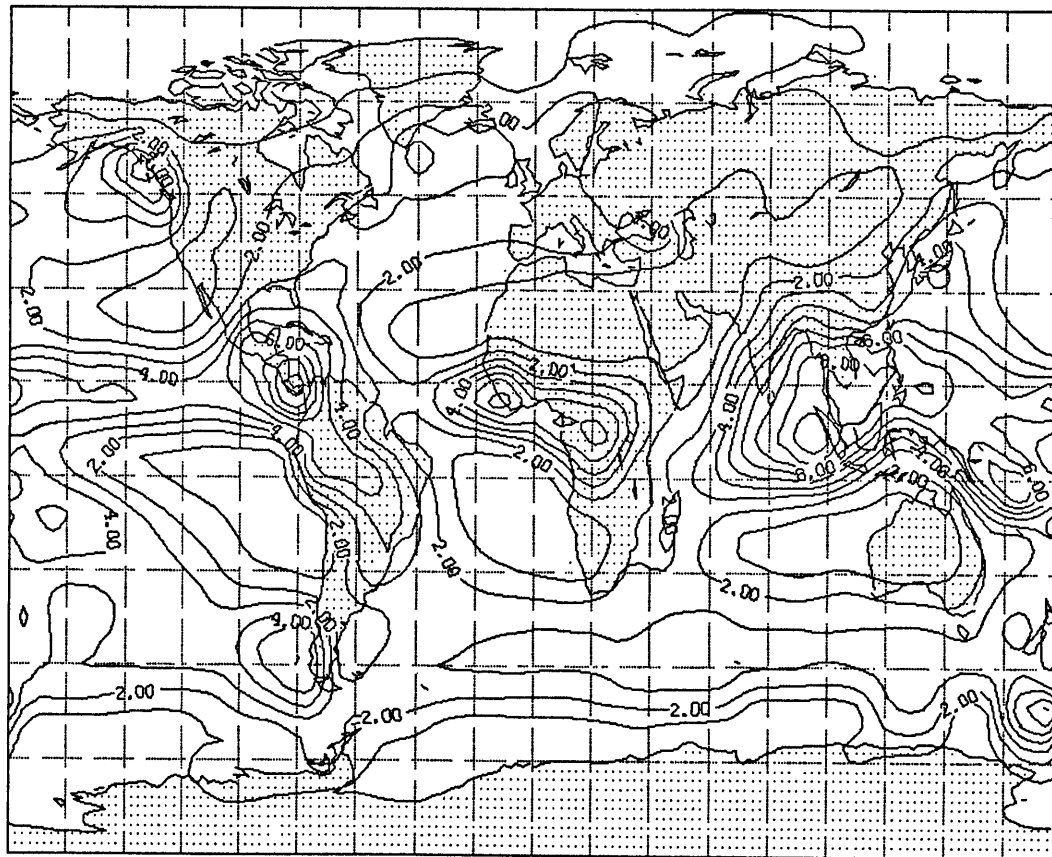
CØNTØUR FRØM 0.0   TØ 0.90000E+01 CØNTØUR INTERVAL ØF 0.10000E+01
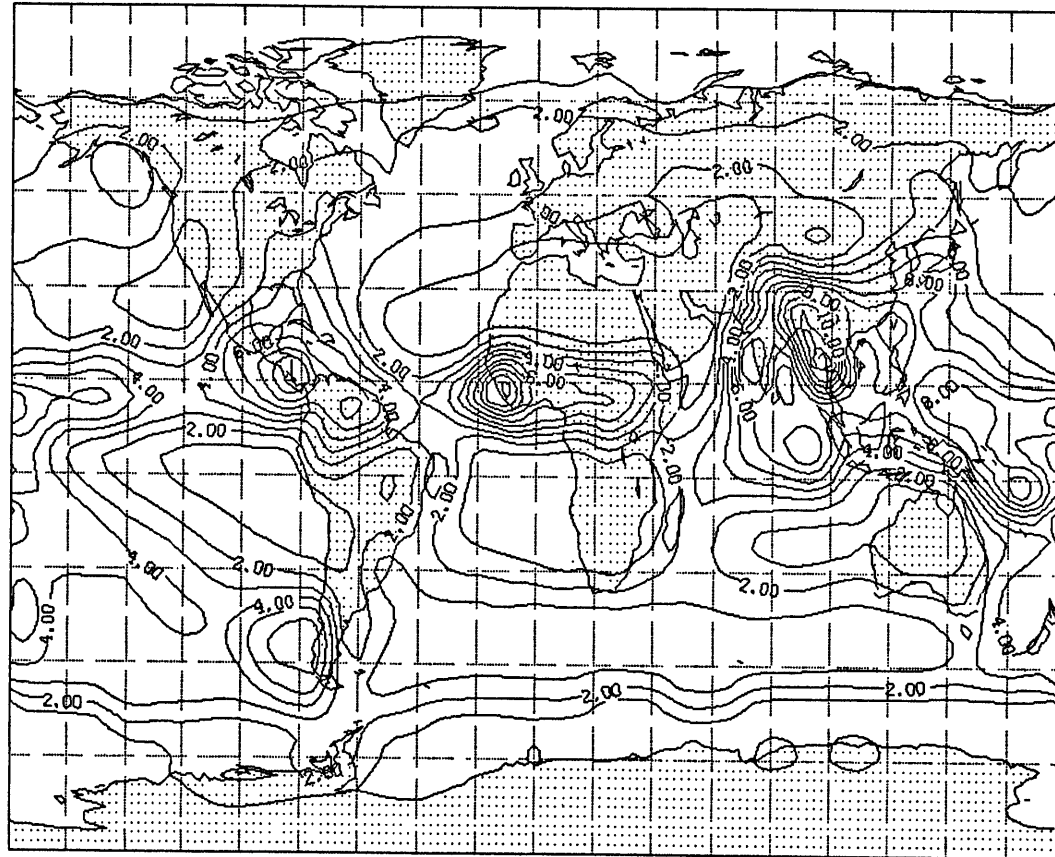
Figure 2.3d   Same as Figure 2.2 but for SON season.

latitudinal migration of the oceanic ITCZ's precipitation band is considerably less than the precipitation regions over land masses, roughly 5°-7° lat. for the former and 20° lat. for the latter. In a seasonal time scale, precipitation rates (i.e., latent heating of the atmosphere) are significantly higher over the three main precipitation areas than over the oceanic ITCZ; this reinforces the isolated and zonally asymmetric nature of tropical heat sources. In an annual mean sense, these differences are smoothed out, and precipitation is more zonally symmetric than for any individual season but still presents a substantial and important degree of zonal asymmetry. However, to talk about "annual mean conditions" is rather academic considering that the summer and winter heating patterns are significantly distinct from each other in many respects. In a seasonal mean sense, tropical precipitation over land is displaced farther poleward in comparison with its annual mean position, and seasonal maximum rainfall rates are considerably higher than the corresponding annual ones.

The question of seasonal versus annual tropical forcing by latent heating merits some discussion. Some studies (Scheneider and Lindzen, 1977; Scheneider, 1977) assumed that the tropical diabatic heating is nearly axisymmetric in the annual mean sense (driving a mean Hadley cell) and that departures of condensational heating from zonal symmetry are small. Hence, the effects of these asymmetries on the mean meridional circulation, for instance, the transports by the stationary eddies, were neglected altogether in those studies. However, for the seasonal forcing, the maximum condensational heating is generally found further

poleward over land, either flanked on the east and west sides by oceanic regions of low precipitation as is the case during southern summer, or adjacent to subtropical deserts as it is for the Asian monsoon region during northern summer. For both cases there is a strong degree of zonal asymmetry which would likely drive east-west circulations of comparable magnitude to the MMC, since the standard deviation of the zonally averaged precipitation is almost as large as the mean. One would then expect the transports by the stationary eddies to be comparable to the transports by the MMC, and that is indeed what is observed, as will be shown in Section 2.2.8.

2.2.2 <u>PRESSURE AND CIRCULATION</u>

<u>PRESSURE AND GEOPOTENTIAL</u>

Global maps of sea level pressure (SLP) for January and July from Godbole and Shukla (1981) are shown in Fig. 2.4a and Fig. 2.4b, respectively.

<u>For January</u> we note the following climatological features:

a) isobars are more zonal in the belt of high pressures on the northern hemisphere, i.e., the subtropical highs of the North Atlantic and North Pacific exhibit a weak circulation in comparison with the three subtropical highs over the southern hemisphere oceans which exhibit prominent circulations associated with them,

b) mean latitude for the subtropical high belt is $\simeq 25°$-$30°$S in the summer hemisphere and $\simeq 34°$-$40°$N in the winter hemisphere,

c) continental lows are found over South America, southern Africa, and northern Australia,

d) the low over northern Australia extends zonally eastward to central Pacific,

e) continental lows are located at more equatorward latitudes than the subtropical highs in the southern hemisphere. We observe that in the longitudinal direction there is an alternating pattern of oceanic highs and continental lows for the summer hemisphere in January.

a
JAN. MEAN (1961-76)

b
JULY MEAN (1961-76)
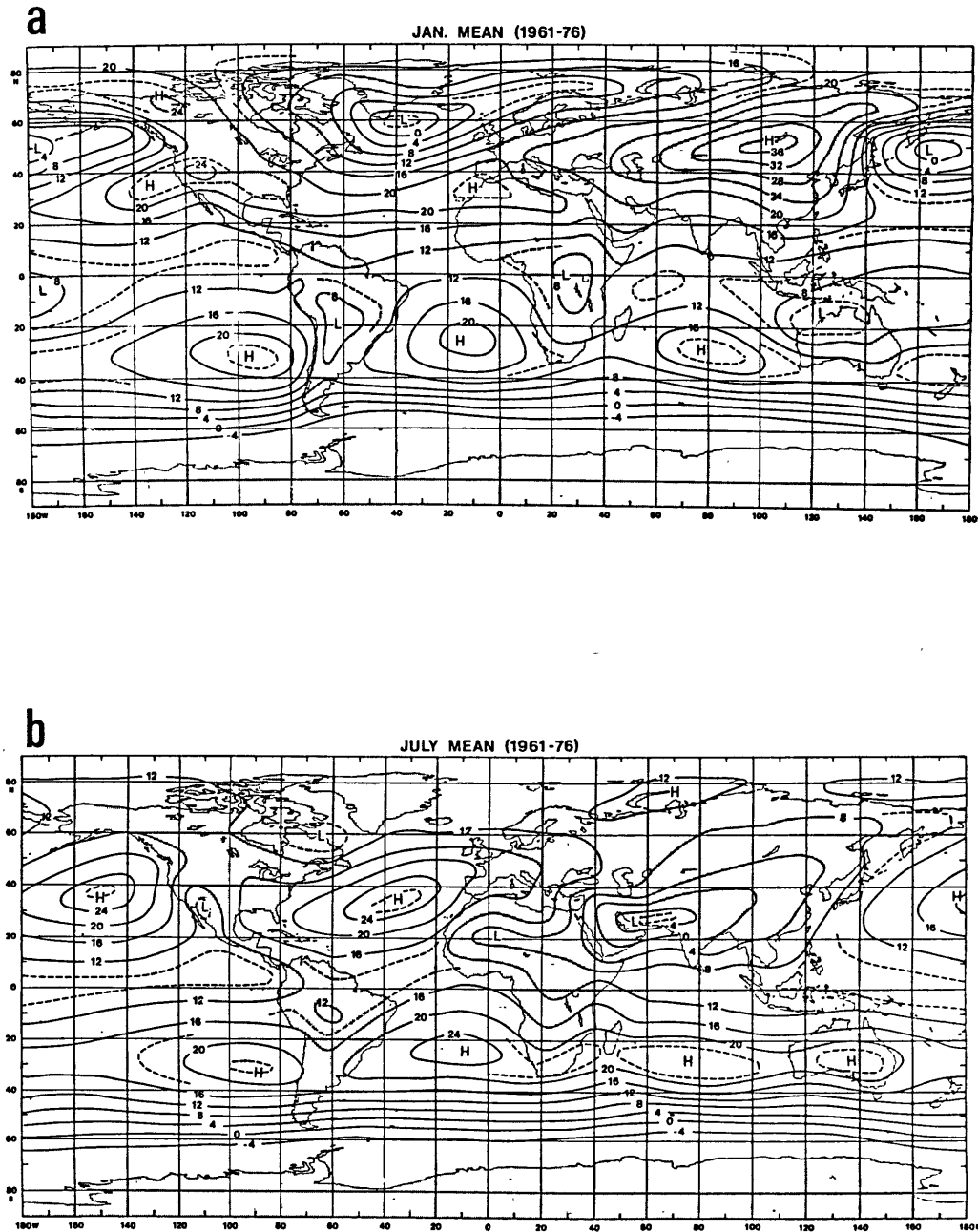
Figure 2.4   Normal sea level pressure distribution for
              a) January and b) July; 1000 mb subtracted from
              the actual pressure values (after Godbole and
              Shukla, 1981).

For July:

> a) the belt of high pressures of the southern hemi-
> sphere is more zonally oriented and spans all longitudes
> (southern summer continental lows have disappeared); its
> average latitude is about the same (slightly south) as
> in January, and its intensity is higher in July,
>
> b) North Atlantic and North Pacific subtropical highs
> are prominent in July, more intense than in January, and
> slightly equatorward of its January mean position,
>
> c) monsoonal lows exist over Mexico, North Africa, and
> Asia; the latter is by far the more intense and
> extensive of the three,
>
> d) zonal asymmetries due to land-sea contrast are not as
> strong in the northern hemisphere summer.

In summary we can say (Godbole and Shukla, 1981) that "for both hemispheres the summer hemisphere is characterized by continental lows and oceanic highs . . . . The location and intensities of the southern hemisphere subtropical highs, which occur over the ocean, are remarkably similar in January and July .... The North Atlantic and South Atlantic subtropical highs are found to attain their maximum intensity at the same time, during July", and for both hemispheres the subtropical high pressures are more zonally oriented during winter.

From maps of geopotential height for the upper levels (not shown here), we observe the following main features: for July the dominant feature is a quite intense high over the Tibetan Plateau extending towards

North Africa, zonally oriented and centered at about 30°N. For the
southern summer season (Krishnamurti et al., 1973), we observe strong
anticyclonic circulation over South America centered at about 15°S
(Bolivian upper-level high), over Africa centered at about 17°S, and
zonally oriented highs in both sides of the equator over the Indonesia
maritime continent region.

CIRCULATION

Fig. 2.5. shows the circulation and isotachs at 850 mb for DJF and
JJA and Fig. 2.6, at 200 mb. These figures are from Sanders (1975).
For the lower-level circulation (850 mb), we notice the following
features:

DJF season, 850 mb (Fig. 2.5a):

a) anticyclonic centers over the three oceans of the southern
hemisphere and also over the North Atlantic and North Pacific,

b) equatorial westerlies in the Indian Ocean and western
Pacific,

c) mostly meridional flow along both flanks of the
Andes, with southerlies to the west and northerlies to
the east.

JJA season, 850 mb (Fig. 2.5a):

a) anticyclonic centers over North and South Atlantic,
North and South Pacific, and Indian Oceans and over Australia,

a
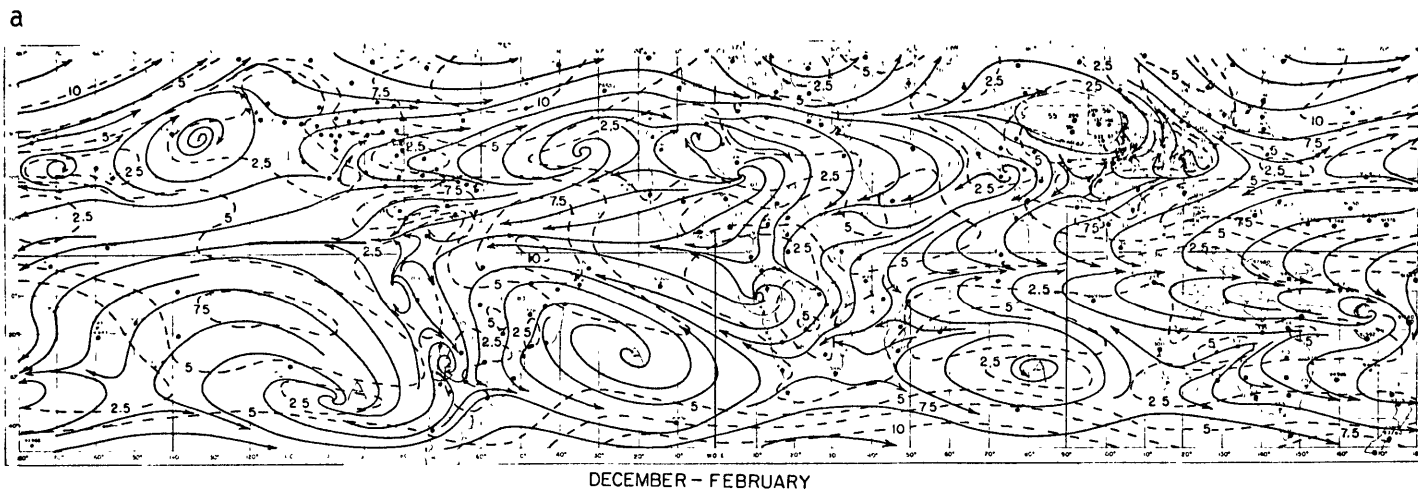
DECEMBER - FEBRUARY

LONG-TERM MEAN 850-mb FLOW. DATA FROM NEWELL(1972), LUFTHANSA(1967), SADLER(1970),and SCHWARTZKOPF(1970). ISOTACHS IN M SEC⁻¹

b

JUNE-AUGUST   SANDERS (1975)

42
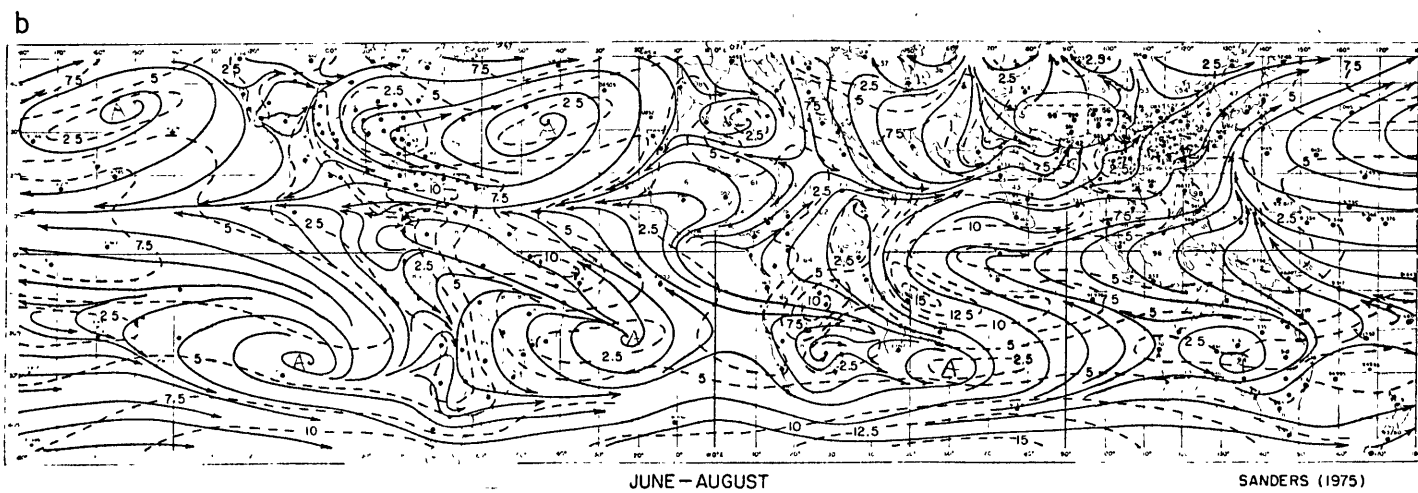
Figure 2.5   Long-term 850 mb tropical flow, a) December-February
              and b) June-August (after Sanders, 1975).

b) equatorial westerlies dominating the Asian and African
monsoon circulations,

c) monsoonal reversal of the flow over the Arabian Sea
in relation to DJF flow,

d) confluence zone over Atlantic and over eastern and
central Pacific found north of its DJF position,

e) still predominantly meridional flow observed along
the Andes.

For the upper-level circulation (200 mb), we observe the following
aspects:

DJF season, 200 mb (Fig. 2.6a):

a) anticyclonic centers over South America ($\simeq$ 13°S
over Bolivia), Africa ($\simeq$ 15°S), northern Australia
($\simeq$ 13°S) and western Pacific ($\simeq$ 11°S, 175°E), all
located at about the same latitude band,

b) three wind speed maxima of the subtropical jet
stream, off the east coast of North America (32°N,
40 m/sec), over northern Africa (28°N, 40 m/sec), and
off the east coast of Asia (35°N, 70 m/sec),

c) extensive region of upper air equatorial easterlies
from Africa to central Pacific.

a

DECEMBER -FEBRUARY

LONG-TERM MEAN 200-mb FLOW. DATA FROM NEWELL (1972), LUFTHANSA (1967), SADLER (1970) and SCHWARTZKOPF (1970). ISOTACHS IN M SEC⁻¹
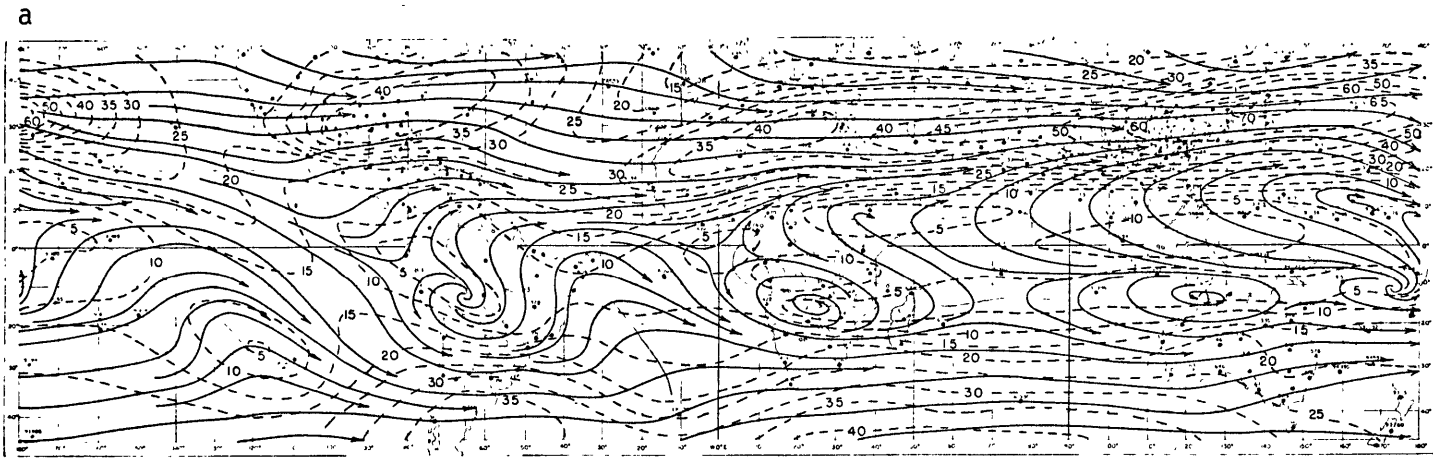
b

JUNE — AUGUST

Figure 2.6   Same as Figure 2.5 but for 200 mb flow.

<u>JJA season, 200 mb (Fig. 2.6b)</u>:

    a) the outstanding feature is the anticyclonic

    circulation centered over the Tibetan Plateau ($\simeq$ 30°N),

    dominating the northern hemisphere upper level

    circulation,

    b) one wind speed maximum of the subtropical jet stream

    is found over southern Australia ($\simeq$ 30°S, 50 m/sec),

    c) the region of upper air equatorial easterlies is

    more extensive than in DJF and spans the whole

    equatorial belt.

The climatological flows depicted in Figs. 2.5 and 2.6 give a clear idea of the degree of zonal asymmetry of the tropical circulations. Both the lower-level and upper-level flows show a considerable complexity with centers of cyclonic and anticyclonic circulation and with easterlies and westerlies throughout the tropics and subtropics. The lower-level flow is made even more complex due to the earth's topography, primarily the Andes and Tibetan Plateau. The upper-level anticyclones have remarkable association with the centers of maximum precipitation.

2.2.3 VELOCITY POTENTIAL AND WALKER AND HADLEY CIRCULATIONS

The velocity vector $\vec{V}$ can be decomposed into the rotational part $\vec{V}_\psi$ and a divergent part $\vec{V}_\chi$, i.e.,

$$\vec{V} = \vec{V}_\psi + \vec{V}_\chi .$$ [2.1]

The velocity potential χ is defined by

$$\vec{V}_\chi = -\nabla\chi$$ [2.2]

and is obtained from a solution of the equation

$$\nabla^2\chi = -\nabla\cdot\vec{V}$$ [2.3]

The east-west and north-south circulations are very clearly revealed by the isopleths of χ and by the streamlines of the divergent velocity vector $\vec{V}_\chi$.

In Fig. 2.7 we show the isopleths of velocity potential for summer and winter (JJA 1967 and DJF 1971 at 200 mb) from Krishnamurti (1971) and Krishnamurti et al. (1973), and in Fig. 2.8, the climatological values of χ for July (850 mb and 200 mb) from van de Boogard (1978).

If lines of velocity potential run parallel to the meridians, then there would be no Hadley-type circulations. On the other hand, if the lines of velocity potential are parallel to latitude circles, then there would be no Walker-type (east-west) circulations. From Fig. 2.7 it is seen that

> the isopleths of χ during northern summer were more
> circular over the region of the summer monsoons and the
> streamlines of the divergent part of the wind were more
> radial than either purely meridional or purely zonal.

a

b
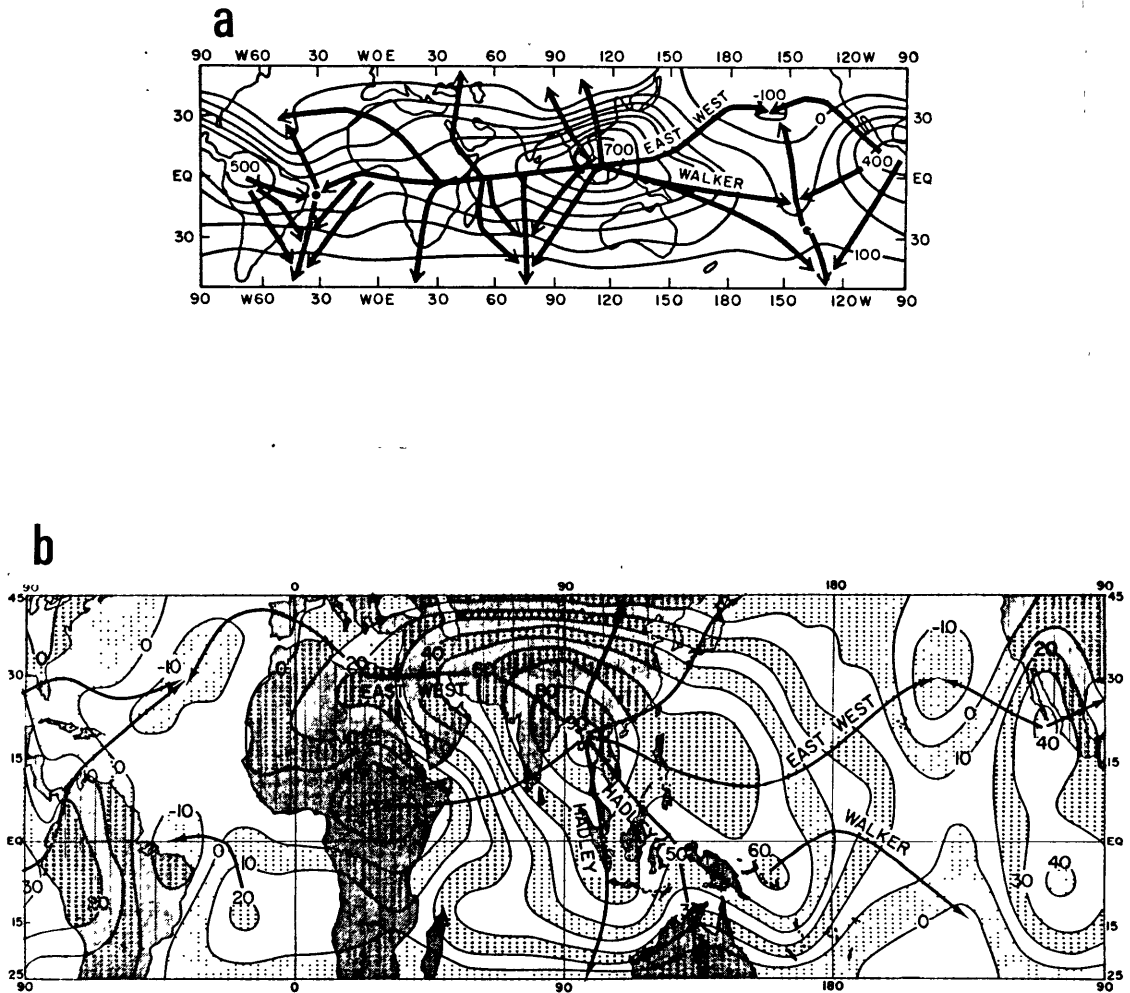
Figure 2.7 Isopleths of the northern winter (a) and northern
summer (b) mean velocity potential at 200 mb, and
streamlines of the divergent part of the wind shown
with arrows (after Krishnamurti et al., 1973 and
Krishnamurti, 1971).

As a consequence, it was inferred that the intensities

of the Hadley and east-west type circulations were

comparable (Krishnamurti et al., 1973).

The same paper also noted that for the northern winter (Fig. 2.7$\hat{b}$)

...[the] isopleths of χ are more parallel to the

latitude circles and the Hadley-type vertical over-

turnings are evidently stronger .... There are two

regions where maximum values of χ are found in the

equatorial latitudes, and streamlines of the divergent

part emanate from these regions .... The two centers of

χ maxima are located over the northwestern part of South

America and the equatorial rainbelt near Borneo ... The

streamlines of the divergent motions converge near 30°N

over the Pacific and Atlantic Oceans directly above the

sea level, subtropical high pressure belts. The

strongest divergent motions are found over eastern Asia

where local contribution to the Hadley circulation

($-\partial\chi/\partial y$) is largest. This is also the region where the

strongest winds, at 200 mb during northern winter, were

noted by Krishnamurti (1961) .... the intensity of this

circulation [east-west] is comparable to that of Hadley-

type circulations .... the intensity of the east-west

circulation during the northern summer is somewhat

stronger than during northern winter.

The climatological values of the velocity potential for July at

200 mb in Fig. 2.8a reproduces the features shown in Fig. 2.7a. For the

lower levels (850 mb) in Fig. 2.8b, we observe that the center of χ

b

200 mb Velocity Potential (contour interval of 10m) —July

a

850 mb Velocity Potential (contour interval of 5m) —July
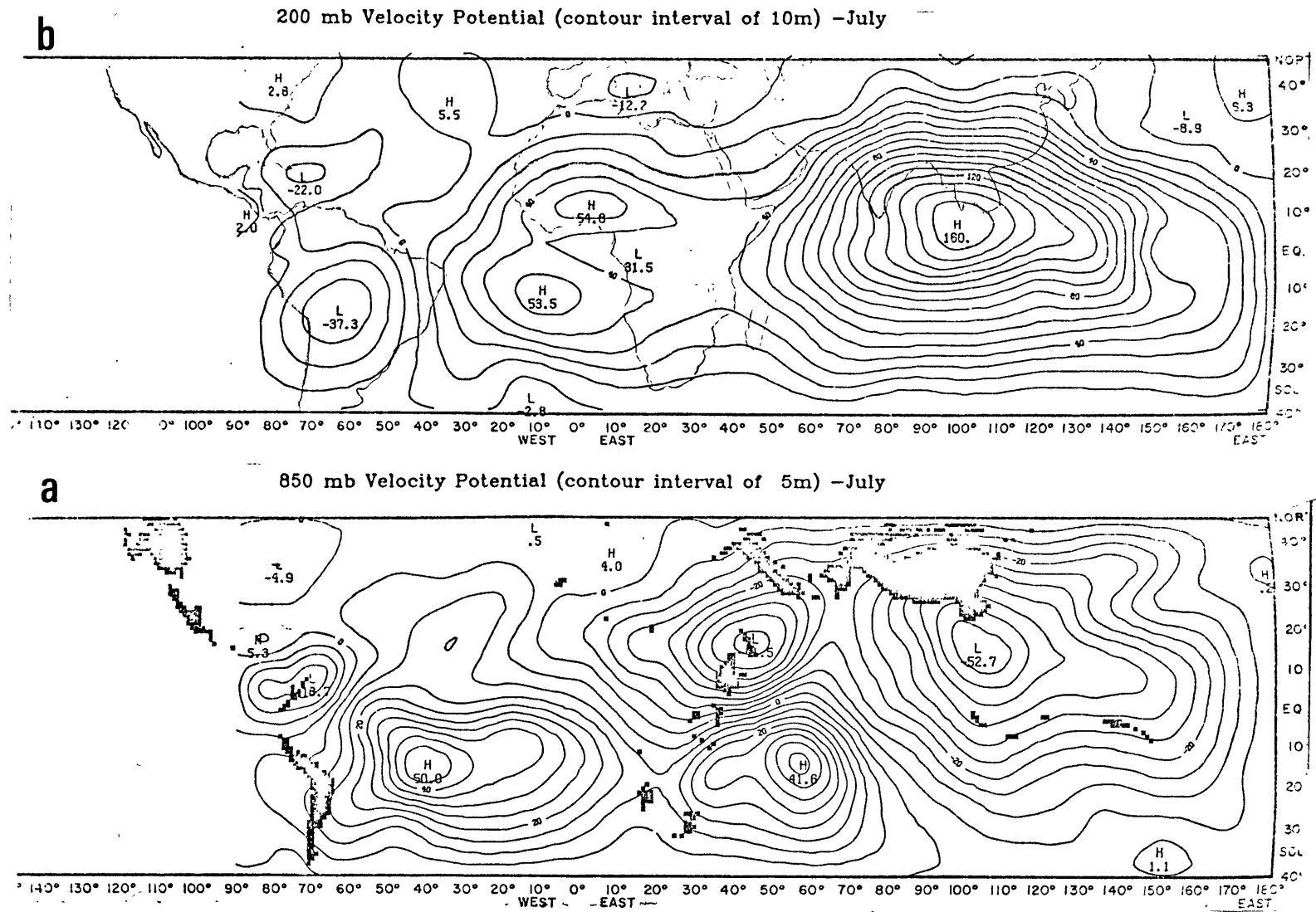
Figure 2.8   Isopleths of the July mean velocity potential at 850 mb (a),
and at 200 mb (b) (units: $10^7 m^2 s^{-1}$, interval every 10 units)
(after van de Boogaard, 1977).

minimum is found over Southeast Asia, consistent with the position of the χ maximum at 200 mb, and that the isopleths of χ are more circular around this center rather than more zonally or meridionally oriented, thus indicating convergence of mass from all directions (although the flow here is complicated by the presence of the Tibetan Plateau topographical barrier). We also note a center of χ minimum over the South Atlantic and Indian Oceans at the latitude belt of the oceanic, sub-tropical highs (values of χ for the eastern Pacific are not shown in Fig. 2.8b).

In Fig. 2.9, we show the mean velocity potential and mean divergent part of the wind at 200 mb during southern summer over South America from Virji (1981). It is clearly seen, from Fig. 2.9 for the streamlines of the divergent flow, that there is an outflow in all directions at 200 mb and that this is consistent with the idea of vertical circulations in a zonal plane (Walker-type) and in a meridional plane (Hadley-type) with comparable intensities.

Schematic diagrams of east-west cells are shown in Fig. 2.10 from Newell (1979) for January and in Fig. 2.11 from Krishnamurti et al. (1973) for summer and winter. In the latter figure the intensity of east-west circulation, I_E at 200 mb, is given by

$$I_E = \frac{1}{(y_2 - y_1)} \int_{y_1}^{y_2} \frac{\partial \chi}{\partial x} \, dy \qquad [2.4]$$

where y_1 and y_2 are the southern and northern limits of the tropical channel of interest, $y_1 = 15°S$ and $y_2 = 15°N$ for northern winter and $y_1 = 0$ and $y_2 = 30°N$ for northern summer. Of interest in Figs. 2.10
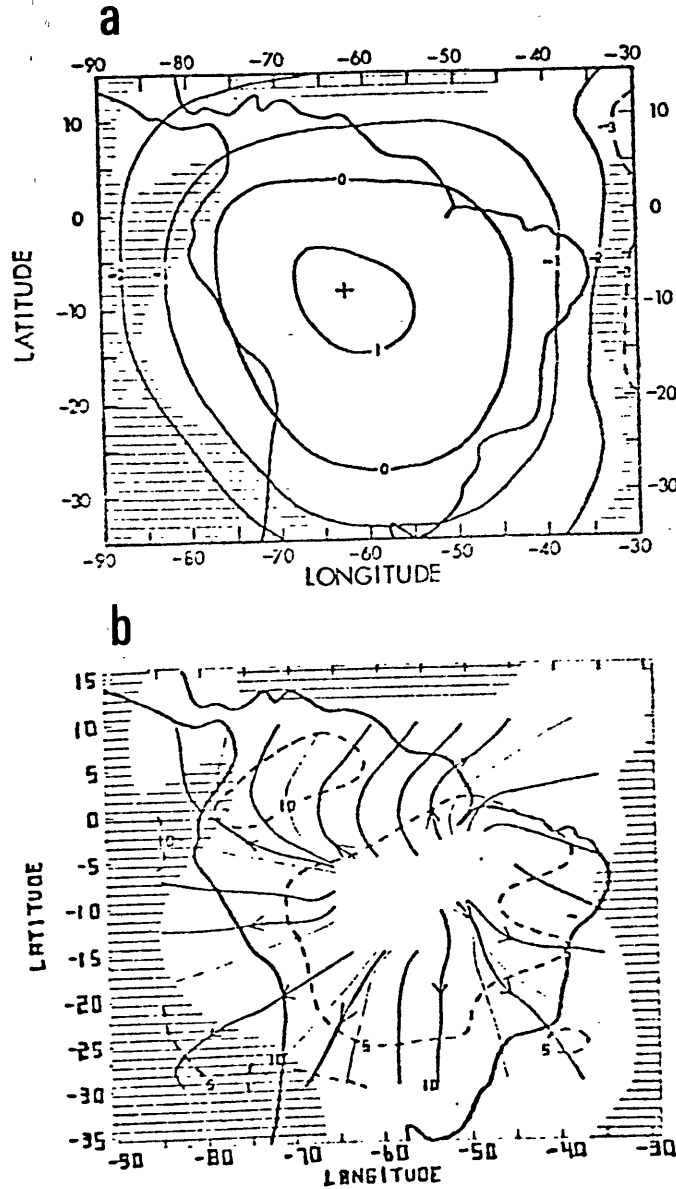
Figure 2.9   Seasonal mean velocity potential at 200 mb (a)(units: $10^7 m^2 s^{-1}$), and seasonal mean divergent part of the wind at 200 mb (b) (units: ms^{-1}) during southern summer (after Virqi, 1979).
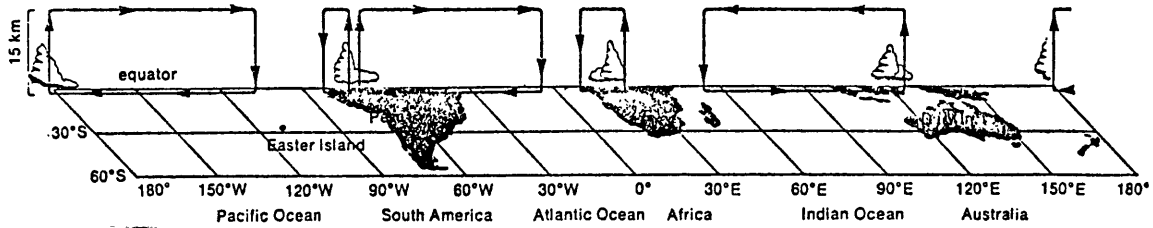
Figure 2.10   Zonal circulations in January as deduced from calcu-
               lations of vertical motion patterns by Boer and Kyle
               (see Chapter 9 of Newell et al.,1974; after Newell,
               1979).
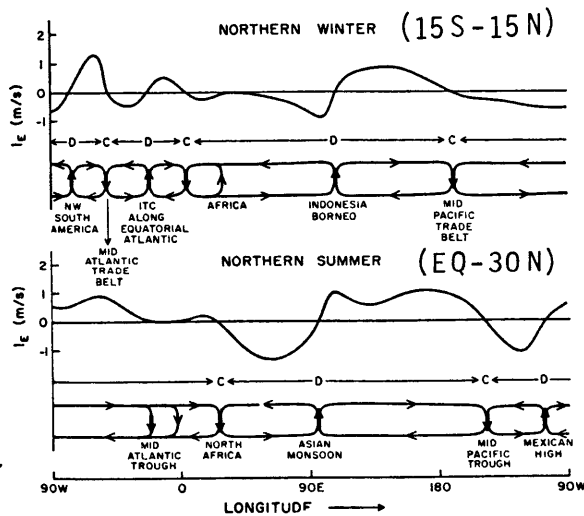
Figure 2.11   Intensity of east-west circulation, I_E, at 200 mb,
               as a function of longitude, and a schematic diagram
               of east-west cells on mass continuity; C and D
               indicate regions of upper tropospheric convergence
               and divergence, respectively (after Krishnamurti
               et al., 1973).

and 2.11 are the locations of ascending and descending motion and the relative range of the eastward and westward branch for each cell. We note that Fig. 2.10 shows the sinking motion taking place at the eastern Atlantic and Pacific Oceans and at the western Indian Ocean. In Fig. 2.11 the cells present more zonal structure, and the descending motion takes place over central Pacific and Atlantic Oceans for the northern winter. This may be due to the latitudinal averaging in the calculations of I_E and also to Fig. 2.11's being based on calculations for one season only, whereas the schematic circulation of Fig. 2.10 is based conceptually on the tropical climatological forcing. It should be pointed out that the idealized longitudinal structure of the cells shown in Figure 2.11 for southern summer is not consistent with rainfall maps.

2.3 FGGE DATA ANALYSIS (GLAS)

2.3.1 BACKGROUND AND DATA SET DESCRIPTION

The study of tropical meteorology has been historically handicapped by the lack of observations. The causes for the lack of a more comprehensive observational network are two-fold. First, because large parts of the tropical and subtropical regions are covered by oceans, and second, because tropical lands traditionally have been much less developed than the midlatitudes. Meteorological reasons are partly responsible for the large regions of low populational density: the impenetrability of the tropical rain forests in the equatorial rainbelt and the inhospitality of the vast subtropical deserts.

However, the perspectives have greatly improved with the advent of satellite-derived meteorological information. Data such as vertical

profiles of temperature and humidity, cloud winds, radiative balance terms at the top of the atmosphere, cloudiness, sea surface temperature, etc., are becoming routinely available and are being used to improve the forecasts of numerical weather forecasting models. This added capability, along with the improvement of the ground-based observational network, has contributed to closing the observational gap in the tropics.

The FGGE (First GARP Global Experiment) program was carried out during 1979 as the first attempt to gather meteorological data in a global scale with the aid of satellites and to use these data in the integration of General Circulation Models (GCM's). Data collection included radiowind, airplane, ship and satellite data. From Dec. 1978 through Feb. 1980, global data was collected every 6 hours. Density of coverage was substantially augmented during two special observing periods (Jan.-Feb. and May-June 1979).

Paegle and Baker (1982) describe the GLAS analysis system (Halem et al., 1982) as "...consist[ing] of an objective analysis scheme, which makes use of the continuity provided by a first guess, which is a 6 h forecast from the previous analysis. The first guess is then corrected by all the data collected with a ±3 h window, about each analysis time. The analysis scheme (Baker et al., 1981) ... takes into account the density and the quality of the observations." The model used is the GLAS fourth-order global atmospheric model described in Kalnay-Rivas et al. (1977) and Shukla et al. (1981).

The FGGE data collection was the most encompassing and complete global data-gathering operation for the earth's atmosphere to date. However, we recognize that for data-sparse regions the GLAS analysis may

be unduly influenced by the model's particular physical parameteriza-tions. For instance, for large expanses of the tropical and southern hemisphere oceans where vertical profiles of atmospheric quantities are seldom obtainable, satellite-derived vertical profiles of temperature and cloud-track winds were utilized in the FGGE experiment. Because of its less-than-perfect representation of physical processes, the model might tend to generate unrealistic fields. However, every 6 hours a new set of observations was inputed, and the model was corrected to adjust itself to the observations. If we assumed that observational errors are not large, it is hoped that even for data-sparse areas this method of constraining the model to follow whatever observations are available would limit the model's drift from the actual climatology.

The data set analyzed in this section was derived through this data-assimilation procedure for the period January 5 through March 5, 1979 (Special Observing Period-1, SOP-1). It would have been desirable to include Dec. 1978 in our analysis to obtain a better representation of mean southern summer conditions and also to analyze the data for the JJA season. Unfortunately, only data for those two months was available to the author when the analysis was conducted.

To check the validity of the FGGE data set assimilated by the GLAS GCM, we will compare it with the same data set assimilated by the European Center for Medium-Range Weather Forecast (ECMWF) GCM. If the model's particular physical parameterization is incorrectly influencing the results, we would expect the results of the two GCM's to differ significantly. Also, we will compare the generated diabatic heating field with independently obtained heights of the top of precipitating

cumulus clouds; these heights provide a crude estimate of the areal
distribution of latent heating. We believe that the model's physical
parameterization has not caused the simulated fields to depart, to a
large degree, from the true fields in the scale of motion with which we
are concerned (planetary scale).

2.3.2 DIABATIC HEATING AND VERTICAL VELOCITY

Total diabatic heating, as shown in Figs. 2.12, 2.13, and 2.14, is
calculated in the GLAS model as the sum of individual diabatic heating
components: latent heat of condensation, net radiative heating, sensible
heating, vertical diffusion of heat, and adiabatic adjustment. For the
tropical troposphere generally only the first 3 terms are important, with
sensible heating being important only in the lowest part of the
atmosphere. Heat budgets studies (Katayama, 1974; Cornejo-Garrido and
Stone, 1977; Kalnay, 1981, personal communication) have shown that latent
heating is the largest diabatic heating term in the tropics. Without
incurring much error, one can think of the distribution of diabatic
heating presented in the figures below as being predominantly the
distribution of latent and radiative heating, and one can confidently say
that its longitudinal variations can be almost exclusively attributed to
zonal variations in latent heating since the net radiative heating
presents much less zonal asymmetry as well.

Global distribution of total diabatic heating at 400 mb (approximate
level of maximum heating) is shown in Fig. 2.12. We observe a maximum in
excess of 7°K/day over northeastern South America and a succession of
zonally oriented maxima > 7°K/day and up to 11°K/day roughly centered at

GLAS-GCM WIT' FGGE DATA ASSIMILATION

DEG K/DAY DIAB/.TIC HEATING 400 MB

5 JAN TO 5 MAR 1979

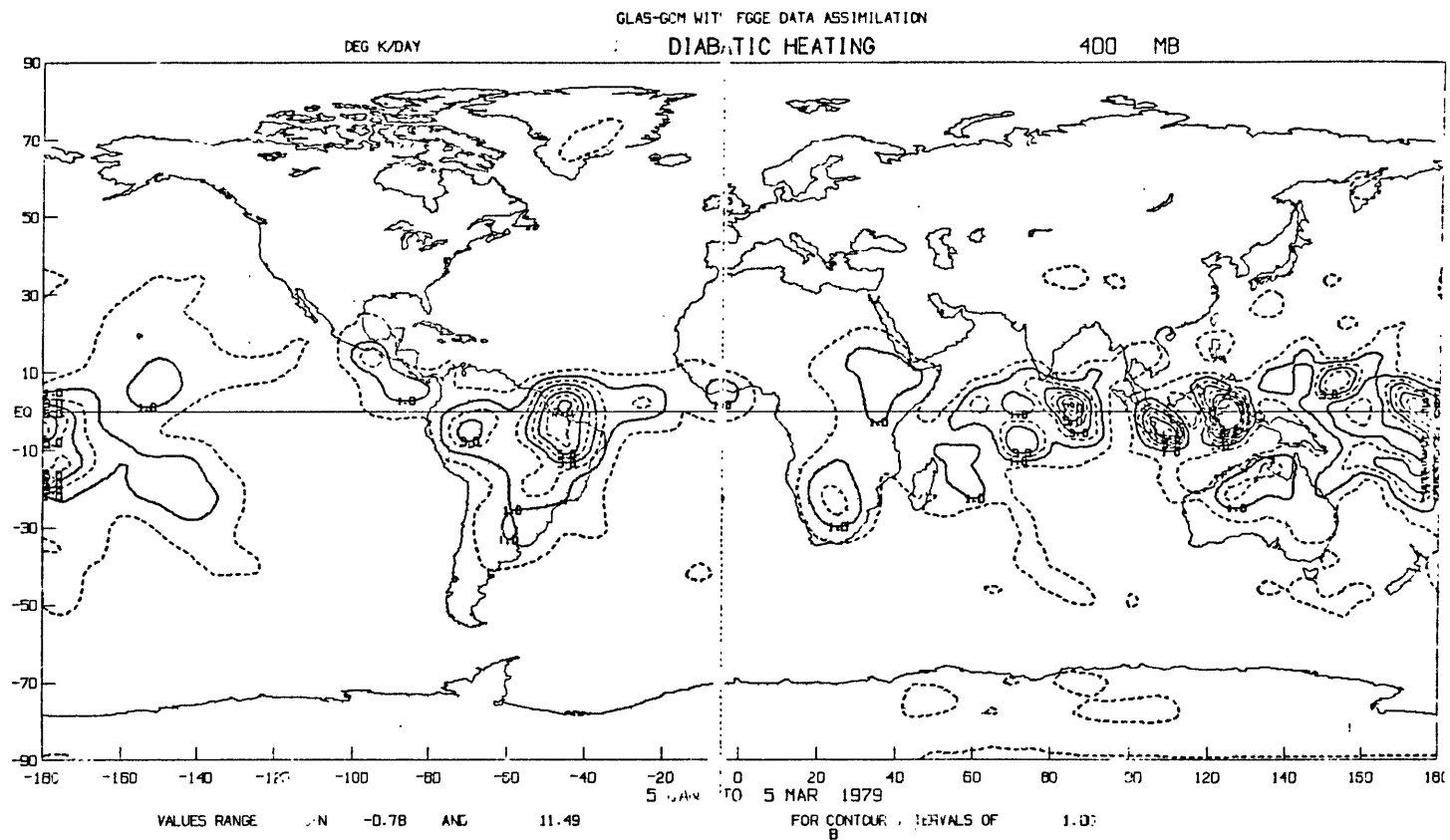VALUES RANGE N -0.78 AND 11.49 FOR CONTOUR . ItRVALS OF 1.0:
B

Figure 2.12 Diabatic heating distribution at 400 mb for Jan-Feb, 1979
(units: K/day, interval every unit).

the equator, from the eastern Indian Ocean eastward to central Pacific.
There is a region of heating over south Africa but of smaller intensity.
We note the occurrence of strong diabatic heating over the western
Pacific centered at the dateline and the band of heating of the SPCZ
protruding into the southern hemisphere in a NW-SE orientation. This
maximum heating over the western Pacific appears to be displaced eastward
of its climatological position for the southern summer season (compare
with Figs. 2.1 and 2.2a).

In Fig. 2.13 we show the global distribution of total diabatic
heating averaged for the atmospheric column from 100 to 1000 mb. The
geographical distribution resembles, to a great degree, the one of
Fig. 2.12 at 400 mb. We remark that values of up to 4°K/day,
corresponding roughly to precipitation rates of up to 15 mm/day, are
observed over South America. The conspicuous feature in Fig. 2.13, in
addition to the existence of isolated heat sources over the tropics, is
the realization that tropical diabatic heating provides the most intense
heat source for the whole troposphere. We note that the main features of
Figure 2.13, i.e., diabatic heating maxima over South America, Indonesian
maritime continent, and western Pacific including the SPCZ are consistent
with the precipitation distribution shown in Figure 2.3a.

To provide a clearer picture of zonal asymmetries in the diabatic
heating field, we averaged the total diabatic field from 100 mb to
1000 mb and from 30°S to 14°N. The choice of this latitudinal band is
due to the observation that most of the heating is found within this band
for the southern summer. The result of this averaging and also the
corresponding distribution of vertical velocity (omega velocities) is
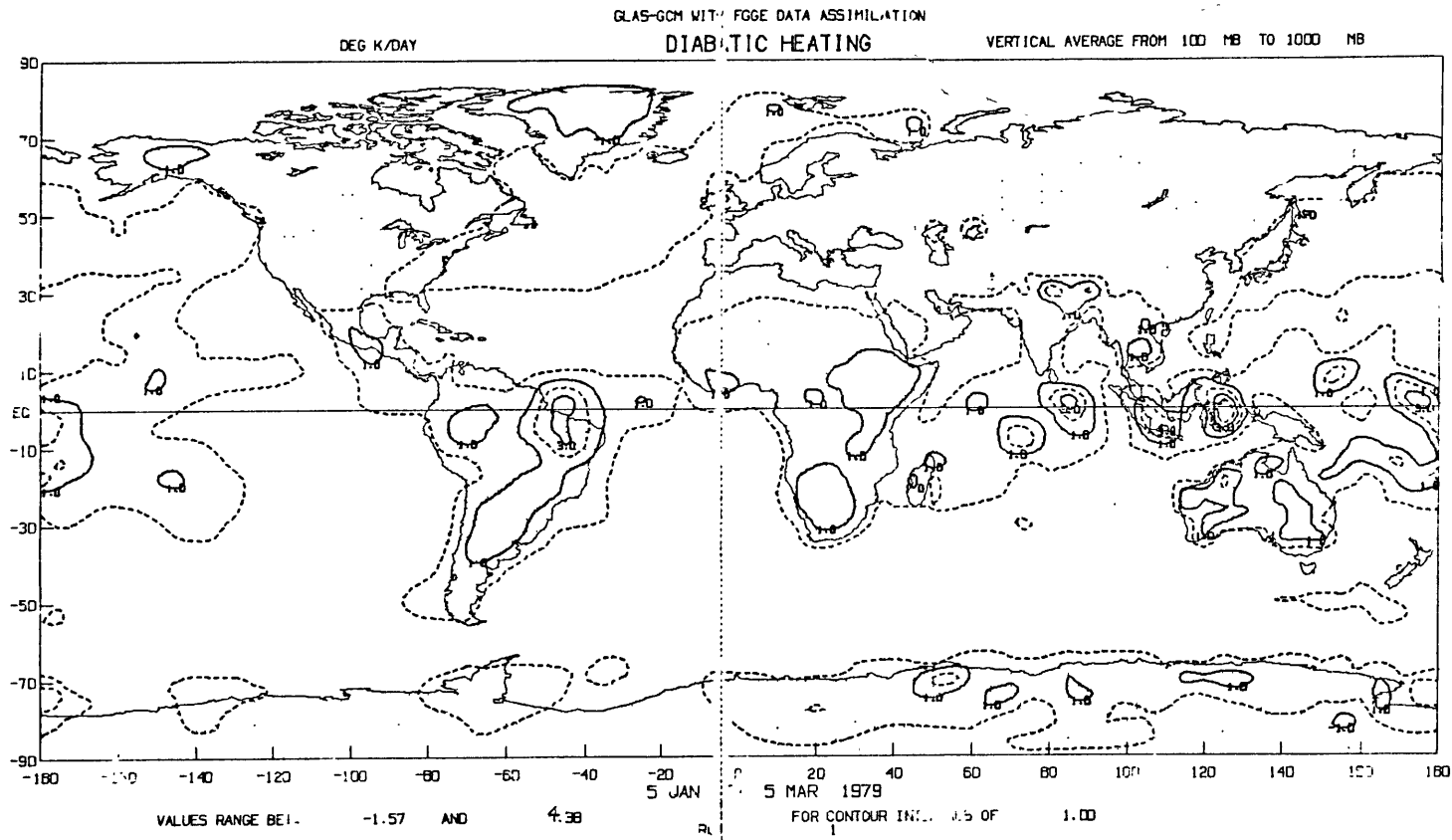depicted in Fig. 2.14. Here the east-west asymmetries in diabatic

Figure 2.13   Vertically averaged diabatic heating distribution for Jan-Feb, 197ⁿ
(units: K/day, interval every unit).

heating (solid line) and vertical omega velocity (thin line) are striking. Note the heating regions of South America, Africa, Indonesia-Phillipines, and western Pacific and the cooling regions of eastern Atlantic, Indian and Pacific Oceans. The vertical omega velocity follows the diabatic heating lines quite well, indicating that the main thermodynamic balance is between diabatic heating (cooling) and adiabatic expansion (contraction).

In Figure 2.14 the African heat source seems to attain a magnitude comparable to the other three heat sources, a feature that was not seen in Figure 2.12, for the global distribution of diabatic heating at 400 mb

TABLE 2.1

MAXIMUM DIABATIC HEATING RATES IN °K/DAY

FOR REGIONS OF STRONG HEATING

DURING SOP-1*

Level (mb)	South America	Southern Africa	Central Africa	Indonesia	Western Pacific
200	0.6	0.1	- 0.2	1.2	0.5
250	1.3	0.2	- 0.1	2.8	1.2
300	2.7	1.2	0.5	4.8	2.5
400	7.2	2.2	1.5	10.5	6.0
500	5.5	1.7	1.5	9.0	6.0
700	4.2	2.0	2.0	5.0	4.2
850	1.5	3.7	4.0	3.0	3.0
1000**	0.5	2.5	3.5	0.2	0.2

* SOP-1 : Special Observing Period of FGGE, January 5 to March 5, 1979.

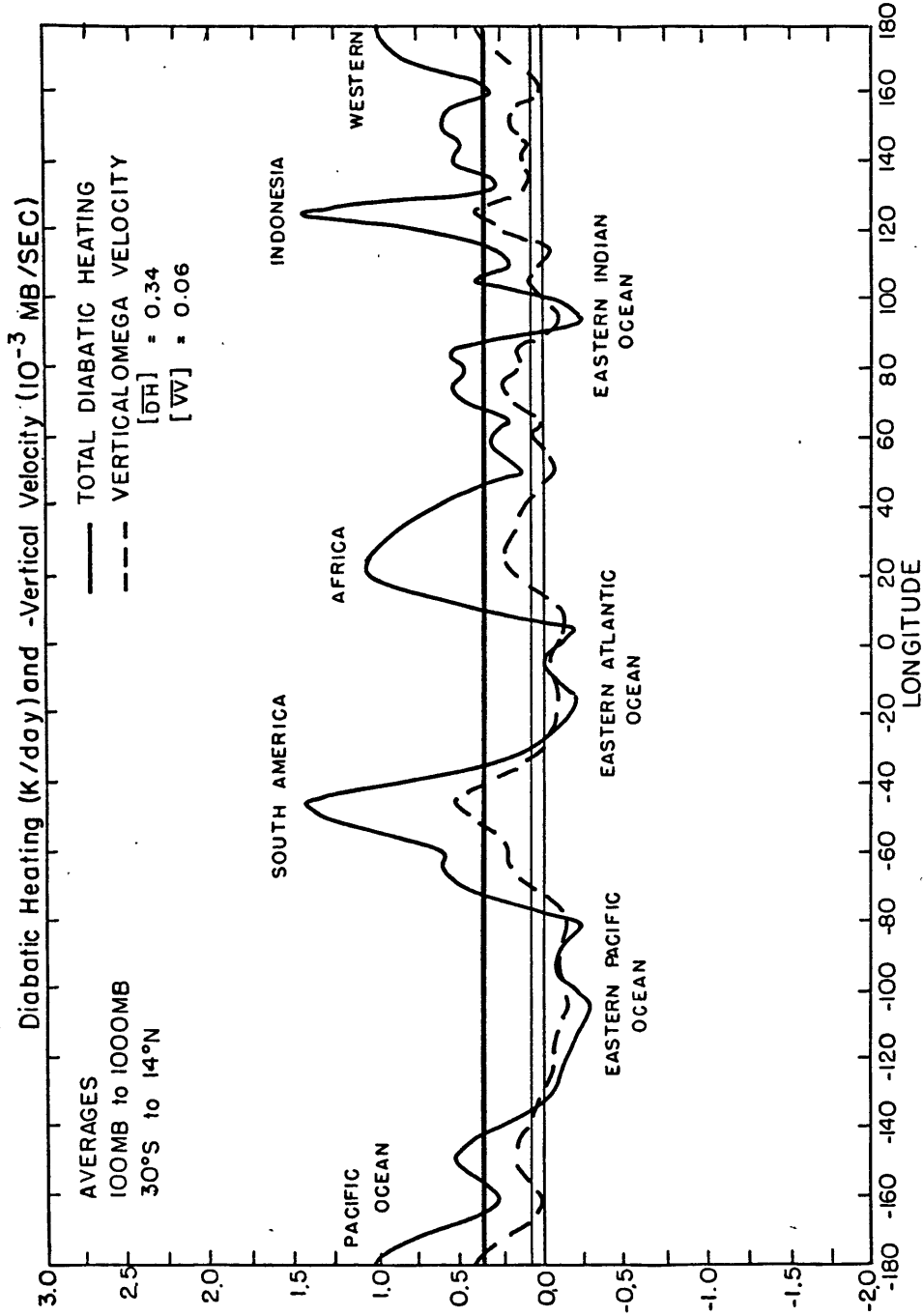** For areas where the ground is above the 1000 mb surface, the heating rates were extrapolated.

Figure 2.14 Vertically and latitudinally averaged diabatic heating (thick line, units: K/day) and vertical omega velocity (thin line, units:10^{-3}mbs-1) for Jan-Feb, 1979; zonal averages of diabatic heating (thick straight line) and vertical omega velocity (thin straight line) are indicated.

where the maximum heating rates over Africa are slightly over 2°K/day,
which is much less than heating rates over South America (up to 7°K/day)
and Indonesia - western Pacific (up to 10°K/day). This apparent paradox
in Figure 2.14 can be understood as caused by the latitudinal and vertical
averaging employed. In Table 2.1 we list the approximate maximum heating
rates from 200 to 1000 mb for the different heat sources. It is readily
seen from Table 2.1 that the diabatic heating over southern and central
Africa was rather shallow with maximum rates at the lower levels so that
the vertical averages show two broad regions of heating (albeit not large)
over southern and central Africa (Figure 2.13). When these two broad
areas of somewhat weak and shallow heating were averaged latitudinally
from 14°N to 30°S, they produced the maximum of Figure 2.14 at
approximately 25°E. The vertical omega velocity at 400 mb in Figure 2.15
shows that the magnitude of the ascending motions over southern Africa is
at most 1/4 of that for the other heating regions. Also, the analysis of
vertical omega velocities for other levels (not shown here) shows that
$|\partial\omega/\partial p|$ at the upper levels is considerably smaller for the southern
Africa heat source than it is for the other heat sources, i.e, there is a
very weak divergence maximum associated with that heat source.

The global distribution of vertical omega velocity at 400 mb is shown
in Fig. 2.15. Although the field is much noisier than the diabatic
heating field, it reproduces well the main features found in Fig. 2.12. It
shows highest negative values (rising motion) over the convectively active
regions. Very large positive values at high latitudes are not real but
were introduced artificially by the numerical scheme of the GLAS model
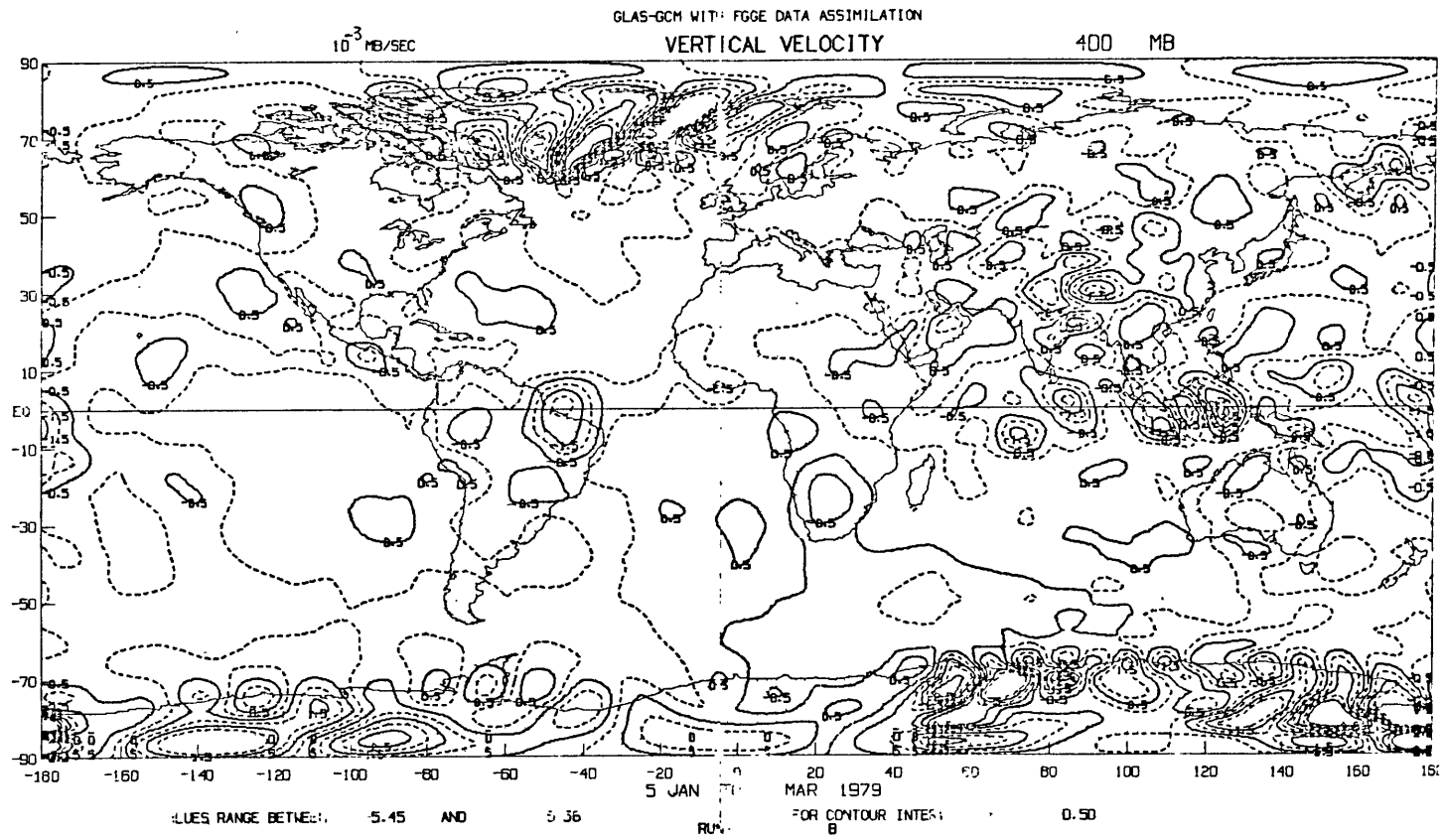(Kalnay, 1981, personal communication).

GLAS-GCM WIT' FGGE DATA ASSIMILATION

VERTICAL VELOCITY   400   MB

10^-3 MB/SEC

Figure 2.15   Vertical omega velocity at 400 mb for Jan-Feb, 1979
              (units 10^{-3} mbs^{-1}, interval every 0.50 units).

To provide a check on the validity of the model-derived distribution of diabatic heating, we present Fig. 2.16, which shows the global distribution of cloud top heights as derived from independent radiation calculations from Susskind (1982). It matches reasonably the geographical distribution of diabatic heating of Figs. 2.12 and 2.13 for the tropics. Importantly, it confirms the existence of isolated convective regions throughout the tropics exhibiting strong zonal gradients.

2.3.3 HORIZONTAL WINDS

To gain some idea of the spatial and temporal coverage of the FGGE observing system, we show in Figure 2.17a the geographical distributions of rawinsonde stations, satellite temperature soundings, and cloud-track winds. An assessment of the FGGE observing system is given by Halem et al. (1982).

The global distributions of the zonal component of the wind at 850 and 200 mb are shown in Fig. 2.17b and Fig. 2.17c, respectively. We observe the following features for 850 mb:

a) mostly easterlies throughout the tropics with
maximum in excess of 10 m/sec over central equatorial
Pacific,

GLAS RETRIEVED CLOUD TOP PRESSURE JAN 1979
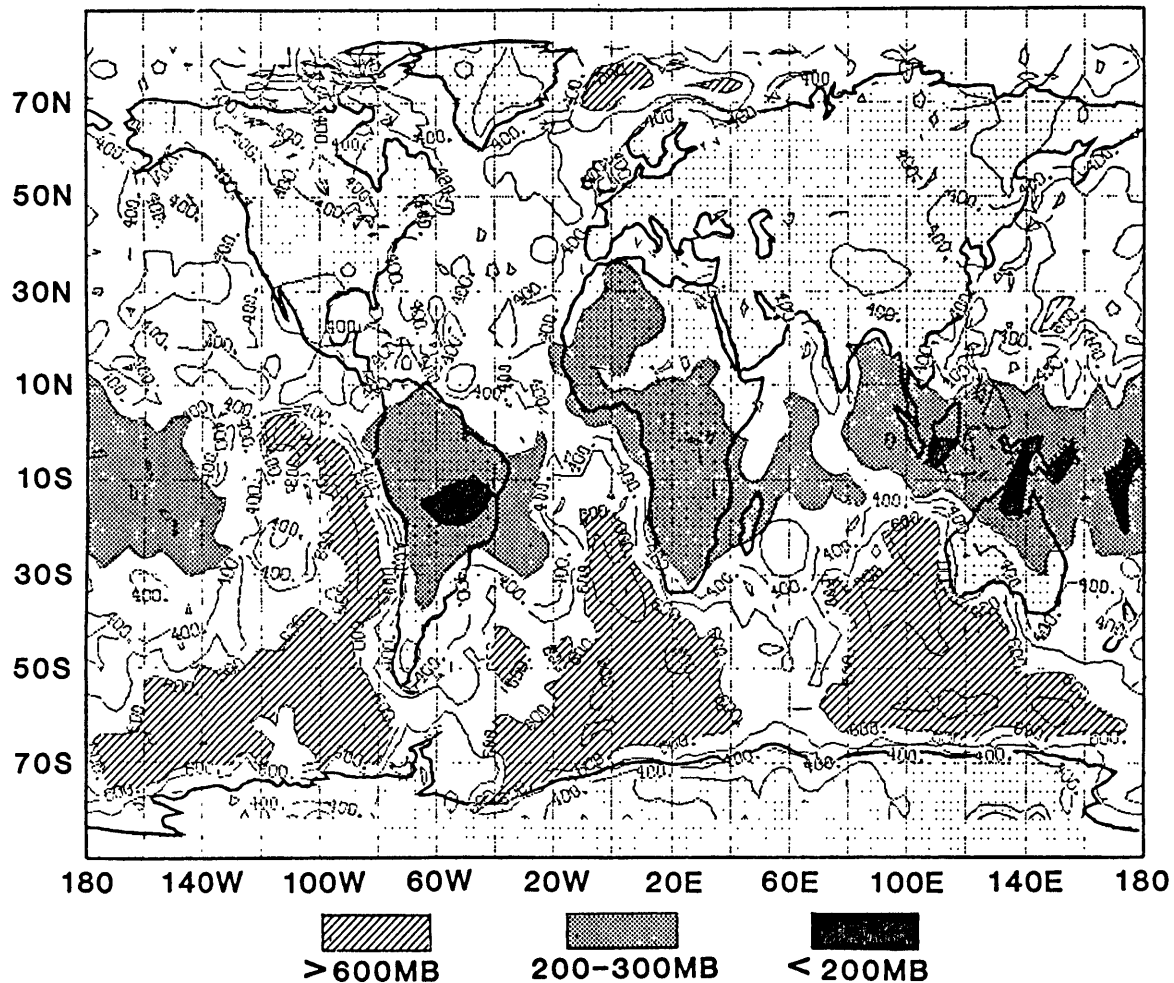
>600MB   200-300MB   <200MB

Figure 2.16 Average effective cloud top pressure, weighted by cloud fraction, retrieved by GLAS for January 1979. Only the areas of highest clouds (P_c < 300 mb) and lowest clouds (P_c > 600 mb) are shaded.(after Susskind et al., 1982).
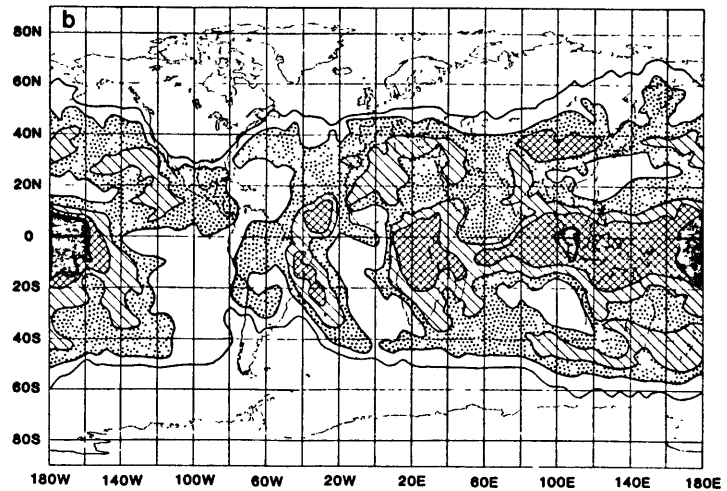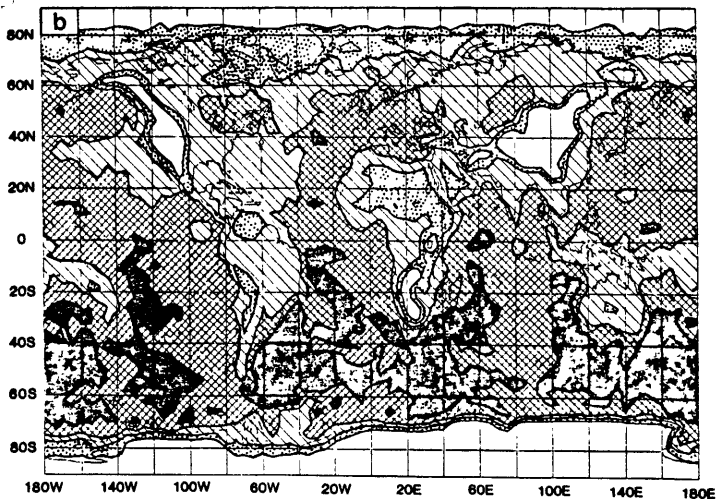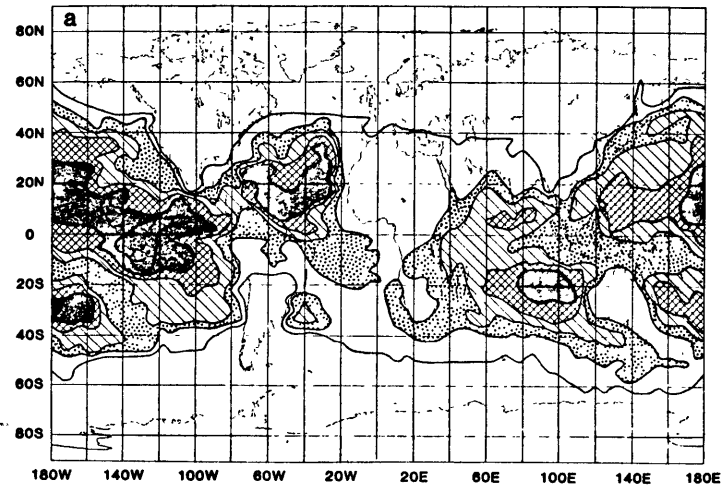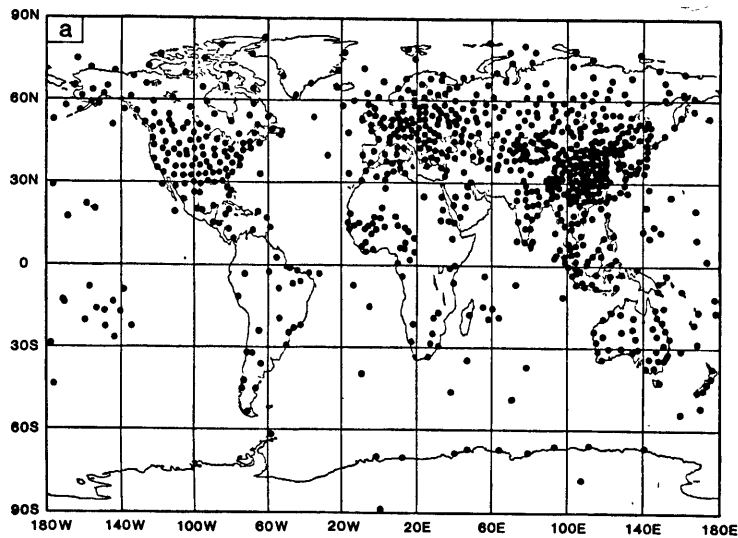
Figure 2.17a   Geographical distributions of a) rawinsonde stations reporting at 0000 GMT
9 January 1979, b) satellite temperature soundings per day for the period
5-21 January 1979, and cloud-track winds per day for the period 5-21 January
1979, c) low-level (below 700 mb) winds, d) high-level (above 400 mb) winds
after Halem et al., 1982).

Figure 2.17b Zonal velocity at 200 mb for Jan-Feb, 1979
(units: ms^{-1}, interval every 5 units.
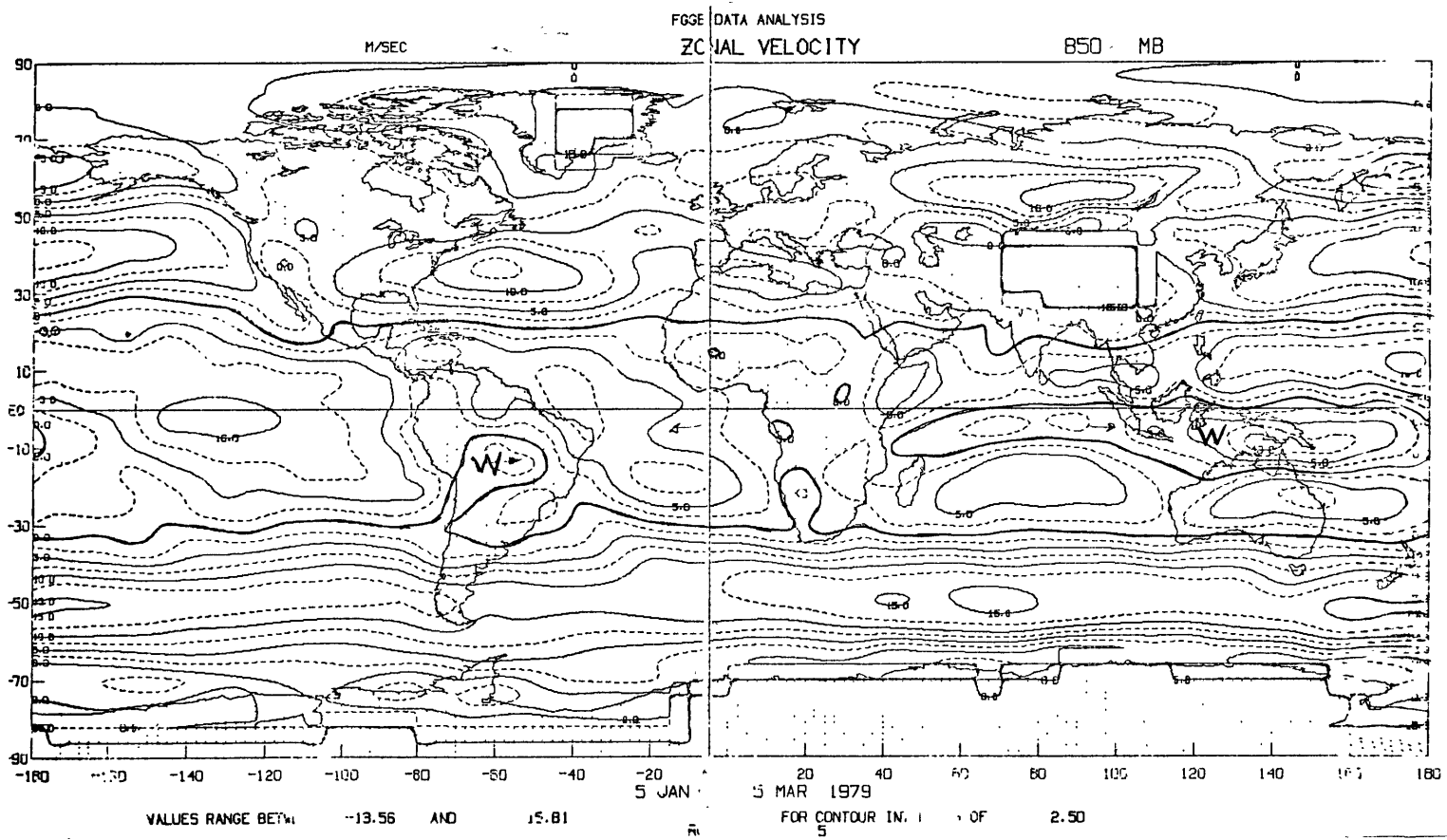
Figure 2.17c   Same as Figure 2.17b but at 850 mb (interval every 2.5 units).

b) existence of equatorial westerlies extending from the western Indian Ocean eastward to the dateline and from the equator to 15°S, exhibiting maximum of more than 10 m/sec just south of the Phillipines and also over South America and southern Africa.

For 200 mb we observe several quite interesting features:

a) the existence of weak equatorial easterlies (wind speeds < 7 m/sec) at the upper levels from eastern Atlantic westward to the dateline and over a smaller area of South America,

b) the position of the upper level easterlies corresponding approximately with the position of lower level westerlies,

c) the meandering subtropical jet stream at about 30°N, showing three maxima in wind speed, off the east coast of North America (u > 50 m/sec), over the Persian Gulf (u > 40 m/sec) and just south of Japan (u > 65 m/sec),

d) in the southern hemisphere the jet stream is weaker (u < 35 m/sec), and is located farther poleward (45° to 50°$\underset{S}{N}$).

Figs. 2.18a and 2.18b depict the global distributions of the meridional component of the wind at 850 mb and 200 mb. For 850 mb we observe that the meridional wind is generally weak, and the maximum (v ≃ -6m/sec) is found off the east coast of South America at about 25°S;
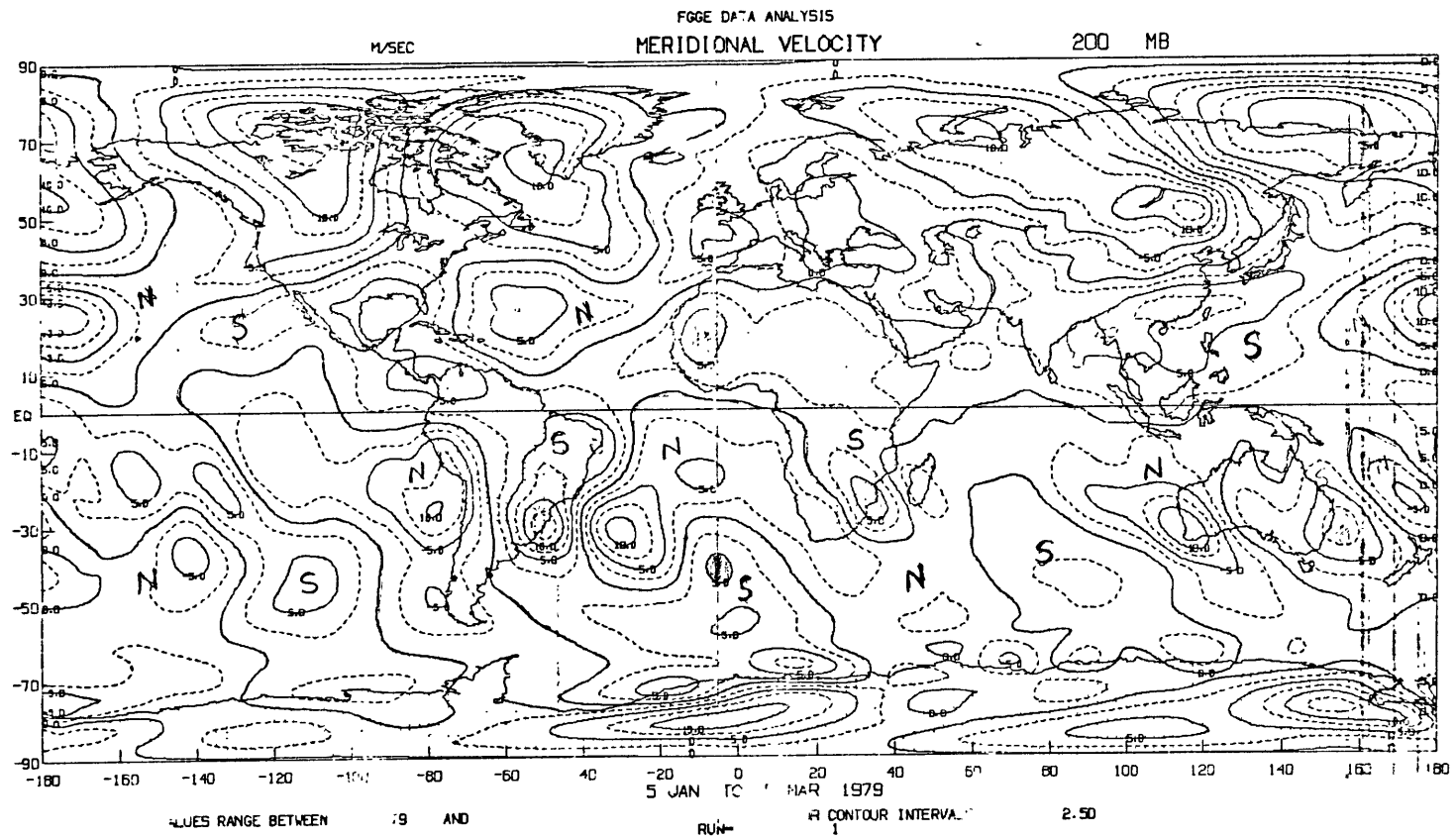
Figure 2.18a   Meridional velocity at 200 mb for Jan-Feb, 1979
             (units: ms^{-1}, interval every 2.5 units).
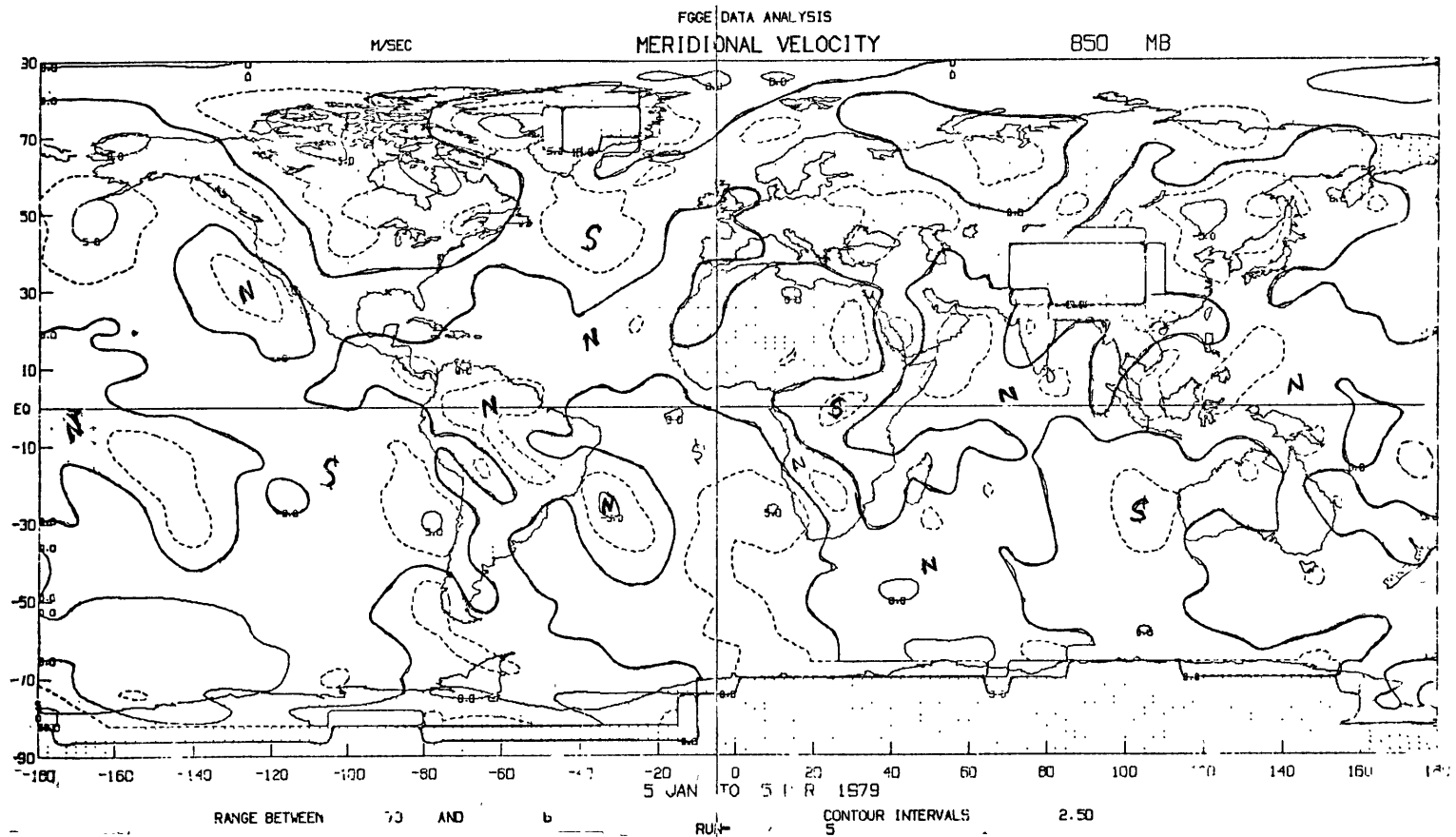
Figure 2.18 b Same as Figure 2.18a but at 850 mb.

also, it is noteworthy to observe the occurrence of both southerlies and northerlies in the tropics and subtropics of both hemispheres. At 200 mb the striking feature is the waves over South America (Kalnay and Halem, 1981) and adjacent oceans and over Australia and adjacent oceans. At around 30°S we observe northerlies off the west coast of South America, southerlies over the continent, and northerlies again off the east coast. The maximum magnitude of these meridional winds is in excess of 15 m/sec, and the zonal scale of the wave (1/2 of the wavelength), $\simeq 2 \times 10^3$ to 3×10^3 km, is rather short. At about the same latitude band, i.e., 30°S, we see northerlies over eastern Australia, southerlies over the western part of that continent, and northerlies again over the western Pacific. This pattern bears similarity with the one over South America; however, the magnitude of the meridional winds is about half as large as that of the meridional winds over South America, and the scale of the wave is somewhat larger, $\simeq 3 \times 10^3$ to 4×10^3 km. The same pattern, northerlies - southerlies - northerlies, is found over southern Africa and adjacent oceans, although the amplitude of the wave is considerably smaller.

2.3.4 GEOPOTENTIAL HEIGHT AND TEMPERATURE

Global distributions of geopotential heights at 1000 mb and 200 mb are shown in Figs. 2.19a and Fig. 2.19b, respectively. At the lower levels, Fig. 2.19a, we observe the alternating pattern of highs and lows
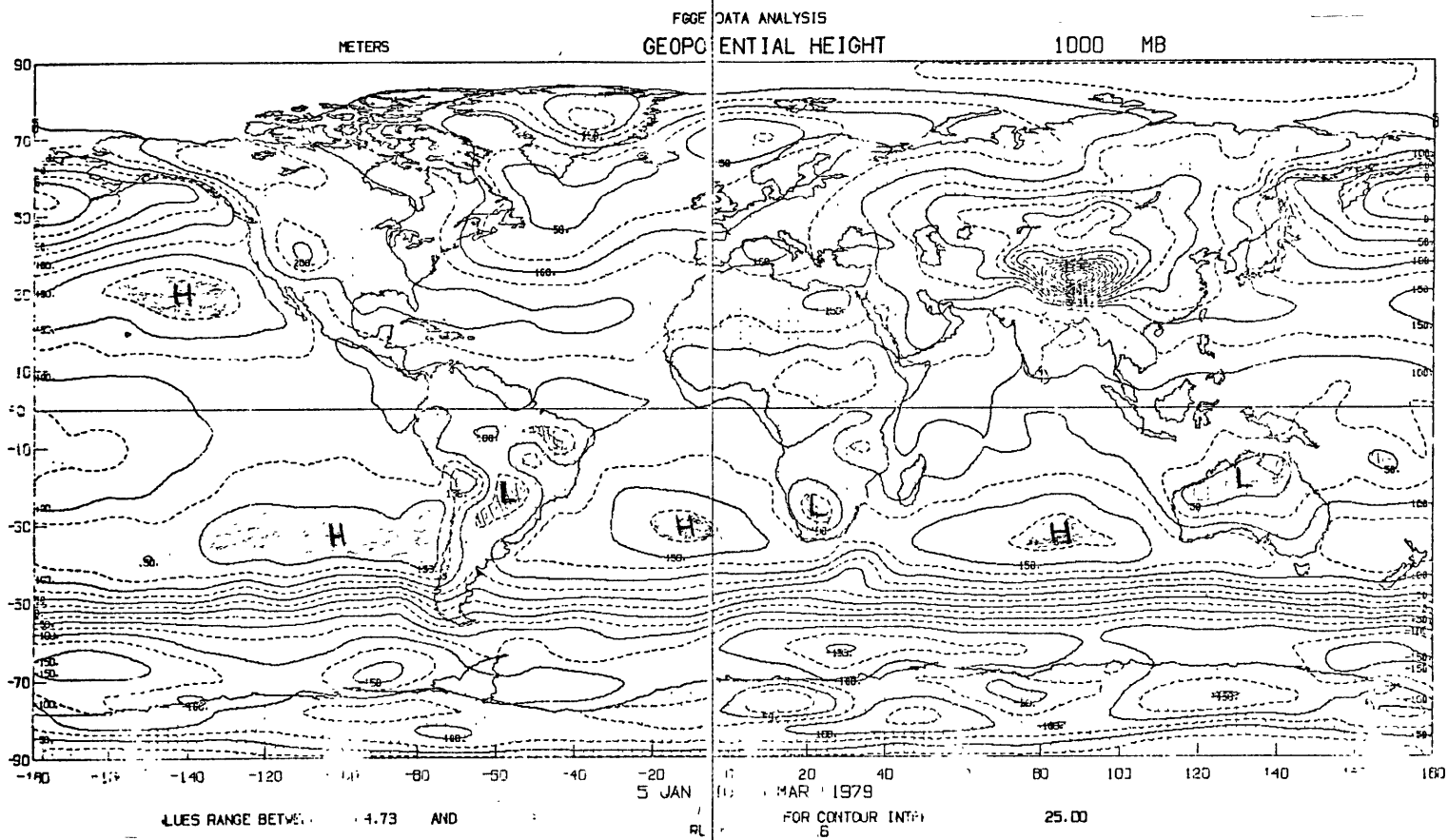
Figure 2.19a   Geopotential height at 1000 mb for Jan-Feb, 1979
(units: ms⁻¹, interval every 25 units.

FGGE DATA ANALYSIS

METERS   GEOPOTENTIAL HEIGHT   200   MB

VALUES RANGE +   :0791.19   AND   -2.66   FOR CONTOUR   -VALS OF   50.00

5 JAN   5 MAR 1979
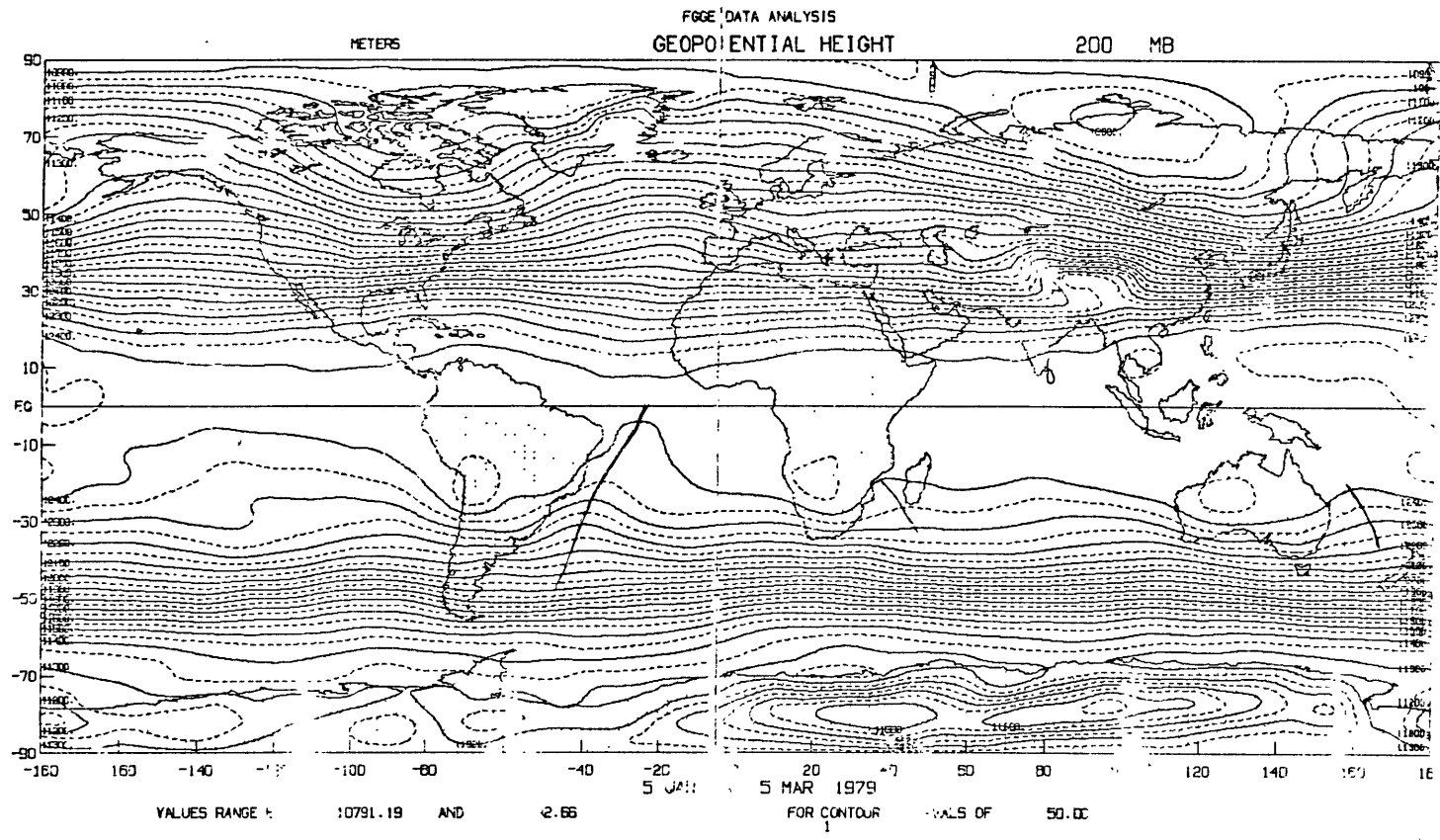
Figure 2.19b Same as Figure 2.19a but at 200 mb (interval every 50 units).

in the southern hemisphere with continental lows and oceanic highs. The northern hemisphere subtropical belt of high pressures is more zonally oriented. Fig. 2.19b, for the upper levels, shows some very interesting features. Now we see continental highs over South America, southern Africa, and northern Australia, approximately at the same position where the continental lows were found at the lower levels. In this respect, one can say that the tropical atmosphere is considerably "baroclinic" with the circulation reversing from the lower to the upper levels (Paegle and Baker, 1982). Also note the oceanic troughs off the east coast of the continents in the southern hemisphere and the large magnitude of the geopotential perturbation over South America. For the northern hemisphere we point out that the closely spaced isopleths of geopotential height off the east coast of North America, Persian Gulf, and south of Japan is consistent (geostrophically) with the observed subtropical jet stream wind speed maxima.

In Figs. 2.20a and 2.20b, we show the temperature field at 850 mb and 200 mb, respectively. We simply notice that for the lower levels, Fig. 2.20a, the higher temperatures over land correspond to the position of the continental lows of Fig. 2.19a; and for the upper levels, Fig. 2.20b, there is a large degree of zonal asymmetry caused by the standing wave pattern of the southern hemisphere (as depicted, for instance, by the 241°C isothern), and the wave reaches a very large amplitude over South America and adjacent oceans.

2.3.5 VORTICITY AND STREAMFUNCTION

If u and v represent the time mean zonal and meridional velocities, respectively, then the vorticity is given by

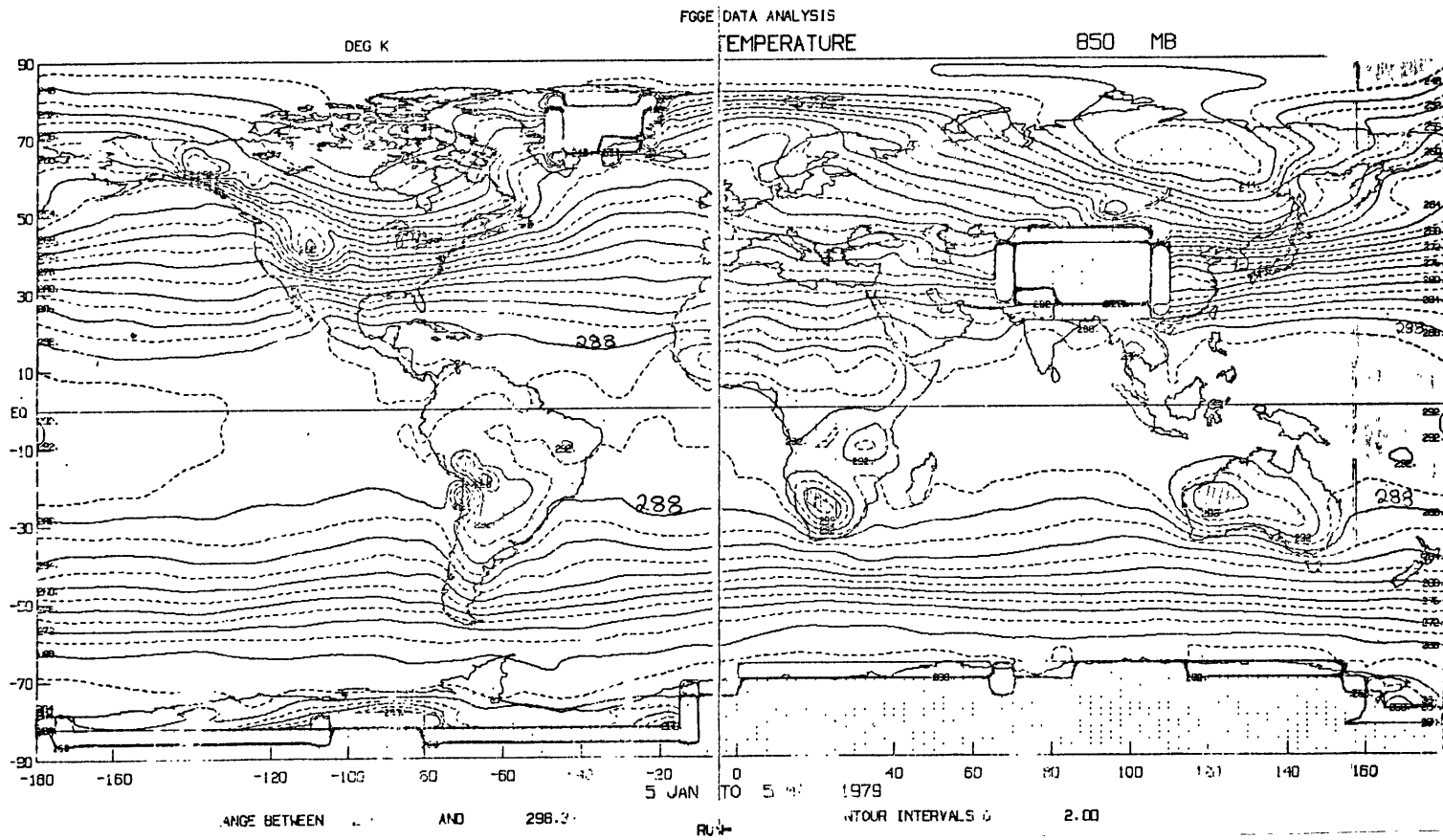Figure 2.20a   Temperature at 850 mb for Jan-Feb, 1979
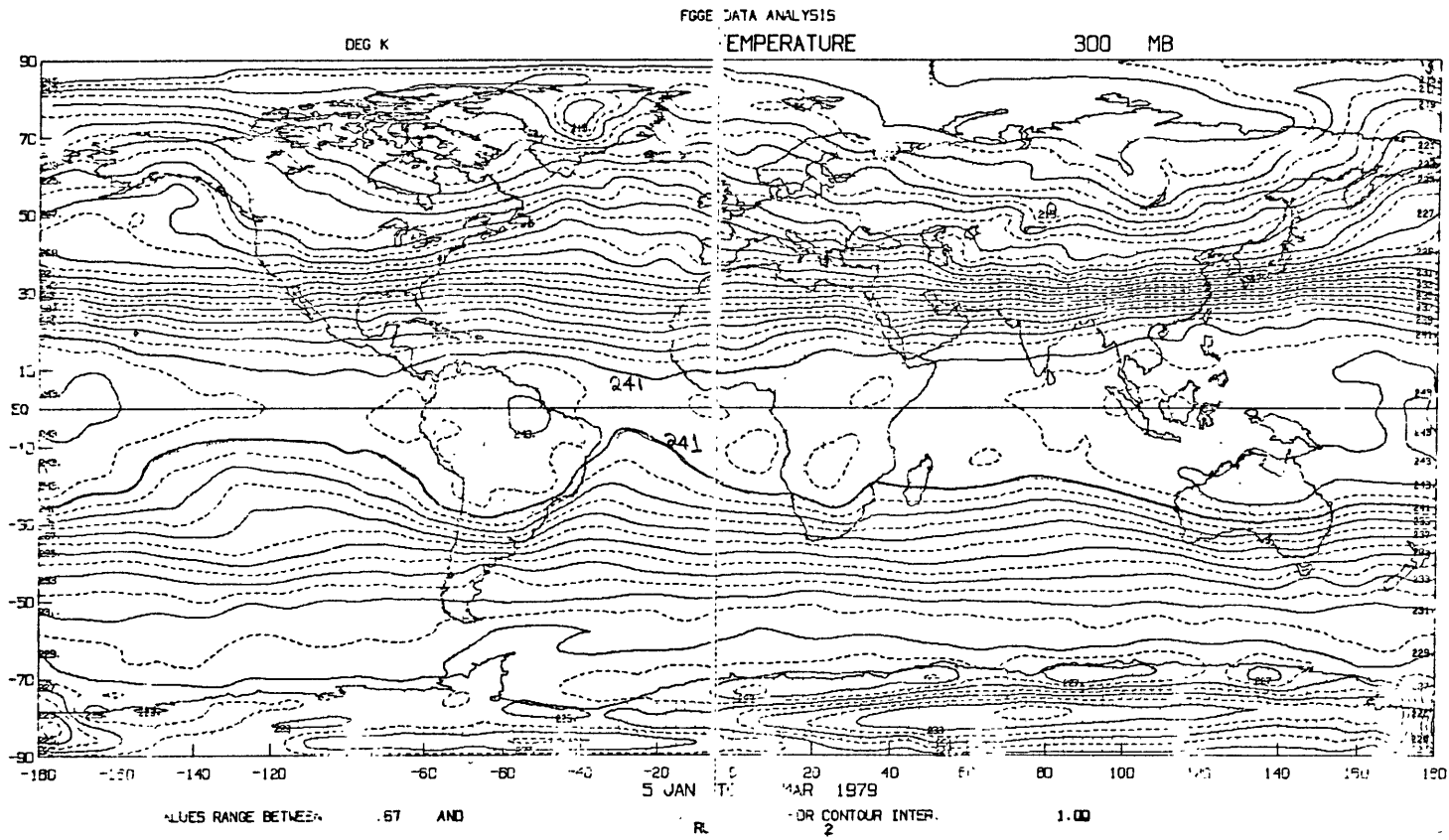(units: K, interval every 2 units.

Figure 2.20b   Same as Figure 2.20a but at 300 mb
               (interval every 1 units).

$$\xi \;=\; \nabla^2 \Psi \;=\; \frac{\partial v}{\partial x} - \frac{\partial u}{\partial y} + u \, \frac{\tan \theta}{a} \qquad\qquad [2.5]$$

where Ψ is the time-mean streamfunction and may be obtained by solving the Poisson equation [2.5] with appropriate boundary conditions.*

In Figs. 2.21a and 2.21b, we show the fields of vorticity ξ at 850 and 200 mb from which the streamfunction was computed. The seasonal fields of Ψ at 850 mb and 200 mb are shown in Figs. 2.22a and 2.22b.**
For the upper levels, Fig. 2.22b, we can make the following remarks:

a) anticyclonic circulation over South America,

southern Africa, and northern Australia,

b) the large-amplitude stationary waves of the tropics

and subtropics in the southern hemisphere, particularly

the wave over South America and adjacent oceans,

c) westerlies over most of the tropics and subtropics

in the northern hemisphere and the position of the jet

stream are evident (large $|\nabla\Psi|$),

---

* To solve the Poisson equation [2.5] we used NCAR routines with undetermined boundary conditions at the poles. The same routines were used to solve the Poisson equation for the velocity potential of Section (2.3.6), below. For the lower levels we did not solve the Poisson equation taking into account the topographical barriers (Tibet, Greenland and Antarctica at 700 mb) as a boundary-value problem. Instead, a value was assigned to the grid points with topography, and the computations were carried out; thus, the streamfunction and velocity potential values near topography may have been incorrectly affected by this procedure.

** We remark that the maximum of $\nabla^2\Psi$ is not necessarily at the same location as the maximum of Ψ which is also true for the divergence $(-\nabla^2\chi)$ and the velocity potential (χ).

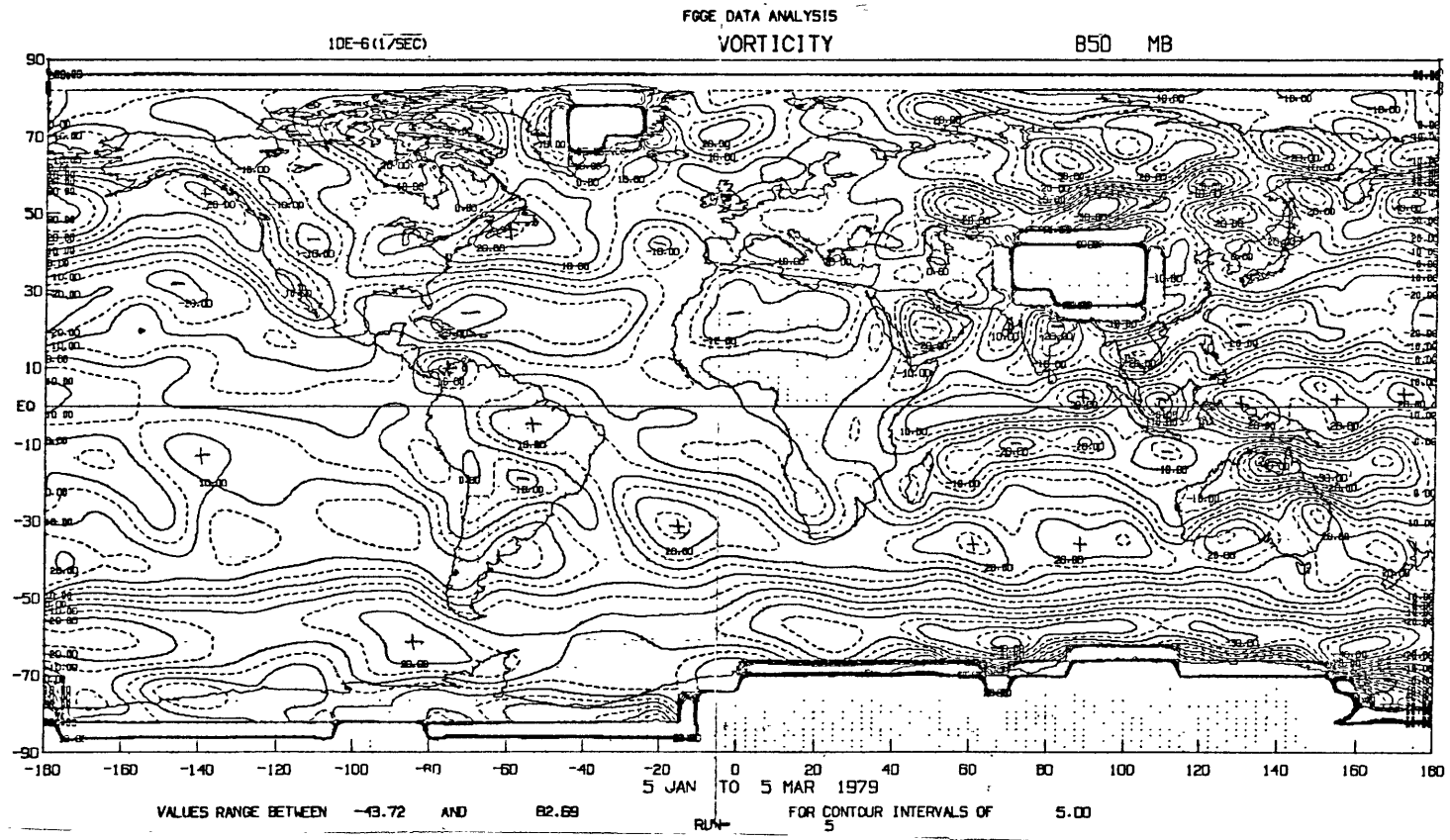Figure 2.21a   Vorticity at 850 mb for Jan-Feb, 1979
                (units: $10^{-6}s^{-1}$, interval every 5 units.
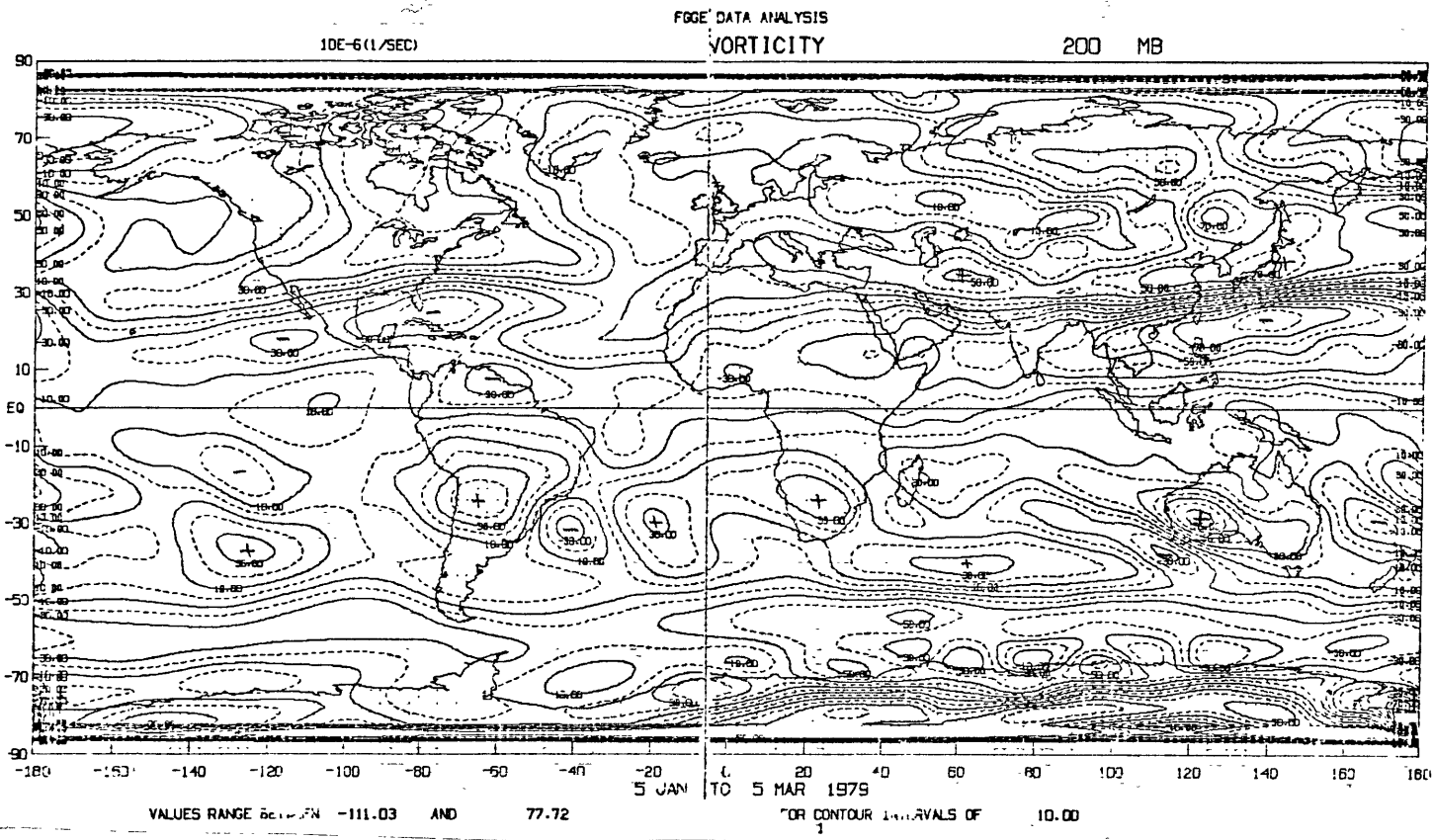
Figure 2.21b   Same as Figure 2.21a   but at 200 mb
(interval every 10 units).
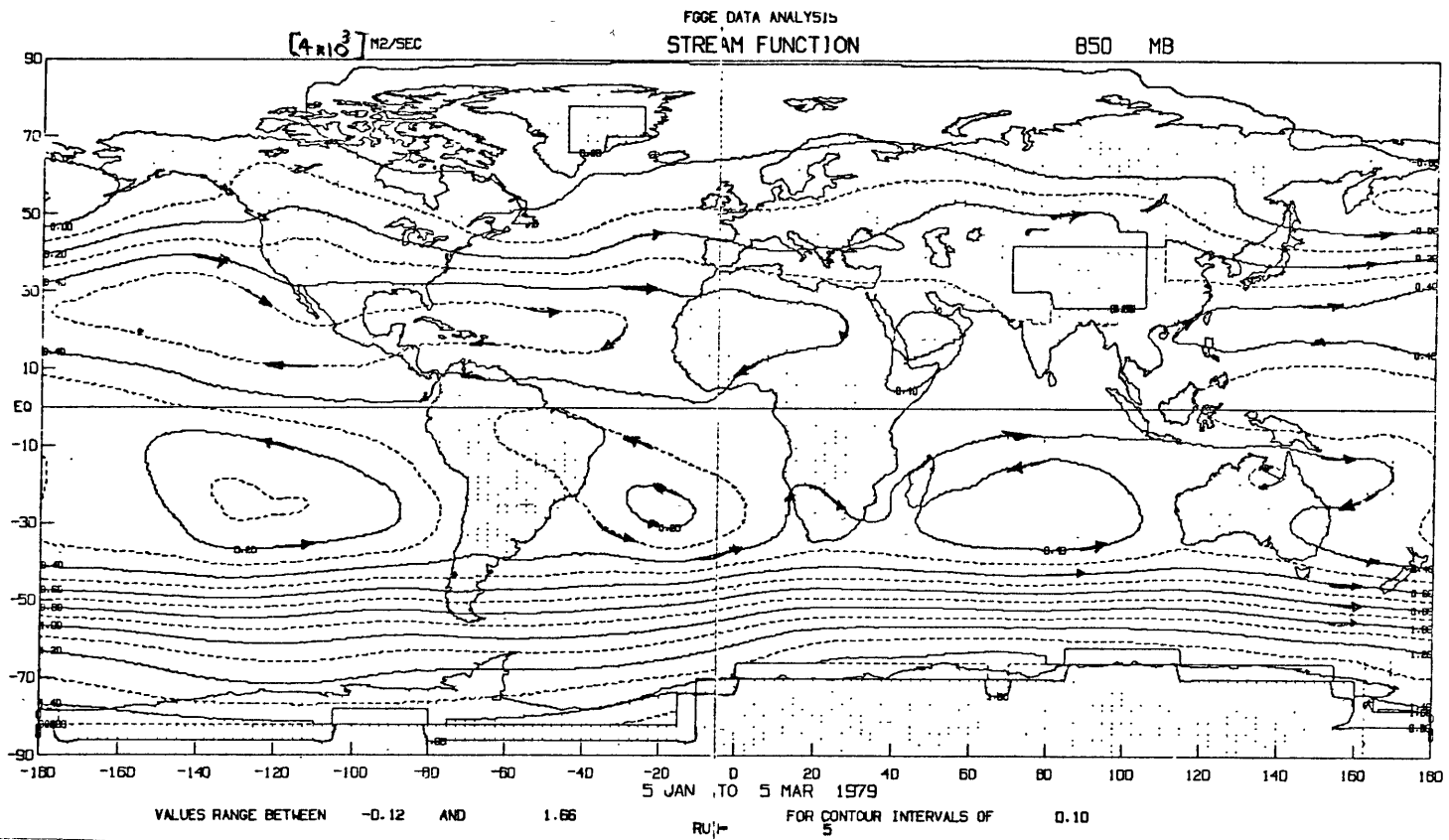
Figure 2.22a   Streamfunction at 850 mb for Jan-Feb, 1979
(units: 4×10^3 m^{2}s^{-1}, interval every 0.10 units).

Figure 2.22b   Same as Figure 2.22a but at 200 mb
(interval every 0.01 units).

d) three regions of maximum velocity in the three waves

of the subtropical jet stream, off the coast of North

America, over the Persian Gulf, and south of Japan.

The rotational part of the wind for the lower levels, Fig. 2.22a, shows strong anticyclonic circulation over the three oceans of the southern hemisphere and weaker and more zonally oriented anticyclonic circulation in the subtropics of the northern hemisphere. Also note weaker cyclonic circulation over the tropical continents in the southern hemisphere.

2.3.6 DIVERGENCE AND VELOCITY POTENTIAL

The time mean velocity potential χ is defined as

$$\nabla^2 \chi = \frac{\partial u}{\partial x} + \frac{\partial v}{\partial y} + v \frac{\tan \theta}{a} \quad . \qquad [2.6]$$

The distribution of χ is found by solving the Poisson equation [2.6] with appropriate boundary conditions (see footnote on page ?).

The divergence field (R.H.S. of Eq. [2.6]) at 700 mb and 200 mb is shown in Figs. 2.23a and 2.23b, respectively. This field was used to compute χ by numerically solving the Poisson equation. The fields of velocity potential at 700 and 200 mb are depicted in Figs. 2.24a and 2.24b, respectively. It is worth remarking again that if the lines of velocity potential are parallel to latitude circles, then there would be no Walker-type (east-west) circulations. Lastly, if the lines are circular, then the circulation is neither purely Hadley-type nor purely Walker-type but a mix of the two. Let it be called Hadley-Walker
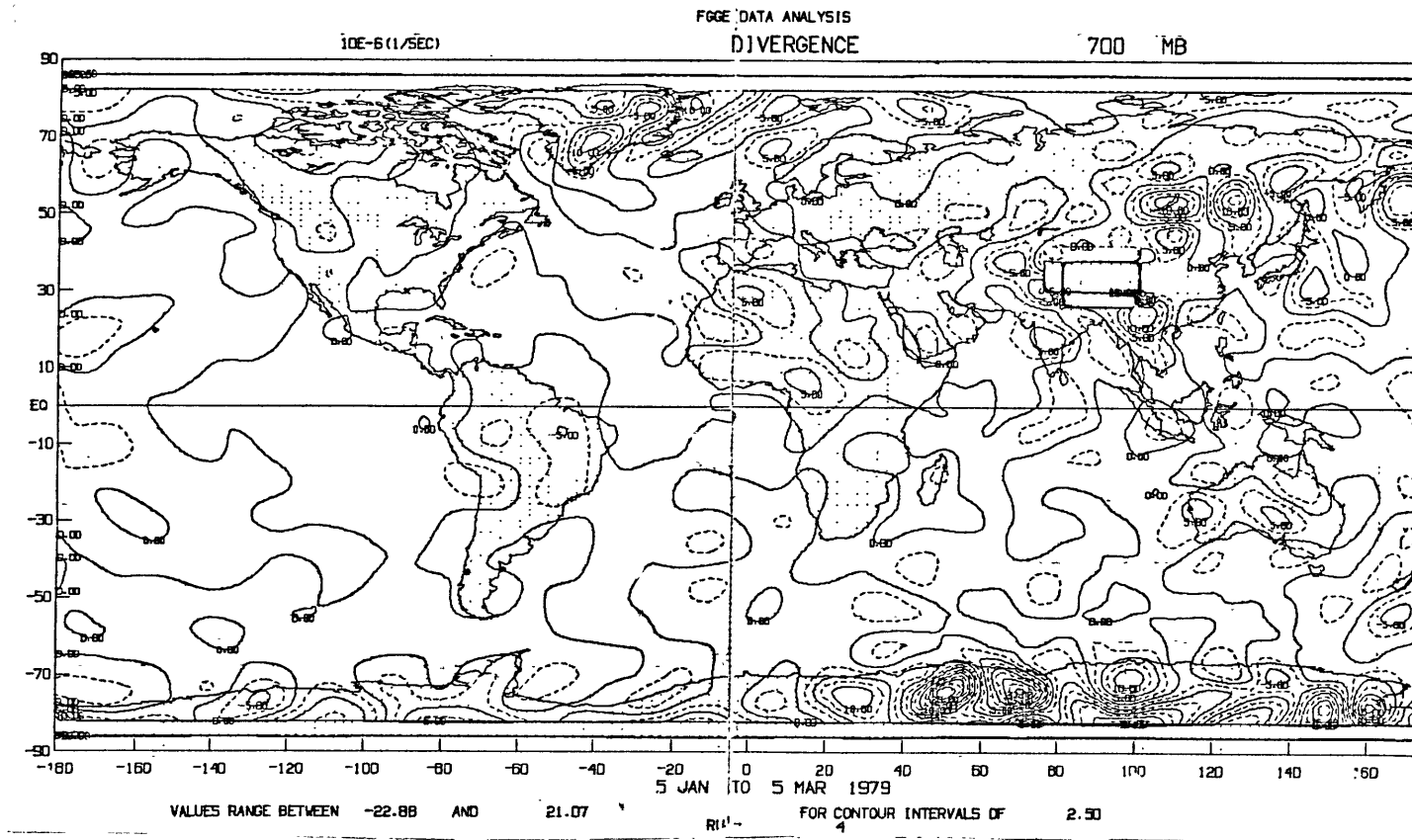
Figure 2.23a   Divergence at 700 mb for Jan-Feb, 1979
(units: 10^{-6} s^{-1}, interval every 2.5 units).
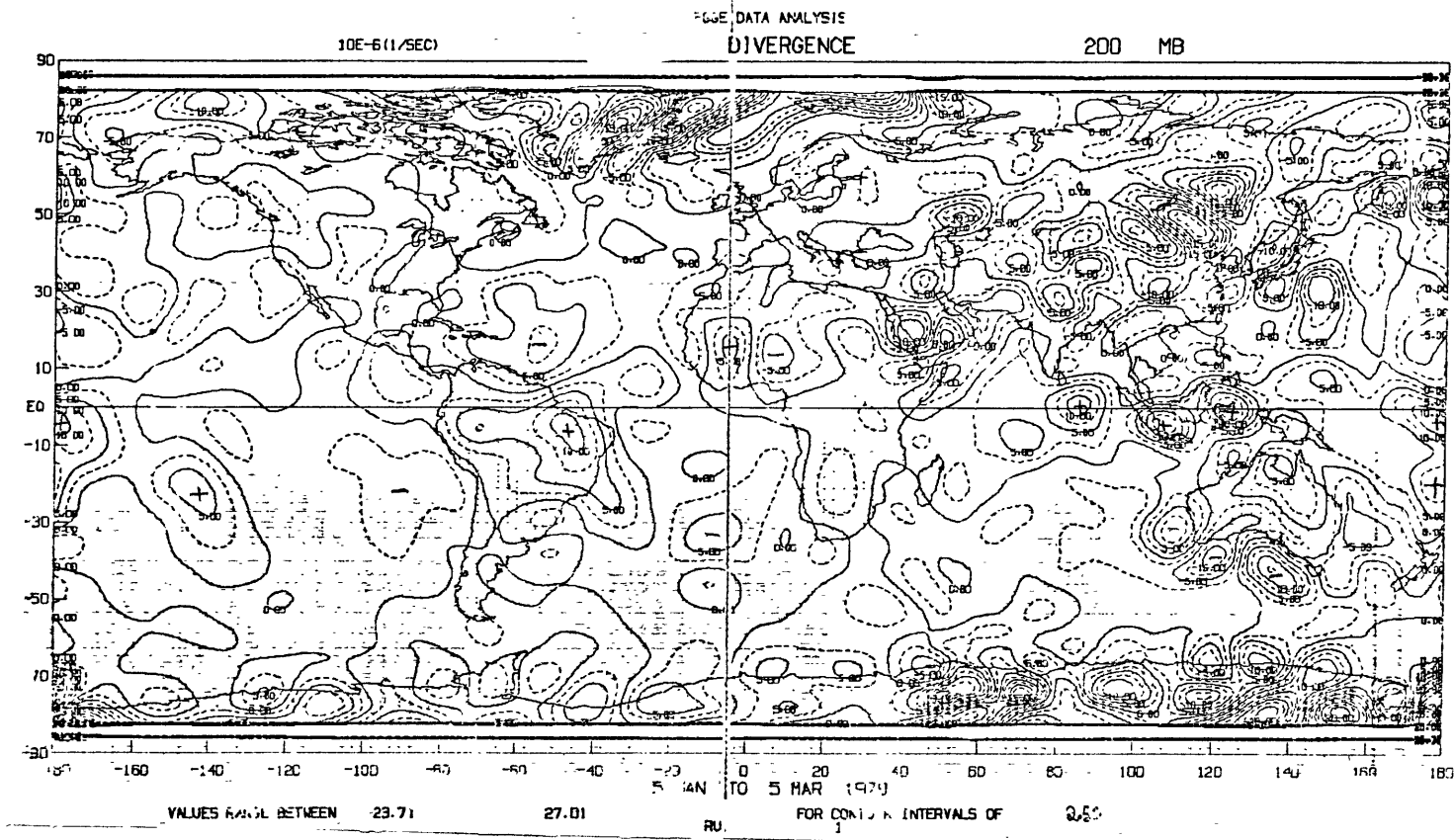
Figure 2.23b   Same as Figure 2.23a but at 200 mb.

circulations. With this in mind we now analyze the fields of velocity potential.

The analysis of Fig. 2.24b (200 mb) reveals the following interesting features:

a) the isopleths of χ indicate the existence of two major centers of rising motion, one over Brazil ($\approx 13°S$) and the other over western Pacific ($\approx 10°S$),

b) centers of sinking air are found over eastern Pacific and Atlantic Oceans in the southern hemisphere and over the Atlantic in the northern hemisphere,

c) the local character of the Hadley-type circulations is evident, i.e., they do not occur uninterruptedly along the tropical belt, but the strongest north-south overturnings are observed over a relatively short longitudinal span north of South America and over a broader region in western Pacific and Indonesian maritime continent,

d) the maximum in wind speed of the subtropical jet stream is found to lie northwest of these regions of maximum meridional divergent winds,

e) the isopleths of χ are more nearly zonal (indicating predominantly north-south overturnings) from the central Indian Ocean eastward to the dateline in the northern hemisphere, and those are the longitudes where

the broad maximum of wind speed in the subtropical jet
stream is observed,

f) isopleths of χ around the low center over South
America are more circular, indicating an upper-level
spillover of mass in all directions,

g) planetary-scale east-west circulations, with
rising motions centered over South America and
western Pacific and sinking motions over the
Atlantic and Pacific Oceans,

h) the westward branch of the Pacific cell extends for
half of the circumference of the earth,

i) it is remarkable that the position of the upper air
easterlies (Fig. 2.17a) over western Pacific and Indian
Oceans, Africa, and South America corresponds quite well
with the westward branches (i.e., the divergent winds
being easterlies) of the two east-west cells,

j) over central Pacific we note a vigorous east-west
circulation (the isopleths of χ are more parallel to
meridians and $|\nabla\chi|$ is large),

k) the intensity of the divergent part of the wind is
comparable to the rotational part for the tropics;
elsewhere, the divergent part becomes very small and the
rotational part is at least an order of magnitude greater,

Figure 2.24a   Velocity potential at 700 mb for Jan-Feb, 1979
(units: 4×10^6 m^{2}s^{-1}, interval every 0.10 units).
Lines with arrows indicate approximate direction
of divergent flow.

FGGE DATA ANALYSIS

$(4 \cdot 10^6)$ M2/SEC · VELOCITY POTENTIAL · 200 MB

VALUES RANGE FROM -2.47 AND 1.31 · FOR CONTOUR INTERVALS OF 0.20
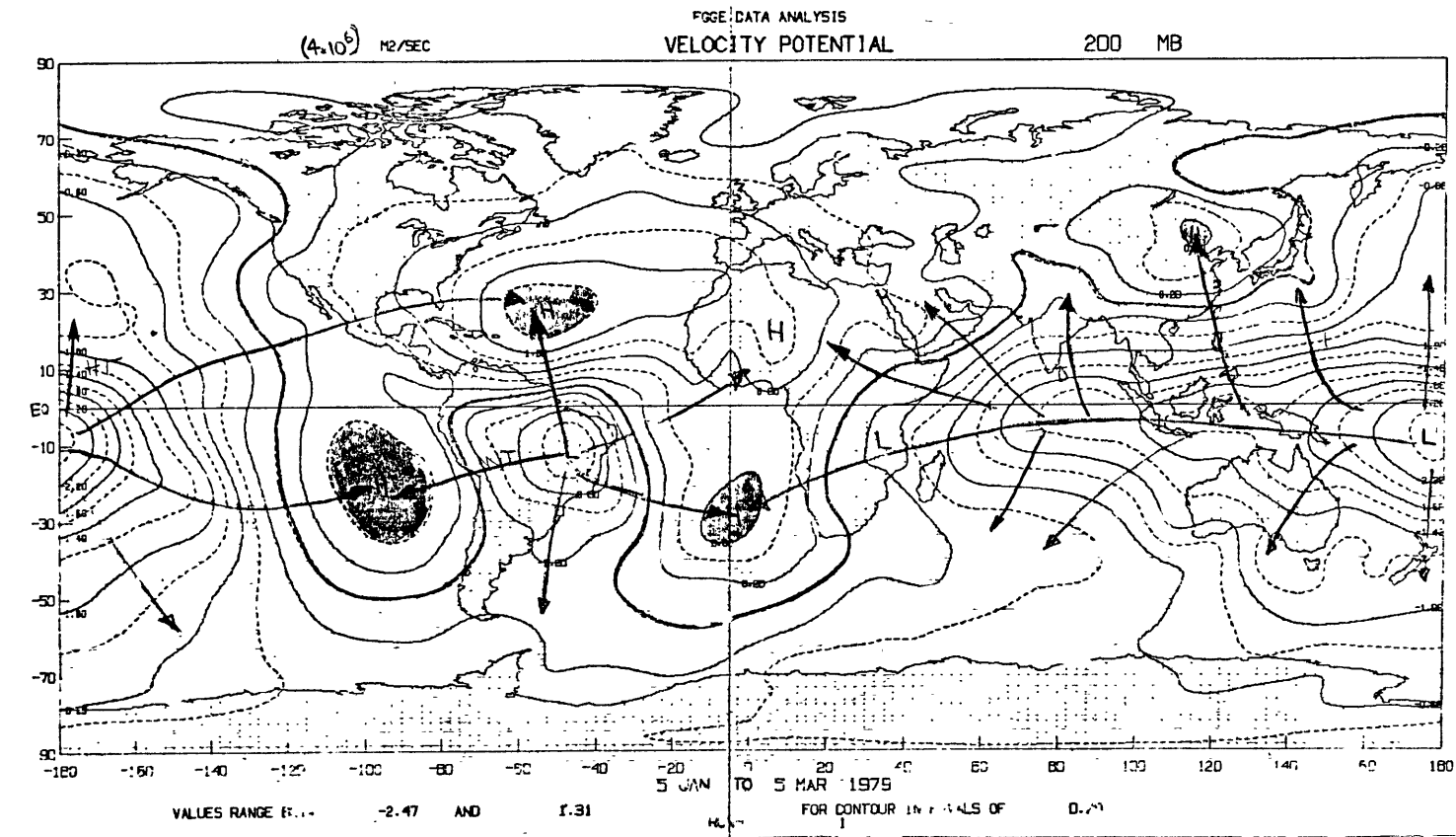
5 JAN TO 5 MAR 1979

Figure 2.24b Same as Figure 2.24a but at 200 mb
(Interval every 0.20 units).

1) the trough of the isopleths of χ over the central

Pacific and western Atlantic in the southern hemisphere

agrees well with the position and alignment of the

SPCZ and the southern Atlantic convergence zone (SACZ)

as revealed by cloudiness and precipitation maps and by

the diabatic heating field in Fig. 2.12 and 2.13.

The isopleths of χ for the lower levels (Fig. 2.24a) help us visualize the tridimensional, thermally direct circulations in the tropics. Here we see two centers of convergent motion, one over South America, the other over western Pacific, in very close correspondence with the upper-level centers of divergent motion. Also the position of the observed low-level equatorial westerlies over the Indian Ocean and western Pacific agrees with the position of the lower branch of the eastern hemisphere Walker-type cell. Due to their proximity to the earth's surface, the patterns at 700 mb are not as clearcut as the ones at 200 mb, but they are consistent with the patterns at the upper levels. The magnitudes of $\nabla\chi$ both for 200 and 700 mb indicate that the Walker-type and the Hadley-type circulations are of comparable strength. The upper-level convergence seen from χ has remarkable association with the surface highs.

The position of the centers of rising motion is consistent with the distribution of diabatic heating (Fig. 2.12), i.e., an isolated heat source over northeastern South America and a longitudinally oriented band of heating from the Indian Ocean eastward to the western Pacific. According to the traditional view, there are three east-west cells during the southern hemisphere sunmmer (see Fig. 10), the two discussed above

and one more with rising motion over the convectively active region of
southern Africa. This latter cell, with rising motion over the continent
and sinking motion over the Atlantic Ocean to the west and the Indian
Ocean to the east, is not seen in Fig. 2.24. Its nonexistence is
consistent with the rather weak diabatic heating over southern Africa
($<3°K/day$ at 400 mb as compared to heating of up to $11°K/day$ for the
other two regions) for that particular period.

2.3.7 HORIZONTAL FLUXES OF MOMENTUM

In this and the next section, we will present calculations of
horizonal flux of momentum pertaining to the FGGE data set for Jan-Feb
1979. All the previous FGGE data analysis in this chapter dealt with
time-mean quantities, and it would be of interest to have some idea about
the shorter term variability (within a season) of the tropical
circulations. We selected to show global maps of the meridional flux of
zonal momentum by the time-mean circulation ($\overline{UV}$) and by the transient
eddies ($\overline{U'V'}$) at 200 mb in Figs. 2.25 and 2.26, respectively.*

The upper-level meridional fluxes of zonal momentum by the time-mean
circulation (Fig. 2.25) are generally very small for the equatorial belt,
and the maximum values are reached in the subtropics of both hemispheres.
The three wave pattern of the subtropical jet stream (the "meandering" of
the jet stream) is seen in the alternating pattern of poleward and
equatorward fluxes at the latitudes of maximum wind speeds. Convergence
of this flux (not presented here) shows regions of deposition of westerly

---

* $(^-)$ bars denote time-mean quantities, ( )' primes refer to departures
from time mean, [( )] square brackets, to zonal mean quantities and ( )*
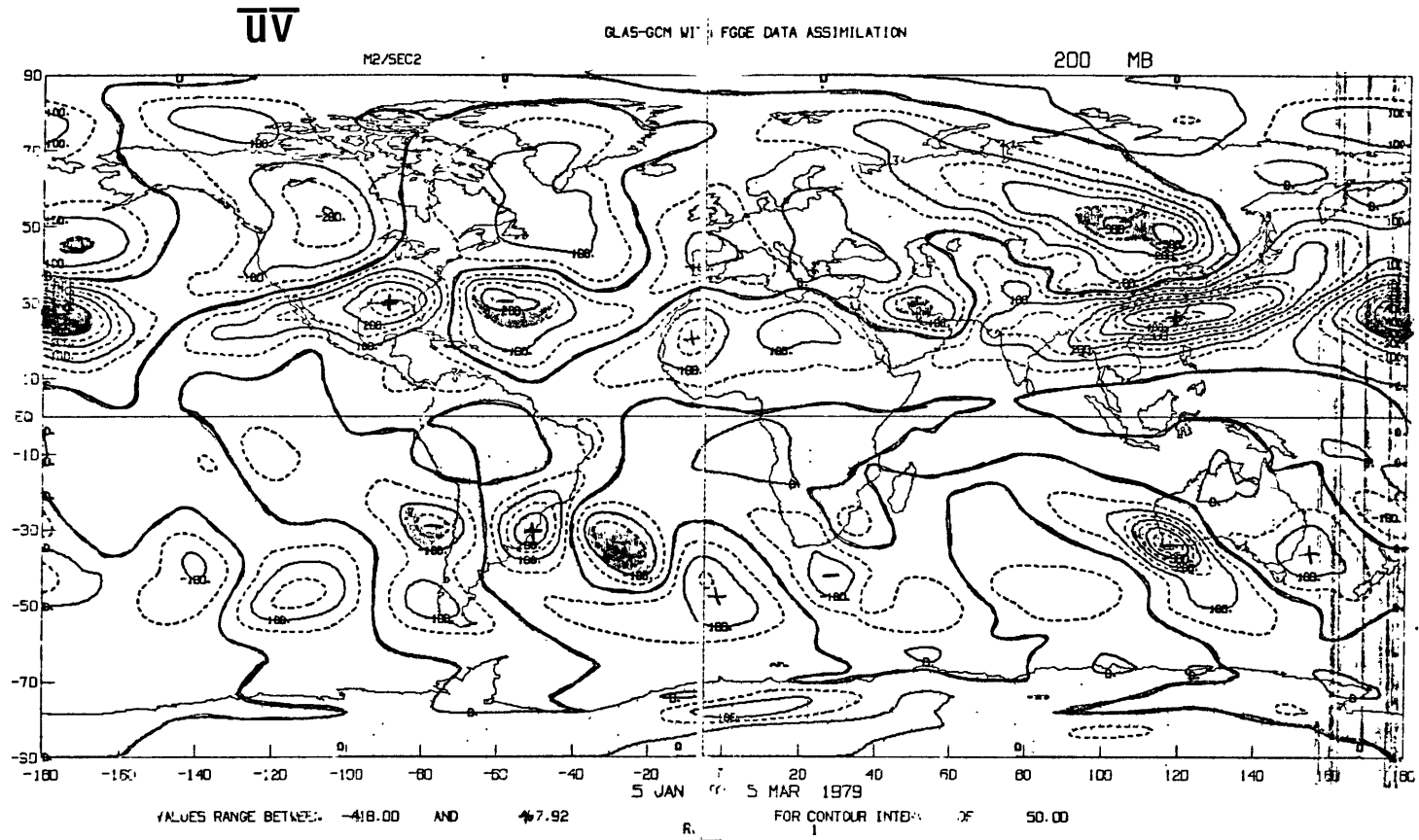stars, to departures from zonal mean.

Figure 2.25 Global distribution of $\overline{uv}$ at 200 mb for Jan-Feb, 1979
(units: m^2s^{-2}, interval every 50 units).

momentum (i.e., accelerating westerlies) to the west of the maximum in the wind speed, one off the east coast of United States and the other south of Japan, and a region of deposition of easterly momentum (decelerating westerlies) to the east of those maxima. For the southern hemisphere the fluxes are not as large as the ones for the northern hemisphere and are associated with the regions of large meridional velocities over South America and adjacent oceans and over Australia and adjacent oceans.

The meridional transport of zonal momentum by the transient eddies (Fig. 2.26) at 200 mb shows predominantly poleward fluxes in the sub-tropics and midlatitudes of both hemispheres with higher values for the winter hemisphere (northern hemisphere). Note that the fluxes by the transient eddies are generally smaller than the fluxes by the time-mean circulation, and like the latter, very small in the equatorial belt. Although their magnitude is about 1/3 to 1/2 of the fluxes by the time-mean circulation, they are likely to play an important role in the maintenance of the time mean zonal wind. We observe, for instance, that for two areas, southern Central Pacific and eastern North Pacific, $|\overline{U'V'}| > |\overline{U}\,\overline{V}|$. In the next two chapters, we will develop models of the tropical circulation forced by time mean diabatic heat sources, and we will be leaving out the effects of transience. It is worth keeping this in mind because transient eddies may be important in explaining some aspects of the maintenance of the time mean circulation.

2.3.8 ZONALLY AVERAGED HORIZONTAL FLUXES OF MOMENTUM

It is sometimes of interest to regard the atmospheric circulation as axially symmetric and to study its zonally averaged state. The time-mean,

$$\overline{u'v'}$$

GLAS-GCM WIT: FGGE DATA ASSIMILATION

M2/SEC2   200   MB

5 JAN TO 5 MAR 1979

VALUES RANGE B· ·N -106.46 AND   187.10 *   FOR CONTOUR I.· /VALS OF   20.00
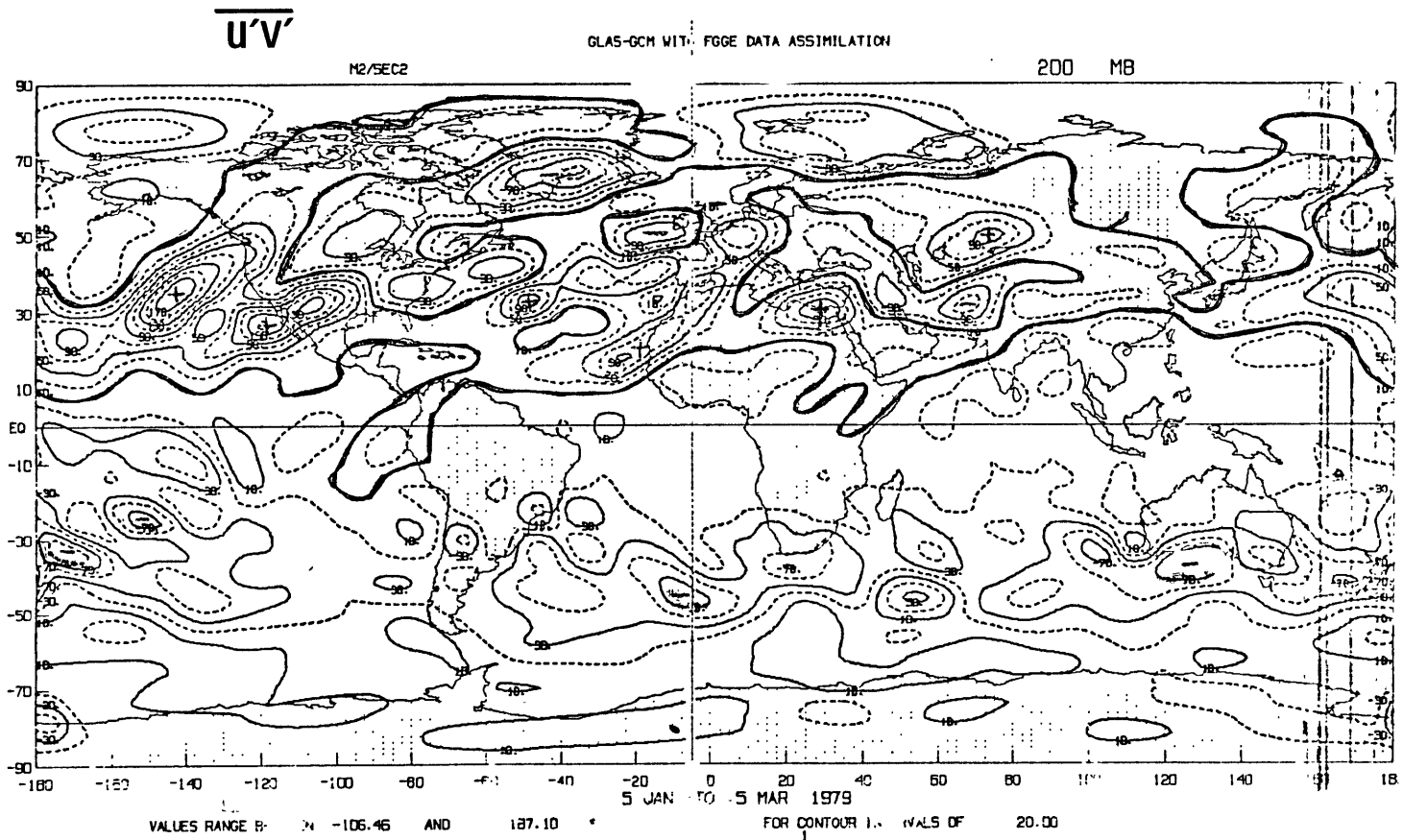
Figure 2.26   Global distribution of $\overline{u'v'}$ at 200 mb for Jan–Feb, 1979
(units: $m^2 s^{-2}$, interval every 20 units).

zonally averaged meridional flux of zonal momentum can be written as

$$[\overline{UV}] = [\overline{U}][\overline{V}] + [\overline{U^*V^*}] + [\overline{U'V'}] \qquad [2.7]$$

where the terms in the R.H.S. of [2.7] are the flux of zonal momentum by the mean meridional circulation (MMC), stationary eddies (SE) and transient eddies (TE), respectively.

In Fig. 2.27 we show latitudinal profiles of the zonally averaged fluxes at 200 mb (approximately the level of maximum fluxes). For the tropics and subtropics, the fluxes are small in the southern hemisphere, and the flux by the MMC peaks at $\approx 20°N$, by the SE at $\approx 25°N$ and by the TE at $\approx 30°N$. It is important to note that the three fluxes are comparable in magnitude in the tropics at that level. Also, for comparison, the climatological values of the fluxes based on data from Oort (1982) were included in Fig. 2.27. There is agreement between the two sets of data in terms of the sign and magnitude of the fluxes.

Similarly, we present in Fig. 2.28 the divergence of the meridional fluxes of Fig. 2.27. It is evident that the divergence of the three fluxes are of the same order of magnitude in the tropics, the values being larger in the northern hemisphere. The convergence of $[\overline{U}][\overline{V}]$ is maximum (i.e., maximum deposition of westerly momentum by the MMC) at $\approx 15°N$ and $\approx 20°N$ for $[\overline{U^*V^*}]$ and $[\overline{U'V'}]$. The convergence of $[\overline{U}][\overline{V}]$ is the largest of the three for the tropics, but for the southern hemisphere subtropics, the convergence of $[\overline{U'V'}]$ is larger than the other two terms.

Figure 2.27 Zonally averaged fluxes of horizontal momentum by the MMC (thick line), TE (thin line), and SE(dashed line) at 200 mb for Jan-Feb, 1979 (units:m^2s^{-2}); climatological values from Oort (1982) are indicated.

Divergence of horizontal momentum fluxes (10^{-3}cm/s^2)
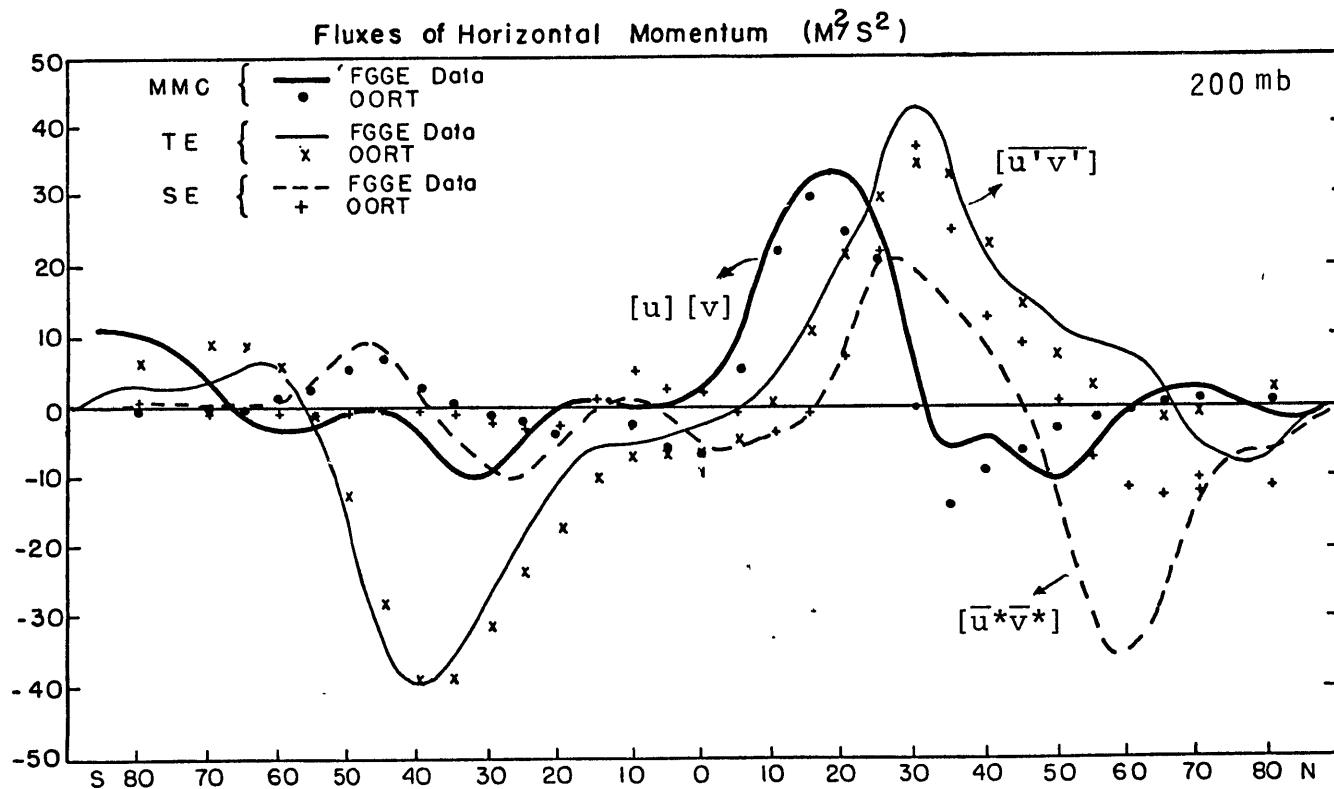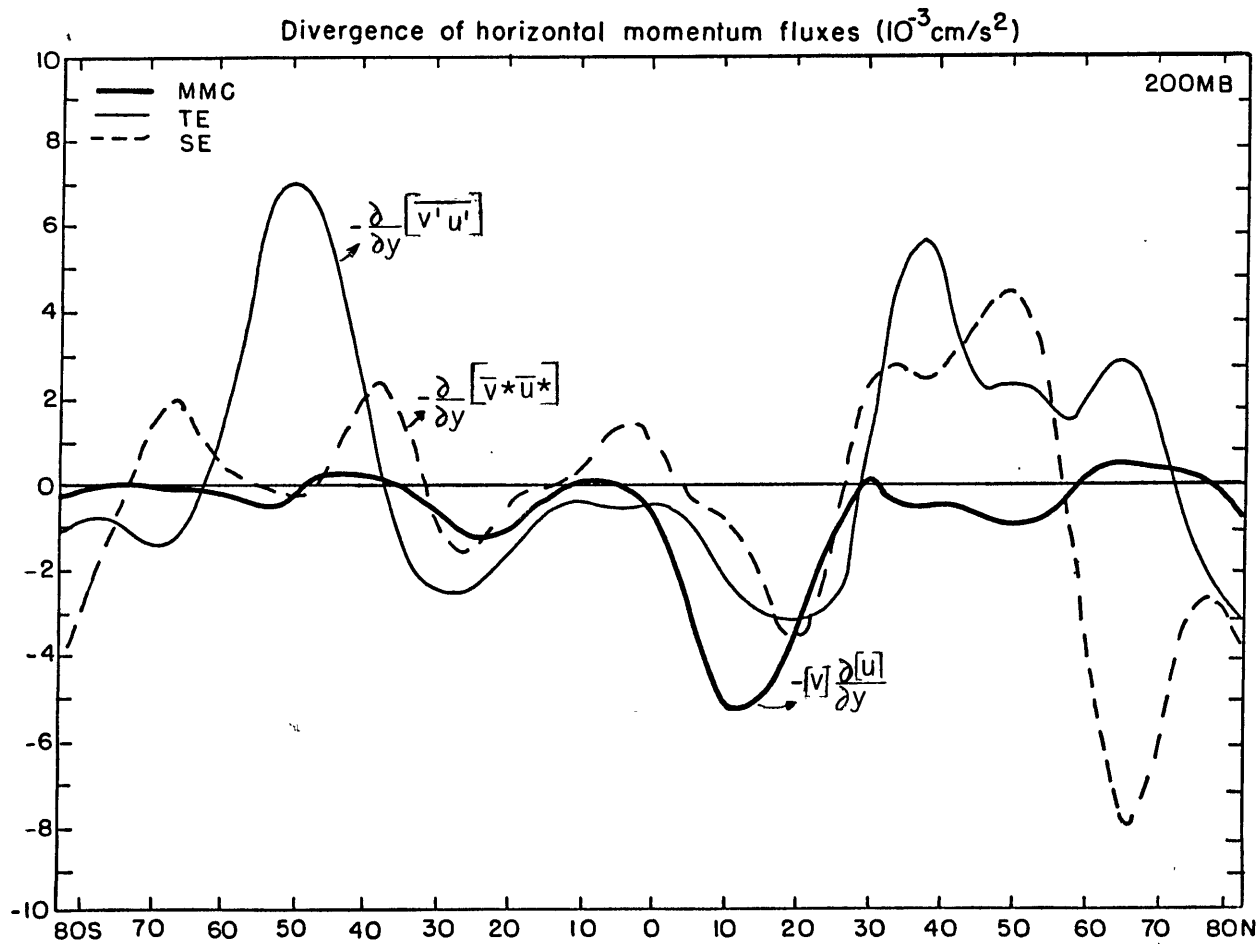
Figure 2.28   Zonally averaged divergence of horizontal momentum
fluxes by the MMC (thick line), TE (thin line), and
SE (dashed line) at 200 mb for Jan-Feb, 1979
(units: 10^{-3} cms^{-2}).

In some axisymmetric models the zonally averaged eddies were assumed to be very small, and only the contributions by the MMC were taken into account. Figs. 2.27 and 2.28, by showing that the eddy fluxes and divergences have about the same magnitude as the flux and divergence by the MMC, seem to indicate that the contributions by the stationary and transient eddies should be included as forcing terms in axisymmetric models of the seasonal, zonally averaged tropical circulation.

2.4 FGGE DATA ANALYSIS (ECMWF)

The FGGE data set was also assimilated into the integration of the ECMWF GCM following a somewhat different data assimilation technique as was used with the GLAS model. In this section we will briefly compare the results of the two analyses and expand our data analysis to include the FGGE data for the northern summer months. Let us keep in mind that if the data analyses of the two different models yield similar results, then we can be reasonably assured that the particular model's physical parameterization did not modify the results (as compared to reality) to a significant extent, although we can not completely rule out that possibility.

Monthly means -- from January through August 1979 -- of various meteorological quantities (winds, streamfunction, velocity potential, and zonally averaged momentum fluxes) for 200 mb and 850 mb, were available for this analysis.

2.4.1 COMPARISON OF FGGE DATA ANALYSIS AT GLAS AND AT ECMWF

To compare ECMWF and GLAS analyses we selected to show the fields of streamfunction and velocity potential at 200 mb for January and February 1979. Figs. 2.29a and b show the streamfunction for January

and February 1979, respectively, at 200 mb. This figure should be compared with Fig. 2.22 for the GLAS model. The agreement is quite good in terms of wind speeds and directions, position and orientation of the troughs in the southern hemisphere, features of the subtropical jet stream of the northern hemisphere such as the three-wave pattern, and the longitudinal position and speed of the region of maximum velocities. The large-amplitude short wave in the subtropics over South America was also similar in the two analyses.

Velocity potential fields for January and February 1979 at 200 mb are shown in Figs. 2.30a and b, respectively, and these are compared with Fig. 2.24b for the GLAS model. The distribution of isopleths of velocity potential is very similar in the two analyses. Minimum values are found over South America and the Western Pacific, and maximum over the subtropical oceans. The intensity and direction of the principal Hadley-Walker circulations are approximately the same in Figs. 2.30 and 2.24b. However, there is a difference between the two analyses that is worth mentioning. The center of low-velocity potential at the upper level over South America is displaced southeasterly and has an elongated shape (Fig. 2.30) for the ECMWF analysis, as opposed to that feature from the GLAS analysis, which is more nearly circular and is centered over northeastern South America. The ECMWF model analysis seems to bear a closer relation to reality in that respect, since January and February 1979 were months of large positive precipitation anomalies over the coast of Brazil (A. D. Moura, 1982, personal communication).

Figure 2.29a   Mean January 1979 stream function at 200 mb
              (units: 10^7 m^2s^{-1}, interval every unit)
              (from ECMWF FGGE data analysis).
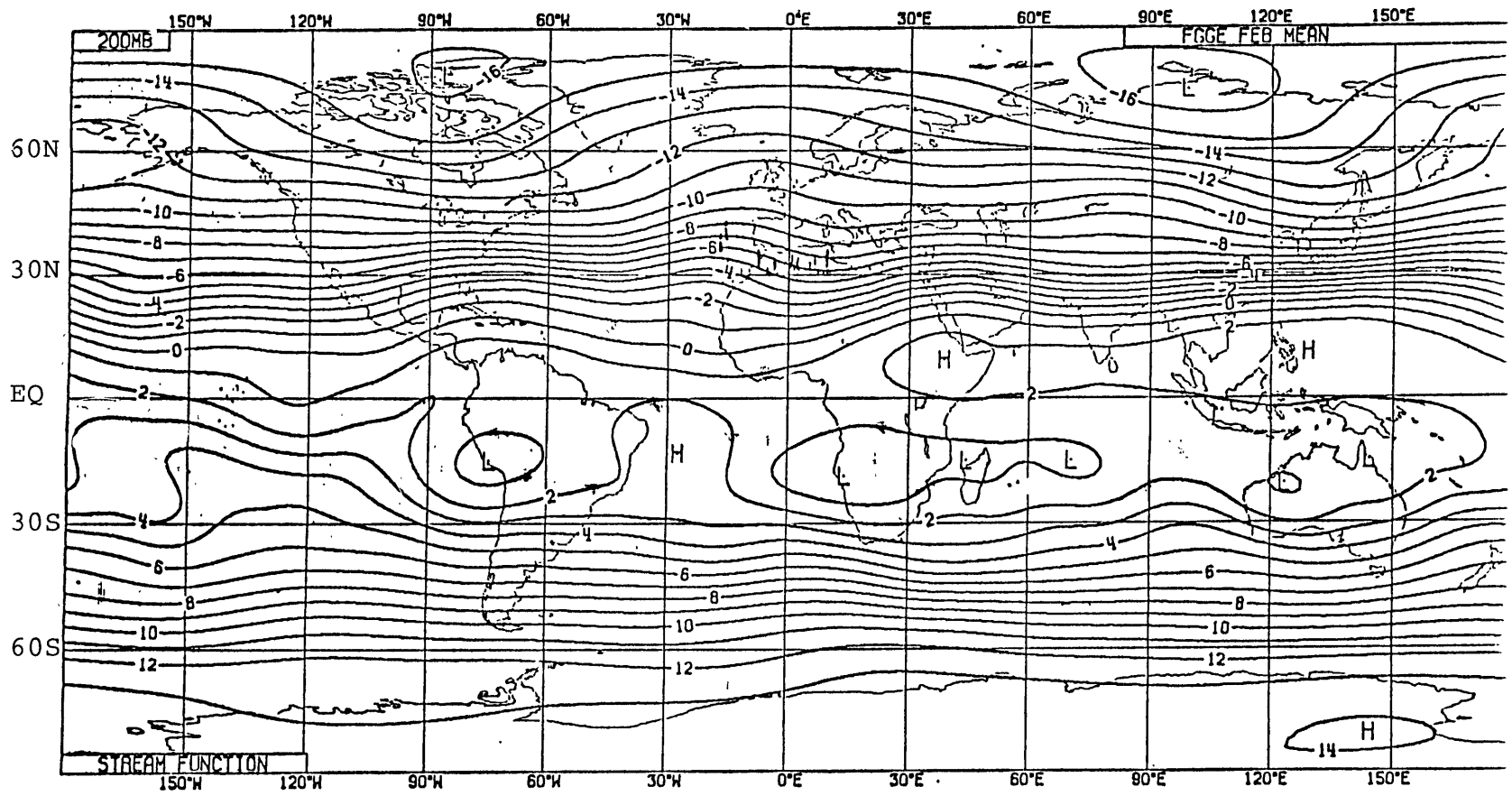
Figure 2.29b Same as Figure 2.29a but for February 1979.
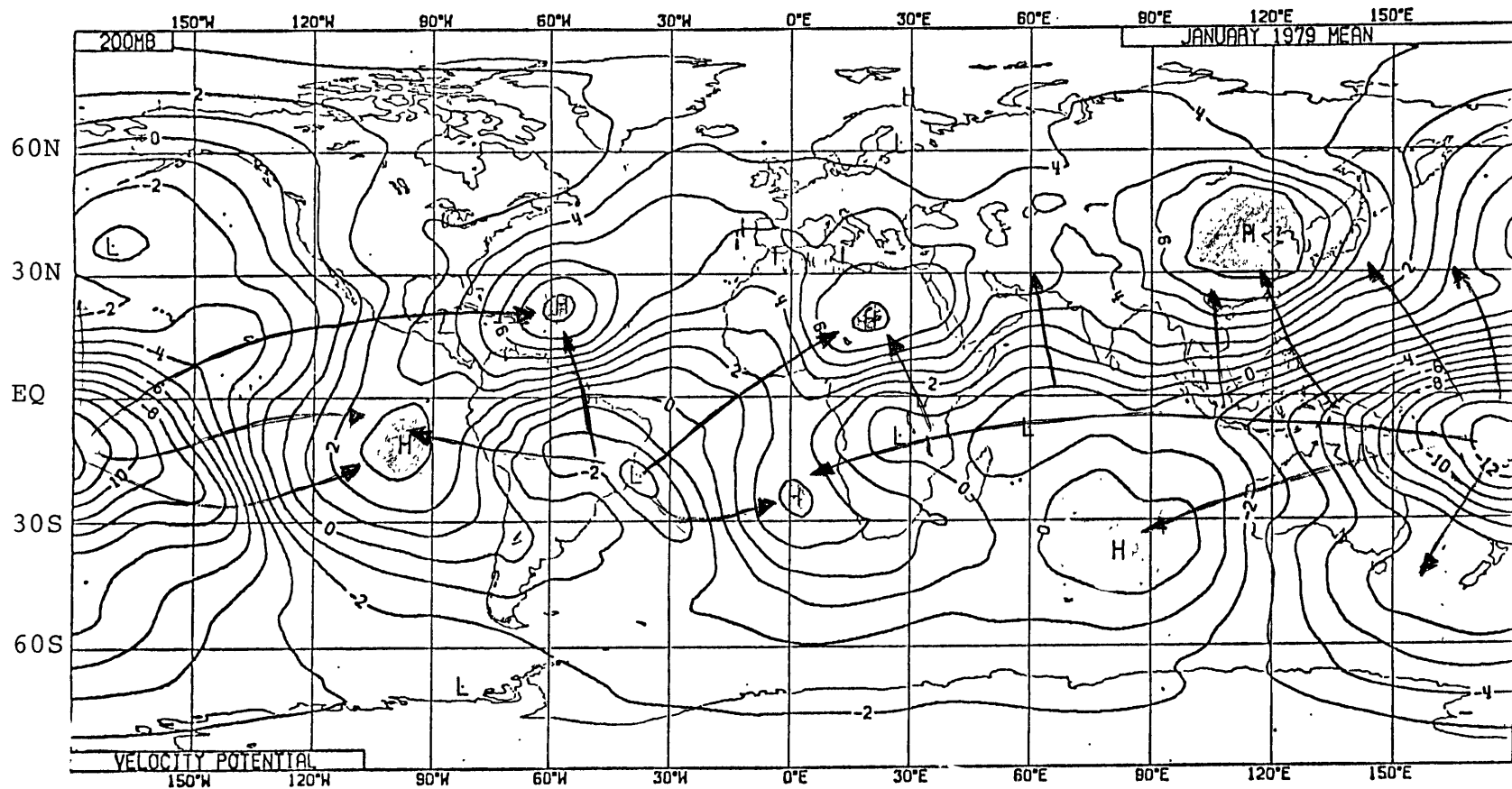
Figure 2.30a   Same as Figure 2.29a but for velocity potential.
Lines with arrows indicate approximate direction
of divergent flow.
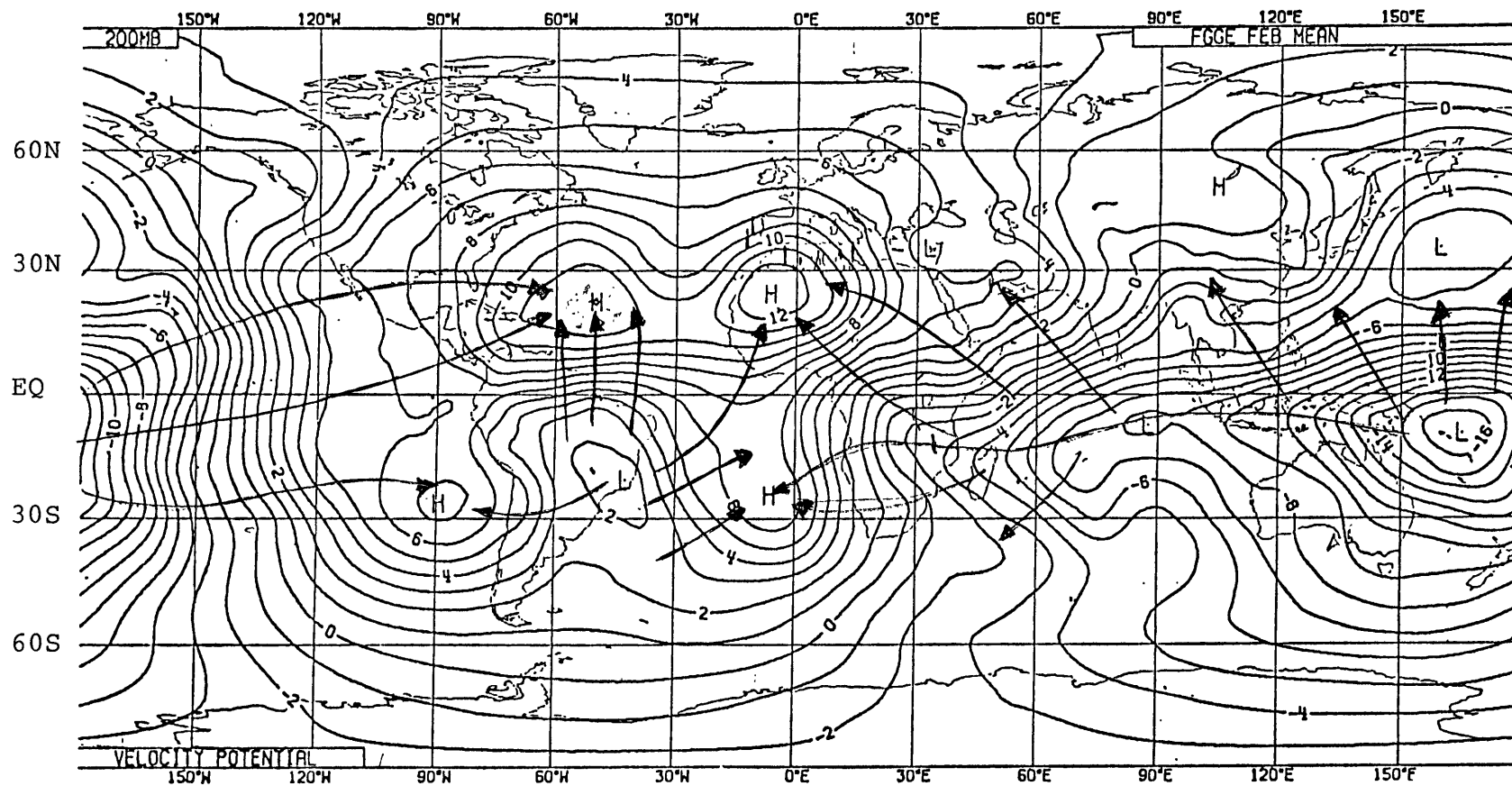
Figure 2.30b   Same as Figure 2.29a but for February 1979 velocity potential.
Lines with arrows indicate approximate direction of divergent
flow.

Comparison of several other fields for January and February 1979 (not shown here) indicates that the two FGGE data analyses, one carried out with the GLAS model and the other with the ECMWF model, generally yield quite similar results. Unfortunately, diabatic heating fields from the ECMWF analysis were not available to the author. Since diabatic heating, primarily latent heating, is the most important forcing of tropical circulations, one would have more confidence in the FGGE data assimilation techniques if the two models produced similar distributions of that quantity. Obviously, this and other comparisons will be necessary to check the validity of the FGGE data assimilation techniques.

2.4.2 ECMWF FGGE DATA ANALYSIS FOR JULY 1979

In this section we extend the FGGE data analysis of the previous sections to include northern summer conditions. Streamfunction and velocity potential at 200 mb and 850 mb, which are shown in Figs. 2.31 and 2.32, respectively, are based on the FGGE data analysis at the ECMWF for July 1979.

Fig. 2.31a, for the streamfunction at 200 mb, shows a broad region of anticyclonic circulation centered roughly over the Tibetan Plateau and weaker regions of anticyclonic circulation over the Indonesian maritime continent in the southern hemisphere, and over Mexico. We also note the southern hemisphere subtropical jet stream located around 30°S with two wind speed maxima, one over Australia and the other over the Central Pacific at 150°W. The streamfunction at 850 mb (Fig. 2.31b) shows, in the northern hemisphere, anticyclonic circulations over the North Atlantic and North Pacific and cyclonic circulation centered over
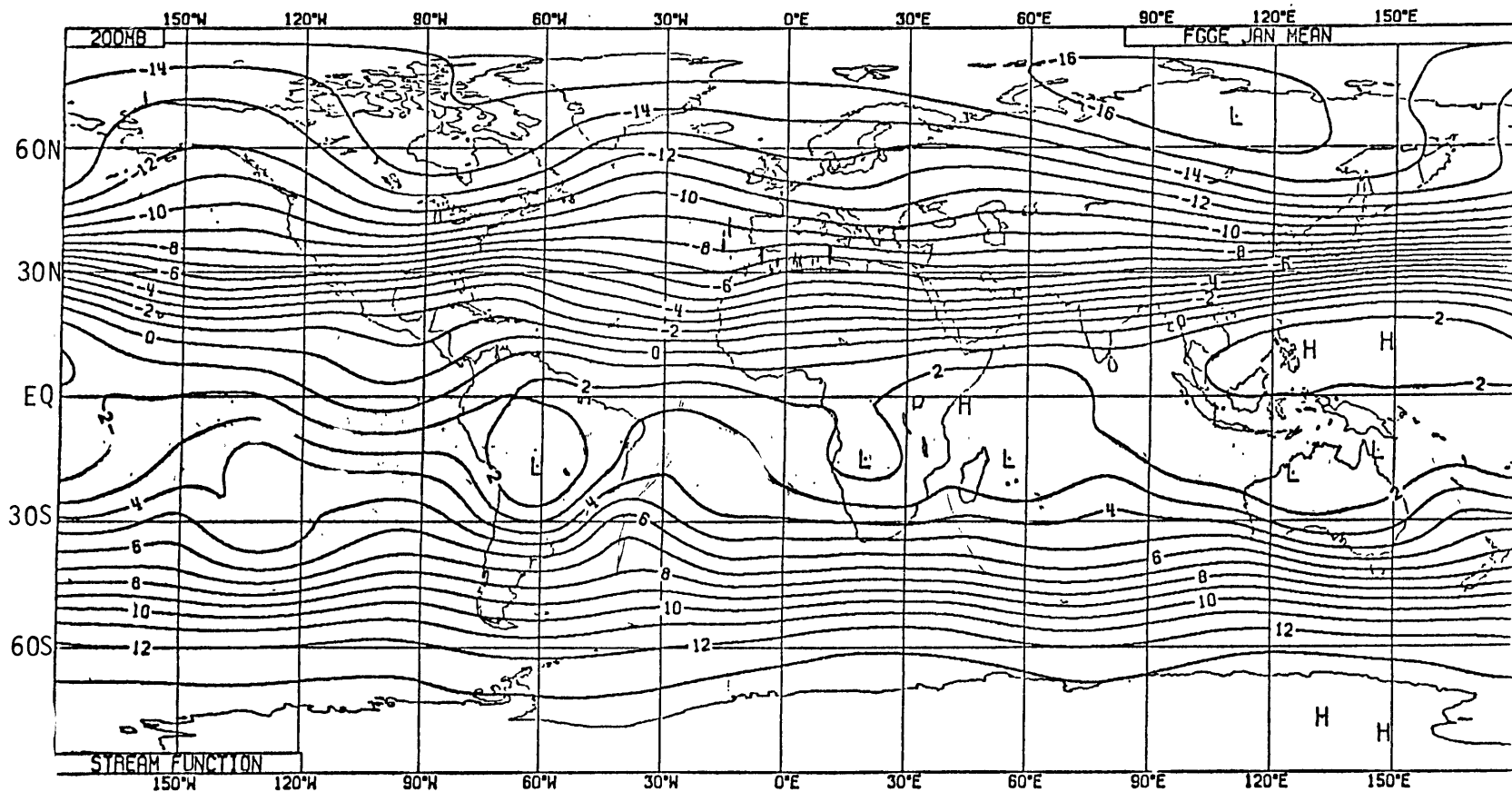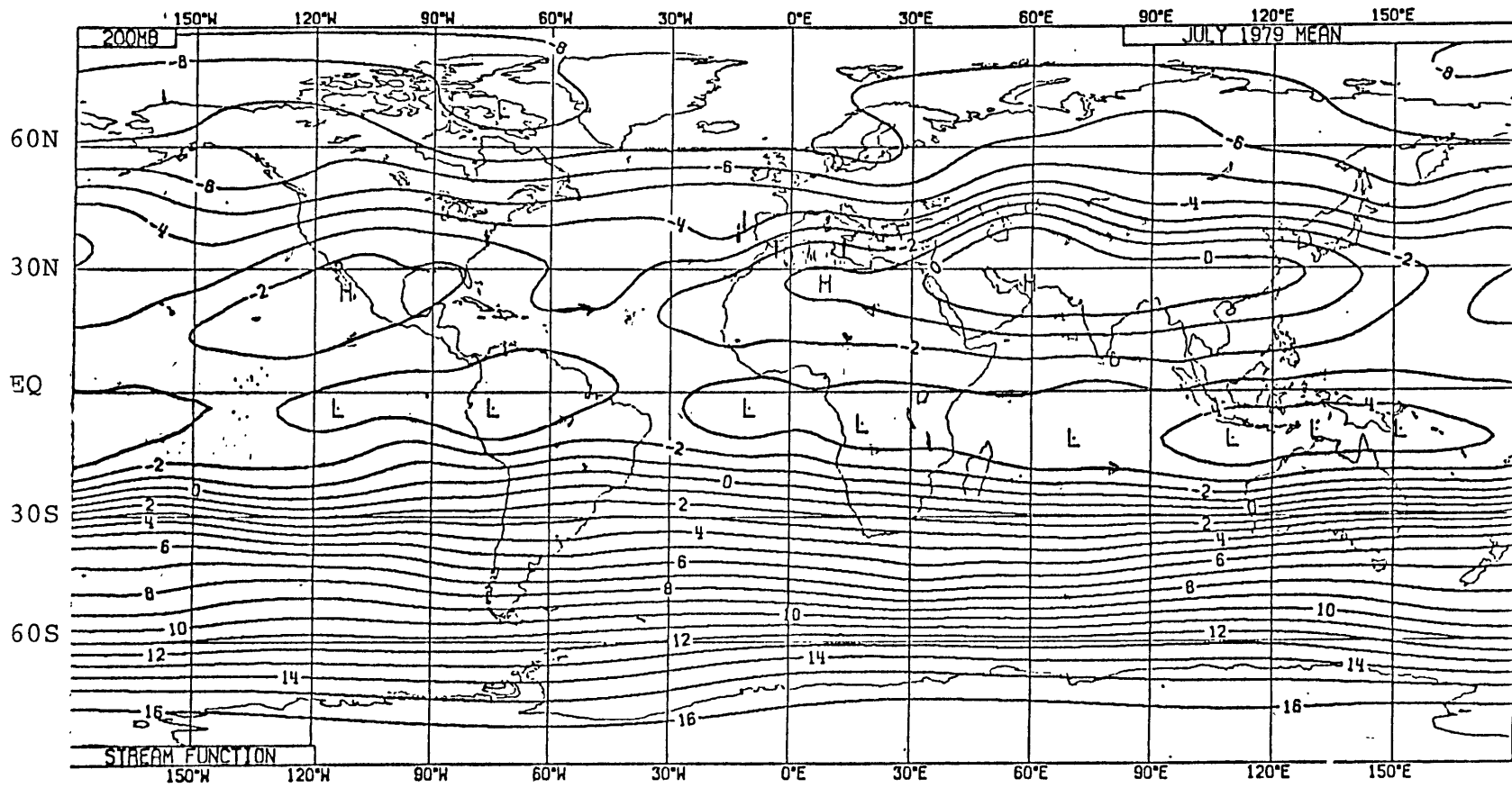
Figure 2.31a   Mean July 1979 stream function at 200 mb
               (units: 10^7 m^2s^{-1}, interval every unit)
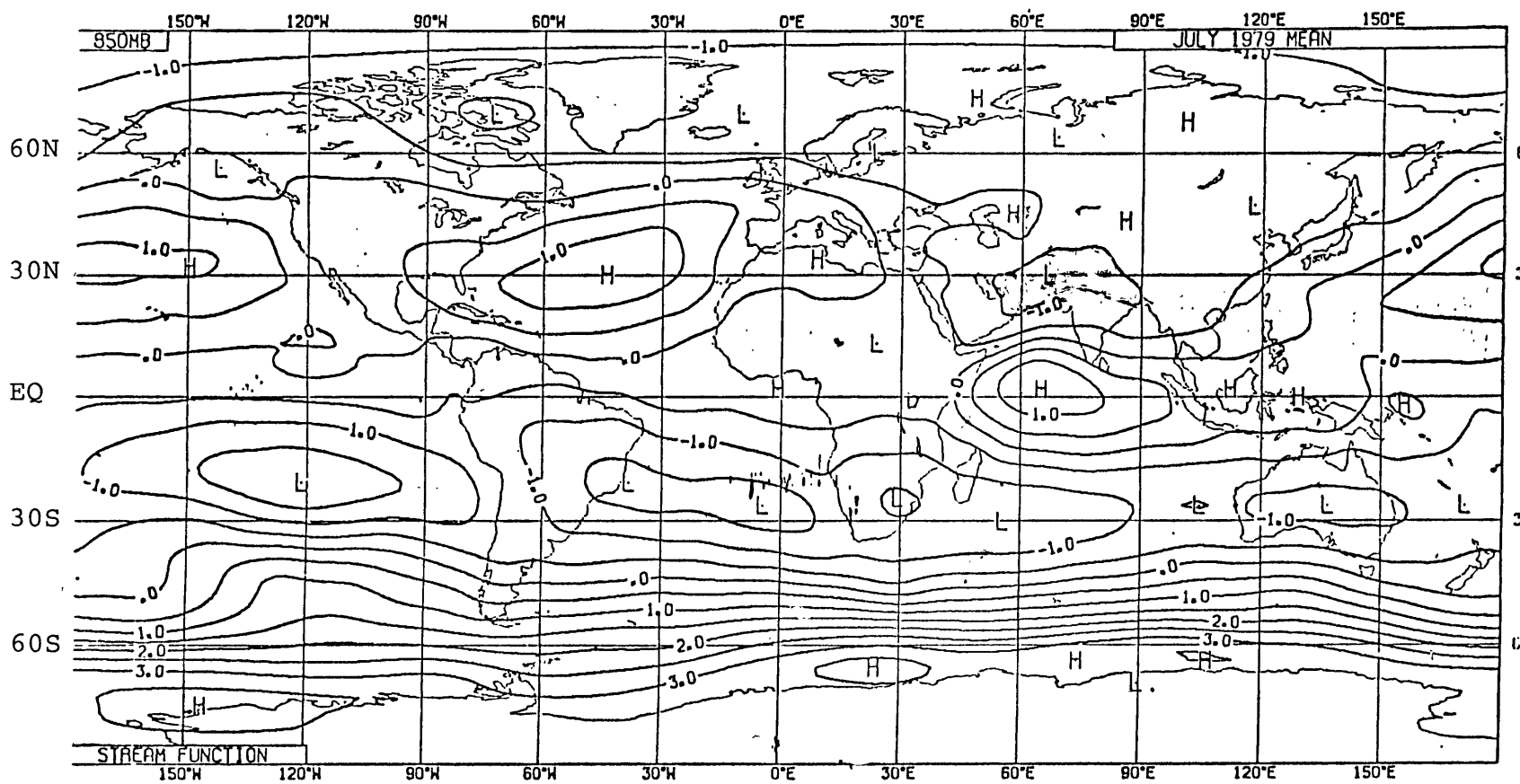   (from ECMWF FGGE data analysis).

Figure 2.31b   Same as Figure 2.31a but at 850 mb.

Pakistan. For the southern hemisphere there is an almost continuous belt of anticyclonic circulation in the subtropics.

We show the velocity potential at 200 mb in Fig. 2.32a. The striking feature is the strong divergent flow over the Indian Ocean east of the minimum of velocity potential over the China Sea (centered at $\simeq$ 15°N). It is clearly seen that there is an upper-level outflow of mass in all directions with strongest divergent motions to the west and south of the low center. Another center of upper-level divergent motion, although somewhat weaker, is found over southern Mexico ($\simeq$ 22°N). Centers of upper-level convergent motion are observed over the eastern South Pacific, South Atlantic, southern Africa, and the Mediterranean Sea. Comparing this figure with the climatological velocity potential field for July (Fig. 2.8b) and with maps of precipitation, we see that the center of upper-level divergent motions over the eastern hemisphere seems to be displaced eastward of its climatological position (which is south of Southeast Asia over the Indian Ocean) for July 1979. The upper-level velocity potential for June and August 1979 (not shown here) exhibits the same behavior, i.e., the low center over the eastern hemisphere seems to be displaced eastward of its climatological position.

The velocity potential at 850 mb is shown in Fig. 2.32b. There is general agreement between the upper- and lower- level nonrotational flows, i.e., lower level centers of convergent (divergent) flow are found in the general position where the upper- level centers of divergent (convergent) flow are observed to exist.

The summer and winter thermally direct circulations, as inferred from the analysis of lower- and upper-velocity potential flow, differ in
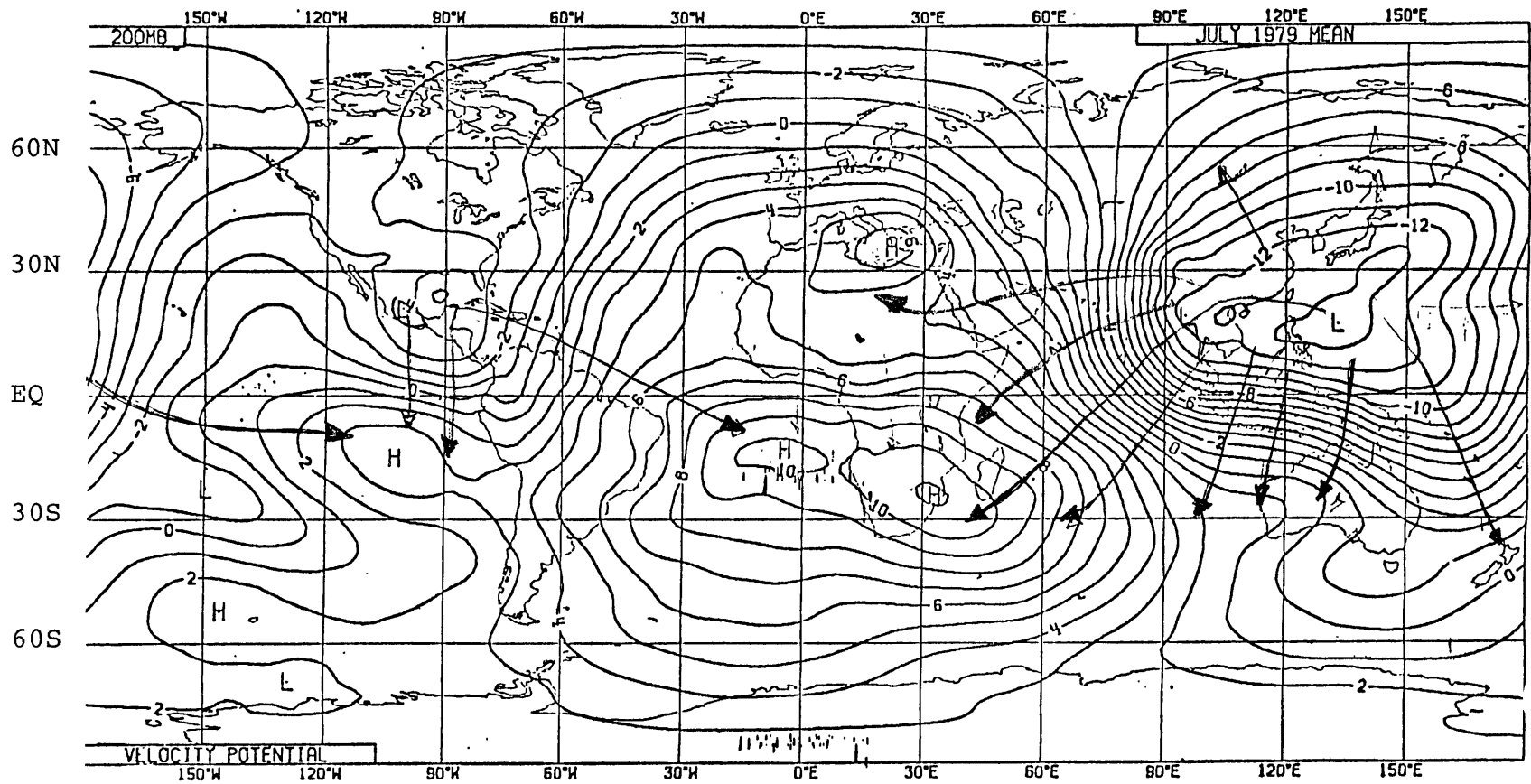
Figure 2.32a   Same as Figure 2.31a but for velocity potential.
Lines with arrows indicate approximate direction
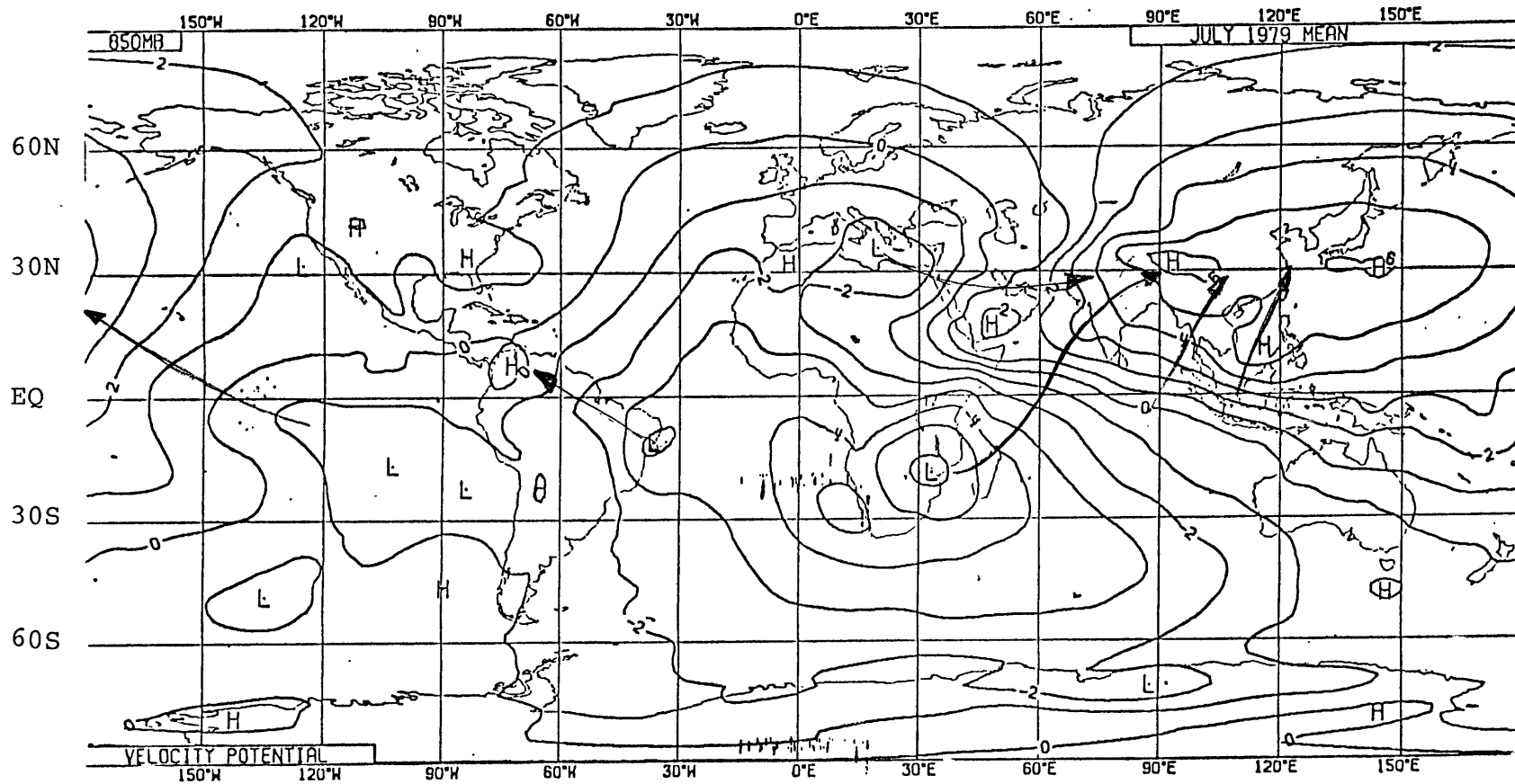of divergent flow.

Figure 2.32b   Same as Figure 2.32a but at 850 mb. Lines with arrows
indicate approximate direction of divergent flow.

two important respects. First, as it might be anticipated, the centers
of rising motion follow the sun's motion; in southern summer they are
found in southern latitudes; and in northern summer, in northern
latitudes. Second, during the southern summer there seem to exist two
significant heat sources with strong associated divergent flows (one over
South America, the other over Indonesia-western Pacific); whereas during
northern summer, the Southeast Asian monsoonal heat source is by far the
most intense for that season and generates the strongest and most
extensive divergent flows of any season.

2.5 SUMMARY OF OBSERVATIONAL RESULTS

In this chapter we have attempted to identify zonal asymmetries in
the thermal forcing and to relate them to the observed asymmetries in the
circulation. Climatological maps of cloudiness and precipitation revealed
significant east-west as well as north-south asymmetries in the
convective heating of the tropical atmosphere, which is the major energy
drive for the planetary-scale tropical motions. The GLAS Jan-Feb, 1979
FGGE data analysis of diabatic heating and vertical velocity confirmed
the presence of these large asymmetries and provides a quantitative
picture for the thermal sources, with heating rates up to $10^{\circ}K/day$ at the
model's level of maximum heating ($\simeq$ 400 mb).

Precipitation zonal asymmetries were seen to be related to the
presence of continents straddling the equatorial region. The degree of
precipitation asymmetry was shown to be greater for the southern summer
because the longitudinal land-sea contrast is more marked for the
southern hemisphere. For the northern summer the precipitation

distribution is less zonally asymmetric. Also, it was seen that the
position of the precipitation maximum within the tropical continents
moves in a SE-NW direction from southern summer to northern summer and
vice-versa. It was suggested that this orientation is due to the
establishment of the northern hemisphere monsoonal circulations or, in
the last instance, to north-south land-sea contrasts with a tropical
continent lying north of an equatorial ocean.

The scale and intensity of the latent heating sources were observed
to have considerable geographical dependence. Highest heating rates were
seen to occur over the Indonesian maritime continent and South America,
whereas the southern Africa heat source is somewhat weaker. The
meridional scale of the heat sources is about the same, 20° to 30° of
latitude, but their zonal scales vary by a large measure. Over South
America (for summer and winter) and Africa (for southern summer), they
are also relatively confined in the longitudinal direction. Northern
summer precipitation over equatorial Africa presents a more zonally
symmetric distribution and a narrower latitudinal scale. The zonal scale
of the heat source over the Indonesian maritime continent is much larger
than its meridional scale for both summer and winter seasons. During the
northern summer there is a succession of intense heat sources displaced
in a longitudinal direction and extending from the western Pacific
westward to India, spanning over 1/3 of the earth's circumference. These
heat sources are tilted horizontally in a NW-SE orientation.

The atmospheric circulation in the tropics was observed to depart a
great deal from a state of zonal symmetry. Lower and upper level
equatorial westerlies are a persistent feature of the time-averaged

tropical flow, as are the centers of strong anticyclonic circulation over the subtropical oceans at the lower level and over the tropical continents at the upper level. The sea level pressure shows a characteristic pattern of semi-permanent subtropical highs over the eastern portions of the oceanic basins and continental lows over the tropical continents during the summer season. The sea level isobars are more parallel to latitude circles in the winter hemisphere.

It is noteworthy that the subtropical jet stream of the upper troposphere during northern hemisphere winter presents a wavenumber 3 structure with three regions of maximum wind speed. This wavenumber 3 structure is not clearly seen in the southern hemisphere subtropical jet stream during southern summer where the jet stream presents just one clearly distinguishable maximum. This is suggestive of an association between the tropical heat sources and the wind speed maxima, i.e., there is a marked wavenumber 3 structure in the heat sources during northern winter, whereas the heat sources are considerably less asymmetric during southern winter.

Analysis of the velocity potential and the divergent part of the wind provided a clearer picture of the thermally direct, large-scale mass overturnings in the tropics. Major areas of divergent motions at the upper level (indicating ascending air) are seen over South America and the Indonesia western Pacific region during the southern summer and a quite vigorous divergent circulation centered over the Southeast Asian monsoon region during northern summer. Convergent upper-level motions are observed over the subtropical oceans and deserts. The picture for the lower level is approximately reversed from the upper level, i.e., convergent motions over the tropical continents and divergent motions

over subtropical oceans and deserts. North-south mass overturnings exist but are confined to the longitudes of the heat source. The east-west (Walker-type) and north-south (Hadley-type) mass overturnings are of comparable strength.

There is a close association between the position and intensity of the divergent circulations and the location of the centers of precipitation maxima and their gradients. The centers of divergent circulation appear where precipitation peaks, and the divergent motions are strongest where precipitation gradients are large, e.g., over Saudi Arabia for the monsoon season. The position of the upper-air easterlies and lower-level westerlies bears correspondence with the westward branch of the east-west circulations (divergent winds being easterlies at the low level and westerlies at the upper level). This agreement seems to indicate that the planetary-scale, stationary asymmetric circulations in the tropics are predominantly forced by condensational heating.

In summary, we can say that localized and intense heat sources over the tropics give rise to strong upward motion with associated convergence at the lower levels and divergence at the upper levels and cause large-scale subsidence around the source region. The cloudless and low-precipitation areas of the subtropical oceans and deserts are thus likely related to this large-scale subsidence.

CHAPTER 3: <u>SIMPLE LINEAR MODEL</u>

Although the main focus of this study is on the <u>nonlinear</u> response of the large-scale tropical circulation forced by isolated diabatic heating sources, we feel that the study of a simple analytic linear model is quite useful in providing some basic understanding about the linear equatorial dynamics. In the present chapter we develop a very simple analytic linear model, linearized about a given basic state and forced by idealized heat sources.

We attempt to address the following question: to what extent does a linear model forced by isolated heat sources simulate features of the planetary-scale atmospheric motions in the tropics, and when are nonlinearities likely to be important? To start to answer this question one should understand the physics of linearized solutions. In this chapter we review some basic concepts of linear solutions forced by ,zonally asymmetric diabatic heating, and in Chapter 5 we will compare linear and nonlinear solutions.

The results of this linear model compare well with results of previous linear studies (Webster, 1972; Gill, 1980) and seem to provide an explanation for some features of the time-averaged large-scale circulation in the tropics.

3.1 <u>LINEAR MODEL DESCRIPTION</u>

3.1.1 <u>MODEL EQUATIONS</u>

The linearized dynamics of hydrostatic steady-state perturbations about a given basic state on a stratified atmosphere in an equatorial β-plane driven by differential heating and controlled by friction, can be written in log-p coordinates as

$$U_0 \frac{\partial u}{\partial x} - \beta y v = - \frac{\partial \phi}{\partial x} - u/\tau_f \qquad [3.1]$$

$$U_0 \frac{\partial v}{\partial y} + \beta y u = - \frac{\partial \phi}{\partial y} - v/\tau_f \qquad [3.2]$$

$$\frac{\partial u}{\partial x} + \frac{\partial v}{\partial y} + \frac{\partial w}{\partial z} - \frac{w}{H} = 0 \qquad [3.3]$$

$$U_0 \frac{\partial T}{\partial x} + S(z)w = \dot{Q} \qquad [3.4]$$

Within the scope of this simple analysis we will not attempt to specify how the mean flow U_0 is maintained but just say that it is in balance with a mean geopotential field and Reynold stresses.

In [3.1]-[3.4], x and y are the eastward and northward distances; $z = -H \ln (p/p_s)$ is the vertical coordinate where H is the scale height, p the pressure and p_s is a standard pressure value (usually $p_s = 1000$ mb); u and v are the eastward and northward velocities, $w = dz/dt$ is a measure of the vertical velocity; ϕ is the geopotential; T is the temperature; S(z) is the static stability; and $\beta = 2\Omega/a$ (= 2.28×10^{-11} $m^{-1}s^{-1}$); Q is the diabatic heating; and τ_f is a constant Rayleigh friction relaxation time.

BOUNDARY CONDITIONS

    a) periodic in x [3.5]

    b) motions are equatorially confined, i.e., all fields $\to 0$ as $|y| \to \infty$

    c) zero mass flux at the ground (assumed flat) and at the top of the atmosphere, thus we take $w = 0$ at the top and bottom of the atmosphere.

We will make an additional assumption about the thermodynamic equation [3.4]. Heat budget studies for the tropics (Katayama, 1964; Cornejo-Garrido and Stone, 1977) indicate that

$$U_0 \frac{\partial T}{\partial x} \ll S(z) w \simeq \dot{Q} ,$$

thus we will neglect the temperature advection term. Eq. [3.4] then becomes

$$S(z)w = \dot{Q} \quad .\qquad\qquad [3.6]$$

This simple form of Eq. [3.6] has an important advantage: vertical and horizontal dependencies easily separate out. If the advection term is not neglected in [3.4], vertical and horizontal dependencies do not separate out easily and an eigenvalue-eigenfunction approach has to be used as in Pedlosky (1980, Ch. 9).

3.1.2. NONDIMENSIONALIZATION

Equations [3.1], [3.2], [3.3], and [3.6] are now nondimensionalized by the following scaling

$$x,y \rightarrow L, \quad u, v \rightarrow U$$

$$z \rightarrow H, \quad w \rightarrow \frac{H}{L} U$$

$$\phi \rightarrow \beta L^2 U$$

$$S(z) \rightarrow S_0, \quad \dot{Q} \rightarrow Q_0$$

where So and Qo are typical (constant) values of the static stability and of the diabatic heating, respectively, and L is a typical scale of the forcing.

The nondimensional set of equations can be written as

$$R_0 \frac{\partial u}{\partial x} - yv = - \frac{\partial \phi}{\partial x} - E_0 u \qquad\qquad [3.7]$$

$$R_0 \frac{\partial v}{\partial x} + yu = - \frac{\partial \phi}{\partial y} - E_0 v \qquad\qquad [3.8]$$

$$\frac{\partial u}{\partial x} + \frac{\partial v}{\partial y} + \frac{\partial w}{\partial z} - w = 0 \qquad\qquad [3.9]$$

$$S(z)w = Q(x,y,z) \qquad\qquad [3.10]$$

where all variables now are nondimensional and the nondimensional

numbers are given by

$$R_0 = \frac{U_0}{\beta L^2}, \qquad\qquad E_0 = (\beta L \tau_f)^{-1}$$

where Ro is the Rossby number. The velocity scale is related to heating

by $U = Q_0 L / S_0 H$.

3.1.3 METHOD OF SOLUTION

From [3.7] - [3.10] we can obtain an equation for v (the vorticity

equation):

$$\left\{ (E_0 + R_0 \frac{\partial}{\partial x})(\frac{\partial^2}{\partial x^2} + \frac{\partial^2}{\partial y^2}) + \frac{\partial}{\partial x}\right\} v = \left\{ y\frac{\partial}{\partial x} - (E_0 + R_0 \frac{\partial}{\partial x})\frac{\partial}{\partial y}\right\} \pounds Q,$$

$$[3.11]$$

$$\text{where} \qquad \pounds = \frac{1}{S(z)}(\frac{\partial}{\partial z} - 1) \quad .$$

The solution of [3.11] is completely determined by the distribution of

heating Q(x,y,z) and the boundary conditions for v.

The prescribed diabatic heating Q(x,y,z) is an idealization of heat

sources over tropical continents and radiative cooling over the tropical

oceans and is assumed to be of the form

$$Q(x,y,z) = Q_0(z) Q(x,y) \quad . \qquad\qquad [3.12]$$

The distribution of $Q_0(z)$ is shown in Figure 3.1 and corresponds to

a vertically distributed heating associated with deep convection given by

$Q_0(z) = \sin kz$ where $k = \pi/H_{top}$. The functions X(x) and Y(y),

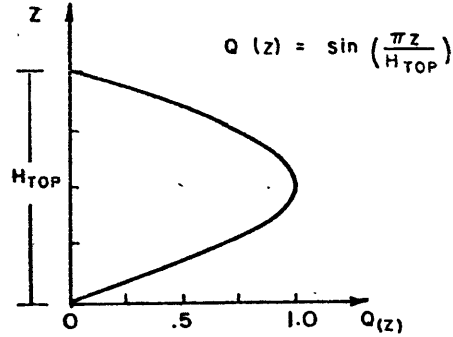describing the horizontal distribution of heating, will be shown in

Section 3.3 below.

Figure 3.1 Vertical structure of prescribed heating given by
$Q_0(z)$ = sin kz where k = π/H_{top}.

With the heating as given by [3.12], v admits solutions of the form

$$v\ (x,y,z)\ =\ A(z)\ V(x,y)\quad .\qquad\qquad [3.13]$$

Then Eqs. [3.11] - [3.13] give the vertical structure equation

$$A(z)\ =\ \frac{1}{S(z)}(\frac{\partial}{\partial z}-1)Q_o(z)\ =\ \frac{1}{S(z)}(k\ \cos\ kz\ -\ \sin\ kz)\qquad [3.14]$$

and the horizontal structure equation

$$\{(E_0\ +\ R_0\ \frac{\partial}{\partial x})\ (\frac{\partial^2}{\partial x^2}\ +\ \frac{\partial^2}{\partial y^2})\ +\ \frac{\partial}{\partial x}\}\ V(x,y)\ =$$

$$[3.15]$$

$$\{y\frac{\partial}{\partial x}\ -\ (E_0\ +\ R_0\ \frac{\partial}{\partial x})\frac{\partial}{\partial y}\}Q(x,y)\quad .$$

The solution of [3.15] is found by expanding V and Q as

$$\{\begin{matrix}V(x,y)\\Q(x,y)\end{matrix}\}\ =\ \sum_{m=-M}^{M}\ \sum_{\ell=0}^{L}\ \{\begin{matrix}V_{m,\ell}\\Q_{m,\ell}\end{matrix}\}\ \psi_\ell(y)\ e^{-imx}\qquad [3.16]$$

where $\Psi_\ell(y) = e^{-y^2/2}H_\ell(y)$ is the ℓth-order Hermite function, such that

$$\int_{-\infty}^{\infty} \psi_n \psi_m \, dy = \pi^{1/2} \, 2^m \, m! \, \delta_{nm} \qquad [3.17]$$

and

$$\frac{d^2\psi_\ell}{dy^2} = \ell(\ell-1)\psi_{\ell-2} - (\ell+{}^1/2)\psi_\ell + {}^1/4\psi_{\ell+2} \quad . \qquad [3.18]$$

From [3.15] using [3.16] - [3.18], we obtain

$$\varepsilon_m(\ell+1)(\ell+2)V_{m,\ell+2} + [im - \varepsilon_m(m^2+\ell+{}^1/2)] \, V_{m,\ell} + \frac{\varepsilon_m}{4}V_{m,\ell-2} =$$

$$[{}^1/2(im+\varepsilon_m)Q_{m,\ell-1} + (im-\varepsilon_m)(\ell+1)Q_{m,\ell+1}] = \Theta_{m,\ell} \qquad [3.19]$$

where $\varepsilon_m = \varepsilon - imR_0$.

For each m the system of equations [3.19] splits up into two symmetries and can be written, for $n = 0,2,4, \ldots$, as

$$\begin{bmatrix} \varepsilon_m(\frac{1}{2}-m^2+im/\varepsilon_m) & \varepsilon_m(1.2) & 0----\\ \varepsilon_m/4 & \varepsilon_m(-\frac{5}{2}-m^2+im/\varepsilon_m) & \varepsilon_m(3.4) \\ 0 & \varepsilon_m/4 & \varepsilon_m(-\frac{9}{2}-m^2+im/\varepsilon_m) \\ \vdots & 0 & \varepsilon_m/4 \\ \vdots & \vdots & 0 \end{bmatrix} \begin{bmatrix} V_{m,0} \\ V_{m,2} \\ V_{m,4} \end{bmatrix} = \begin{bmatrix} \Theta_{m,0} \\ \Theta_{m,2} \\ \Theta_{m,4} \end{bmatrix} \qquad [3.20]$$

and for $n = 1,3,5 \ldots$ as

$$\begin{bmatrix} \varepsilon_m(-\frac{3}{2}-m^2+im/\varepsilon_m) & \varepsilon_m(2.3) & 0----\\ \varepsilon_m/4 & \varepsilon_m(-\frac{7}{2}-m^2+im/\varepsilon_m) & \varepsilon_m(4.5) \\ 0 & \varepsilon_m/4 & \varepsilon_m(-\frac{11}{2}-m^2+im/\varepsilon_m) \\ \vdots & 0 & \varepsilon_m/4 \\ \vdots & \vdots & 0 \end{bmatrix} \begin{bmatrix} V_{m,1} \\ V_{m,3} \\ V_{m,5} \end{bmatrix} = \begin{bmatrix} \Theta_{m,1} \\ \Theta_{m,3} \\ \Theta_{m,5} \end{bmatrix} \qquad [3.21]$$

The two tri-diagonal matrix systems [3.20] and [3.21] are solved by the matrix factorization method for each m (Isaacson and Keller, 1966, pp. 55-56). The terms of the series [3.16] converge as fast as $1/n$ for large n. This model is similar to the one used by Moura and Shukla (1981) where in their model ε_m is simply a constant Rayleigh friction coefficient.

Once v is known, u can be calculated from [3.9], using [3.10] and [3.12] and an expansion similar to [3.16], resulting in

$$U_{m,\ell} = \frac{i}{m} [-{}^1/2 \, V_{m,\ell-1} + (\ell+1) \, V_{m,\ell+1} - Q_{m,\ell}] . \qquad [3.22]$$

Having obtained u and v, we calculate the geopotential ϕ from [3.7], i.e.,

$$\phi_{m,\ell} = \frac{i}{m} [\varepsilon_m U_{m,\ell} - {}^1/2 \, V_{m,\ell-1} - (\ell+1) \, V_{m,\ell+1}] . \qquad [3.23]$$

The "vertical velocity" w is directly determined by [3.10].

3.2   LINEAR MODEL RESULTS

3.2.1   PRELIMINARIES

In this section we will exhibit the linear response to various distributions of forcing functions. In particular, the change of the response with longitudinal scale and distribution and with latitude of thermal sources will be discussed. Here we will use simple arguments based on the linearized vorticity and temperature equation as an aid to comprehending the linear response.

The equatorial β-plane vorticity (ξ) equation is derived from [3.1], [3.2] and [3.3] as

$$(U_0 \frac{\partial}{\partial x} + \tau f^{-1})\xi + \beta v = \beta y(\frac{\partial}{\partial z} - \frac{1}{H})w \ .$$

[3.24]

In the tropics, vertical advection is dominant in the thermodynamic equation for deep heat sources, i.e., $w \sim Q/S$, and Eq. [3.24] becomes

$$(U_0 \frac{\partial}{\partial x} + \tau f^{-1})\xi + \beta v = \beta y(\frac{\partial}{\partial z} - \frac{1}{H})Q/S.$$

[3.25]

It is immediately seen that for symmetric heating, a vorticity maximum/minimum pair is formed on opposite sides of the equator. The distance of this pair away from the equator is found by differentiating the R.H.S. of [3.25] with respect to y. For the forcing y-structure

$$Q(y) = e^{-\frac{1}{\alpha}(y/y_s)^2}$$

they are at a distance $(\alpha/2)^{1/2} y_s$. At the equator the generation of vorticity is zero and the flow is strongly convergent (Lao and Lim, 1982).

In the inviscid limit $\tau f^{-1} \rightarrow 0$, and for large horizontal scales, i.e., $R_0 \ll 1$ ($m \ll m_s = (\beta/U_0)^{1/2}$), the β and stretching terms must balance, i.e.,

$$v \sim y(\frac{\partial}{\partial z} - \frac{1}{H})w \sim \frac{y}{S}(\frac{\partial}{\partial z} - \frac{1}{H})Q.$$

[3.26]

For a deep heat source with maximum amplitude above, the heating is balanced by upward motion ($w > 0$) at the lower levels, and there is generation of positive vorticity (($\partial/\partial z - 1/H)w > 0$). It follows from [3.26] that there is poleward meridional flow, accordingly the low-level trough must be to the west of the heat source (Gill, 1980; Hoskins and Karoly,

1981). When the thermal source is moved away from the equator, the Coriolis parameter increases (in simple terms, $\beta v \sim f \partial w/\partial z$), so that the poleward meridional flow is even stronger; and likewise will be the low-level trough to the west of the heat source.

3.2.2 SCALE CONSIDERATIONS

We examine the dimensionless set of equations [3.7] through [3.10] which, in simplified form, can be written as

$$R_0 u_x - yv = - \phi_x - E_0 u, \qquad [3.27]$$

$$R_0 v_x + yu = - \phi_y - E_0 v; \qquad [3.28]$$

and combining the continuity and thermodynamic equations,

$$u_x + v_y = - Q/H_Q, \qquad [3.29]$$

where $H_Q = Q/Q_z$ is a nondimensional heating scale height.

a) Near-equatorial balances: $y \ll 1$

The relevant balances are given by

$$R_0 u_x + \phi_x + E_0 u = 0 \qquad [3.29a]$$

and

$$R_0 v_x + \phi_y + E_0 v = 0. \qquad [3.29b]$$

If the advection term dominates, i.e., $E_0 \ll R_0$, the near-equatorial balances are between pressure gradient force and zonal advection. If m and ℓ are the inverse of the zonal and meridional local scale of variation of the heating Q, respectively, and are assumed to be proportional to the scale of the response, the magnitudes of u and v are proportional to

$$|u| \sim \frac{m}{(m^2 + \ell^2)} \ |Q|/H_Q,$$

[3.30a]

and

$$|v| \sim \frac{\ell}{(m^2 + \ell^2)} \ |Q|/H_Q \ .$$

[3.30b]

It is seen that for a forcing function centered on the equator with $\ell = \ell(y)$ being a slowly varying function of latitude near the equator, $\ell < m$ and thus, $u > v$. For instance, if the heating function has a Gaussian latitudinal profile $(Q(y) = e^{-y^2/2})$, then ℓ is very small near the equator $(\ell = 0$ at $y = 0)$ and as a consequence the meridional motions are small. On the other hand, if the heating function is centered at a distance away from the equator and dQ/dy is large near the equator, then ℓ will not be small and cross-equatorial flow will be significant. Zebiak (1982), studying a linear model similar to ours also derived some conclusions about the relative magnitudes of u and v based on simple scale arguments.

For the case where $R_0 \ll E_0$, the near-equatorial balances are between pressure gradient force and frictional terms, and the magnitudes of u and v are also approximately given by [3.30]. For the tropics, advective and frictional relaxation time scales are about the same order; therefore, we would expect a three-way balance near the equator among pressure gradient force, advection and friction.

b) Balances away from the equator: $y > 1$

If we assume $R_0 \ll 1$, i.e., $m \ll m_S = (\beta/U_0)^{1/2}$, and also, weak frictional dissipation, i.e., $E_0 \ll 1$, then the O(1) balances away from the equator are approximately geostrophic

$$yv - \phi_x = 0 \qquad \text{and}$$

[3.31a]

$$yu + \phi_y = 0.$$

[3.31b]

In this case, the magnitudes of u and v are proportional to

$$|u| \sim \frac{\ell}{(m^2 + \ell^2)} \, |Q|/H_Q,$$

and

[3.32a]

$$|v| \sim \frac{m}{(m^2 + \ell^2)} \, |Q|/H_Q \; .$$

[3.32b]

Here, because of the geostrophic coupling of u and v, we see that the magnitudes of the horizontal components of the wind as given by [3.32] present an inverse scale dependency as compared to [3.30]. For m $\ll$ ℓ (long-wave approximation), we have u $\gg$ v, and the balances are

$$O(1) \; : \; yu + \phi_y = 0, \quad E_0 v, R_0 v_x < O(R_0)$$

[3.33a]

$$O(R_0) \; : \; R_0 u_x - yv + \phi_x + E_0 u = 0, \; \text{for} \; E_0 = O(R_0).$$

[3.33b]

For heating centered away from the equator, say at y = 1, the magnitudes of u and v will be of the same order when $\ell \sim m$, i.e., if we assume that the heating meridional scale changes slowly near the region of maximum heating. It follows that the meridional motions can attain considerable magnitude. For heating centered at the equator and of zonal scale much larger than meridional scale (m $\ll$ ℓ), the magnitude of v will be small throughout the domain, near the equator because of the slow y-variation of the forcing, and away from the equator due to the geostrophic constraint.

In our simplified analysis in the present chapter, we are not taking into consideration the effects of vertical and meridional advections by the zonal mean winds. We are implicitly assuming that $\ell[\overline{v}]$, $[\overline{w}]/H \ll m[\overline{u}]$, i.e., the zonal advection by the mean flow is the dominant advection. In the next chapter, we will relax this constraint

and assess the importance of meridional and vertical advections of momentum and temperature. Also, by assuming that the scale of motion is determined by the scale of the forcing, we are not taking into consideration the scales determined internally by the system. Thus, relations [3.30] and [3.32] should be thought of as order of magnitude approximations for the forcing region only.

3.2.3 RESULTS

We use the following set of dimensional parameters:

$$
\begin{aligned}
L &= 10° \\
H &= 7.5 \text{ km} \\
S_0 &= 4°\text{K/km} \\
(Q_0/C_p) &= 5°\text{K/day} \\
U_0 &= 5 \text{ m/s} \\
\tau_f &= 7 \text{ days.}
\end{aligned}
\qquad [\text{E.34}]
$$

With this choice of dimensional parameters, $U = 2.2$ m/s, and the nondimensional numbers take the values

$$R_0 = 0.18 \qquad \text{and} \qquad E_0 = 0.05. \qquad [\text{E.35}]$$

Equations [3.20] through [3.23], for v, u and ϕ, will be solved for a number of cases in which we vary the zonal scale and latitudinal position of isolated heat sources. Also, the sensitivity of the response to changes in the parameter R_0 (mean zonal wind) will be discussed. Lastly, we examine a case where we attempt to represent typical heating patterns for the southern summer. All the results are presented for the 700 mb level in nondimensional form, and dimensional values are given by [E.34].

a) <u>Zonal</u> <u>Scale</u> <u>of</u> <u>Forcing</u>

To a first approximation the zonal scale of the condensational heating
in the tropics is given by the longitudinal dimension of the tropical
continents. This is probably the case with respect to contiguous land
masses straddling the equatorial area (e.g., South America and Africa).
The heat sources over the Indonesian Archipelago connect continuously with
those over the western Pacific, and in this case, the zonal scale is larger
and is not determined directly by the size of a tropical continent, for a
large part of it seems to lie over the ocean. Still an open problem in
dynamic meteorology is the question whether the scales of tropical heat
sources are mostly determined by the dynamics of the flow field (e.g.,
large-scale convergence organizing smaller-scale cumulus convection) or
whether the lower boundary condition (e.g., land versus ocean) plays a more
determinant role. It is our contention that over land, the scale of the
heat sources is determined to a first order solely by the dimensions of the
tropical land masses. This point will be discussed in more detail in the
concluding section, Chapter 6.

Figure 3.2 shows the four different x-structures used (see
Appendix A). Their zonal scales are approximately a) 36°, b) 45°, c) 60°,
and d) 90°. The y-structure is simply the zeroth order Hermite Function
$\psi_0(y)$ (Gaussian). We start by examining in more detail the response to
forcing (a). All figures in the remainder of this chapter refer to the
lower-level response. Given the simple vertical structure of the forcing,
the upper-level solution is similar; just the sign is reversed. For this
case $E_0 = 0.05$ and $R_0 = 0$.

Zonal and meridional velocities, geopotential and vorticity are shown
in Figure 3.3 for the forcing (a) of Figure 3.2. We observe a pair of low

centers (Figure 3.3c) symmetric about the equator, to the west of the heat source, and about 15° away from the equator. Cyclonic circulation develops around the low centers, and in the source region the meridional flow is poleward. Near the equator, easterlies prevail to the east of the source and westerlies, to the west, but the wind distribution presents marked zonal asymmetry, with the region of easterlies extending much farther than the region of westerlies. This asymmetry was explained by Gill (1980) in terms of propagation of equatorial waves away from the source, a Kelvin wave to the east and the lowest order Rossby mode to the west, for a heating function symmetric about the equator. The phase speed of the fastest moving Rossby mode is 1/3 of that of the Kelvin wave (Matsuno, 1966), or for the stationary case, dissipation acts three times as strongly for the Rossby mode to the west than for the Kelvin wave to the east. Gill (1980) also suggested that the observed asymmetry in the east-west circulations (see Figures 2.10 and 2.11) may be explained in terms of the above mechanism. We will return to this point in the discussion section, Chapter 6. The vorticity field, Figure 3.3d, shows a minimum/maximum pair, symmetric about the equator and 10° of latitude away from the equator. We remark that the maximum wind speeds are found at the equator with the magnitude of the westerly jet approximately twice as large as that of the easterly wind maximum.

In Table 3.1 we present minimum and maximum values of zonal and meridional winds, geopotential and vorticity for the forcings of Figure 3.2.
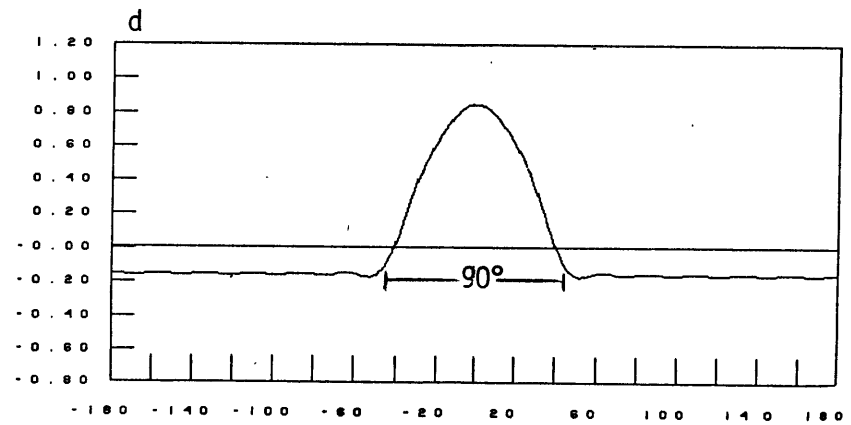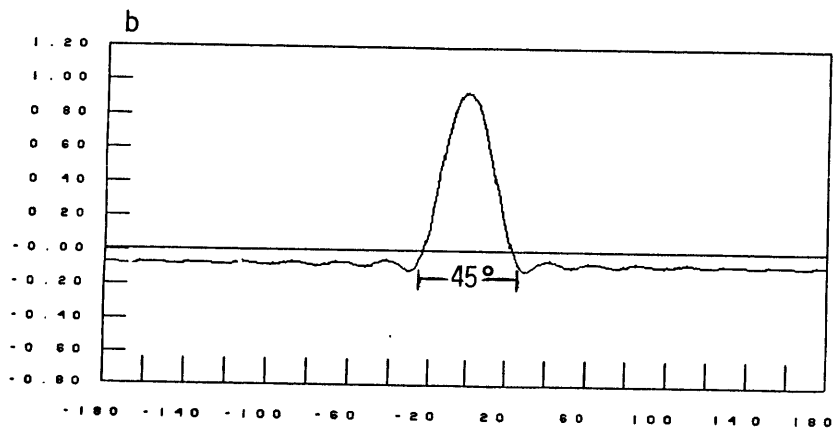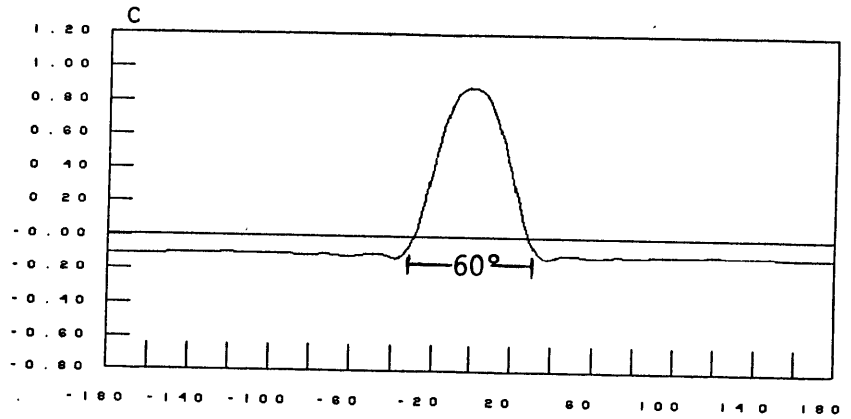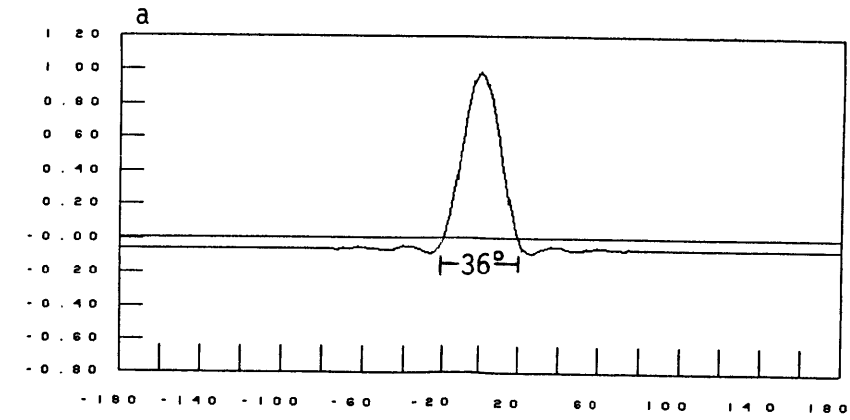
Figure 3.2   Longitudinal structure of forcing.   Scales are approximately a) 36°, b) 45°, c) 60°, and d) 90°

EO-.051 RO- 0.000 FORCING:1W-36 IN X HEO IN Y
ZONAL WIND
a

SIMPLE LINEAR MODEL

VALUES RANGE BETWEEN   -1.08   AND   2.19   FOR CONTOUR INTERVALS OF   0.20
RUN= 2

EO-.051 RO- 0.000 FORCING:1W-36 IN X HEO IN Y
GEOPOTENTIAL
c

SIMPLE LINEAR MODEL

VALUES RANGE BETWEEN   -1.37   AND   0.48   FOR CONTOUR INTERVALS OF   0.20
RUN= 5

EO-.051 RO- 0.000 FORCING:1W-36 IN X HEO IN Y
MERIDIONAL WIND
b

SIMPLE LINEAR MODEL

VALUES RANGE BETWEEN   -0.46   AND   0.46   FOR CONTOUR INTERVALS OF   0.10
RUN= 3

EO-.051 RO- 0.000 FORCING:1W-36 IN X HEO IN Y
VORTICITY
d

SIMPLE LINEAR MODEL

VALUES RANGE BETWEEN   -1.79   AND   1.79   FOR CONTOUR INTERVALS OF   0.25
RUN= 6

Figure 3.3   Zonal (a) and meridional (b) velocities, geopotential (c) and vorticity (d) for forcing (a) of Figure 3.2.

Table 3.1

Minimum and Maximum Values of u, v, ϕ and ξ

for Different Zonal Scale of Forcing

Forcing x-scale	u		v		ϕ		ξ	
	MIN	MAX	MIN	MAX	MIN	MAX	MIN	MAX
36°	-1.08	2.19	-0.46	0.46	-1.37	0.48	-1.79	1.79
45°	-1.29	2.69	-0.43	0.43	-1.61	0.60	-2.17	2.17
60°	-1.69	3.24	-0.43	-0.43	-2.01	0.80	-2.65	2.65
90°	-2.39	4.01	-0.38	-0.38	-2.50	1.18	-3.18	3.18

We show, in Figure 3.4, winds and geopotential for the different forcings. As the zonal scale of the forcing is increased, u, ϕ and ξ increase, whereas v slightly decreases. This is consistent with the scale arguments of the previous section (Eqs. [3.30] and [3.32]) for heating centered at the equator.

b) <u>Latitudinal Position of Forcing</u>

Here we vary the latitudinal position of the forcing. The forcing now is located at approximately 12°S and its zonal structure is the one given in Figure 3.2a (zonal scale ≈ 36°). E_0 = 0.05 and R_0 = 0.0 for this case. The forcing's horizontal structure and the fields of u, v and ξ are shown in Figure 3.5. In Figure 3.6 geopotential and wind vectors are shown for this case and for the case with heating centered at the equator, which is reproduced here for comparison.

When the heat source is moved away from the equator, zonal winds (Figure 3.5b) are maximum away from the equator, and unlike the case
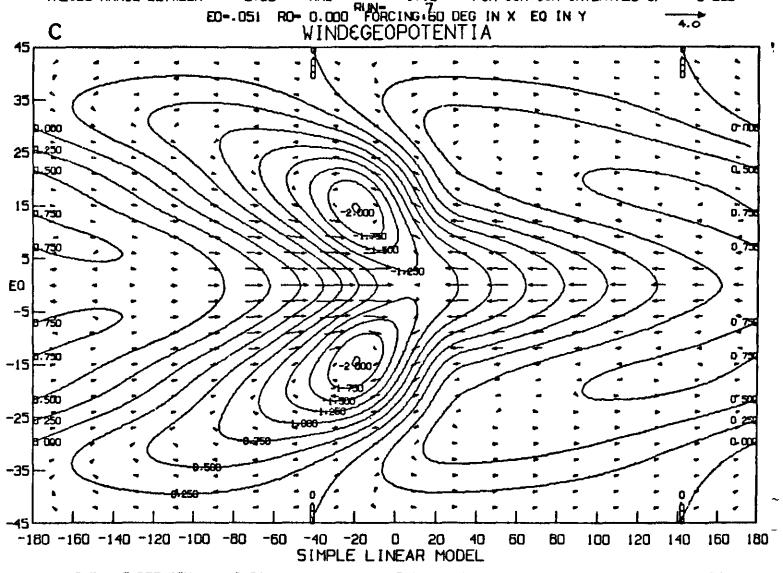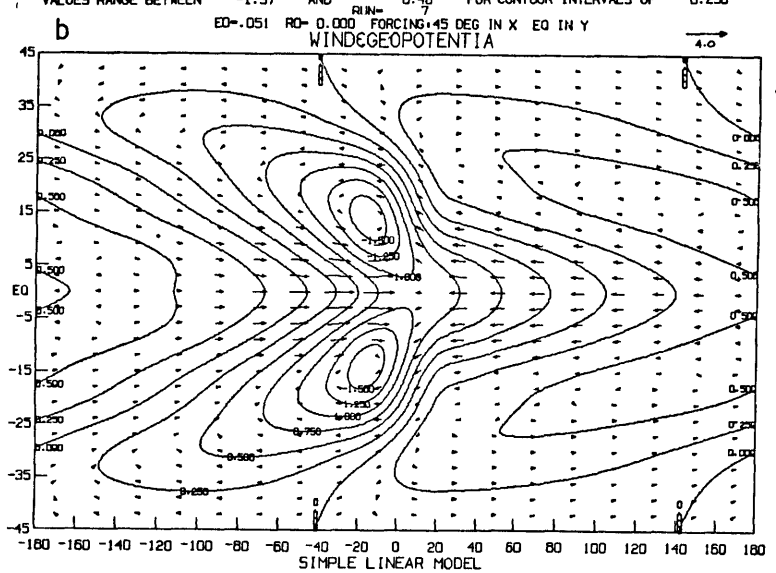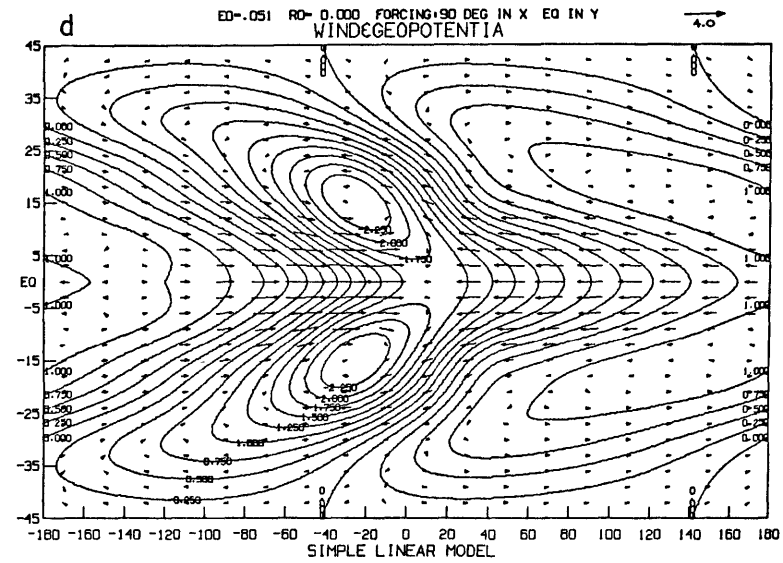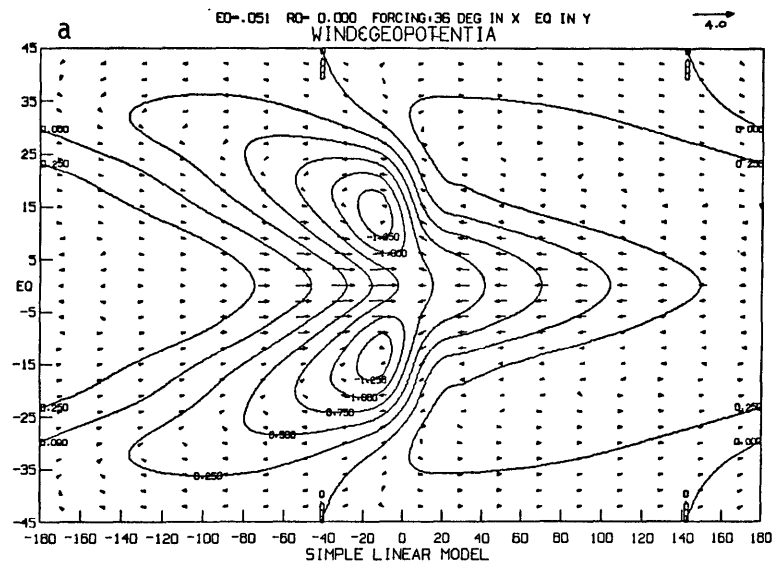
Figure 3.4   Geopotential and wind corresponding to forcings with zonal scales of 36°(a), 45°(b), 60°(c), and 90°(d) (see Figure 3.2).

a

ED=-.051 RO= 0.000 FORCING:36 DEG IN X HERMITE
DIABATIC HEATING

SIMPLE LINEAR MODEL

VALUES RANGE BETWEEN   -0.08   AND   0.98   FOR CONTOUR INTERVALS OF   0.10
RUN= 4

b

ED=-.051 RO= 0.000 FORCING:36 DEG IN X HERMITE
ZONAL WIND

SIMPLE LINEAR MODEL

VALUES RANGE BETWEEN   -1.36   AND   2.46   FOR CONTOUR INTERVALS OF   0.25
RUN= 2

c

ED=-.051 RO= 0.000 FORCING:36 DEG IN X HERMITE
MERIDIONAL WIND

SIMPLE LINEAR MODEL

VALUES RANGE BETWEEN   -1.36   AND   0.31   FOR CONTOUR INTERVALS OF   0.20
RUN= 3

d

ED=-.051 RO= 0.000 FORCING:36 DEG IN X HERMITE
VORTICITY

SIMPLE LINEAR MODEL

VALUES RANGE BETWEEN   -1.56   AND   2.14   FOR CONTOUR INTERVALS OF   0.25
RUN= 6

Figure 3.5   Horizontal structure of diabatic heating forcing (a) and
associated response: b) zonal wind, c) meridional wind, and
d) vorticity.

Figure 3.6   Geopotential and wind vectors for a) forcing at 12°S,
              b) forcing at the equator (contour interval every
              0.5 units for (a) and every 0.25 units for (b)).

for a heat source at the equator, the meridional winds are much stronger and non-zero at the latitude of maximum heating. Also, there is cross equatorial flow (Figure 3.5b). Accompanying the greater meridional velocities near the heat source is an intensified low center to the southwest of the source (Figure 3.6 a). The increase in v and thus in the geopotential field is understood in terms of conservation of vorticity as explained in section 3.2.1.

c) Southern Hemisphere "Realistic" Heating

We attempt in this section to represent a typical heating pattern of the southern hemisphere summer with three heat sources of finite longitudinal extent, centered over South America, Africa and the Indonesian maritime continent, respectively. In Figure 3.7, we show the horizontal structure of the forcing. Note the different zonal scales for each heat source, the cooling regions over the oceans, and the pattern which is centered approximately at 12°S. For this case we take $E_0 = 0.051$ and $R_0 = -0.178$ which is equivalent to a mean easterly zonal wind of 5 m/sec. In Figure 3.8, we present the fields of u, v, ξ, and ϕ plus wind vectors.

The response is concentrated in the hemisphere containing the heat source as meridional velocity and geopotential are small in the northern hemisphere. In the heating hemisphere there is a pattern of lows to the west of the heat source and highs to the east. The strongest circulation is associated with the Indonesian heat source. Maximum winds are easterlies converging into the region of the Indonesian heat source. The circulation associated with the African heat source is smaller in magnitude reflecting weaker heating.

If we conceptually add to this asymmetric heating a symmetric heating representing a hypothetical ITCZ centered at the equator, the geopotential

field created by this axially symmetric heating would be negative at the equator, becoming less negative polewards. For our linear systems, that solution would simply add to the zonally asymmetric solution. The emerging picture would show a geopotential distribution less zonally asymmetric in the northern hemisphere and an alternating pattern of lows and highs in the southern hemisphere. The mean easterlies would add to the zonally asymmetric winds, and the result would be an augmented region of easterlies and a smaller area of westerlies. This picture retains qualitatively some major features of the southern summer tropical circulation.

d) Parameter Sensitivity Analysis

It is of some interest to study the sensitivity of the response to changes in the mean zonal wind and frictional dissipation. The scale analysis of the previous section has shown that near the equator, advection and friction are likely to be important in the dynamical balances. Also, although the mean winds in the tropics are easterlies, it is interesting to see what the solution would be for mean westerly winds. This is a crude way of taking into consideration the observation that there are extensive areas in the tropics for which the time mean winds are westerlies. The simplicity of our model does not allow for taking explicitly a longitudinally varying basic-state.

We show in Figure 3.9 geopotential and wind vector for seven cases where E_0 was kept fixed ($E_0 = 0.051$) and R_0 was varied corresponding to the following mean zonal winds: -10 m/s (a), -5 m/s (b), -2 m/s (c), no zonal wind (d), 2 m/s (e), 5 m/s (f), and 10 m/s (g). For mean easterlies and weak westerlies the solution is not very sensitive to the zonal wind, but for strong mean westerly wind (Figure 3.9g) there is meridional propagation. This result is similar to the results obtained by Hoskins and Karoly (1981).

EO-.051 RO--0.178 FORCING:SH-REALISTIC 12SIN Y
DIABATIC HEATING

SIMPLE LINEAR MODEL

VALUES RANGE BETWEEN   -0.39   AND   0.77   FOR CONTOUR INTERVALS OF   0.10
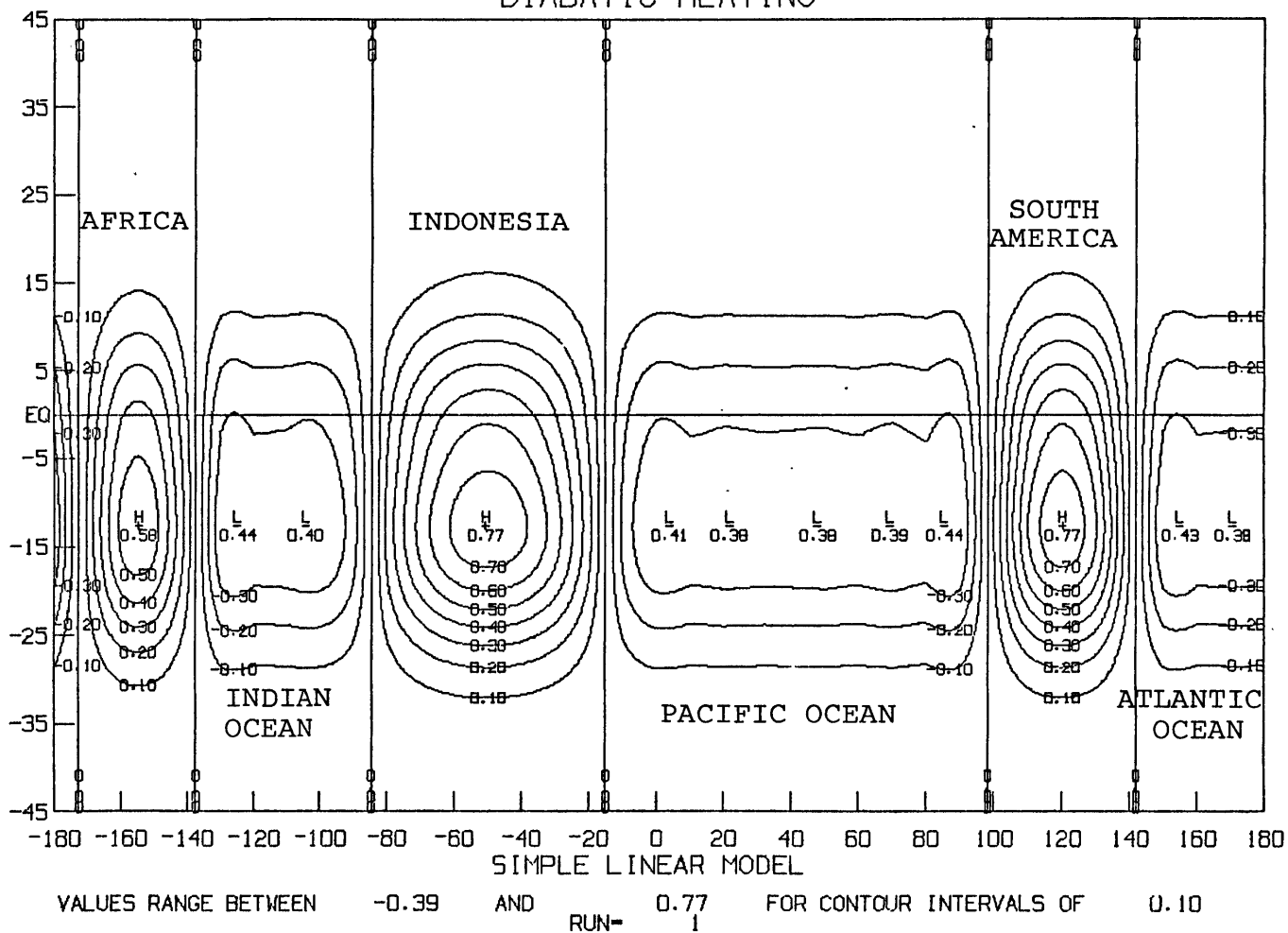
RUN-   1

Figure 3.7   Horizontal structure of southern hemisphere
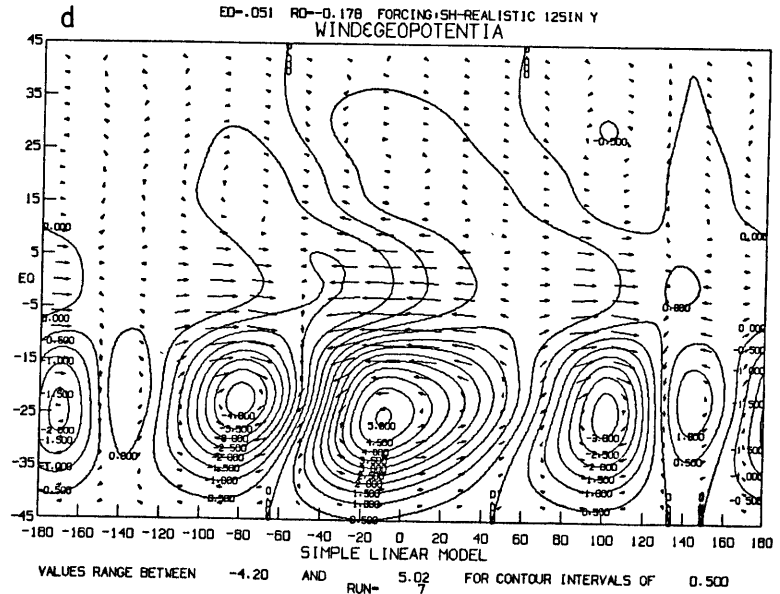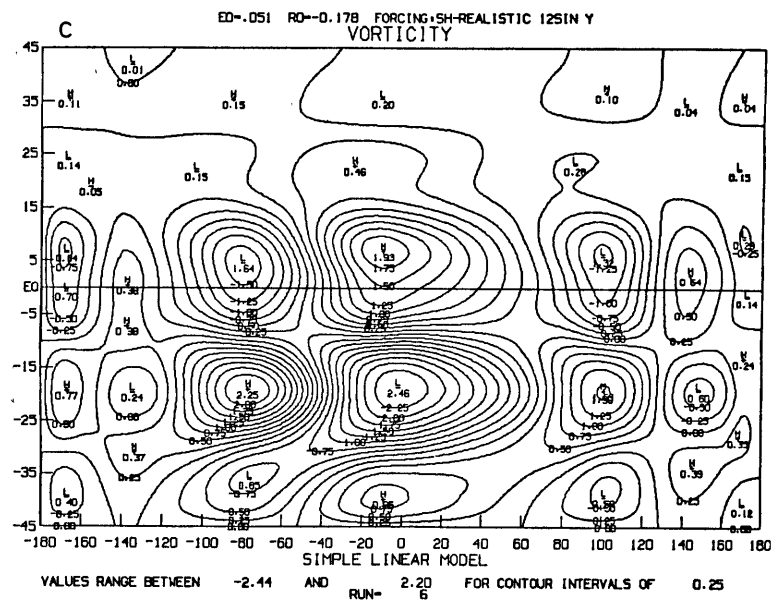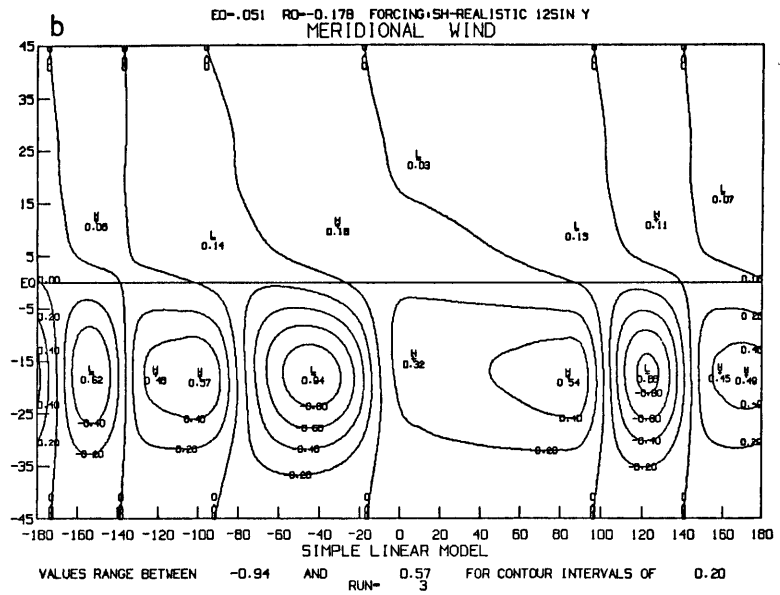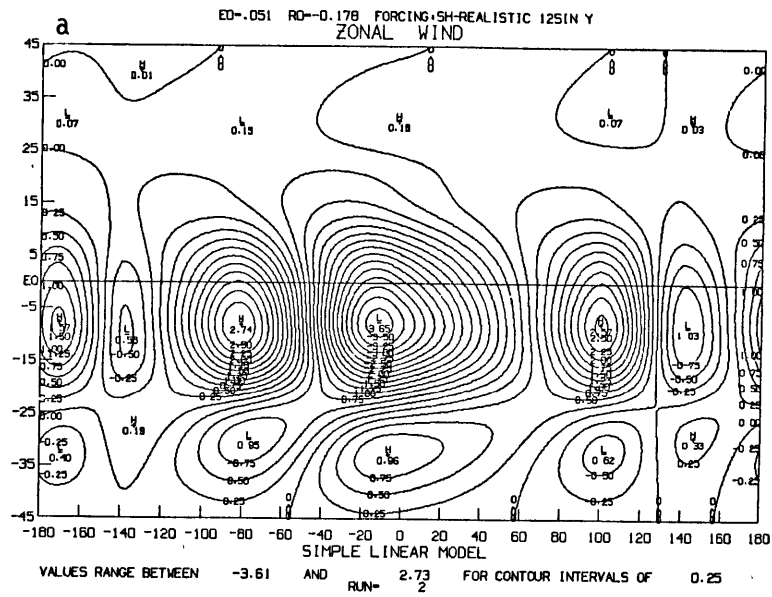"realistic" diabatic heating forcing.

Figure 3.8   a) Zonal wind, b) meridional wind, c) vorticity, and
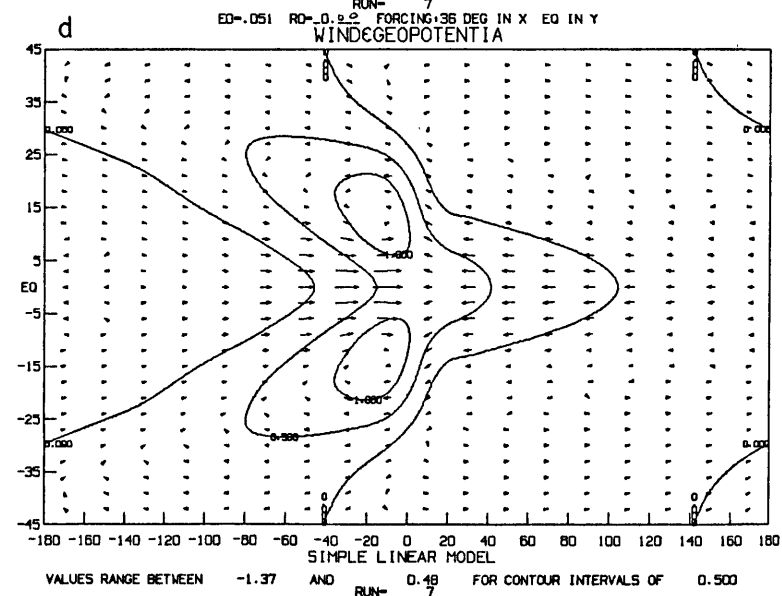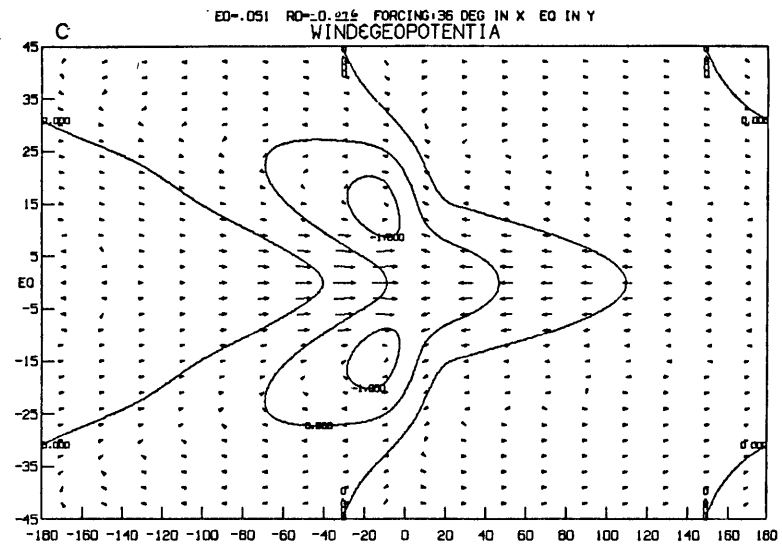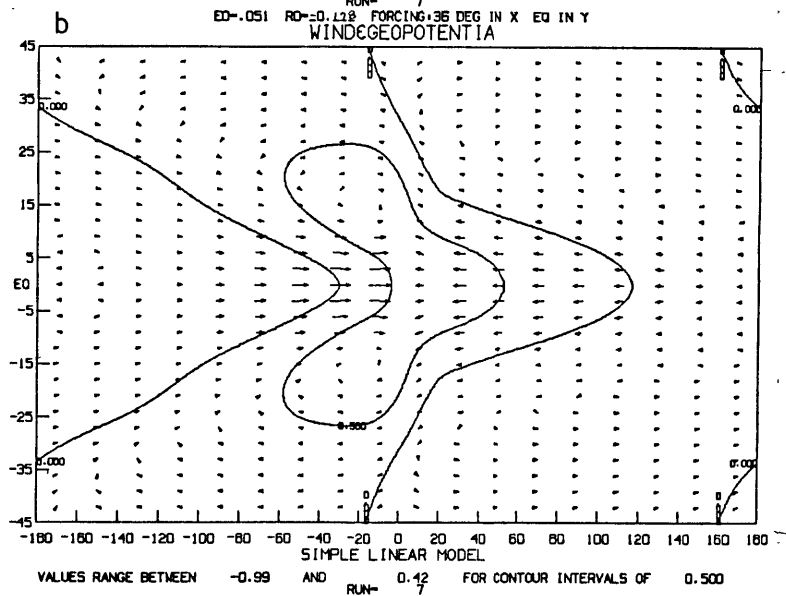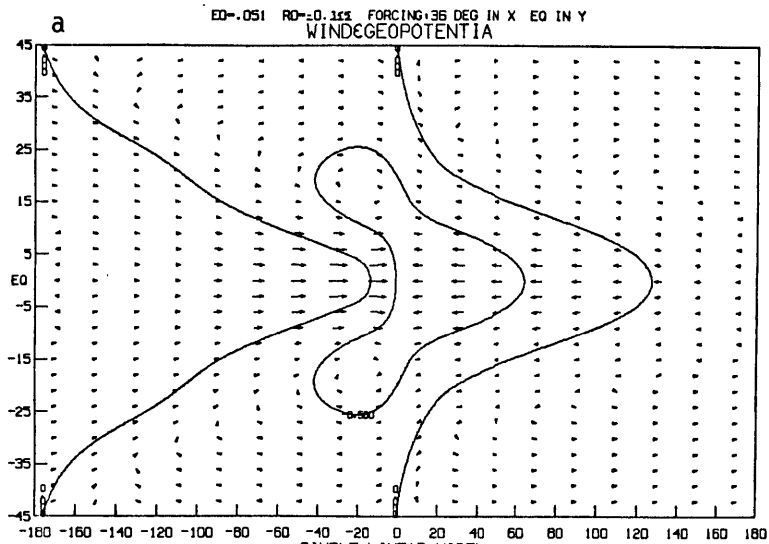   d) geopotential and wind vectors for forcing of Figure 3.7.

ED-.051 RO-=0.1££ FORCING:36 DEG IN X EQ IN Y
WIND&GEOPOTENTIA

a

SIMPLE LINEAR MODEL
VALUES RANGE BETWEEN   -0.94   AND   0.44   FOR CONTOUR INTERVALS OF   0.500
RUN-   7

ED-.051 RO-=0.2₁₆ FORCING:36 DEG IN X EQ IN Y
WIND&GEOPOTENTIA

c

SIMPLE LINEAR MODEL
VALUES RANGE BETWEEN   -1.18   AND   0.45   FOR CONTOUR INTERVALS OF   0.500
RUN-   7

ED-.051 RO-=0.12₈ FORCING:36 DEG IN X EQ IN Y
WIND&GEOPOTENTIA

b

SIMPLE LINEAR MODEL
VALUES RANGE BETWEEN   -0.99   AND   0.42   FOR CONTOUR INTERVALS OF   0.500
RUN-   7

ED-.051 RO-=0.₉₂ FORCING:36 DEG IN X EQ IN Y
WIND&GEOPOTENTIA

d

SIMPLE LINEAR MODEL
VALUES RANGE BETWEEN   -1.37   AND   0.48   FOR CONTOUR INTERVALS OF   0.500
RUN-   7

Figure 3.9   Geopotential and wind vectors for the forcing of Figure 3.2a
at the equator when the basic state wind U_0 takes the following
values: a) -10 m/s, b) -5 m/s, c) -2 m/s, d) no mean wind,
e) +2 m/s, f) +5 m/s, and g) +10 m/s.

e

EO=-.051 RO=±0.275 FORCING:36 DEG IN X EQ IN Y
WIND&GEOPOTENTIA

SIMPLE LINEAR MODEL

VALUES RANGE BETWEEN   -1.64   AND   0.53   FOR CONTOUR INTERVALS OF   0.500
RUN= 7

f

EO=-.051 RO=±0.119 FORCING:36 DEG IN X EQ IN Y
WIND&GEOPOTENTIA

SIMPLE LINEAR MODEL

VALUES RANGE BETWEEN   -1.99   AND   0.93   FOR CONTOUR INTERVALS OF   0.500
RUN= 7

g

EO=-.051 RO=±0.355 FORCING:36 DEG IN X EQ IN Y
WIND&GEOPOTENTIA

SIMPLE LINEAR MODEL

VALUES RANGE BETWEEN   -2.54   AND   2.98   FOR CONTOUR INTERVALS OF   0.500
RUN= 7

Figure 3.9 Continued.

CHAPTER 4: <u>NONLINEAR MODEL</u>

In the previous chapter, scale analysis has stressed the importance of advection for the dynamical balances in the tropical regions. A simple linear model was used to study the response of the tropical atmosphere to a zonally asymmetric perturbation heating for a given mean zonal flow. The results of this linearized advection analysis pointed to the need of taking into account nonlinearities, which is what we are attempting to do in this chapter.

It is expected that inertial balances become increasingly important near the equator as the Coriolis force becomes vanishingly small. The observational evidence of easterlies and westerlies in the tropical troposphere indicates that zonal advection of momentum might be important. Schneider (1977) has shown, for an axisymmetric model, that the poleward advection of zonal momentum from the convectively active equatorial belt is very important in maintaining the upper-level subtropical jet stream.

In view of what was said, it is clear that a horizontally unvarying basic flow, as considered in the previous chapter, is not realistic. Easterlies and westerlies at the same latitude are a conspicuous feature of the time mean tropical circulation. In the present section we develop a simple, primitive equation, nonlinear model to attempt to take into account the full nonlinear character of the problem. Purposedly the model's physics is made very simple so that, unlike complex GCM's, it can hopefully yield simple physical interpretation.

4.1 DESCRIPTION OF THE MODEL

4.1.1 GOVERNING EQUATIONS

Equatorial β-plane geometry is used since we are primarily interested in the response of the tropical atmosphere to forcing within the tropics.

The governing equations for this problem are the zonal and meridional momentum, hydrostatic, continuity and thermodynamic equations. In log-p vertical coordinates (Eliassen, 1949; Holton, 1975) on an equatorial β-plane, they are, respectively,

$$\frac{\partial u}{\partial t} + u\frac{\partial u}{\partial x} + v\frac{\partial u}{\partial y} + w\frac{\partial u}{\partial z} - \beta y v = -\frac{\partial \phi}{\partial x} + F_x \qquad [4.1]$$

$$\frac{\partial v}{\partial t} + u\frac{\partial v}{\partial x} + v\frac{\partial v}{\partial y} + w\frac{\partial v}{\partial z} + \beta y u = -\frac{\partial \phi}{\partial y} + F_y \qquad [4.2]$$

$$\frac{\partial \phi}{\partial z} = \frac{R}{H}T' \qquad [4.3]$$

$$\frac{\partial u}{\partial x} + \frac{\partial v}{\partial y} + \frac{\partial w}{\partial z} - \frac{w}{H} = 0 \qquad [4.4]$$

$$\frac{\partial T'}{\partial t} + u\frac{\partial T'}{\partial x} + v\frac{\partial T'}{\partial y} + w\frac{\partial T'}{\partial z} + S_0(z)w = \frac{1}{Cp}[\dot{Q}_L + \dot{Q}_R]. \qquad [4.5]$$

The vertical coordinate is $z = -H \ln(p/p_s)$ where H is the scale height and p_s is a reference pressure value taken equal to 1000 mb. For an isothermal atmosphere z is the actual height, $w = \frac{dz}{dt}$ is a measure of vertical velocity, and H, the density scale height, is given by $H = R\bar{T}_0/g$ where $\bar{T}$ is a global average temperature. For $\bar{T}_0=255K$, $H \simeq 7.5$ km. This value will be used thereafter. T' is the departure of the actual temperature T from the basic state temperature $T_0(z)$.

The static stability is given by

$$S_0(z) = \frac{dT_0(z)}{dz} + \kappa \frac{T_0(z)}{H} \qquad [4.6]$$

where To is a basic-state temperature, assumed to be a function of z only. This basic-state temperature is in hydrostatic balance with a basic-state geopotential

$$\frac{d\phi_0(z)}{dz} = \frac{R}{H} T_0(z). \qquad [4.7]$$

The remaining symbols in equations [4.1] through [4.7] have the usual meaning and are defined in the list of symbols in Appendix H.

BOUNDARY CONDITIONS

1) all fields are periodic in x

2) all fields vanish as $y \to \pm \infty$

3) vertical boundary conditions: no mass flow at the bottom and "top" of the model that is assumed to be a rigid lid.

In the log-p coordinate system the lower boundary condition is given by (Holton, 1975, pp. 57-58)

$$\frac{d\Phi}{dt} = g \, w_{phys} \quad \text{at} \quad z = -H \, \ln(p_B/p_s) \qquad [4.8]$$

where $p_B(x,y,t)$ is the variable surface pressure and w_{phys} is the actual vertical velocity. The departures of p_B from p_s are small so that to a good approximation we can apply the surface boundary condition at the coordinate surface z=0, i.e., $p_B = p_s$.

Remembering that $\Phi(x,y,z,t) = \phi(x,y,z,t) + \phi_0(z)$ we obtain from [4.8] an equation for the local variation of geopotential for the lower boundary

$$\frac{\partial \phi}{\partial t} + u \frac{\partial \phi}{\partial x} + v \frac{\partial \phi}{\partial y} + w\left(\frac{\partial \phi_0}{\partial z} + \frac{\partial \phi}{\partial z}\right) = g\, w_{phys} \quad \text{at} \quad z = 0. \qquad [4.9]$$

Neglecting $\dfrac{\partial \phi}{\partial z}$ as compared to $\dfrac{\partial \phi_0}{\partial z}$ and making use of the hydrostatic relation [4.7] to eliminate $\dfrac{\partial \phi_0}{\partial z}$ we arrive at the following expression

$$\frac{\partial \phi}{\partial t} + u \frac{\partial \phi}{\partial x} + v \frac{\partial \phi}{\partial y} + w \frac{R}{H} T_S = g\, w_{phys} \quad \text{at} \quad z = 0, \qquad [4.10]$$

where T_S is the lower boundary temperature and is assumed to be constant and equal to 300 K.

Heating at the bottom surface, Ekman pumping (frictional convergence in the boundary layer) and topography can produce a vertical velocity at the lower boundary. The effect of the earth's topography can be taken into account by considering a vertical velocity forced at the surface

$$w_{topog} = \vec{U}_S \cdot \nabla h(x,y) \quad \text{at} \quad z = 0 \qquad [4.11]$$

where $h(x,y)$ represents the height of the topography and $\vec{U}_S$ is a reasonable estimate of the horizontal wind at the surface. Such a representation of topographical effects is rather crude, but on the other hand, the model's low resolution would preclude a realistic representation of the earth's topography.

4.1.2 PHYSICAL PARAMETERIZATION

In keeping with the main goal of this work that focuses on the study of nonlinear dynamics in tropical motions forced by isolated heat sources,

we will keep the model's physics very simple so as to make it possible to easily identify the effect of nonlinearities.

FRICTIONAL DISSIPATION AND RADIATIVE PROCESSES

Frictional dissipation and radiative processes are parameterized as simple linear damping laws (Rayleigh friction and Newtonian cooling). Friction is parameterized as a linear function of wind speed

$$F_x = -u/\tau_f \quad \text{and} \quad F_y = -v/\tau_f \qquad [4.12]$$

where the τ_f is the relaxation time for momentum dissipation and is assumed to be constant.

Newtonian cooling is parameterized as proportional to the temperature departure from the radiative equilibrium temperature

$$\dot{Q}_R = -(T-T_E)/\tau_r \qquad [4.13]$$

where T_E is a prescribed radiative equilibrium temperature and τ_r is a constant temperature relaxation time.

For the actual calculations, τ_f and τ_r are taken to be equal to 10 days, and we write

$$\dot{Q}_R = -(T_o(z) - T_E)/\tau_r - T'/\tau_r \qquad [4.14]$$

where the first term in the R.H.S. of [4.14] will be prescribed.

STATIC STABILITY

To a first approximation the vertical temperature of the tropical atmosphere is close to the moist adiabatic lapse-rate. In a climatological

sense it does not depart significantly from that state seeing that
imbalances in the vertical column that arise due to diurnal solar heating
of the surface are quickly restored by convective adjustments, and the
lapse-rate remains nearly moist adiabatic. Also, because the horizontal
temperature gradients are small in the tropics, S_0 is approximately
constant horizontally except in clouds. Based on data from Newell
et al. (1974), the static stability S_0 is taken equal to 4°K/km.

LATENT HEATING

The main asymmetric forcing in our study will be the heating of the
large-scale environment by the condensation of water vapor in deep
cumulus clouds (hot towers). Heat budget studies (Katayama, 1964;
Cornejo-Garrido and Stone, 1977) have indicated that this is the leading
diabatic heating term for the tropical regions, it being larger than net
radiative heating and sensible heating of the atmosphere.

As evidenced from the precipitaton maps shown in Chapter 2, latent
heating in the tropics presents strong zonal asymmetries. To a first
approximation it can be thought of as being made of isolated heat sources
over the continents and a narrow continuous band (ITC) over the oceans.
We recognize, however, that precipitation maps (Figs. 2.2 and 2.3) have
shown that only for South America and Africa can the heat sources be
thought of as isolated; the Indonesian-Western Pacific heat source is
broader and more nearly zonally oriented.

Because the main focus of this study is on zonal asymmetries, we
will be concerned only with the isolated heat sources over continents,
i.e., the discontinuous character of the latent heating along the zonal
direction. Of course, in a more realistic representation of large-scale
circulations forced by diabatic heating in the tropics, the axisymmetric

part of the heating including the narrow ITCZ also has to be taken into account. There has been, however, a great deal of theoretical work on the symmetric circulations (Schneider and Lindzen, 1977; Schneider, 1977; Held and Hou, 1980), and we felt it was more appropriate for our study to concentrate on the asymmetric forcing.

The latent heating will be prescribed in the model and not allowed to vary with time. We realize that small-scale cumulus cloud formation is to a great extent organized by meso- and large-scale moisture convergence at the lower level. This implies that precipitation is dynamically coupled to the flow field. How the large-scale flow affects cumulus dynamics is not yet well understood and only recently, due to its importance to GCM's, has this subject provoked theoretical (Arakawa and Schubert, 1974; and others) and observational study (Houze, 1973; and many others). Also several studies (Schneider and Lindzen, 1977; Geisler, 1981) have pointed out the importance of momentum transports within the cumulus cloud environment. This so called "cumulus friction" effect is not taken into account in this study.

TOTAL PRESCRIBED DIABATIC HEATING

The vertical profile of diabatic heating adopted is depicted in Fig. 4.1 in nondimensional form. It peaks at 500 mb and goes to zero at 100 mb (top) and 1000 mb (bottom).

The prescribed total diabatic heating in our model comprises two terms: a latent heating term, $\dot{Q}_L$, and a radiative cooling term, $(-T_0(z) - T_E)/\tau_r$. Values for the net radiative cooling for the atmosphere are given by Newell (1974, pp. 11). In the tropics, radiative heating rates of -2.0°K/day are observed near the surface, -0.7°K/day at mid-tropospheric levels and -1.7°K/day at 300 mb; so the radiative heating vertical structure is different from that of the latent heating

which peaks at the middle troposphere. The distributions of diabatic heating used are idealizations of realistic distributions, and their choice was guided by the diabatic heating generated by the GLAS analysis of FGGE data.

In Table 5.1 of the next chapter, the three values of diabatic heating intensity used in numerical integrations of the model are presented as well as their equivalence in terms of precipitation rates.

In the actual integration of the model, we will not attempt to simulate a detailed and realistic distribution of diabatic heating since that would require a fine resolution which would become computationally very expensive for the nonlinear model. Instead we chose to work with idealized heat sources with simple x, y and z structures. That is computationally less expensive because of the coarser resolution. Also, it will yield simpler interpretations of the results still, hopefully, retaining important qualitative features of tropical large-scale circulations. In Chapter 5 we show the various horizontal distributions of latent heating used in this study (Figure 5.1).

RESULTING EQUATIONS

With the physical parameterizations adopted, the governing Eqs. [4.1], [4.2] and [4.5] become

$$\frac{\partial u}{\partial t} + u \frac{\partial u}{\partial x} + v \frac{\partial u}{\partial y} + w \frac{\partial u}{\partial z} - \beta y v = -\frac{\partial \phi}{\partial x} - \frac{u}{\tau_f} \qquad [4.1']$$

$$\frac{\partial v}{\partial t} + u \frac{\partial v}{\partial x} + v \frac{\partial v}{\partial y} + w \frac{\partial v}{\partial z} + \beta y u = -\frac{\partial \phi}{\partial y} - \frac{v}{\tau_f} \qquad [4.2']$$

$$\frac{\partial T'}{\partial t} + u \frac{\partial T'}{\partial x} + v \frac{\partial T'}{\partial y} + w \frac{\partial T'}{\partial z} + S_0 w = \frac{\dot{Q}_T}{C_p}(x,y,z) - \frac{T'}{\tau_r} \qquad [4.5']$$
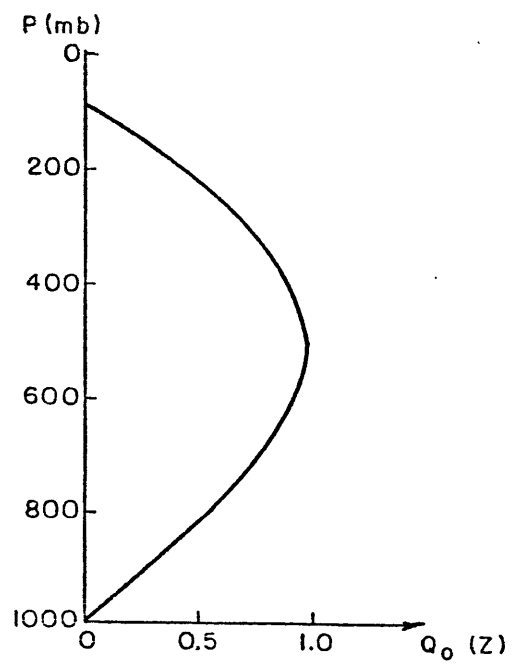
Figure 4.1   Vertical Distribution of Diabatic Heating

where

$$\dot{Q}_T = \dot{Q}_L - (T_o(z) - T_E)/\tau_r$$

is the prescribed total diabatic heating.

4.1.3 NONDIMENSIONALIZATION

Equations [4.1]', [4.2]', [4.3], [4.4], [4.5]', and the vertical boundary condition [4.10] are now nondimensionalized. Denoting new nondimensional variables as starred variables, the scaling will be the following:

$$
\begin{aligned}
x,y &= L(x^*,y^*) \\
z &= Hz^* \\
u,v &= U(u^*,v^*) \\
w &= (HU/L)w^* \\
t &= (\beta L)^{-1} t^* \\
\phi &= (\beta L^2 U)\phi^* \\
T' &= (\beta L^2 U/R)T^* \\
Q_T &= Q_0 \, Q_T^*
\end{aligned}
\qquad [4.15]
$$

where L, H and U are typical scales for horizontal length, vertical length, and horizontal wind speed, and Q_0 is a typical diabatic heating rate.

The new set of nondimensional equations is

$$\frac{\partial u^*}{\partial t^*} + R_0\left(u^* \frac{\partial u^*}{\partial x^*} + v^* \frac{\partial u^*}{dy^*} + w^* \frac{\partial u^*}{\partial z^*}\right) - y^*v^* = -\frac{\partial \phi^*}{\partial x^*} - r_0 u^* \qquad [4.16]$$

$$\frac{\partial v^*}{\partial t^*} + R_0\left(u^* \frac{\partial v^*}{\partial x^*} + v^* \frac{\partial v^*}{\partial y^*} + w^* \frac{\partial v^*}{\partial z^*}\right) + y^*u^* = -\frac{\partial \phi^*}{\partial y^*} - r_0 v^* \qquad [4.17]$$

$$\frac{\partial \phi^*}{\partial z^*} = T^* \qquad [4.19]$$

$$\frac{\partial u^*}{\partial x^*} + \frac{\partial v^*}{\partial y^*} + \frac{\partial w^*}{dz^*} - w^* = 0 \qquad [4.19]$$

$$\frac{\partial T^*}{\partial t^*} + R_0\left(u^* \frac{\partial T^*}{\partial x^*} + v^* \frac{\partial T^*}{dy^*} + w^* \frac{\partial T^*}{\partial z^*}\right) + A_0 w^* = F_0 \, Q_T^* - \gamma_0 T^* \qquad [4.20]$$

and the nondimensional B.C.

$$\frac{\partial \phi^*}{\partial t^*} + R_0 \left(u^* \frac{\partial \phi^*}{\partial x^*} + v^* \frac{\partial \phi^*}{\partial y^*} \right) + N_0 w^* = B_0 \, w^*_{phys} \quad \text{at} \quad z^* = 0 \quad [4.21]$$

where the nondimensional parameters are

$$R_0 = \frac{U}{\beta L^2}, \quad A_0 = \frac{S_0 RH}{(\beta L^2)^2}, \quad F_0 = \frac{Q_0 R}{C_p \beta^2 L^3 U},$$

[4.22a]

$$r_0 = (\beta L \tau_f)^{-1}, \quad \gamma_0 = (\beta L \tau_r)^{-1}, \quad N_0 = \frac{RT_s}{(\beta L^2)^2 U}, \quad B_0 = \frac{gH}{(\beta L^2)^2},$$

where R_0 is the Rossby number.

The dimensional parameters used for the nonlinear integrations are

$L = 10°$	$H = 7.5$ km
$U = 10$ m s^{-1}	$\beta = 2.28 \times 10^{-11}$ (m s)$^{-1}$
$R = 287$ K^{-1} m^2 s^{-2}	$g = 9.81$ m s^{-2}
$(Q_0/C_p) = 5°$K day^{-1}	$S_0 = 4°$K km^{-1}
$\tau_f = \tau_r = 10$ days	$T_s = 300$ K

[4.22b]

With this choice, the nondimensional numbers become

$R_0 = 0.354$	$E_0 = 10.8$	$F_0 = 2.32$
$r_0 = \gamma_0 = 0.05$	$N_0 = 108.8$	$B_0 = 92.5$

[4.22c]

4.2 SPECTRAL REPRESENTATION OF THE MODEL

In this section a spectral model will be developed for the numerical
integration of the set of equations [4.16] through [4.22]. Horizontally,
all variables and the forcing will be expanded in Fourier series in the
x-direction and normalized Hermite Functions in the y-direction. The
rationale for choosing Hermite Functions for the latitudinal expansions
is that this set of basis function allows for great simplicity in the
calculations of Coriolis terms and y-derivatives by virtue of their
recursion relations and also due to the realization that the normal modes
for an equatorial β-plane are expressed in terms of Hermite Functions
(Matsuno, 1966). The forcing function in the model -latent heating in
deep cumulus clouds -in general attains high values in the tropics and
falls off to very small values rather abruptly in the subtropics. That
being the case, the $e^{-y^2/2}$ factor in the Hermite Functions is compatible
with the y-variation in the forcing.

Vertically the model's atmosphere will be divided into 5 layers,
and finite differences will be used to evaluate vertical derivatives.
The set of equations for the spectral coefficients will be numerically
integrated in time until the solution equilibrates the prescribed latent
heating source.

4.2.1 SPECTRAL EXPANSIONS

Expand all fields as

$$
\begin{bmatrix} u^* \\ v^* \\ w^* \\ \phi^* \\ T^* \\ Q_T^* \end{bmatrix} = Re\left\{ \sum_{m=-M}^{M} \sum_{\ell=0}^{L} \begin{bmatrix} U_{m,\ell} \\ V_{m,\ell} \\ W_{m,\ell} \\ \phi_{m,\ell} \\ T_{m,\ell} \\ Q_{m,\ell} \end{bmatrix} \Psi_\ell(y)\, e^{-imx} \right\} \qquad [4.23]
$$

where

$$\Psi_\ell(y) = \frac{H_\ell(y)e^{-y^2/2}}{(2^\ell \, \ell! \, \pi^{1/2})^{1/2}}$$

is the normalized Hermite Function (NHF) of order ℓ with $H_\ell(y)$ being the ℓth order Hermite polynomial and the spectral coefficients $U_{m,\ell}$, $V_{m,\ell}$, $W_{m,\ell}$, $\phi_{m,\ell}$ and $T_{m,\ell}$ are functions of only z and t (see Appendix B for a summary of NHF properties).

Substituting the spectral expansions [4.23] into the nondimensional set [4.16] through [4.21] in order to eliminate the x and y dependencies and to obtain a set of equations for the spectral coefficients, we apply the standard procedure: multiply the set of equations through by $e^{inx}\Psi_k(y)$ and then integrate from $-\pi$ to π in x and from $-\infty$ to ∞ in y. After making use of the recursion relations for NHF

$$y\Psi_\ell = (\frac{\ell}{2})^{1/2} \Psi_{\ell-1} + (\frac{\ell+1}{2})^{1/2} \Psi_{\ell+1}$$

$$\frac{d\Psi_\ell}{dy} = (\frac{\ell}{2})^{1/2} \Psi_{\ell-1} - (\frac{\ell+1}{2})^{1/2} \Psi_{\ell+1}$$

[4.24]

and the orthonormality relations for Fourier series and NHF

$$\frac{1}{2\pi} \int_{-\pi}^{\pi} e^{-i(m-n)x} dx = \begin{cases} 1 & m = n \\ 0 & m \neq n \end{cases}$$

[4.25]

$$\int_{-\infty}^{\infty} \Psi_k(y) \, \Psi_\ell(y) \, dy = \begin{cases} 1 & k = \ell \\ 0 & k \neq \ell \end{cases}$$

[4.26]

we obtain the following set of equations for the spectral coefficients

$$\frac{\partial U_{m,\ell}}{\partial t} = -R_0 C(U)_{m,\ell} + [(\frac{\ell+1}{2})^{1/2} V_{m,\ell+1} + (\frac{\ell}{2})^{1/2} V_{m,\ell-1}]$$

$$+ im \phi_{m,\ell} - r_0 U_{m,\ell} \qquad [4.27]$$

$$\frac{\partial V_{m,\ell}}{\partial t} = -R_0 C(V)_{m,\ell} + [(\frac{\ell+1}{2})^{1/2} (U_{m,\ell+1} + \phi_{m,\ell+1})$$

$$+ (\frac{\ell}{2})^{1/2} (U_{m,\ell-1} - \phi_{m,\ell-1})] - r_0 V_{m,\ell} \qquad [4.28]$$

$$\frac{\partial \phi_{m,\ell}}{\partial z} = T_{m,\ell} \qquad [4.29]$$

$$\frac{\partial W_{m,\ell}}{\partial z} = W_{m,\ell} + im U_{m,\ell} - [(\frac{\ell+1}{2})^{1/2} V_{m,\ell+1} + (\frac{\ell}{2})^{1/2} V_{m,\ell-1}]$$

$$[4.30]$$

$$\frac{\partial T_{m,\ell}}{\partial t} = -R_0 C(T)_{m,\ell} - A_0 W_{m,\ell} + F_0 Q_{m,\ell} - \gamma_0 T_{m,\ell} \qquad [4.31]$$

and the boundary condition

$$\frac{\partial \phi_{m,\ell}}{\partial t} = -R_0 CH(\phi)_{m,\ell} + N_0 W_{m,\ell} + B_0 W(phys)_{m,\ell} \qquad [4.32]$$

where $C(A)_{m,\ell}$ is the spectral representation of the tridimensional advection of the quantity A

$$u \frac{\partial A}{\partial x} + v \frac{\partial A}{\partial y} + w \frac{\partial A}{\partial z} = \sum_{m=-M}^{M} \sum_{\ell=0}^{L} C(A)_{m,\ell} \psi_\ell(y) e^{-imx} \qquad [4.33]$$

and $CH(A)_{m,\ell}$ is the spectral representation of the horizontal advection

$$u \frac{\partial A}{\partial x} + v \frac{\partial A}{\partial y} = \sum_{m=-M}^{M} \sum_{\ell=0}^{L} CH(A)_{m,\ell} \psi_\ell(y) e^{-imx} \qquad [4.34]$$

4.2.2 CALCULATION OF NONLINEAR TERMS

Let A and B be two variables expressed in terms of a set of basis orthogonal functions

$$A = \sum_{m=-M}^{M} \sum_{\ell=0}^{L} A_{m,\ell} \; \psi_\ell(y) \; e^{-imx} \qquad [4.35]$$

$$B = \sum_{m=-M}^{M} \sum_{\ell=0}^{L} B_{m,\ell} \; \psi_\ell(y) \; e^{-imx} \qquad [4.36]$$

where Ψ_ℓ is the NHF of order ℓ.

We want to find the spectral coefficients $C_{m,\ell}$ such that

$$AxB = \sum_{m=-M}^{M} \sum_{\ell=0}^{L} C_{m,\ell} \; \psi_\ell(y) \; e^{-imx} \quad . \qquad [4.37]$$

The transform method will be utilized for the calculation of the nonlinear interaction coefficients. Briefly, the method consists of the following steps (see Appendix C for details on the transform method and its advantages and for references about spectral methods):

1) define a set of grid-points (x_i, y_j) (physical space) and evaluate

$$A(x_i, y_j) = \sum_{m=-M}^{M} \sum_{\ell=0}^{L} A_{m,\ell} \; \psi_\ell(y_j) \; e^{-imx_i} \qquad [4.38]$$

$$B(x_i, y_j) = \sum_{m=-M}^{M} \sum_{\ell=0}^{L} B_{m,\ell} \; \psi_\ell(y_j) \; e^{-imx_i} \qquad [4.39]$$

for each grid-point for all pairs (x_i, y_j),

2) carry out the nonlinear multiplication in the physical space for all grid-points (x_i, y_j),

3) tranform the product AxB in physical space to spectral space, i.e., find

$$C_{m,\ell} = \int_{-\pi}^{\pi} \int_{-\infty}^{\infty} [AxB](x,y) \; \psi_\ell(y) \; e^{-imx} \; dy \; dx. \qquad [4.40]$$

In the actual calculation of advection terms, a derivative has to be evaluated before step 1, such as in the calculations of $u \frac{\partial A}{\partial x}$, $v \frac{\partial A}{\partial y}$ and $w \frac{\partial A}{\partial z}$. Evaluate the horizontal derivatives in the spectral space, i.e.,

$$\frac{\partial A}{\partial x} \rightarrow - (im)A_m$$

$$\frac{\partial A}{\partial y} \rightarrow [(\frac{\ell+1}{2})^{1/2} A_{m,\ell+1} - (\frac{\ell}{2})^{1/2} A_{m,\ell-1}]$$

and $\frac{\partial A}{\partial z}$ is evaluated using finite differences in the vertical. Then proceed to steps 1,2, and 3.

4.2.3 VERTICAL DIFFERENCING SCHEME

The model's atmosphere is divided into 5 layers in the vertical as shown in Fig. 4.2 with rigid lids at the top (100 mb) and bottom (1000 mb). In Section 4.3 we will discuss some of the possible limitations of having a rigid lid at 100 mb. The variables u, v and T' will be evaluated at mid-layer points and w and ϕ in the layer edges. A mid-layer variable is denoted by k even; a variable taken at the edge of the layer, by k odd. Variables vanish at the top boundary, i.e.,

$$(u,v,w,\phi,T') \rightarrow 0 \quad at \; z = z_{p=100 \; mb}. \qquad [4.41]$$
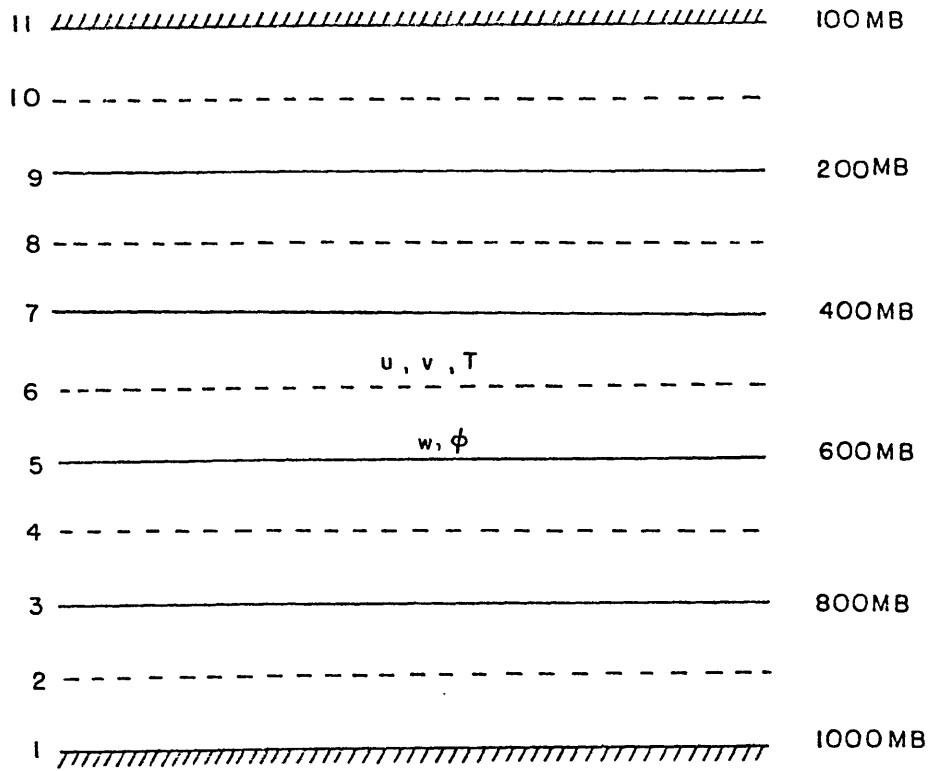
Figure 4.2   Five-Layer Model

If topography is considered, the real vertical velocity at the lower boundary can be approximated by Eq. [4.11] $\left(w_{phys} = \vec{U}_s \cdot \nabla h(x,y)\right)$ where the surface wind $\vec{U}_s$ can be estimated from extrapolating to the ground the wind at the lowest layers of the model, and the topographical height $h(x,y)$ can be represented by

$$h(x,y) = \sum_{m=-M}^{M} \sum_{\ell=0}^{L} h_{m,\ell} \; \psi_\ell(y) \; e^{-imx} \; . \tag{4.42}$$

With topography included, the lower B.C. (Eq. [4.31]) becomes

$$\frac{\partial \phi_{m,\ell}}{\partial t} = -R_0 CH(\phi)_{m,\ell} + N_0 \; W_{m,\ell} + B_0 \; CH(h)_{m,\ell} \; . \tag{4.43}$$

The resulting set of equations consists of 4 prognostic equations for U, V, T and for the geopotential at the lower boundary, and two diagnostic equations.

PROGNOSTIC EQUATIONS

$$\frac{\partial U_{m,\ell}^k}{\partial t} = -R_0 C_{m,\ell}^k(U) + \left[\left(\frac{\ell+1}{2}\right)^{1/2} V_{m,\ell+1}^k + \left(\frac{\ell}{2}\right)^{1/2} V_{m,\ell-1}^k\right]$$
$$+ \; im \; \phi_{m,\ell}^k - r_0 \; U_{m,\ell} \tag{4.44}$$

$$\frac{\partial V_{m,\ell}^k}{\partial t} = -R_0 C_{m,\ell}^k(V) + \left[\left(\frac{\ell+1}{2}\right)^{1/2} \left(U_{m,\ell+1}^k + \phi_{m,\ell+1}^k\right) + \right.$$
$$\left. \left(\frac{\ell}{2}\right)^{1/2} \left(U_{m,\ell-1}^k - \phi_{m,\ell-1}^k\right)\right] - r_0 \; V_{m,\ell}^k \tag{4.45}$$

$$\frac{\partial T_{m,\ell}^k}{\partial t} = -R_0 C_{m,\ell}^k(T) - A_0 \; W_{m,\ell}^k + F_0 \; Q_{m,\ell}^k - \gamma_0 \; T_{m,\ell}^k \; . \tag{4.46}$$

The three equations above are evaluated at k even, and the lower boundary condition

$$\frac{\partial \phi_{m,\ell}^k}{\partial t} = -R_0 CH_{m,\ell}^k(\phi) + N_0 W_{m,\ell}^k + B_0 CH_{m,\ell}^k(h) \quad \text{at } k=1 \qquad [4.47]$$

DIAGNOSTIC EQUATIONS

$$\phi_{m,\ell}^{k+1} = \phi_{m,\ell}^{k-1} + \Delta z \, T_{m,\ell}^k \qquad [4.48]$$

where $\phi_{m,\ell}^1$ is obtained from [4.46], and

$$W_{m,\ell}^{k-1} = \frac{1}{(1+\Delta z^k)} \left[(1-\Delta z^k) W_{m,\ell}^{k-1} + \Delta z^k (-im \, U_{m,\ell}^k \right.$$

$$\qquad [4.49]$$

$$\left. + \left(\frac{\ell+1}{2}\right)^{1/2} V_{m,\ell+1}^k - \left(\frac{\ell}{2}\right)^{1/2} V_{m,\ell-1}^k \right) \right]$$

with $W_{m,\ell}^{11}(z=z_{top}) = 0$.

The prognostic equations for U, V and T will be evaluated at mid-layer points, and the hydrostatic equation will be integrated upward with the bottom B.C. for ϕ given by the prognostic equation [4.46] for $\phi(z=0)$. The continuity equation will be integrated downward with the top B.C. given by w=0 at $z=z_{top}$.

For the calculation of vertical advection terms in Eqs. [4.43], [4.44] and [4.45], mid-layer values for w and edge values for the advected quantitites are calculated. For instance, to evaluate $\left(w\frac{dT}{dz}\right)_{k_{even}}$, first we calculate W at the mid-layer level as $W^k = (W^{k+1} + W^{k-1})/2$ and then approximate

$$\left(\frac{dT}{dz}\right)_k \simeq \frac{T^{k+1} + T^{k-1}}{\Delta z^k} \qquad [4.50]$$

where

$$T^{k+1} = (T^{k+2} + T^k)/2$$

and

$$T^{k-1} = (T^k + T^{k-2})/2 \; .$$

In Table 4.1 and 4.2 we show the dimensional and nondimensional vertical coordinates corresponding to Fig. 4.1.

TABLE 4.1 - VERTICAL COORDINATES OF THE MODEL'S LAYERS

k	LEVEL (mb)	z_{dim} (km)	z_{nd}
1	1000	0	0
2	900	0.7902	0.1054
3	800	1.6736	0.2231
4	700	2.6751	0.3567
5	600	3.8312	0.5108
6	500	5.1986	0.6932
7	400	6.8722	0.9163
8	300	9.0298	1.2040
9	200	12.0708	1.6094
10	150	14.2284	1.8971
11	100	17.2694	2.3026

TABLE 4.2 - VERTICAL LAYER THICKNESS

k	Δz_{dim} (km)	Δz_{nd}
2	1.6736	0.2231
4	2.1576	0.2877
6	3.0410	0.4055
8	5.1986	0.6931
10	5.1986	0.6931

4.2.4 TIME INTEGRATION SCHEME

The prognostic equations (Eqs. [4.43] through [4.46]) will be integrated in time, and the time integration scheme used is a slight modification of the Matsuno (Euler backward) scheme. Schematically, say

$$\frac{dX}{dt} = F$$

is the equation to be integrated numerically in time. The Matsuno scheme is a two-step iterative scheme in that it advances first to an intermediate time step and then to the final time step, i.e.,

$$X^{t*} = X^t + \Delta t \, F^t$$
$$X^{t+\Delta t} = X^t + \Delta t \, F^{t*}.$$

[4.51]

We made some test runs with different time integration schemes and concluded that the Matsuno scheme provided essentially accurate results with less computations than higher order schemes such as the Runge-Kutta 4th order scheme. The number of computations is a critical consideration since the calculation of the nonlinear terms requires a large number of operations, and a higher order or an iterative scheme with many iterations to advance to the next time step would render the integration computationally too expensive.

In the actual numerical integration of equations [4.43] through [4.46], it was found necessary to modify slightly the Matsuno scheme to avoid error growth. The new scheme we call modified Matsuno time integration scheme. Appendix D gives details on how this error growth arises and how it was corrected. In summary, the accumulation of errors occurred in the prognostic equation for the meridional wind v (Eq. [4.44]) due to truncation errors in the computation of $\partial \phi / \partial y$. We found that the problem was corrected by not advancing the geopotential field in the second iteration of the Matsuno time scheme. With this

modification truncation errors remained bounded and the solution converged to a steady-state solution.

The time step Δt for computational stability will be a function of the model's resolution. The finer the resolution, the smaller the time step that still resolves the fastest moving gravity waves. This resolution in the meridional direction is approximately given by the distance between zeros of the highest order Hermite Function (see Fig. B.1 in Appendix B). For Ψ_{20} this scale is $\simeq 0.5$ nondimensionally which, with a scaling L of the order of 10° of latitude, gives a maximum resolution of ≈ 500 km. For this scale, the time step to achieve computational stability will be generally short, of the order of 30 minutes.

4.2.5 METHOD OF INTEGRATION AND FILTERING

In general the numerical integration of a nonlinear system of differential equations aiming at reaching a steady solution is not a simple task. The system may present periodic, quasi-periodic or aperiodic behaviour so as to render a steady-state solution unattainable. Even if such a steady state exists, to reach it may present additional problems if instabilities are excited. The physics of the particular problem being studied may be such as to allow for the excitation of one or more types of instabilities such as baroclinic, barotropic, symmetric, etc. In general, these problems are tackled by artificially increasing or numerically introducing dissipation so as to "force" the solution to a steady-state.

Equations [4.43] through [4.48] were integrated in time for a number of idealized latent heating distributions. With the choice of

dissipation time scales for momentum and temperature (10 days), satisfactory equilibrium conditions have been obtained. To verify if equilibrium conditions have indeed been found, a suitable condition for reaching the steady-state has to be established. The chosen criterion is that the solution should not vary by more than 2% over a period of 10 days. The time evolution of the fields of wind, geopotential and temperature were plotted for selected grid points throughout the integration, which was stopped when the above criterion was met.

It has been found that the solutions converged faster to a steady state when the initial condition for the nonlinear integration was the steady-state solution of a linearized version of the nonlinear model. The procedure was as follows (see Appendix E for details): turn the forcing function on instantaneously at t=0 and integrate a linear version of the model (nonlinear terms removed) until steady-state conditions are reached. In general, after 30 to 40 days the solution has converged to a steady-state. Next, take as the initial condition for the nonlinear integration, the linear steady-state solution and again integrate in time until the solution has approached steady-state conditions. It takes about 40 to 50 days to reach steady-state for most nonlinear integrations. As might be anticipated, the residual imbalances for the nonlinear solution are larger than the ones for the linear solution $(0(10^{-2})$ for the nonlinear solution and smaller for the linear solution). However, these errors are much smaller than the main balances in the equations even in the worst case.

Filtering was used to avoid the occurrence of the spurious growth of the amplitudes of the harmonics close to the truncation wavenumber.

This problem, known as spectral blocking (Puri and Bourke, 1974), is the spectral equivalent of the cascade of energy to the smaller scales in finite-difference models. We use a linear Shapiro filter (Shapiro, 1970) that damps according to the zonal wavenumber. (See Appendix F for details on this filtering technique.) We have found that an eleventh order zonal filter (or twentieth order for the higher resolution integrations) applied every time step is effective in avoiding the cascade of energy to the smallest resolvable scales and the associated spurious amplitude growth of the shortest waves.

We present in Fig. 4.3 the time evolution of wind, geopotential and temperature for selected grid-points throughout the nonlinear integration for a sinusoidal forcing. It is readily seen that at t=40 days the solutions is pretty flat and almost unchangeable for all fields. Similar time evolution graphs for the cases with different forcings (not shown here) also indicate that the numerical solutions have approached a steady state after 50 days of integration.

Numerical integrations were carried out with two different resolutions,

1) 11 Fourier modes in x   2) 20 Fourier modes in x
   10 Hermite modes in y   10 Hermite modes in y
    5 Vertical levels in z   5 Vertical levels in z

The most limiting factor in the actual numerical integration of the model is its high computational cost. It takes 1 hour of CPU time on the GLAS AMDAHL-470 computer to simulate 10 days of integration for the lower resolution and approximately 2 hours of CPU time for the finer resolution. For each time step, $\simeq$ 90% of the time is spent in the computation of the nonlinear terms. From that time, $\simeq$ 80% is spent in

ZONAL WIND { — — — 60°W, 10°S, 700mb·
{ — — — " " 300mb
GEOPOTENTIAL { ———— 60°W, 10°S, 1000mb
{ " " 300mb
TEMPERATURE { —·—·· EQ, 10°S 300mb
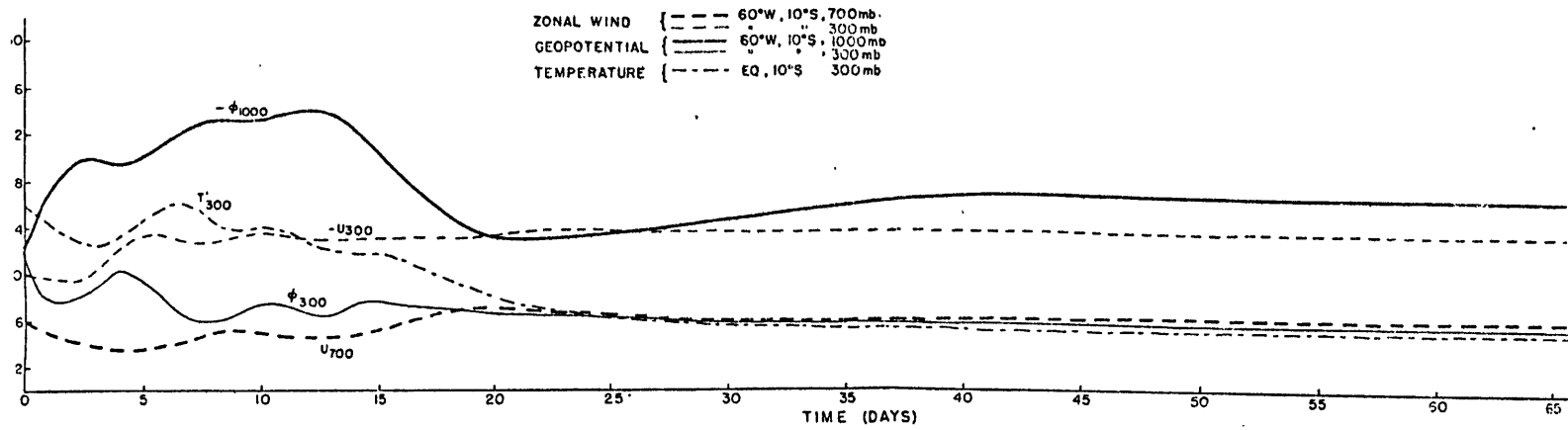
Figure 4. 3   Time evolution of zonal wind at 700 and 300 mb, geopotential at 1000 and 300 mb and

temperature at 300 mb for the model's integration with sinusoidal forcing

the forward and inverse Hermite calculations and $\simeq$ 20% in the Fourier transforms using FFT. To our knowledge, a fast algorithm to compute transforms of Hermite functions the way FFT algorithms do to Fourier series is not known.

Because of the computational cost, we chose the strategy of running several cases with planetary-scale forcing. Consequently, we made use of a low resolution model instead of attempting to realistically represent the condensational heating field, which would require increasing the resolution. Also, with the finer resolution, the number of computations would greatly increase not only because of the higher number of modes, but also because the time step would have to be made shorter to avoid computational instability.

4.3 SOME LIMITATIONS OF THE MODEL

We recall that our approach to the problem of equatorially confined, diabatic heating asymmetric forcing was to develop a model with simple physics yet to retain the nonlinear advection terms in order to compare the linear and nonlinear responses to prescribed heat sources. In keeping with this simplicity we left out a number of important physical processes. In this section we will discuss some of the most relevant limitations of our model.

Foremost among the limitations of our model is the non-inclusion of orographic effects. The major topographic barriers in the tropical regions, the Andes and the Tibetan Plateau complex, certainly affect the time mean circulation in significant ways. They act not only as barriers to the low-level flow but also as elevated heat sources. The upper-level

anticyclonic circulation over Bolivian and Tibetan Plateaus during the respective summers are probably affected by this heat source. Also, by modifying the boundary layer flow, these barriers create regions of low-level convergence and divergence with associated high or low rainfall, respectively. It is probable that, for example, the climatological precipitation maximum in the northwestern part of the Amazon basin is related to convergence caused by the Andes.

Second, we are not taking into account the effects of transience in our model. Therefore, the effects of the baroclinic eddies of midlatitudes and the transient eddies in the tropics and subtropics are suppressed. We have seen in Chapter 2, however, that the divergence of the meridional flux of zonal momentum by the transient eddies has about the same magnitude as the meridional advection of zonal momentum by the time mean circulation.

We do not include a hydrological cycle in our model, and moisture processes are neglected except that cumulus condensational heating, the most important forcing in our model, is prescribed. Of course, tropical precipitation, and thus latent heating, is to a great extent determined by the flow field; a more realistic model should allow for the cumulus clouds and the flow field to interact.

Because the forcing in our model - the latent heat of condensation in deep cumulus clouds - decays rapidly to very small values in the subtropics, we used equatorial β-plane geometry with all fields decaying exponentially away from the equator. Consequently, our results should be interpreted as being valid only to the tropics and subtropics.

Radiative processes are simply modeled as a linear damping law. We realize that radiative cooling at the subtropics is an important factor in driving the sinking branch of the Hadley-type circulations; accordingly, the crude parameterization used in our model will not allow a good representation of the thermally direct circulations in the meridional plane.

Our model does not have a boundary layer where friction is important; surface drag is not included; in addition, we do not attempt to take into consideration the effects of vertical momentum mixing by cumulus clouds in the heating regions. Therefore a good quantitative agreement with observations is not expected.

The upper boundary condition, i.e, a rigid lid of 100 mb, might prevent upward propagation of energy into the stratosphere and thus generate spurious oscillations (Lindzen et al., 1968). It has been suggested (E. Sarachik, personal communication) that the meridional propagation of Rossby waves as in Hoskins and Karoly (1981) might be caused by the impossibility of upward energy propagation due to a low rigid lid as the upper boundary. In our study, however, we are concerned with the local response in the tropics and not with remote response in midlatitudes. Moreover, Geisler (1981), in a study of the linear response of the tropical atmosphere to thermal forcing, conducted experiments for which the rigid top was placed higher in the atmosphere; and he remarked that the results remained essentially the same.

We do not attempt to include the latent heating over the narrow ITCZ. Of course that heating would have an important effect in driving north-south circulations, as shown by Schneider and Lindzen (1977), Schneider (1977) and many others. That being the case, the symmetric circulations generated by our model is not meant to agree well with zonally averaged circulations, seeing that the important ITCZ forcing is not present altogether.

For the free atmosphere Rayleigh friction is too simplified an approximation for representing momentum dissipation processes. A formulation in terms of the vertical turbulent diffusivity of momentum in which the coefficient of diffusivity is a function of height and becomes small at the upper levels would be more appropriate.

CHAPTER 5

NONLINEAR MODEL RESULTS

In this chapter we present the results of the numerical model developed in Chapter 4 for a number of idealized forcing functions. As mentioned before, in the process of numerical integration of equations [4.47] through [4.49], we first find the linear steady-state solution and then, using this solution as the initial condition for the nonlinear integration, we time march the nonlinear model until a satisfactory steady state is reached. Here we will be comparing linear and nonlinear solutions for different choices of latent heating.

5.1 DIABATIC HEATING DISTRIBUTIONS

The vertical distribution of diabatic heating is shown in Figure 4.1 in the previous chapter, and it is assumed not to vary horizontally. The three different horizontal distributions of diabatic heating used in this chapter are shown in Figure 5.1: a) one heat source centered at the equator (1-EQ), b) three heat sources centered at the equator (3-EQ), and c) one heat source centered at 10°S (1-10S). These heat sources are of planetary scale and, in this respect, depart from the localized character (comparable zonal and meridional scales) of realistic diabatic heat sources over tropical continents. The reason for this choice lies in the high computational costs of the nonlinear integrations, so we decided to use a low-order model and run several cases varying the horizontal structure and intensity of the forcing.

The horizontal distributions of $Q_T(x,y)$ in Chapter 3 had no zonal mean ($[Q_T] = 0$) since we were dealing with heating perturbations about a zonal
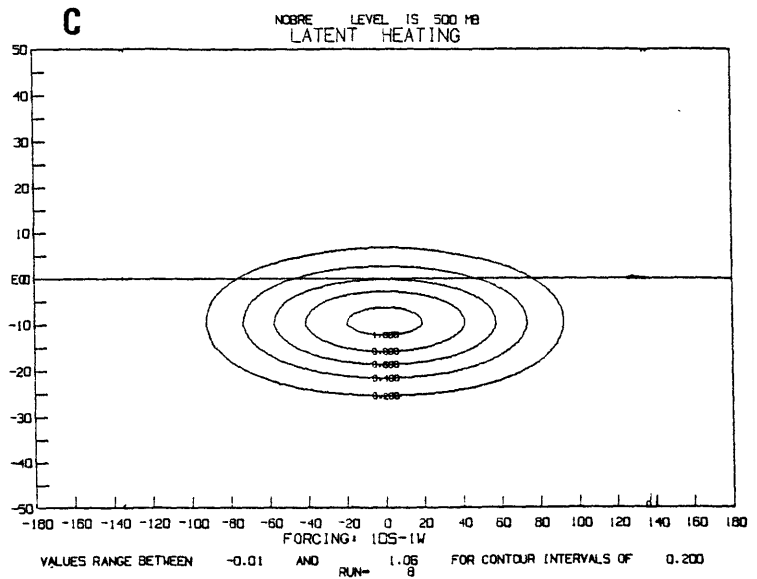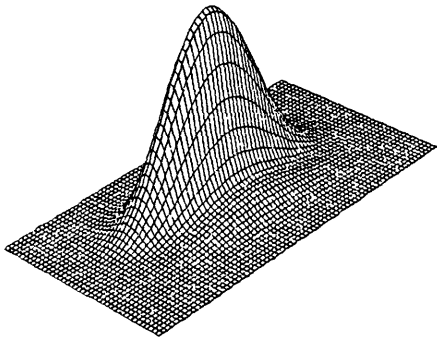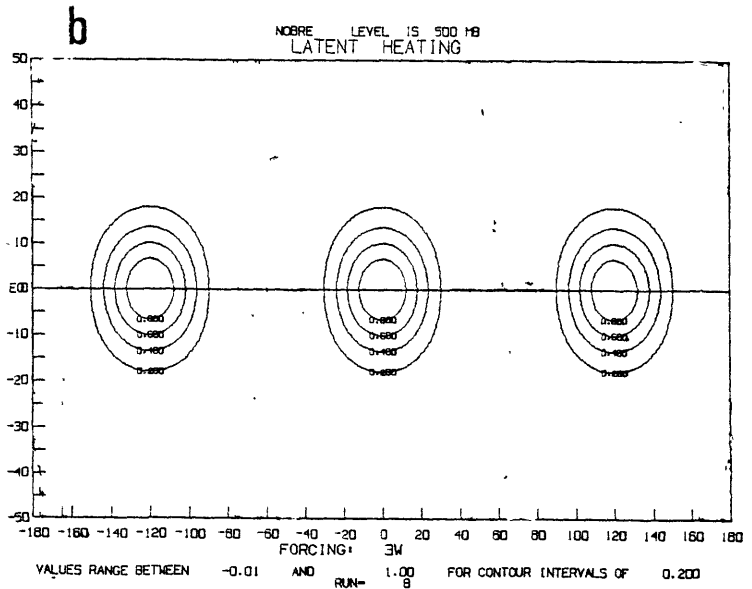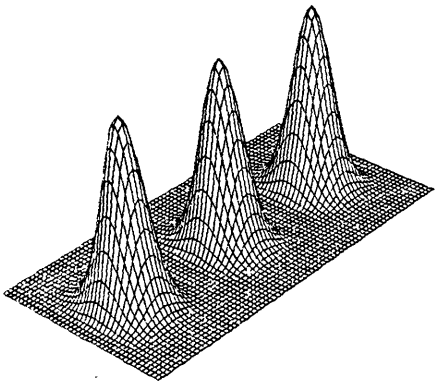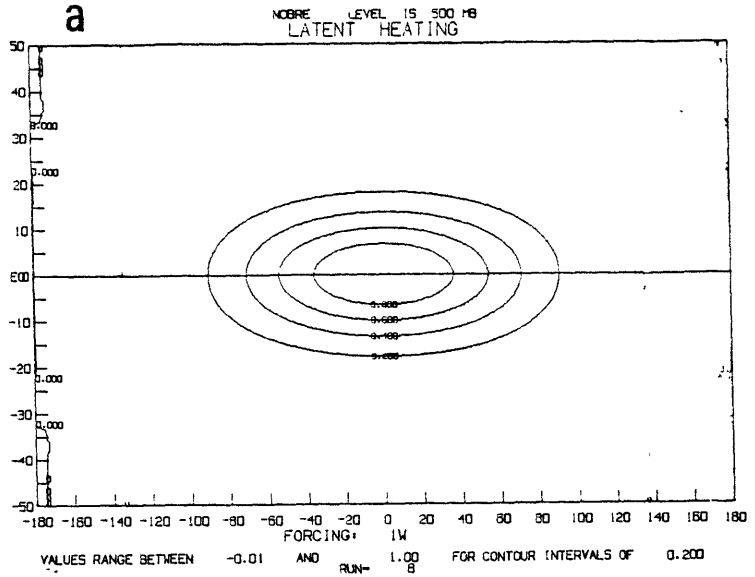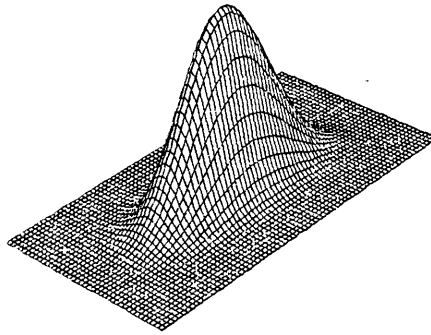
Figure 5.1   Latent heating distributions at 500 mb used in the nonlinear
integrations: a) one heat source at the equator, b) three
heat sources at the equator and c) one heat source at 10°S.

mean heating. Now, for the nonlinear model we prescribe diabatic heating functions whose zonal mean values are non-zero and positive, which is of course more realistic. In a steady-state two-dimensional (2-D) model (latitude x height), this mean heating would drive an axially symmetric circulation. An interesting question arises in connection with the nonlinear integration of 2-D models forced by the zonal mean latent heating in the tropics (ITCZ). If the contribution by the standing eddies is unimportant compared to the MMC transports ($[\overline{u^*v^*}] << [\overline{u}][\overline{v}]$), then the zonally averaged 3-D model solution resulting from a given distribution of heat sources with a non-zero mean would be similar to the 2-D model solution resulting from this zonal mean heating. In section 5.4 we will show some results of integrations with a 2-D nonlinear version of our model and compare them with the zonally averaged solution of the 3-D nonlinear model.

The zonal scale of (1-EQ) and (1-10S) is $\simeq 18 \times 10^3$ km, which is much larger than the scale of any observed tropical heat source. However, the zonal scale of each heat source in (3-EQ) is $\simeq 6 \times 10^3$ km, which is about the same order of magnitude as the scale of observed sources (see Figure 2.14). The intensity of the heat source will be made to vary, and the values used are shown in Table 5.1. In the location of maximum precipitation (and thus of latent heating), these intensities range from 4.6 to 13.8 mm/day and are meant to encompass the whole range of spacial and temporal (interannual) variability of tropical precipitation. There are marked interregional precipitation differences among the tropical continents (e.g., smaller precipitation rates over Africa as compared to over South America and the Indonesian region during the southern summer) and also large interannual variability (Stockenius, 1981).

TABLE 5.1:   DIABATIC HEATING INTENSITIES USED IN THIS STUDY

$\dot{Q}_L$ at 500 mb (k/day)	Vertical Average of $\dot{Q}_L$ (k/day)	Equivalent Precipitation (mm/day)
2.5	1.15	4.6
5.0	2.30	9.2
7.5	3.45	13.8

Probably the most important aspect of realistic distributions of latent heating that we are not considering in our model is the narrow ITCZ over the oceans. It is a permanent feature of the time-mean tropical circulation, and it is generally found in the northern hemisphere (see Figure 2.1). Mechanisms for explaining its narrowness and the fact that it does not lie at the equator have been suggested by Charney (1971) and Schneider and Lindzen (1977) in terms of CISK and warm SST's.

The smallness of the oceanic ITCZ meridional scale (< 1000 km) in comparison with the y-scales of convective regions over tropical continents (O (3000 km)) would make it necessary to increase the latitudinal resolution of the model to represent it. For reasons mentioned at the end of Chapter 4, we decided to keep a low resolution model and to attempt to model only the longitudinally asymmetric character of tropical diabatic heating.

Because we do not attempt to realistically represent diabatic heating sources and sinks, we do not expect our model to agree quantitatively with observations. We are aiming at gaining a qualitative understanding of the zonally nonlinear problem and at seeing to what extent nonlinearities are important and not at being quantitatively accurate. Besides, our model is too simplified — and leaves out important physical processes — to warrant good quantitative agreement with observations.

5.2 PRESENTATION OF RESULTS FOR THE 6 CASES STUDIED

We will present results for six different integrations of the nonlinear model in which the horizontal distribution or the intensity of the forcing was changed. The six cases are shown in Table 5.2. Results are shown in nondimensional form and the conversion factors for u (and v), w, ϕ, T, D (and ξ) are approximately 10 m/s, 7 cm/s, 300 m^2/s^2, 1°C and 9 x 10^{-6} s^{-1}, respectively, according to the dimensions given in [4.22b].

TABLE 5.2: THE SIX INTEGRATIONS OF THE NONLINEAR MODEL

Case*	1-EQ-L	1-EQ-M	1-EQ-H	3-EQ-M	3-EQ-H	1-10S-M
No.	I	II	III	IV	V	VI
Forcing Horizontal Distribution (see Fig. 5.1)	(a)	(a)	(a)	(b)	(b)	(c)
Intensity (mm/day) (see TABLE 5.1)	4.6	9.2	13.8	9.2	13.8	9.2

The fields of zonal, meridional, and vertical winds, and geopotential and wind vectors vorticity and divergence for the six cases of Table 5.2 are shown in Figures 5.2 through 5.25 for a) linear solution at 300 mb, b) linear solution at 700 mb, c) nonlinear solution at 300 mb, and d) nonlinear solution at 700 mb.

---

* The code for each case reads as follows: the first digit codes the number of heat sources (1 = one heat source, 3 = three heat sources); next, its latitudinal position (EQ = at the equator, 10S = at 10°S); and the letter at the end, its intensity (L = 4.6 mm/day (low), M = 9.2 mm/day (medium) and H = 13.8 mm/day (high)).

We present in Tables 5.3a and 5.3b the maximum and minimum values of zonal wind (u), meridional wind (v), vertical wind (w), geopotential (ϕ), temperature (T'), divergence (D) and vorticity (ξ) for the six cases shown in Table 5.2. In Table 5.4 we show the band of longitudes for which easterlies and westerlies are observed for the linear and nonlinear calculations. The longitudes covered by easterlies or westerlies provide a crude estimate of the Walker-type cell longitudinal extent and east-west asymmetry on this circulation.

TABLE 5.3:   MINIMUM AND MAXIMUM VALUES OF VARIABLES FOR THE SIX CASES

a) 300 mb   and   b) 700 mb

a) 300 mb CASE		u min	u max	v min	v max	w min	w max	ϕ min	ϕ max	T' min	T' max	D min	D max	ξ min	ξ max
I 1-EQ-L	L	-0.83	0.73	-0.06	0.06	-0.01	0.06	0	2.12	0	2.66	-0.03	0.12	-1.20	1.20
	NL	-0.70	0.73	-0.06	0.06	-0.01	0.07	0	2.12	0	2.72	-0.04	0.15	-1.13	1.13
II 1-EQ-M	L	-1.67	1.45	-0.12	0.12	-0.02	0.11	0	4.27	0	5.32	-0.06	0.25	-2.41	2.41
	NL	-.77	1.46	-0.11	0.11	-0.03	0.14	0	4.31	0	5.87	-0.08	0.31	-1.96	1.96
III 1-EQ-H	L	-2.50	2.18	-0.18	0.18	-0.04	0.17	0	6.43	0	7.97	-0.10	0.37	-3.62	3.62
	NL	-0.44	2.37	-0.24	0.24	-0.05	0.24	-0.25	6.44	0	10.83	-0.15	0.46	-2.61	2.61
IV 3-EQ-M	L	-0.60	0.98	-0.11	0.11	-0.02	0.11	0	3.84	0	5.22	-0.07	0.25	-1.51	1.51
	NL	-0.53	1.17	-0.18	0.18	-0.03	0.14	0	3.95	0	5.45	-0.10	0.32	-1.66	1.66
V 3-EQ-H	L	-0.90	1.47	-0.17	0.17	-0.03	0.17	0	5.80	0	7.83	-0.10	0.37	-2.27	2.27
	NL	-0.40	1.80	-0.34	0.34	-0.06	0.22	0	5.74	0	8.80	-0.17	0.44	-2.54	2.54
VI 1-10S-M	L	-2.24	1.24	-0.17	0.21	-0.02	0.13	0	5.16	0	5.42	-0.06	0.27	-2.90	3.33
	NL	-1.26	1.49	-0.10	0.28	-0.03	0.15	0	4.31	0	7.49	-0.08	0.35	-2.12	1.49

175

TABLE 5.3 (continued)

b) 700 mb CASE		u min	u max	v min	v max	w min	w max	φ min	φ max	T' min	T' max	D min	D max	ξ min	ξ max
I 1-EQ-L	L	-0.59	0.65	-0.05	0.05	-0.01	0.05	-1.63	0	0	3.51	-0.12	0.04	-0.91	0.91
	NL	-0.64	0.81	-0.06	0.06	-0.01	0.04	-1.71	0	0	2.95	-0.10	0.04	-1.33	1.33
II 1-EQ-M	L	-1.18	1.29	-0.09	0.09	-0.03	0.11	-3.22	0	0	7.01	-0.23	0.08	-1.83	1.83
	NL	-1.23	1.56	-0.13	0.13	-0.02	0.07	-3.39	0	0	5.76	-0.22	0.08	-2.48	2.48
III 1-EQ-H	L	-1.77	1.94	-0.14	0.14	-0.04	0.16	-4.81	0	0	10.51	-0.35	0.12	-2.74	2.74
	NL	-1.63	2.25	-0.22	0.22	-0.03	0.09	-5.17	0	0	8.53	-0.38	0.19	-3.69	3.69
IV 3-EQ-M	L	-0.76	0.71	-0.10	0.10	-0.03	0.11	-2.96	0	0	6.71	-0.29	0.10	-1.43	1.43
	NL	-0.81	0.65	-0.12	0.12	-0.02	0.08	-2.91	0	0	6.61	-0.23	0.12	-1.61	1.61
V 3-EQ-H	L	-1.13	1.06	-0.15	0.15	-0.04	0.16	-4.40	0	0	10.07	-0.44	0.15	-2.14	2.14
	NL	-1.09	0.80	-0.18	0.18	-0.03	0.10	-4.50	0	0	8.84	-0.38	0.17	-2.17	2.17
VI 1-10S-M	L	-0.98	1.70	-0.15	0.11	-0.02	0.11	-3.77	0	0	9.04	-0.22	0.06	-2.12	2.46
	NL	-1.09	1.70	-0.13	0.16	-0.02	0.09	-4.24	0	0	5.48	-0.26	0.08	-2.82	1.70

TABLE 5.4 APPROXIMATE LONGITUDINAL EXTENT OF EASTWARD AND WESTWARD BRANCH

OF EAST-WEST CELLS AT 300 mb AND 700 mb

	LINEAR		300 mb	NONLINEAR	
CASE	EASTERLIES	WESTERLIES		EASTERLIES	WESTERLIES
I	170°	190°		170°	190°
II	170°	190°		160°	200°
III	170°	190°		140°	220°
IV	58°	62°		62°	58°
V	58°	62°		52°	68°
VI	210°	150°		210°	150°

	LINEAR		700 mb	NONLINEAR	
CASE	EASTERLIES	WESTERLIES		EASTERLIES	WESTERLIES
I	195°	165°		200°	160°
II	195°	165°		215°	145°
III	195°	165°		235°	125°
IV	65°	55°		70°	50°
V	65°	55°		77°	43°
VI	140°	220°		175°	185°
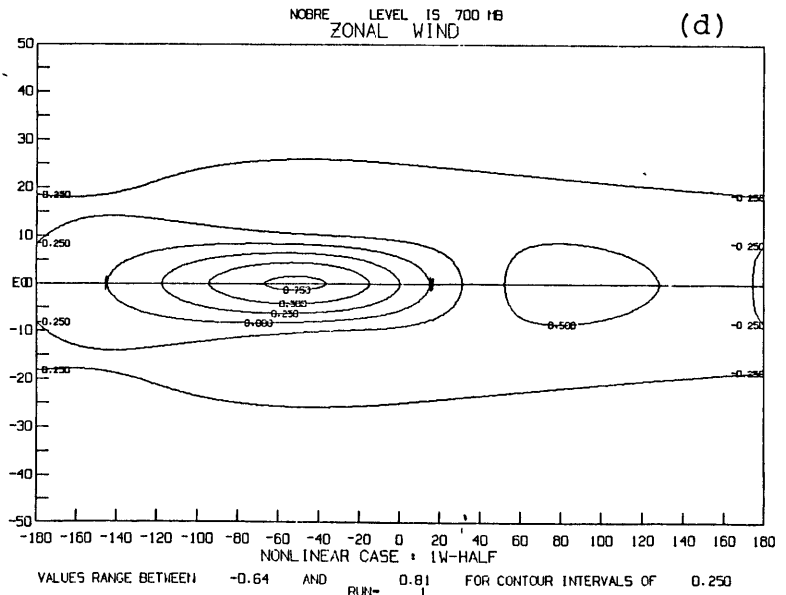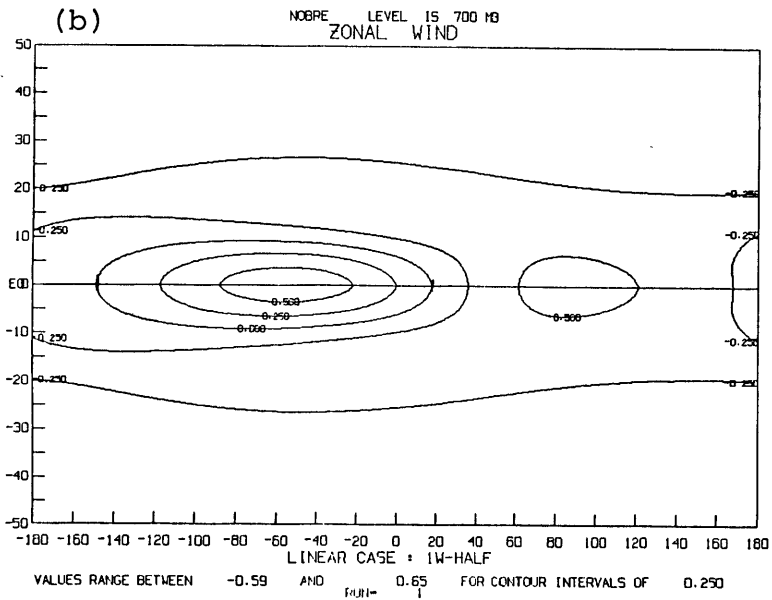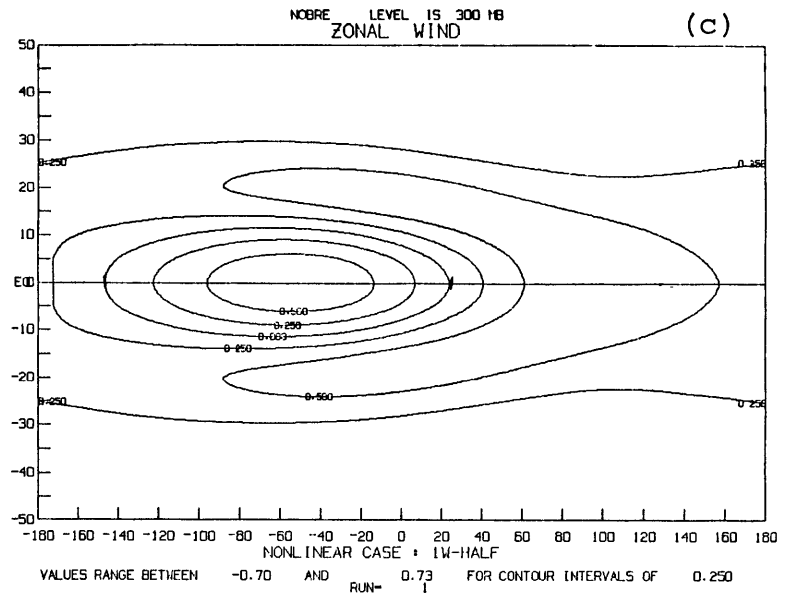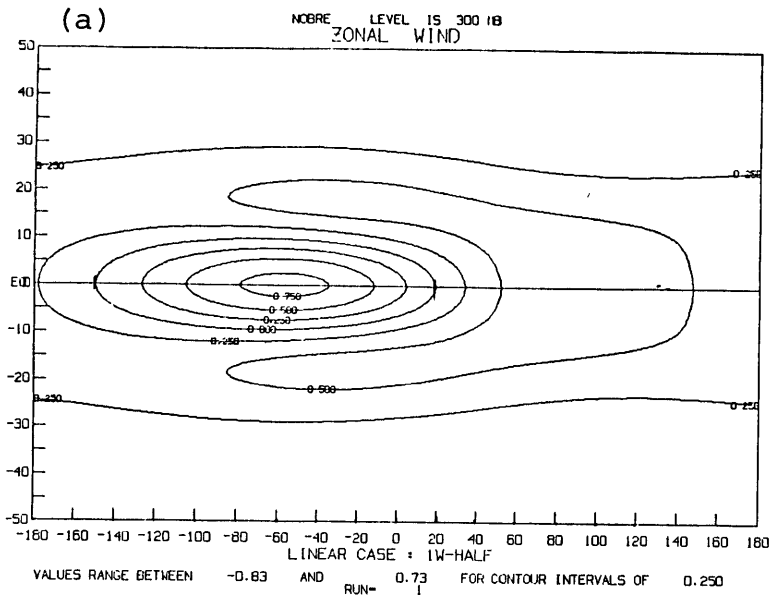
CASE I

Figure 5.2 Zonal wind for Case I. Linear solution at 300 mb (a) and 700 mb(b), and nonlinear solution at 300 mb (c) and 700 mb (d).
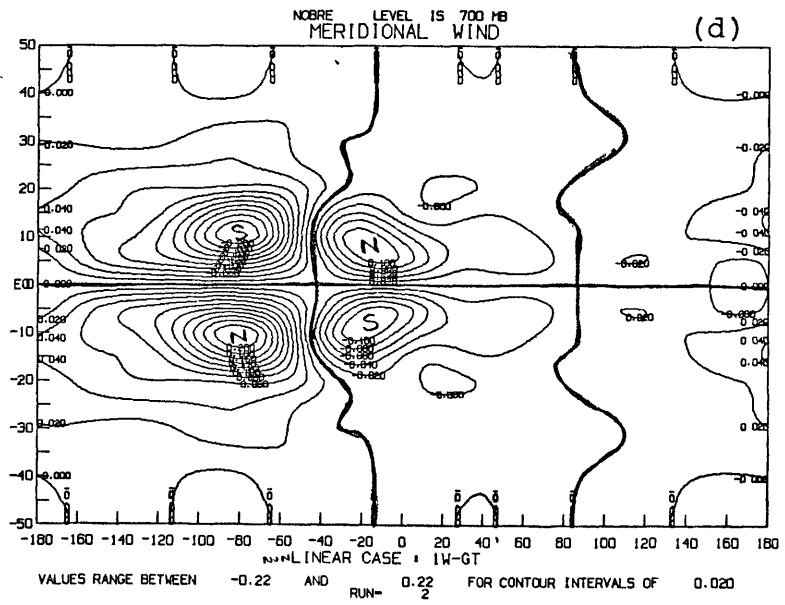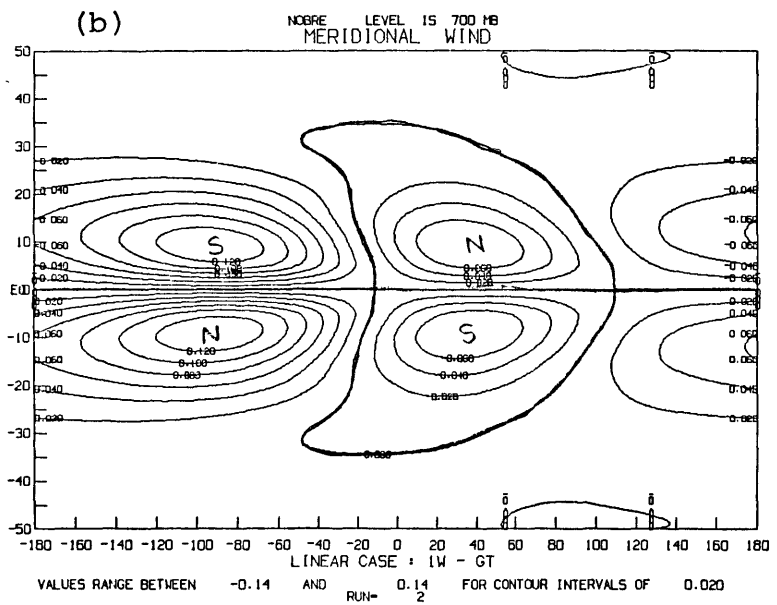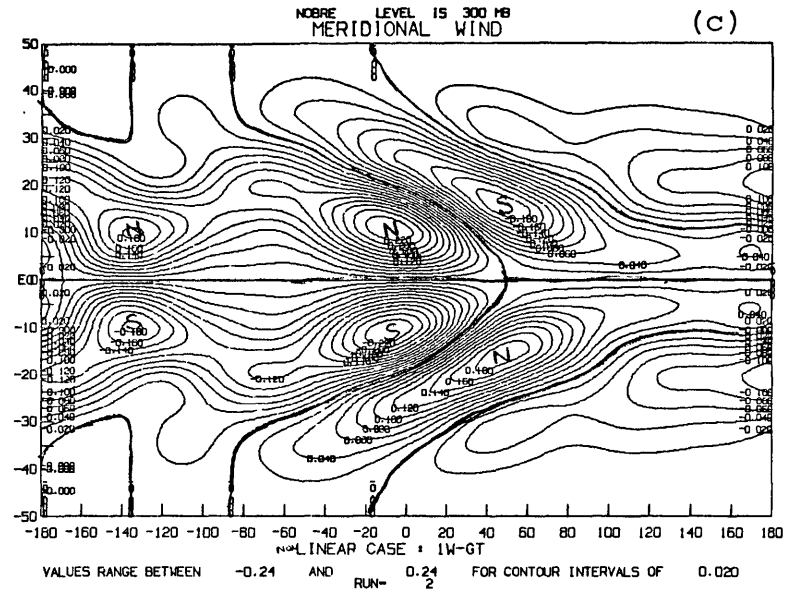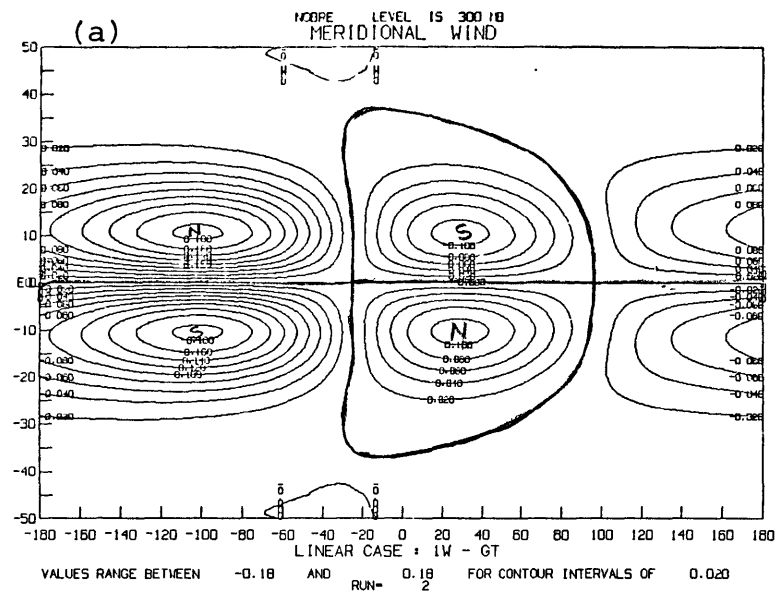
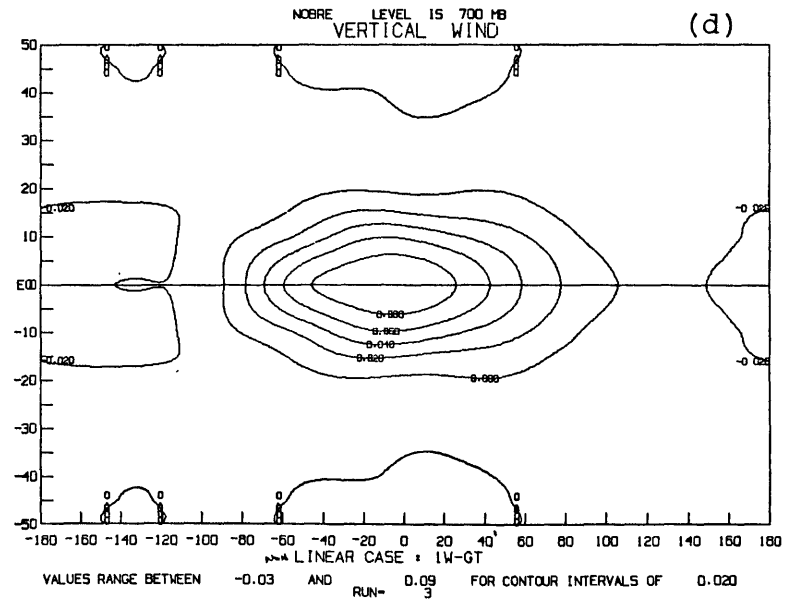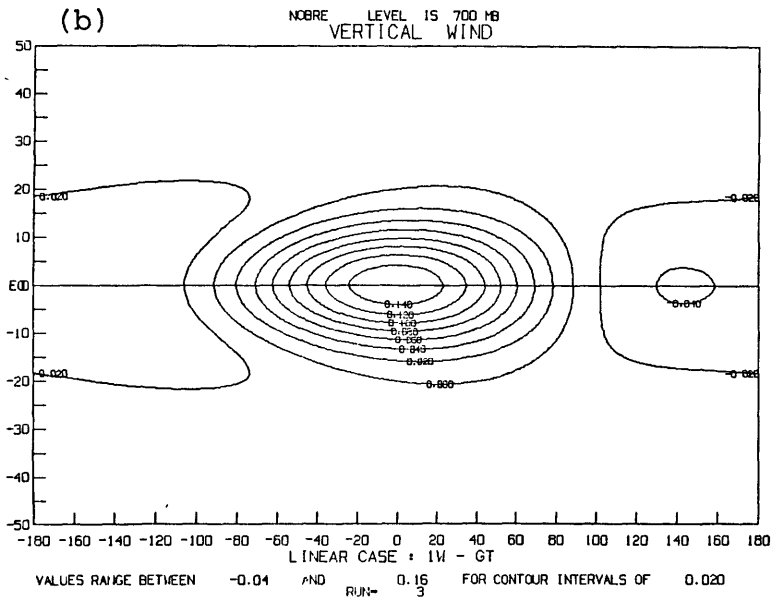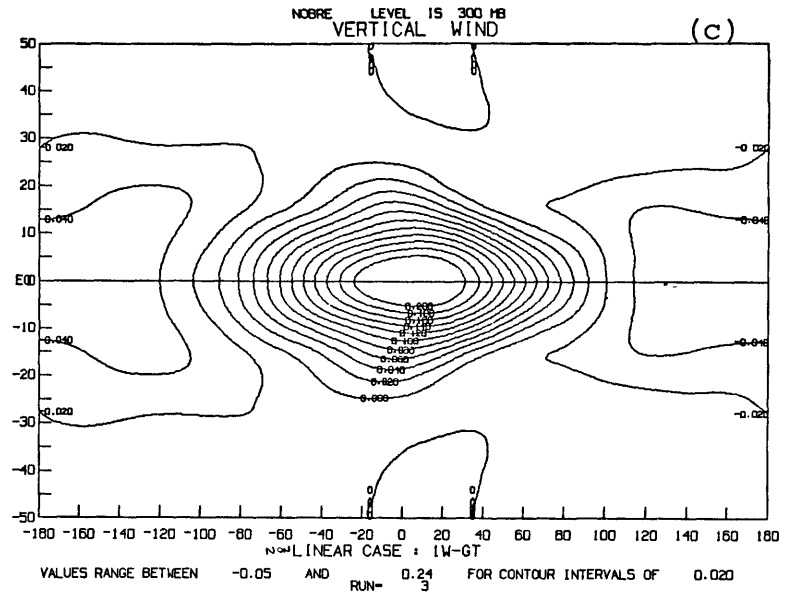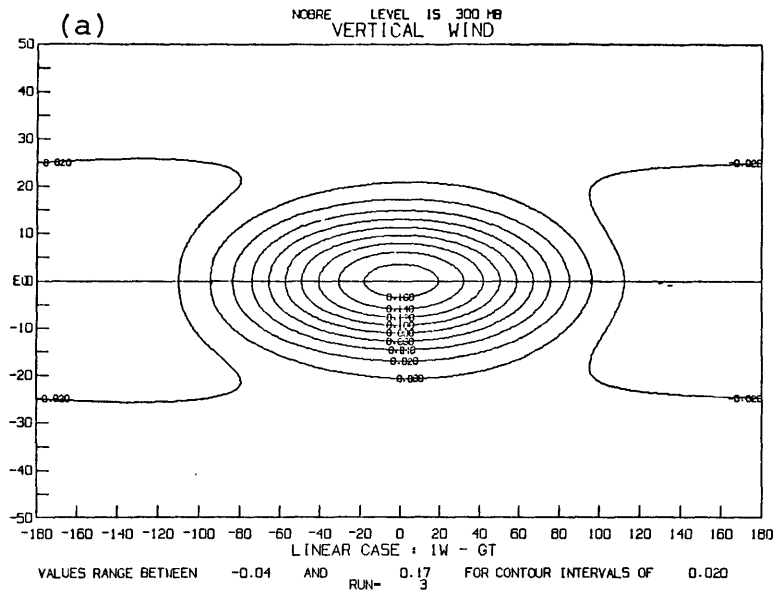CASE I
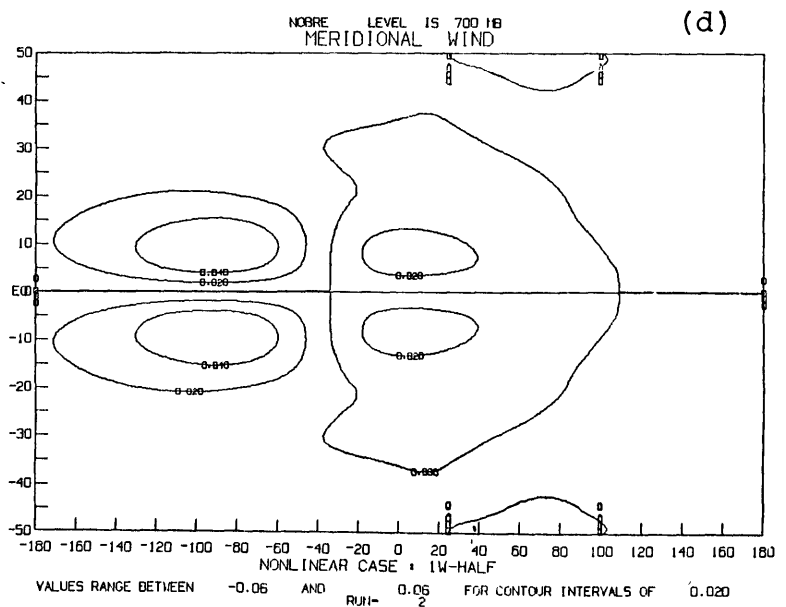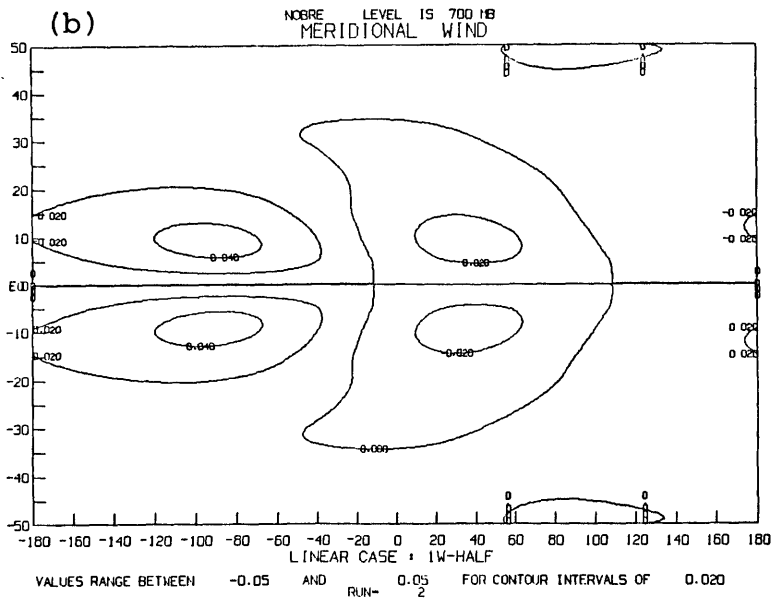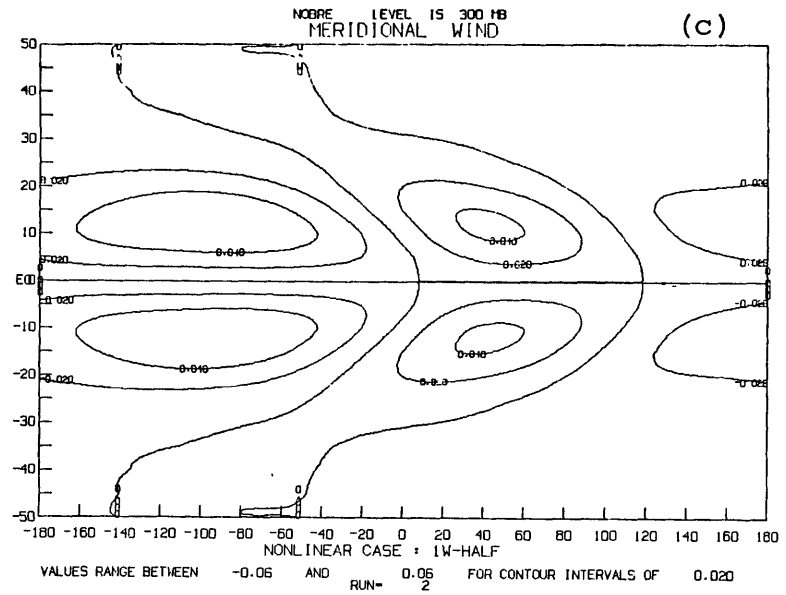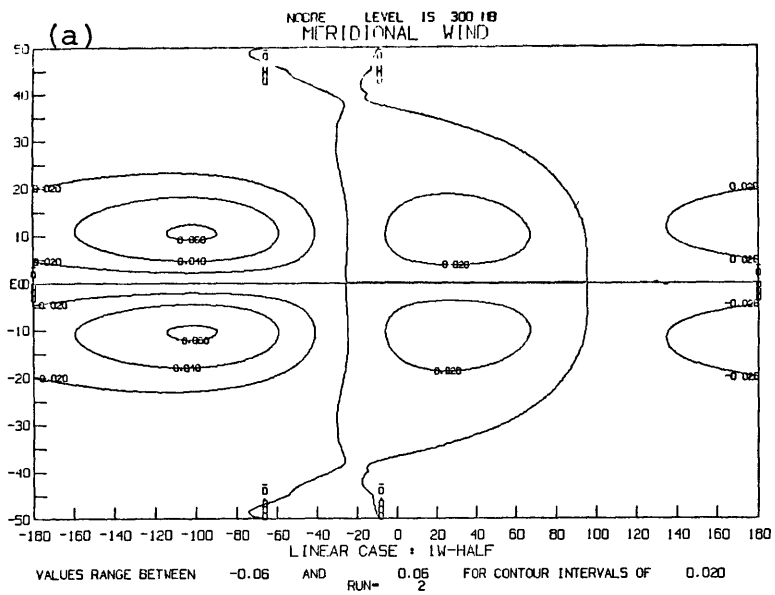
Figure 5.3   Same as figure 5.2 but for meridional wind.
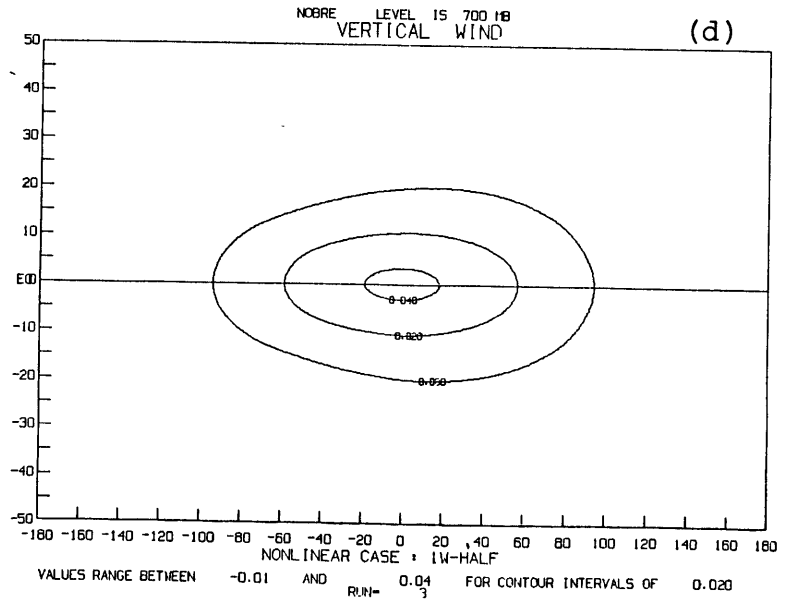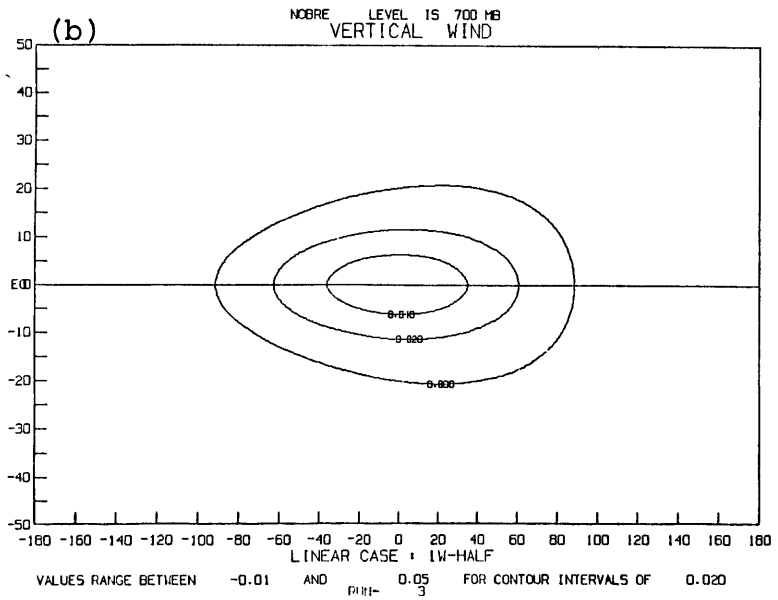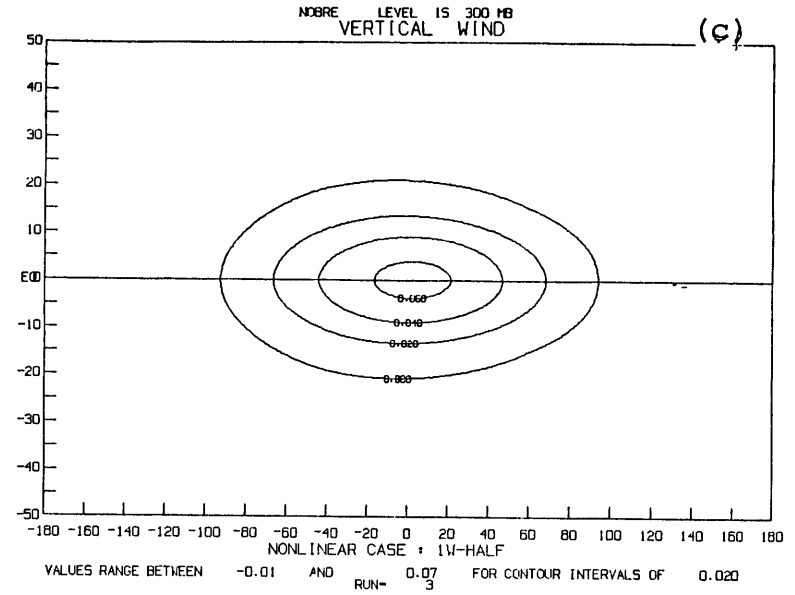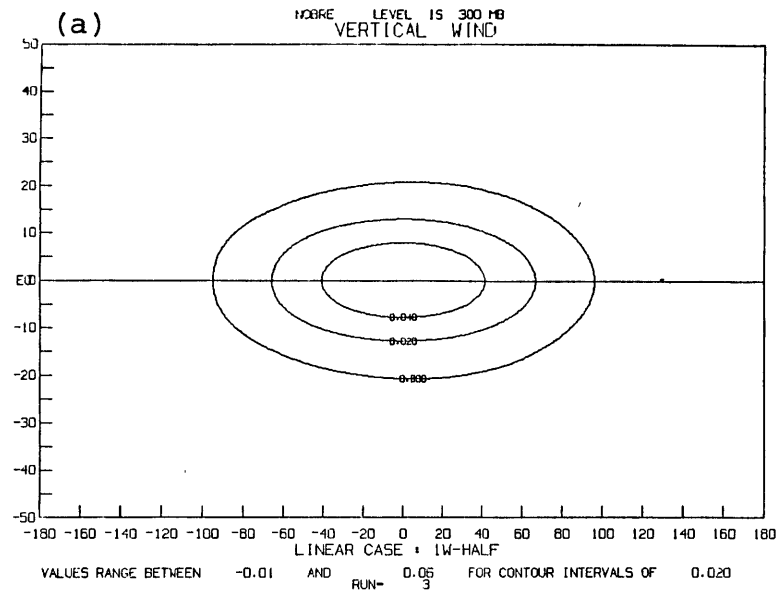
CASE I

Figure 5.4 Same as figure 5.2 but for vertical wind.

CASE I

(a) MOORE LEVEL IS 300 MB
WIND&GEOPOTENTIA

(c) MOORE LEVEL IS 300 MB
WIND&GEOPOTENTIA

LINEAR CASE : 1W-HALF

VALUES RANGE BETWEEN 0.00 AND 2.12 FOR CONTOUR INTERVALS OF 0.250
RUN= 4

NONLINEAR CASE : 1W-HALF

VALUES RANGE BETWEEN 0.00 AND 2.12 FOR CONTOUR INTERVALS OF 0.250
RUN= 4

(b) MOORE LEVEL IS 700 MB
WIND&GEOPOTENTIA

(d) MOORE LEVEL IS 700 MB
WIND&GEOPOTENTIA

LINEAR CASE : 1W-HALF

VALUES RANGE BETWEEN -1.63 AND -0.00 FOR CONTOUR INTERVALS OF 0.250
RUN= 4

NONLINEAR CASE : 1W-HALF

VALUES RANGE BETWEEN -1.71 AND -0.00 FOR CONTOUR INTERVALS OF 0.250
RUN= 4

Figure 5.5 Same as figure 5.2 but for geopotential and horizontal wind vectors.

(a)

NOBRE LEVEL IS 300 MB
ZONAL WIND

(c)

NOBRE LEVEL IS 300 MB
ZONAL WIND

LINEAR CASE : - 1W -

VALUES RANGE BETWEEN   -1.67   AND   1.45   FOR CONTOUR INTERVALS OF   0.250
RUN= 1

NONLINEAR CASE : - 1W -

VALUES RANGE BETWEEN   -0.77   AND   1.46   FOR CONTOUR INTERVALS OF   0.250
RUN= 1

(b)

NOBRE LEVEL IS 700 MB
ZONAL WIND

(d)

NOBRE LEVEL IS 700 MB
ZONAL WIND

LINEAR CASE : - 1W -

VALUES RANGE BETWEEN   -1.18   AND   1.29   FOR CONTOUR INTERVALS OF   0.250
RUN= 1

NONLINEAR CASE : - 1W -

VALUES RANGE BETWEEN   -1.23   AND   1.56   FOR CONTOUR INTERVALS OF   0.250
RUN= 1

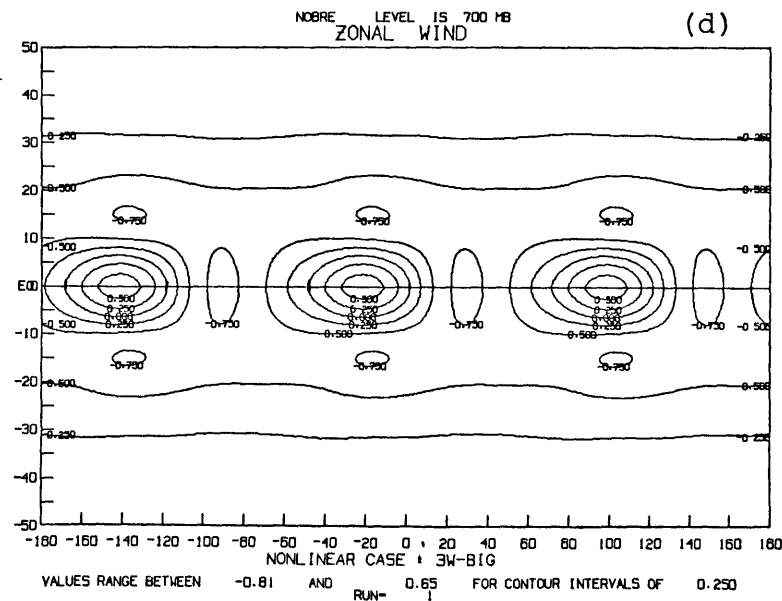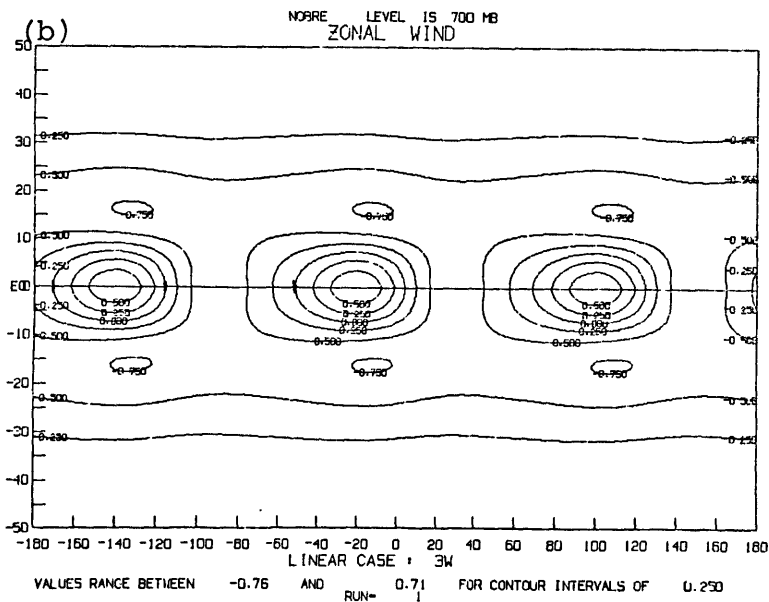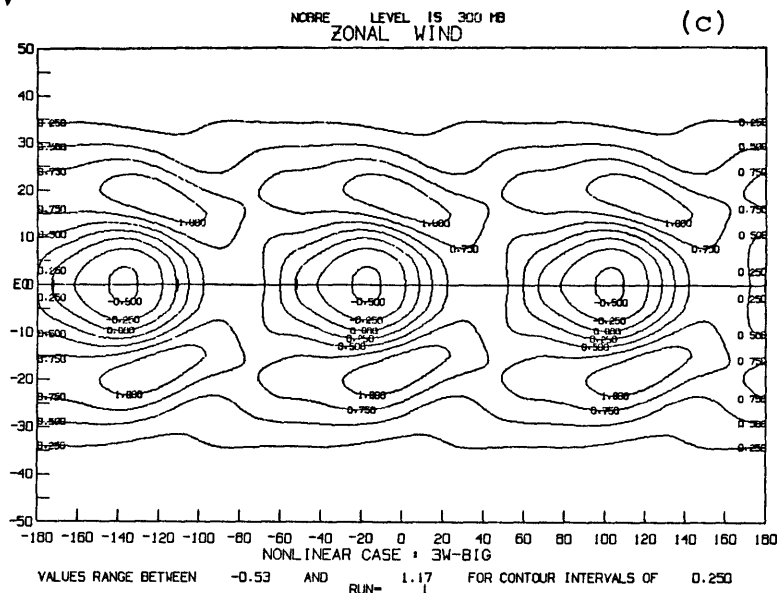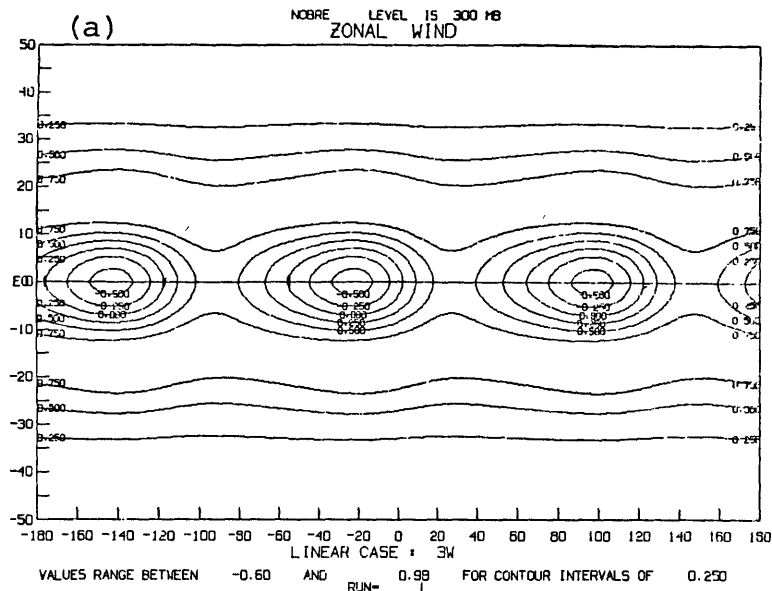Figure 5.6   Same as figure 5.2 but for zonal wind for Case II.

CASE II
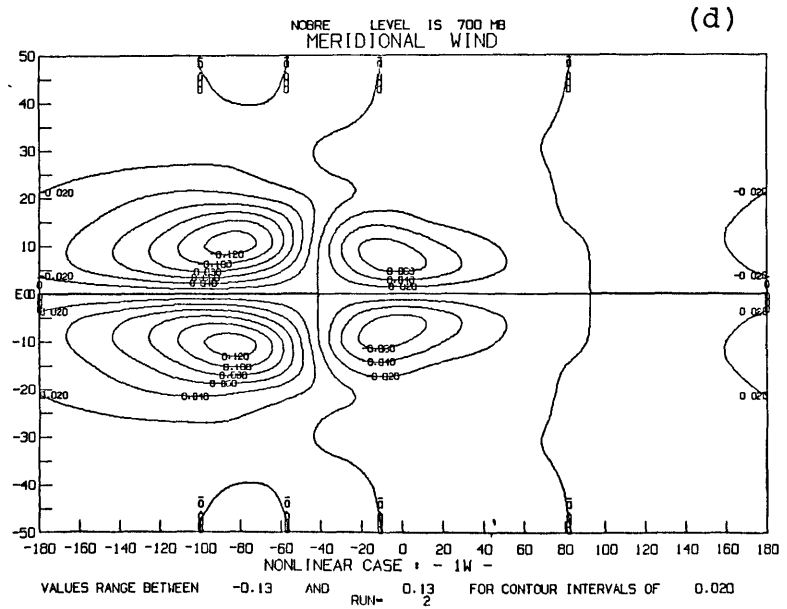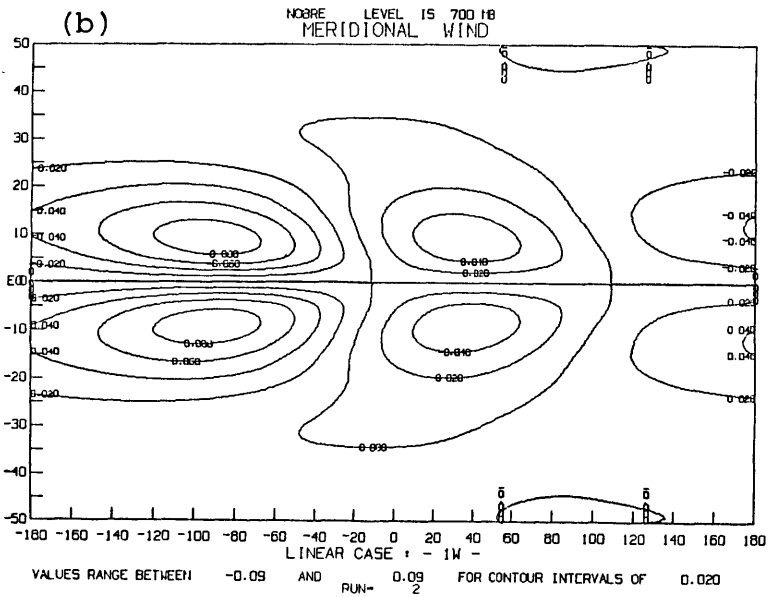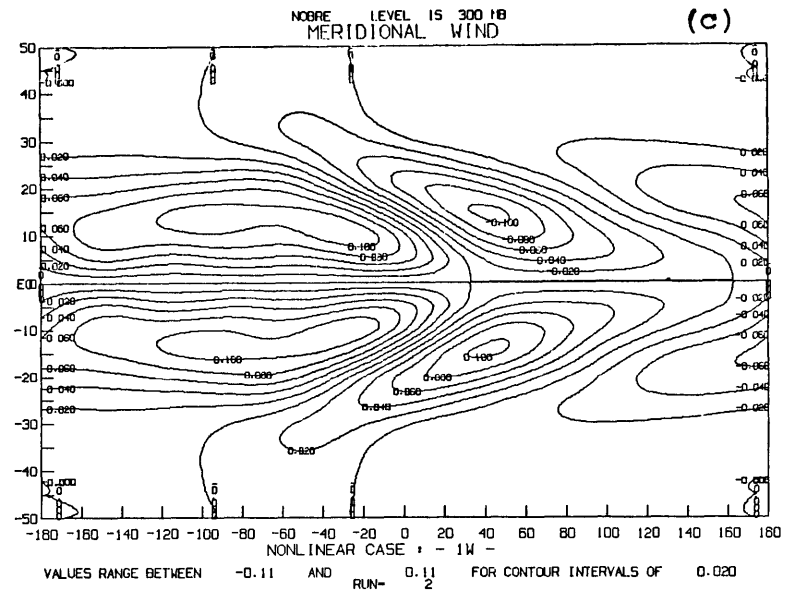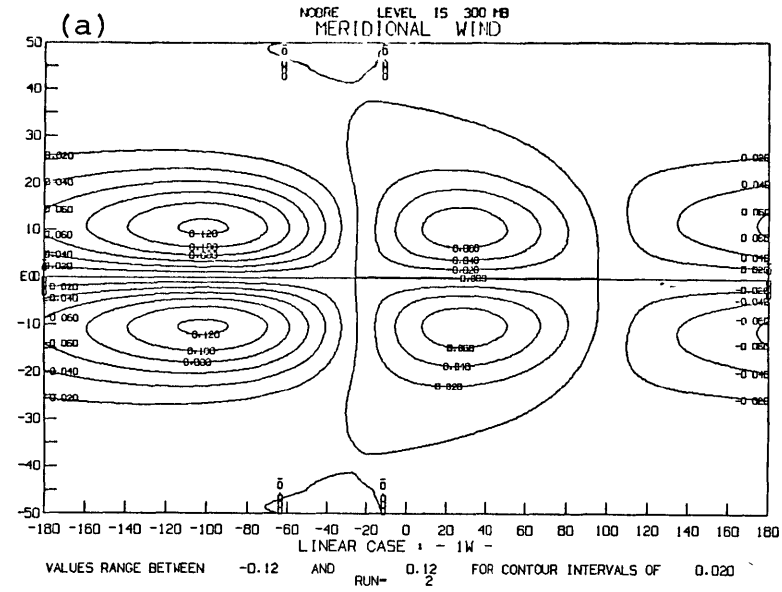
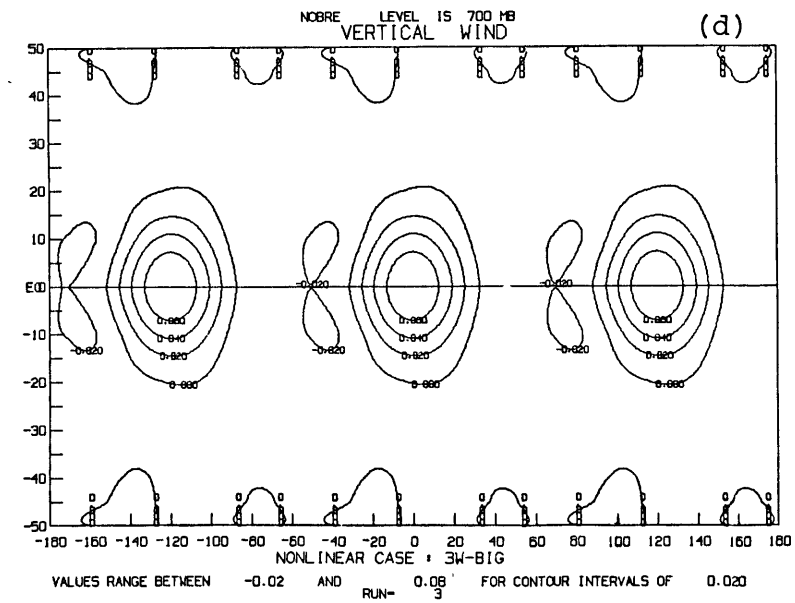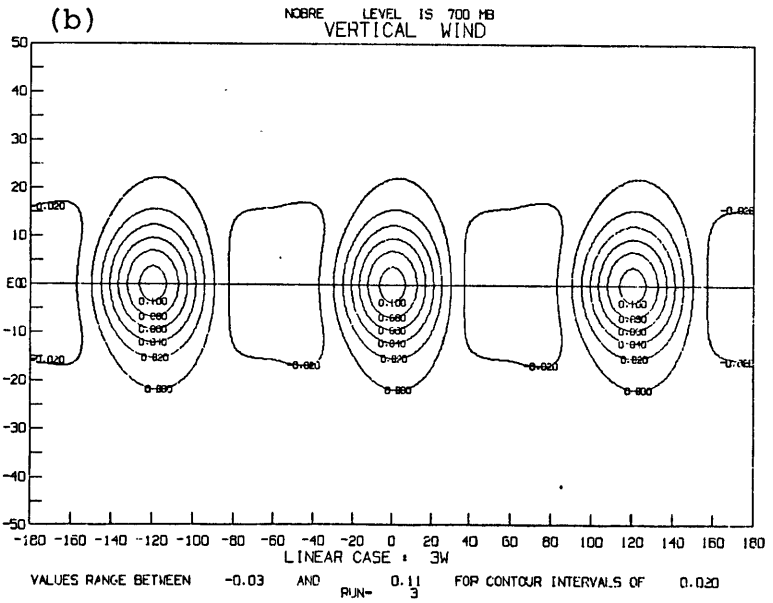

Figure 5.7 Same as figure 5.6 but for meridional wind.
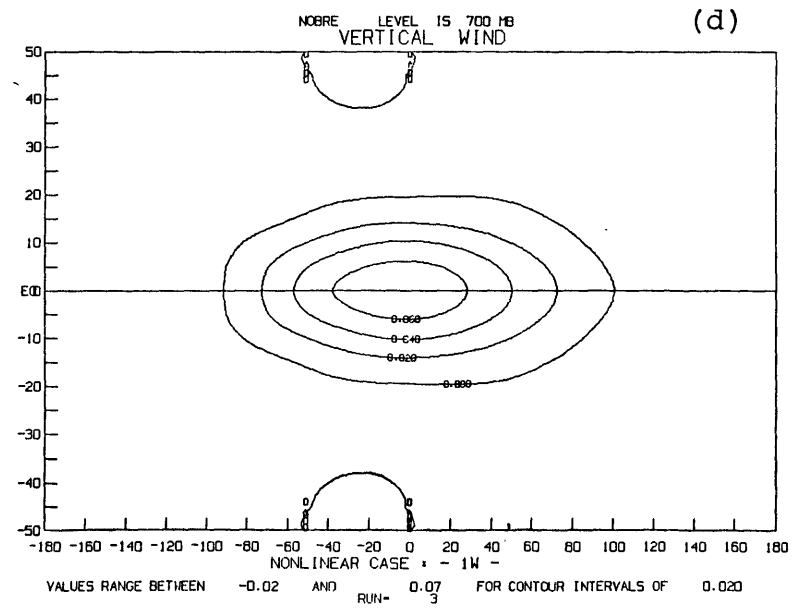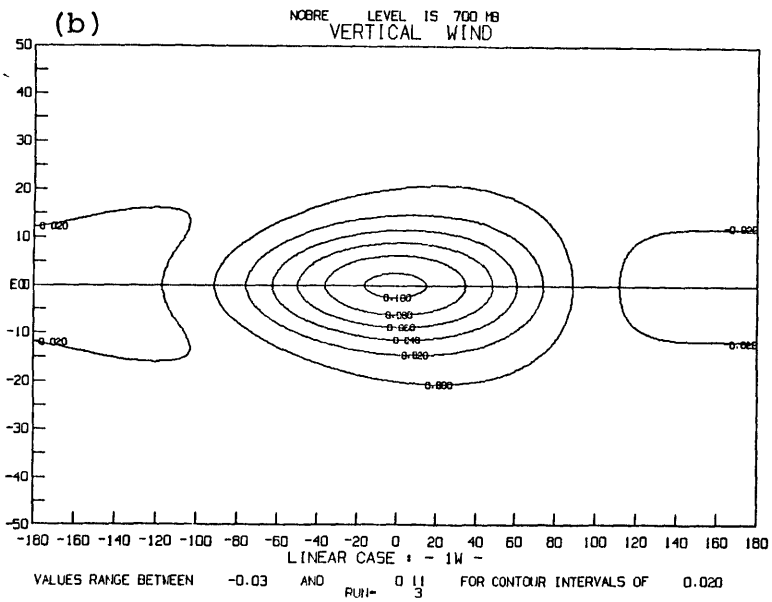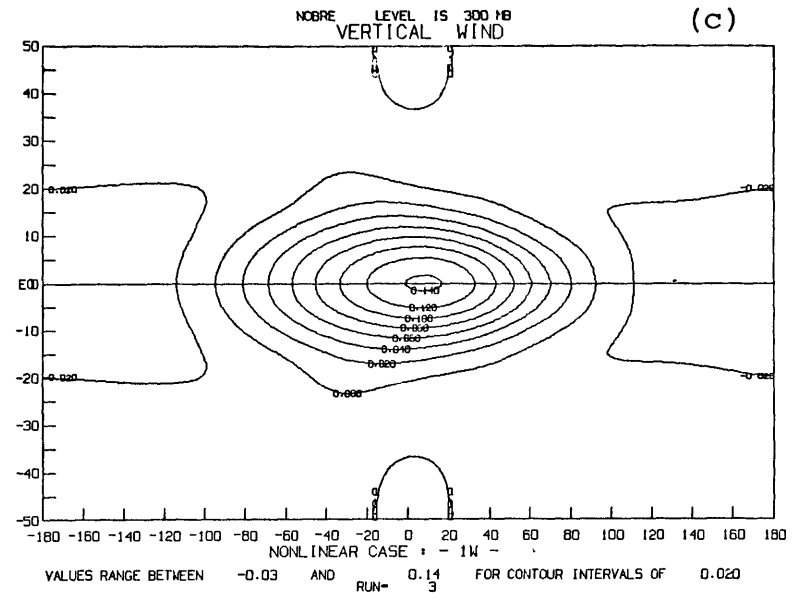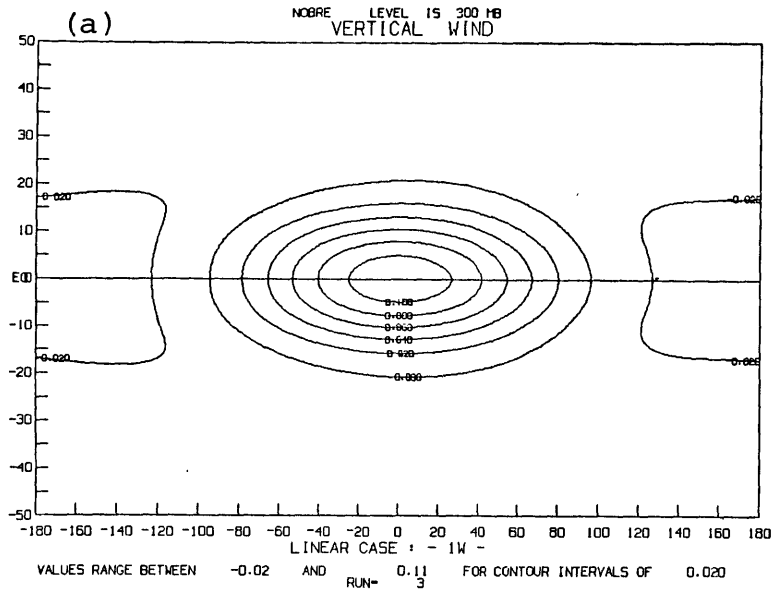
CASE II

Figure 5.8   Same as figure 5.6 but for vertical wind.
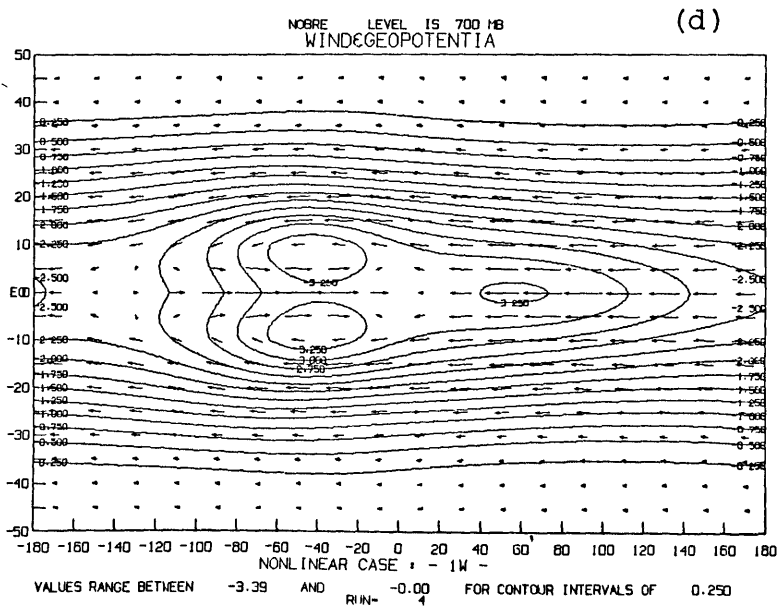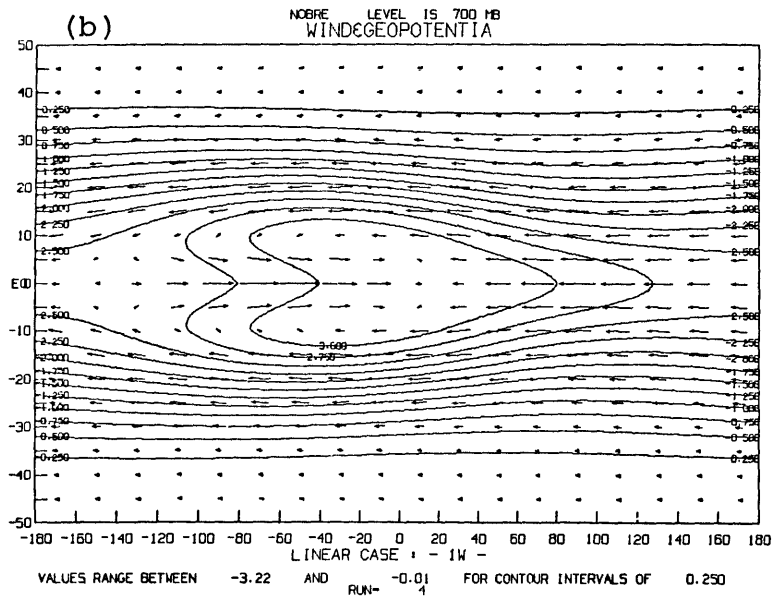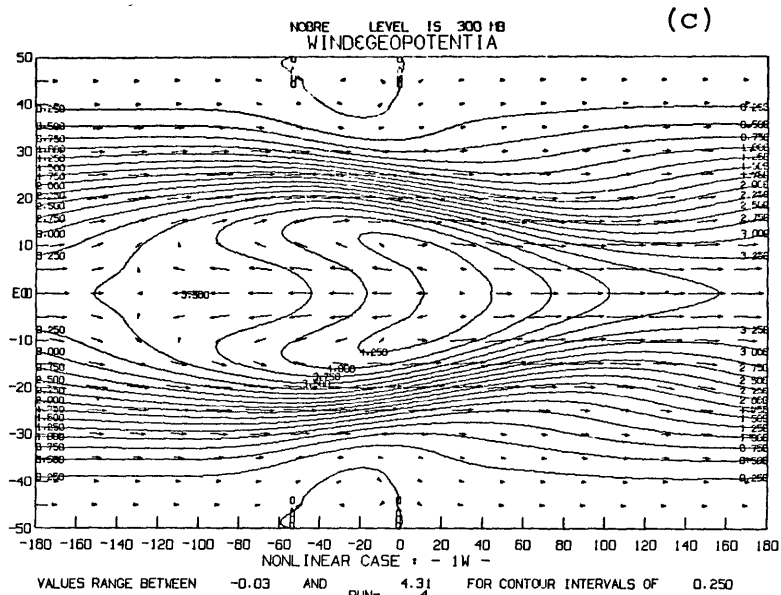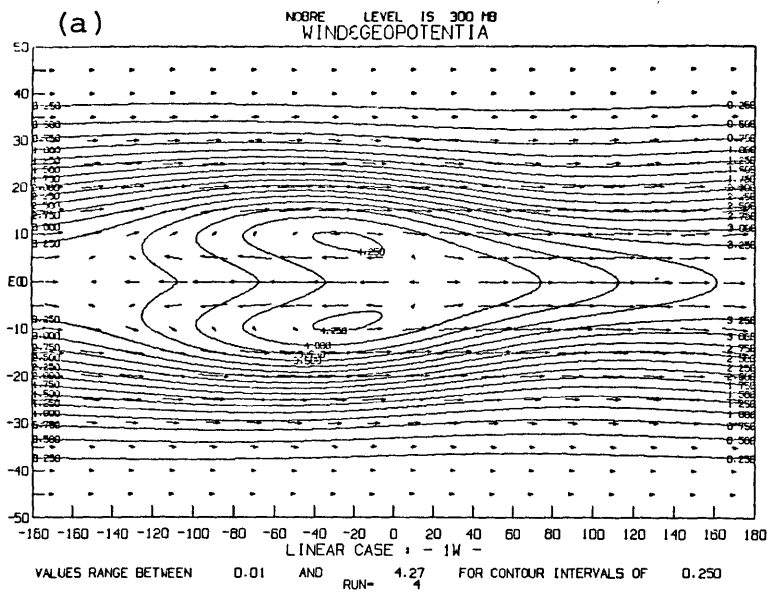
CASE II

Figure 5.9   Same as figure 5.6 but for geopotential and wind vectors.

CASE III

(a)

NOBRE   LEVEL IS 300 MB
ZONAL WIND

LINEAR CASE : 1W - GT

VALUES RANGE BETWEEN   -2.50   AND   RUN-   2.18   FOR CONTOUR INTERVALS OF   0.250

(c)

NOBRE   LEVEL IS 300 MB
ZONAL WIND

LINEAR CASE : 1W-GT

VALUES RANGE BETWEEN   -0.44   AND   RUN-   2.37   FOR CONTOUR INTERVALS OF   0.250

(b)

NOBRE   LEVEL IS 700 MB
ZONAL WIND

LINEAR CASE : 1W - GT

VALUES RANGE BETWEEN   -1.77   AND   RUN-   1.94   FOR CONTOUR INTERVALS OF   0.250

(d)

NOBRE   LEVEL IS 700 MB
ZONAL WIND

LINEAR CASE : 1W-GT

VALUES RANGE BETWEEN   -1.63   AND   RUN-   2.25   FOR CONTOUR INTERVALS OF   0.250

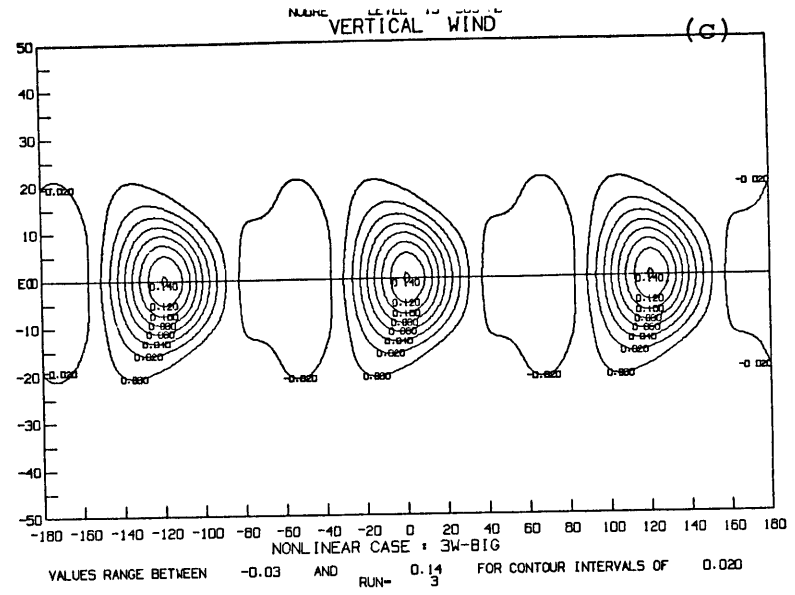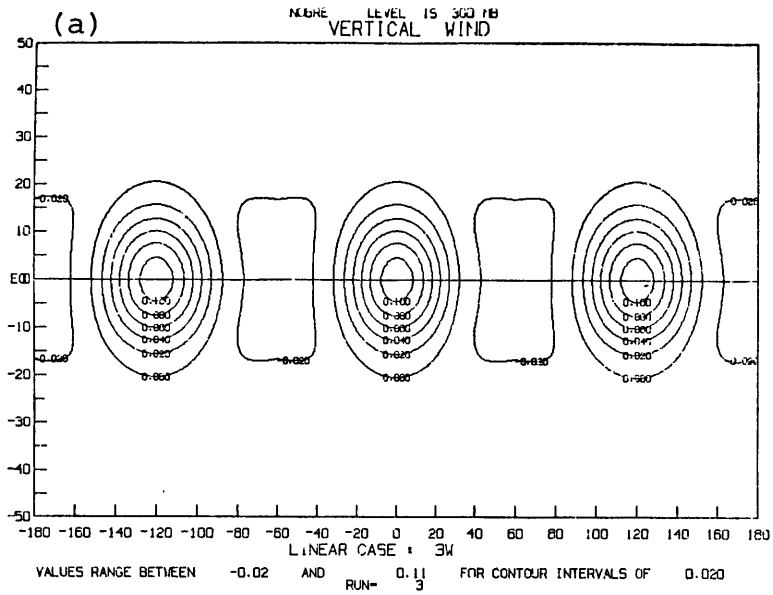Figure 5.10   Same as figure 5.2 but for zonal wind for Case III.

CASE III

Figure 5.11 Same as figure 5.10 but for meidional wind.

CASE III

Figure 5.12   Same as figure 5.10 but for vertical wind.

CASE III

Figure 5.13   Same as figure 5.10 but for geopotential and wind vectors.

CASE IV

(a)

NOBRE   LEVEL IS 300 MB
ZONAL WIND

LINEAR CASE : 3W

VALUES RANGE BETWEEN   -0.60   AND   0.99   FOR CONTOUR INTERVALS OF   0.250
RUN= 1

(c)

NOBRE   LEVEL IS 300 MB
ZONAL WIND

NONLINEAR CASE : 3W-BIG

VALUES RANGE BETWEEN   -0.53   AND   1.17   FOR CONTOUR INTERVALS OF   0.250
RUN= 1

(b)

NOBRE   LEVEL IS 700 MB
ZONAL WIND

LINEAR CASE : 3W

VALUES RANGE BETWEEN   -0.76   AND   0.71   FOR CONTOUR INTERVALS OF   0.250
RUN= 1

(d)

NOBRE   LEVEL IS 700 MB
ZONAL WIND

NONLINEAR CASE : 3W-BIG

VALUES RANGE BETWEEN   -0.81   AND   0.65   FOR CONTOUR INTERVALS OF   0.250
RUN= 1

Figure 5.14   Same as figure 5.2 but for zonal wind for Case IV.

Figure 5.15 Same as figure 5.14 but for meridional wind.

CASE IV
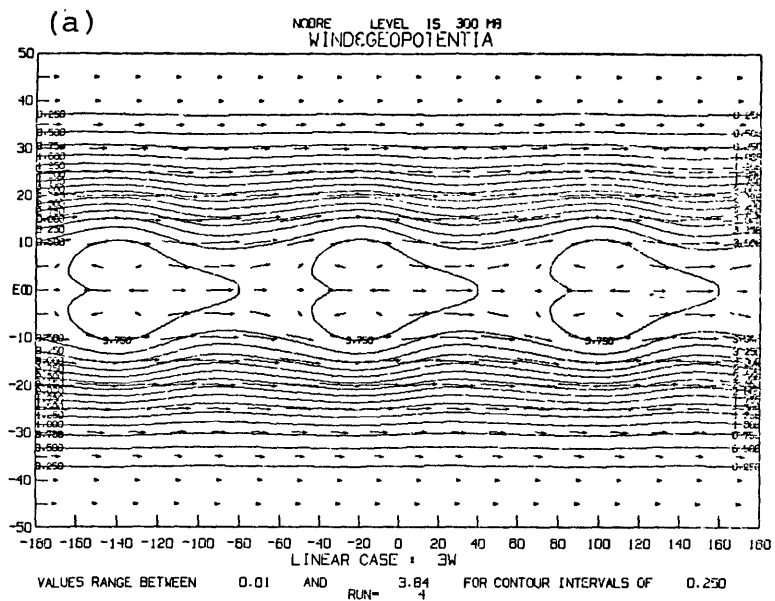

Figure 5.16   Same as figure 5.14 but for vertical wind.

CASE IV
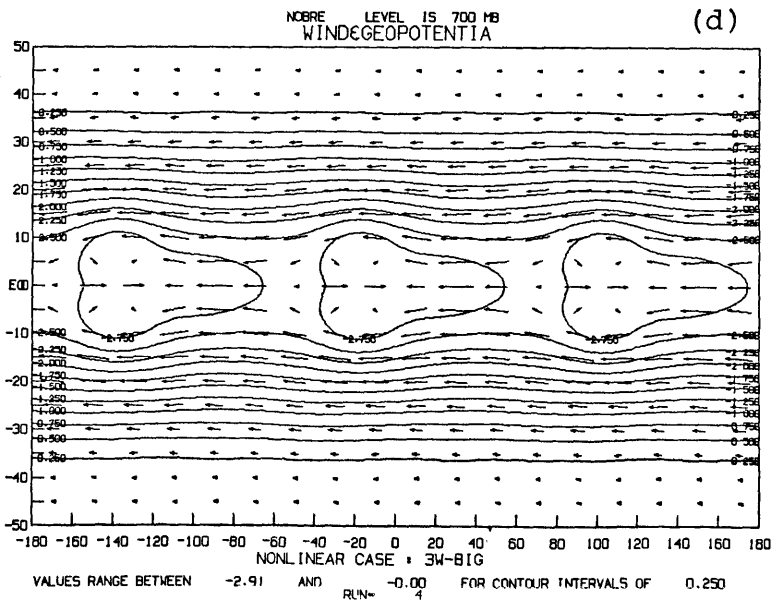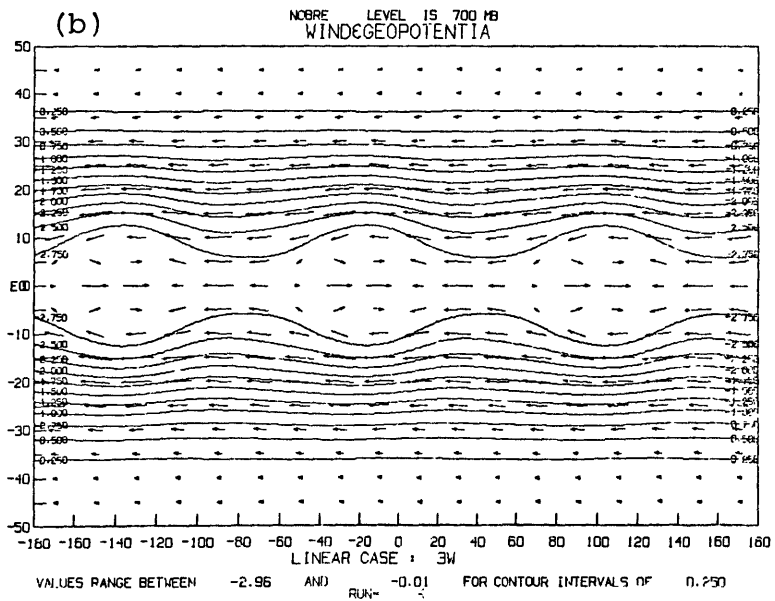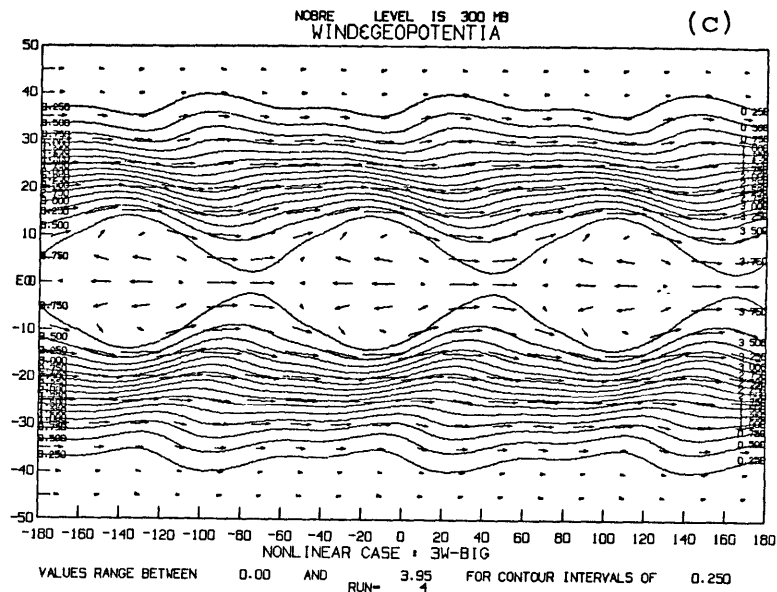
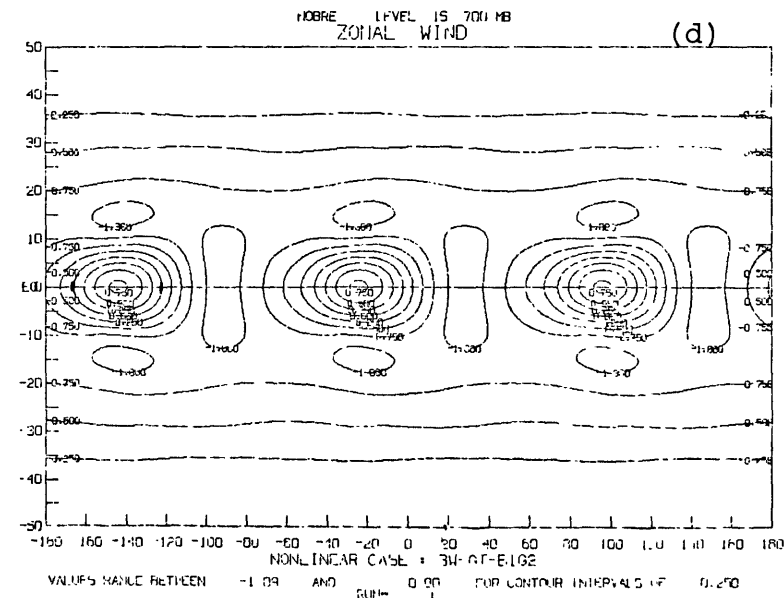Figure 5.17   Same as figure 5.14 but for geopotential and wind vectors.

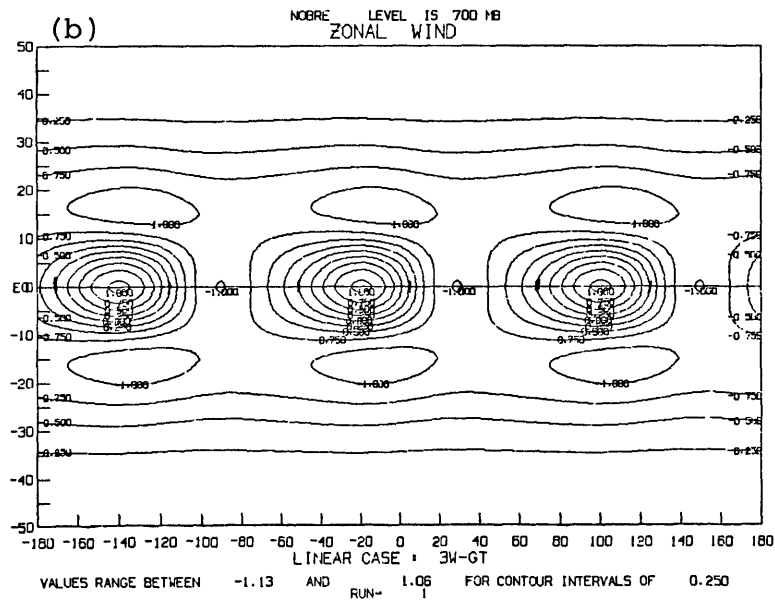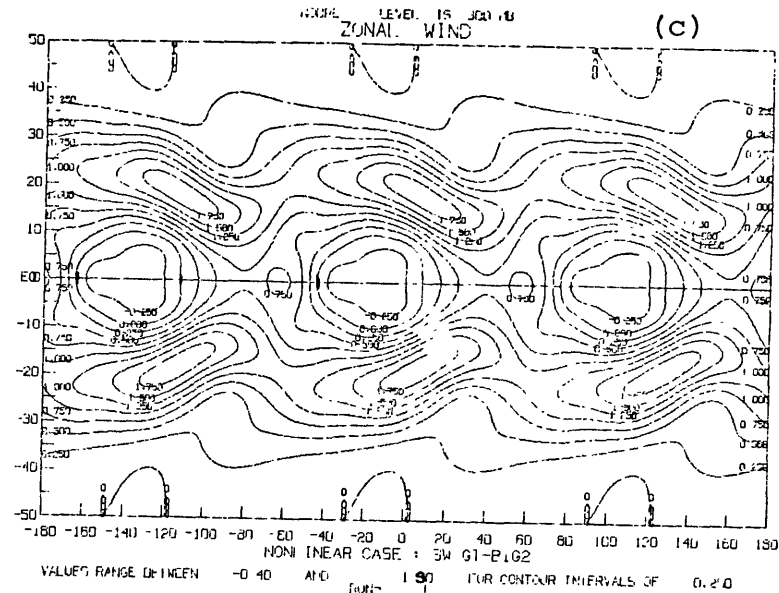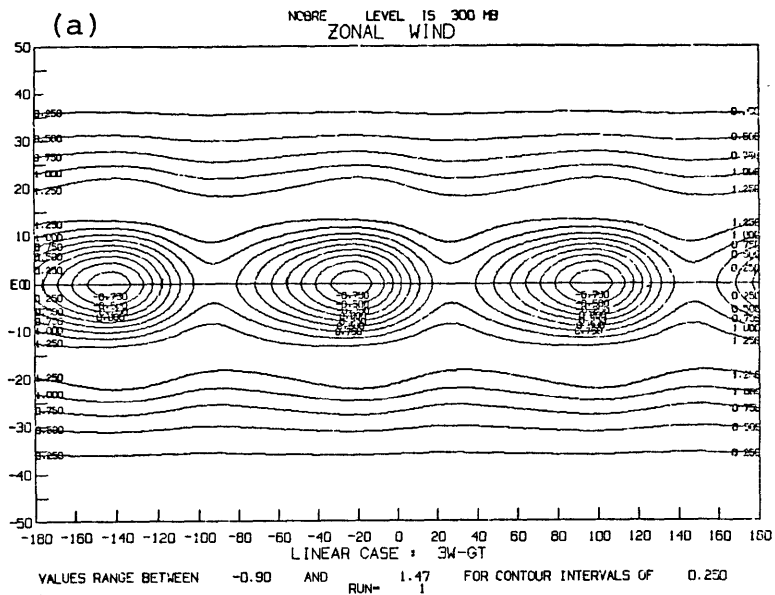CASE V

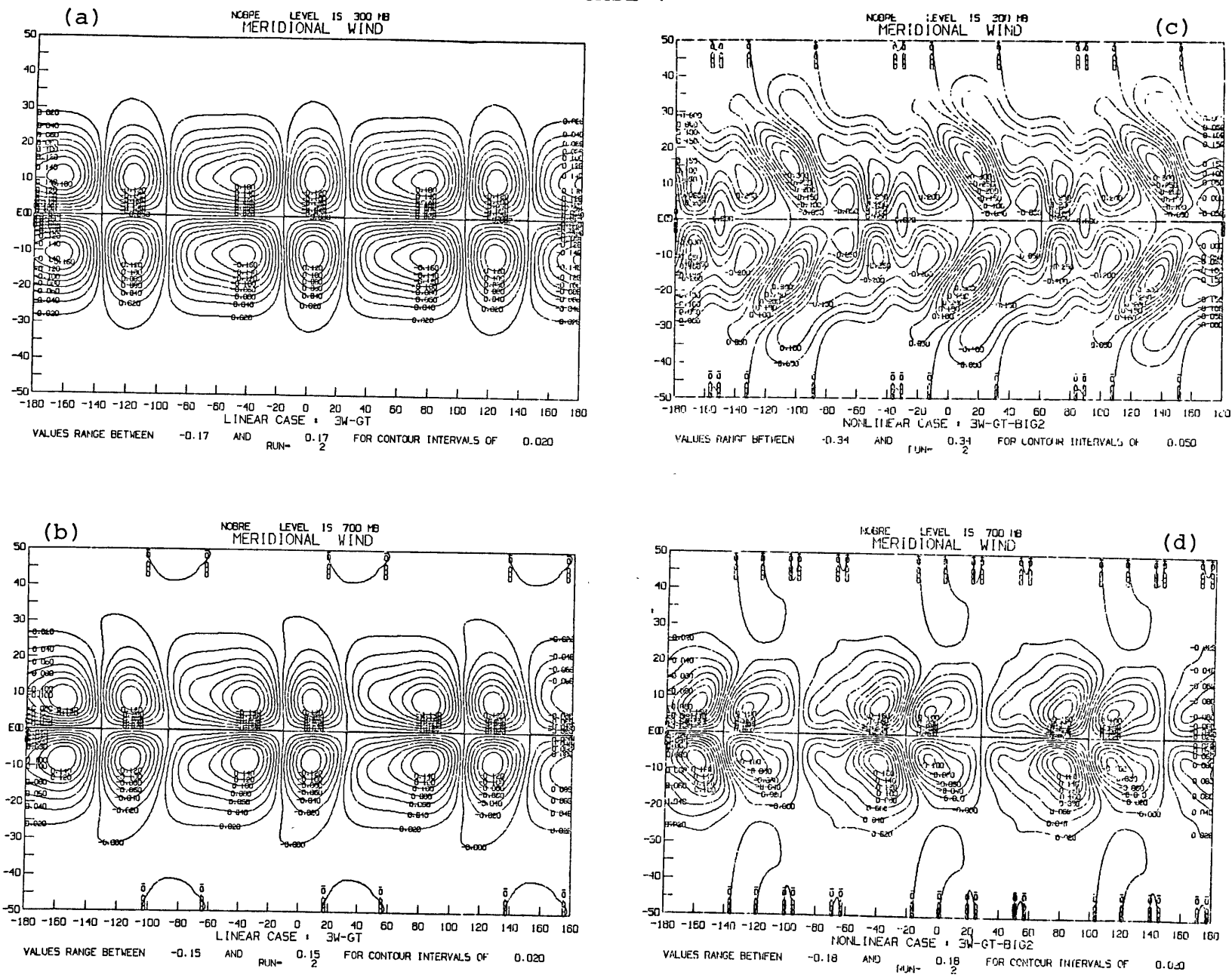Figure 5.18   Same as figure 5.2 but for zonal wind for Case V.

CASE V

Figure 5.19   Same as figure 5.18 but for meridional wind.
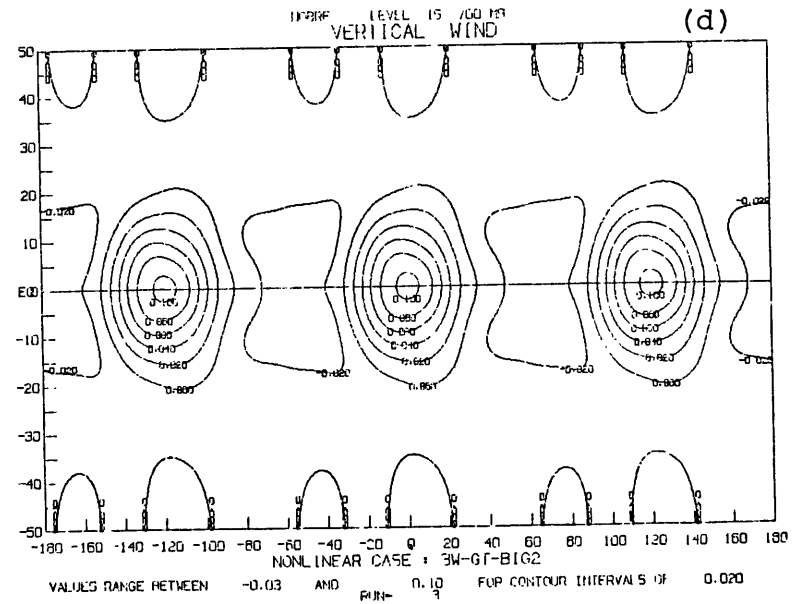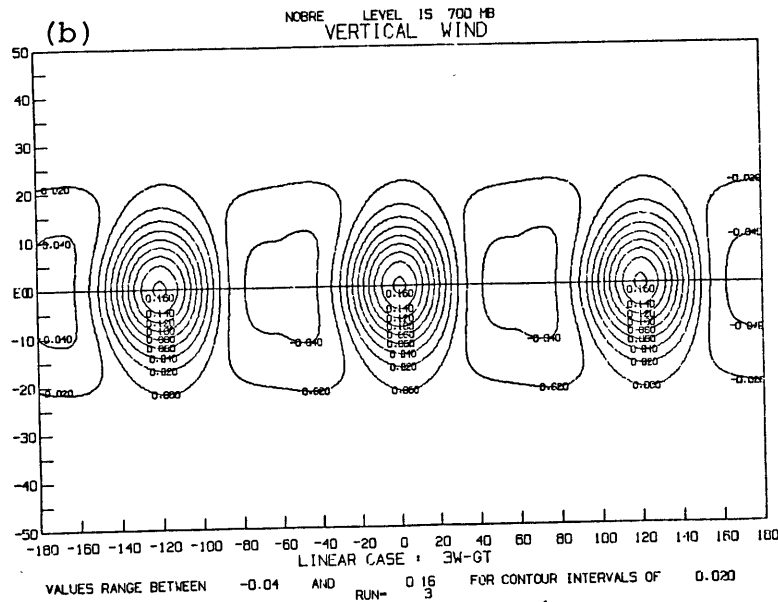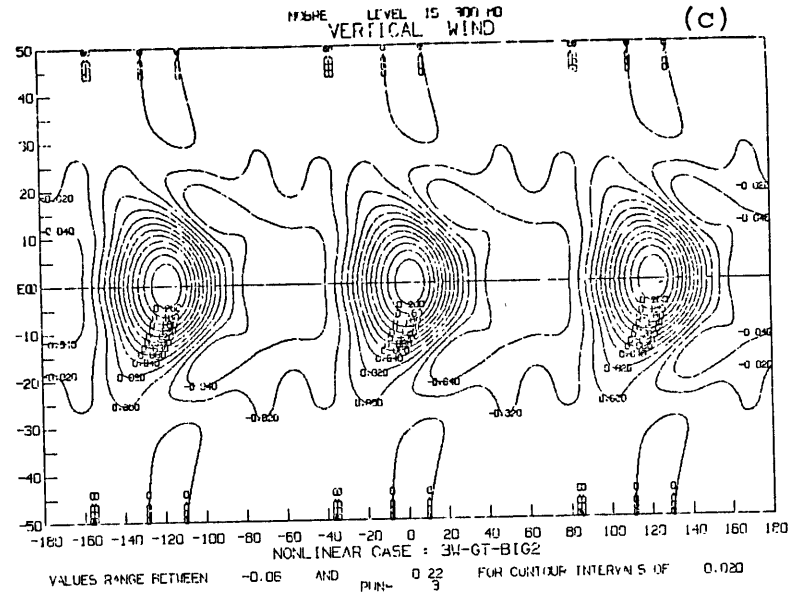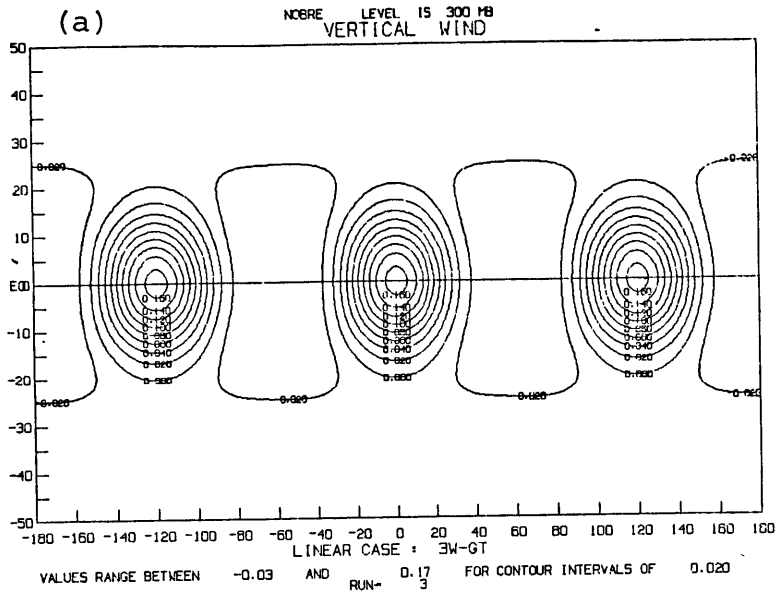Note that interval for (c) is every 0.50 units.

CASE V

Figure 5.20   Same as figure 5.18 but for vertical wind.

CASE V

Figure 5.21   Same as figure 5.18 but for geopotential and wind vectors.

CASE VI

(a)

NOBRE   LEVEL IS 300 MB
ZONAL WIND

LINEAR CASE : IOS-IW

VALUES RANGE BETWEEN   -2.24   AND   1.24   FOR CONTOUR INTERVALS OF   0.250
RUN= 1

(c)

NOBRE   LEVEL IS 300 MB
ZONAL WIND

NONLINEAR CASE : IOS-IW

VALUES RANGE BETWEEN   -1.26   AND   1.49   FOR CONTOUR INTERVALS OF   0.250
RUN= 1

(b)

NOBRE   LEVEL IS 700 MB
ZONAL WIND

LINEAR CASE : IOS-IW

VALUES RANGE BETWEEN   -0.98   AND   1.70   FOR CONTOUR INTERVALS OF   0.250
RUN= 1

(d)

NOBRE   LEVEL IS 700 MB
ZONAL WIND

NONLINEAR CASE : IOS-IW

VALUES RANGE BETWEEN   -1.09   AND   1.70   FOR CONTOUR INTERVALS OF   0.250
RUN= 1

Figure 5.22   Same as figure 5.2 but for zonal wind for Case VI.
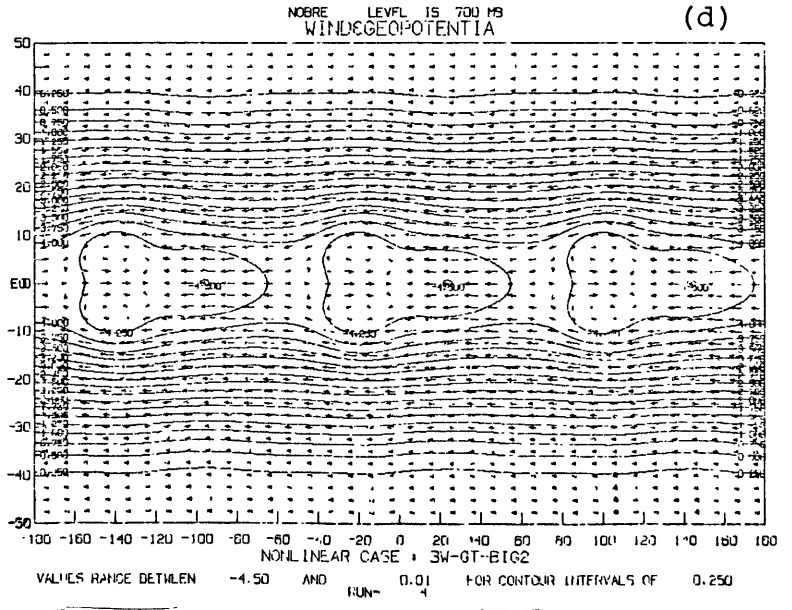
Figure 5.23   Same as figure 5.22 but for meridional wind.

CASE VI

(a)

NOBRE   LEVEL IS 300 MB
VERTICAL WIND

LINEAR CASE : IOS-IW

VALUES RANGE BETWEEN   -0.02   AND   RUN=   0.13   FOR CONTOUR INTERVALS OF   0.020
3

(c)

NOBRE   LEVEL IS 300 MB
VERTICAL WIND

NONLINEAR CASE : IOS-IW

VALUES RANGE BETWEEN   -0.03   AND   RUN=   0.15   FOR CONTOUR INTERVALS OF   0.020
3

(b)

NOBRE   LEVEL IS 700 MB
VERTICAL WIND

LINEAR CASE : IOS-IW

VALUES RANGE BETWEEN   -0.02   AND   RUN=   0.11   FOR CONTOUR INTERVALS OF   0.020
3

(d)

NOBRE   LEVEL IS 700 MB
VERTICAL WIND

NONLINEAR CASE : IOS-IW

VALUES RANGE BETWEEN   -0.02   AND   RUN=   0.09   FOR CONTOUR INTERVALS OF   0.020
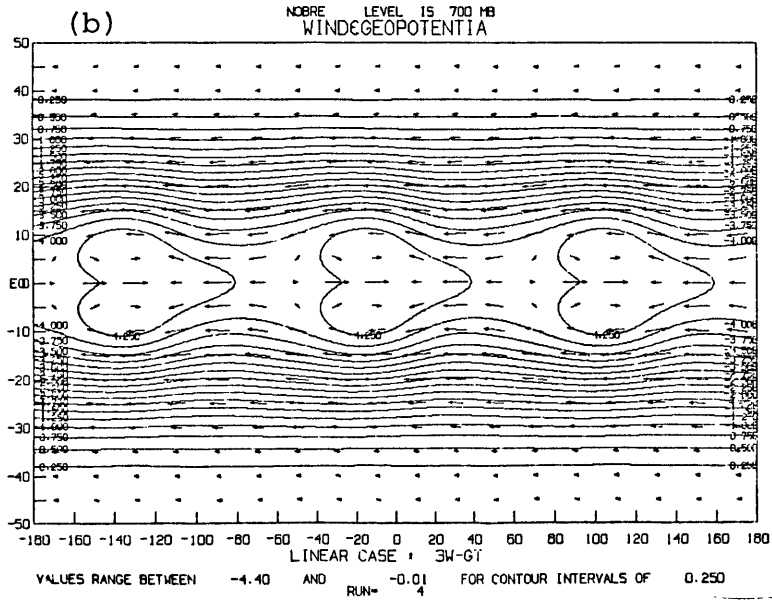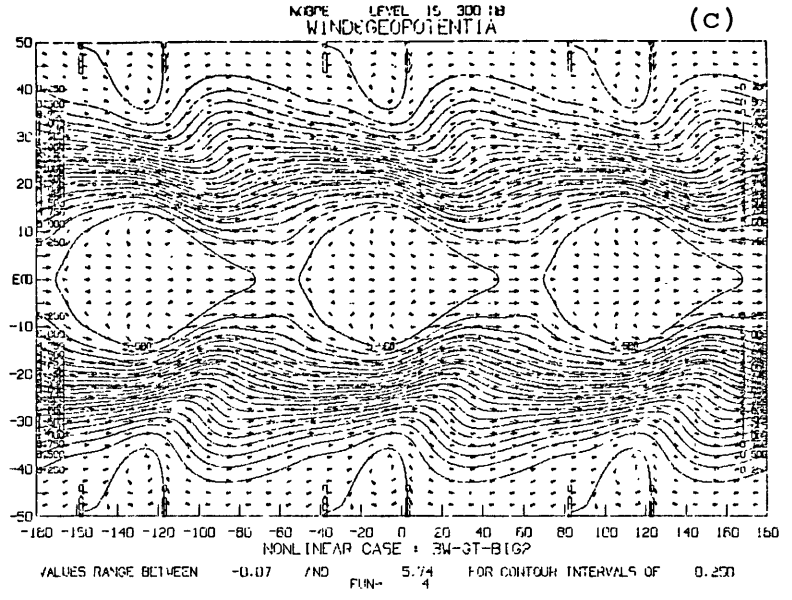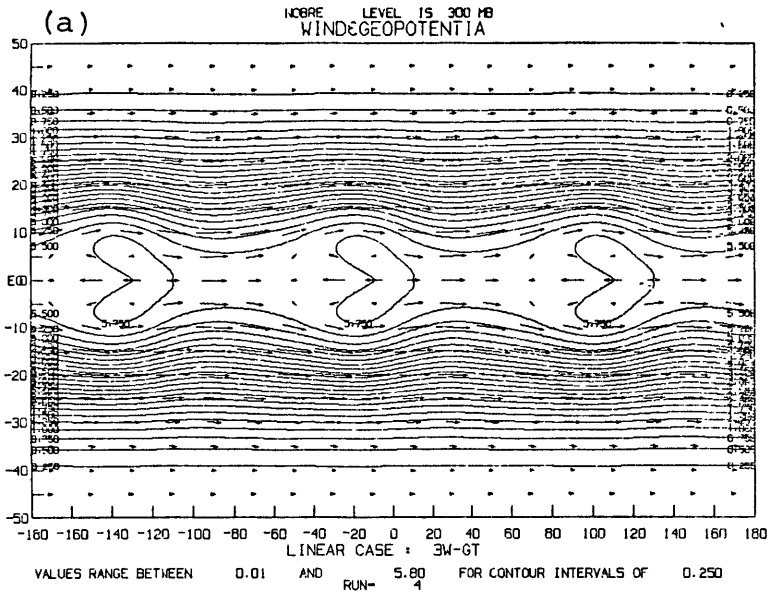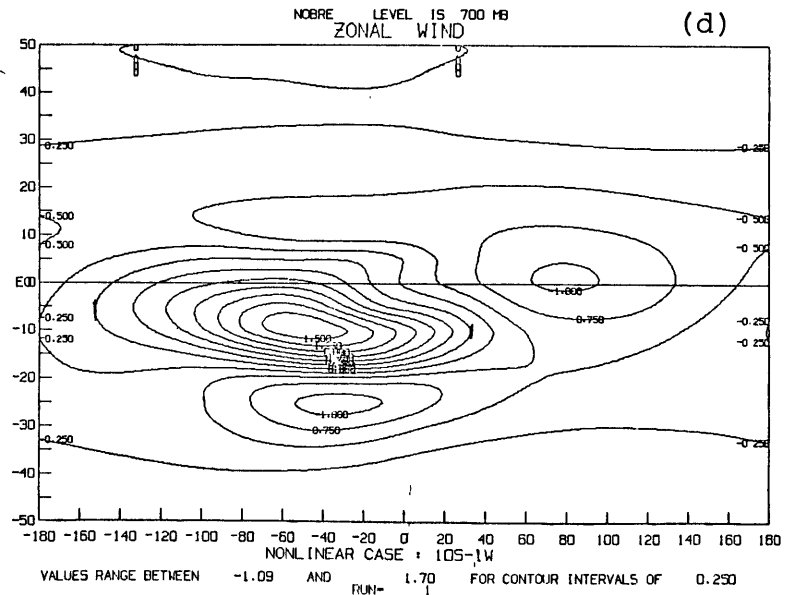3

Figure 5.24   Same as figure 5.22 but for vertical wind.

CASE VI

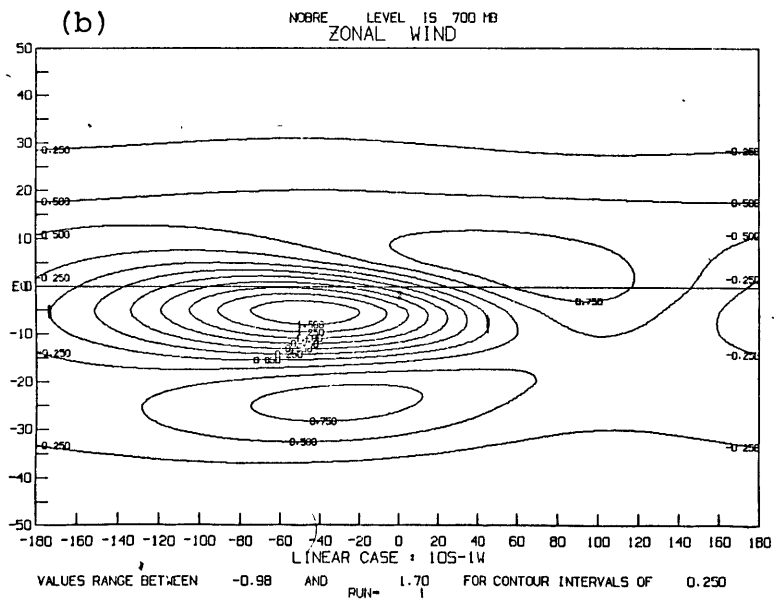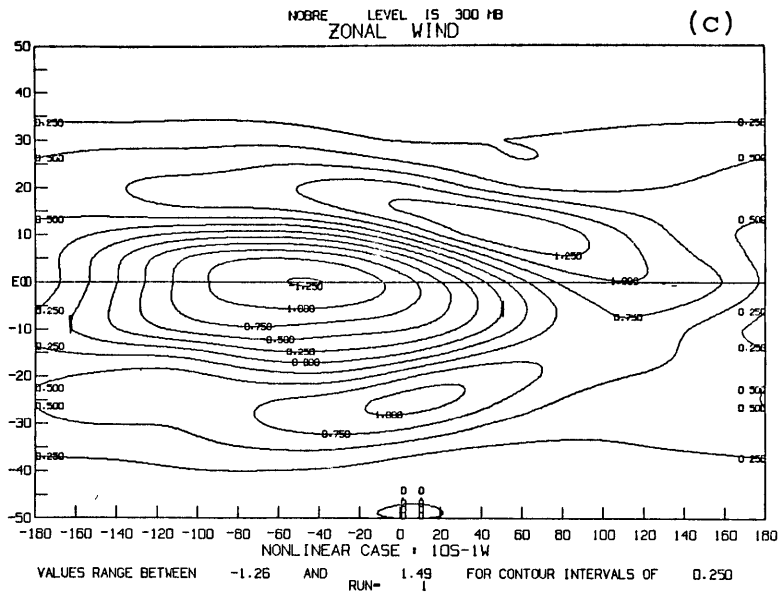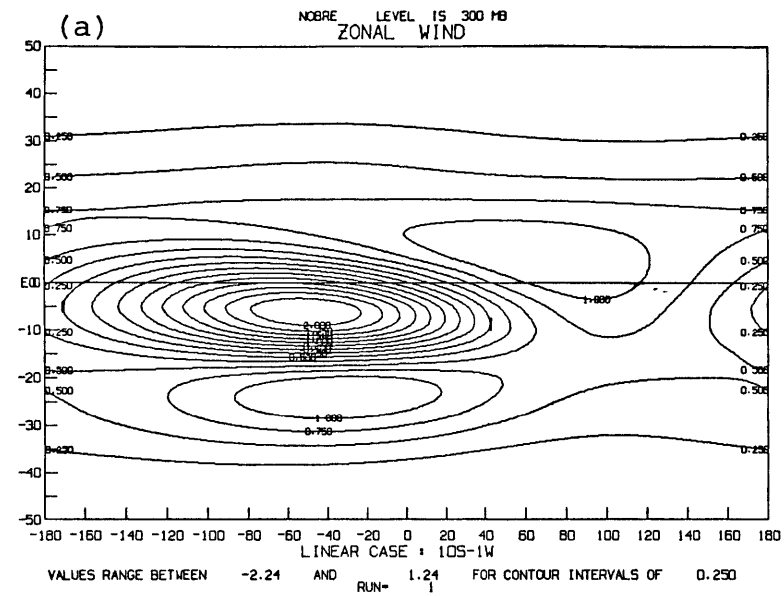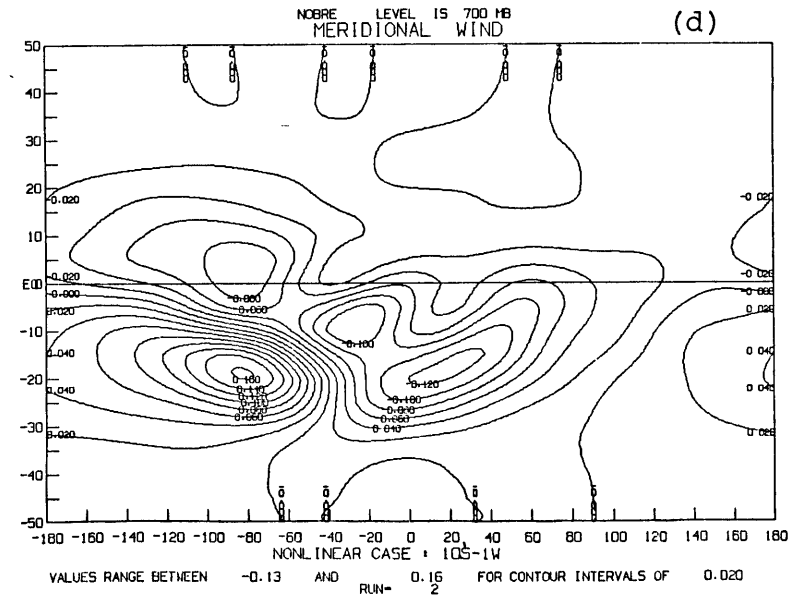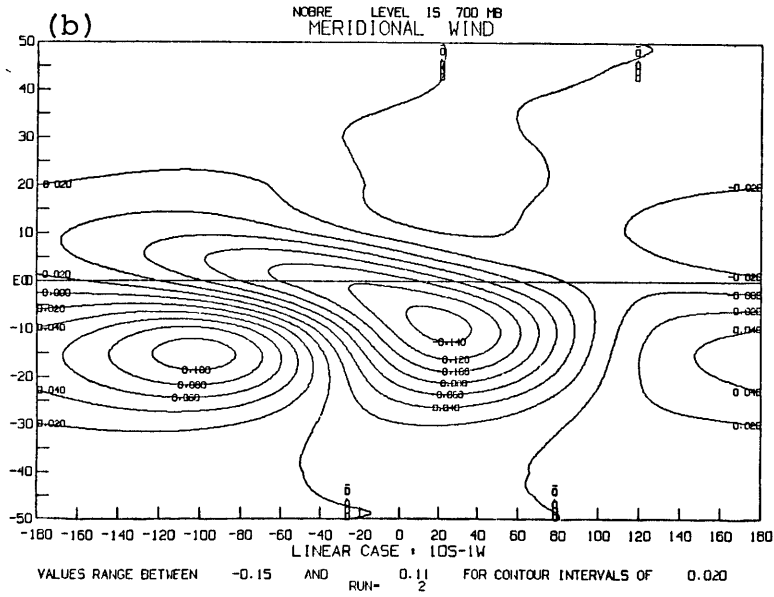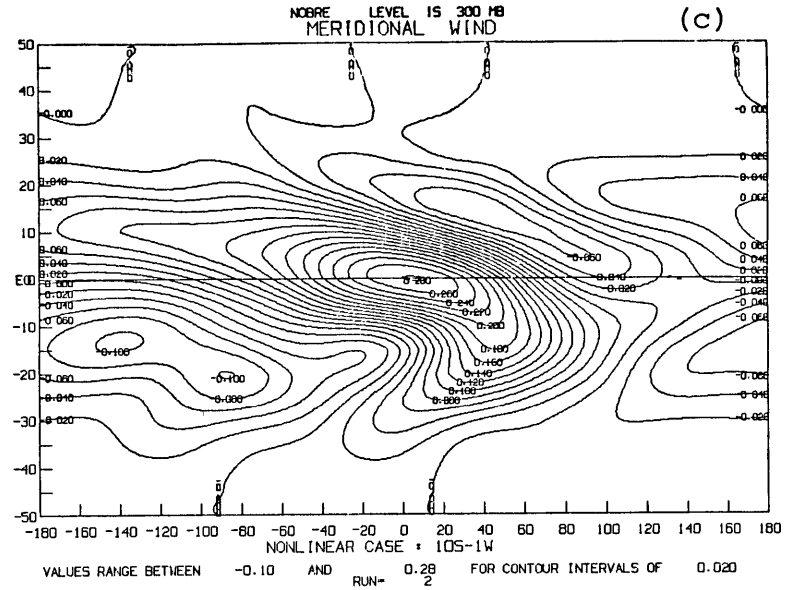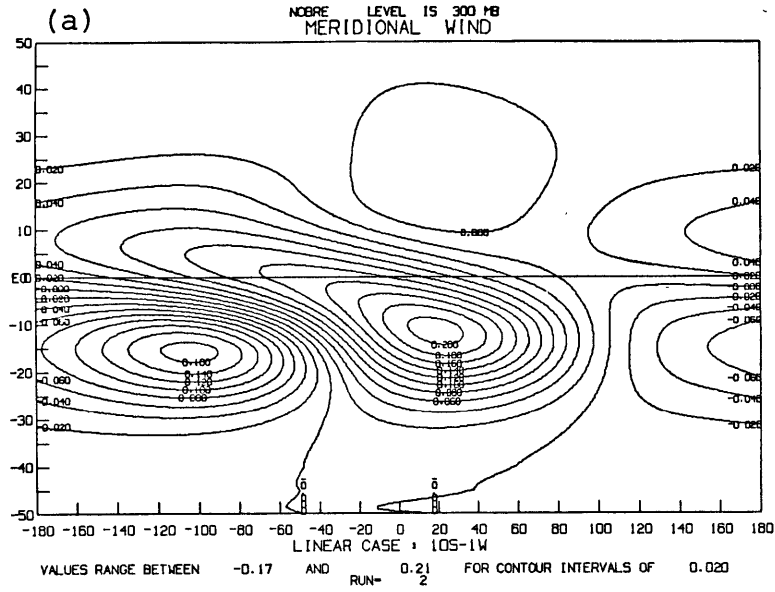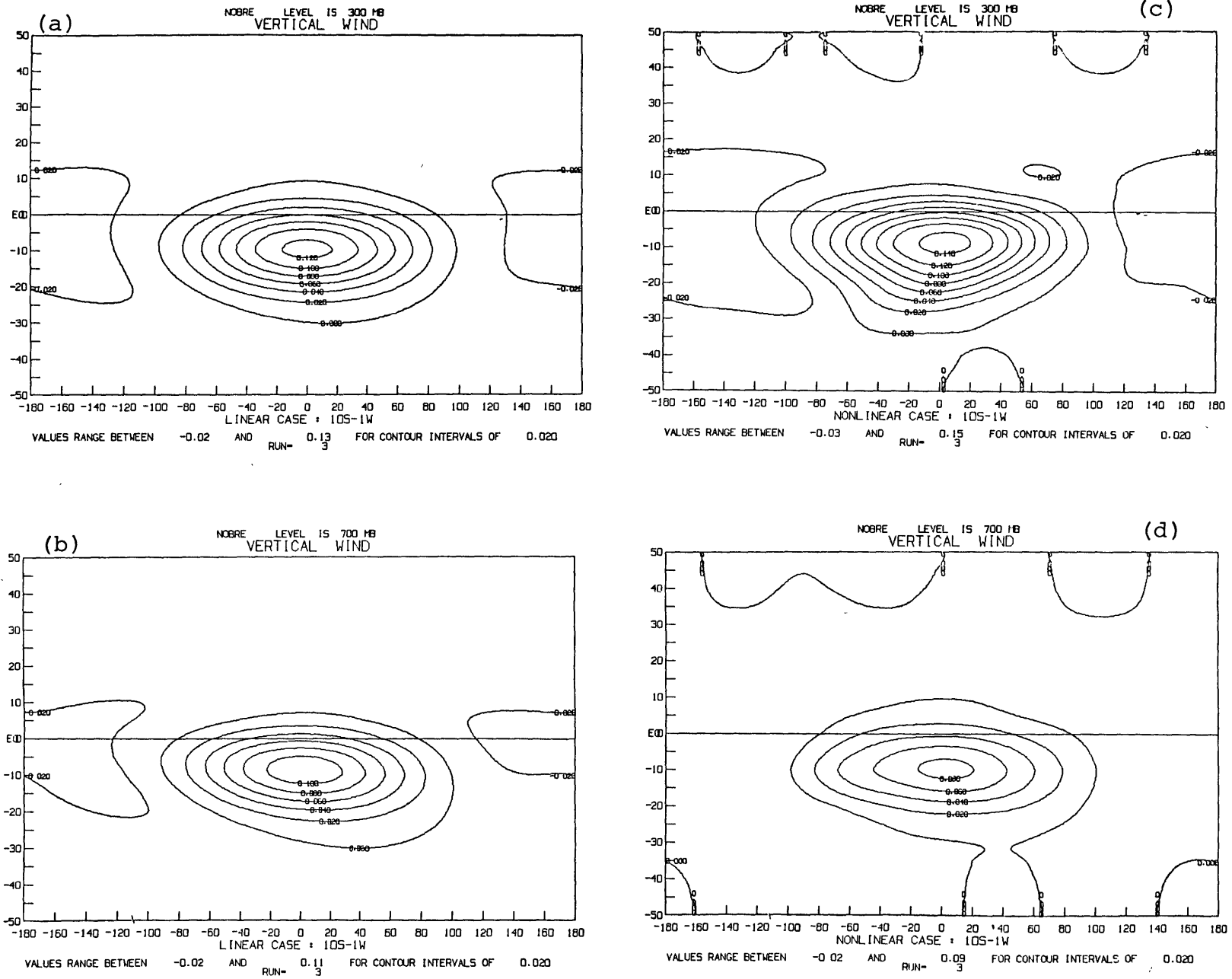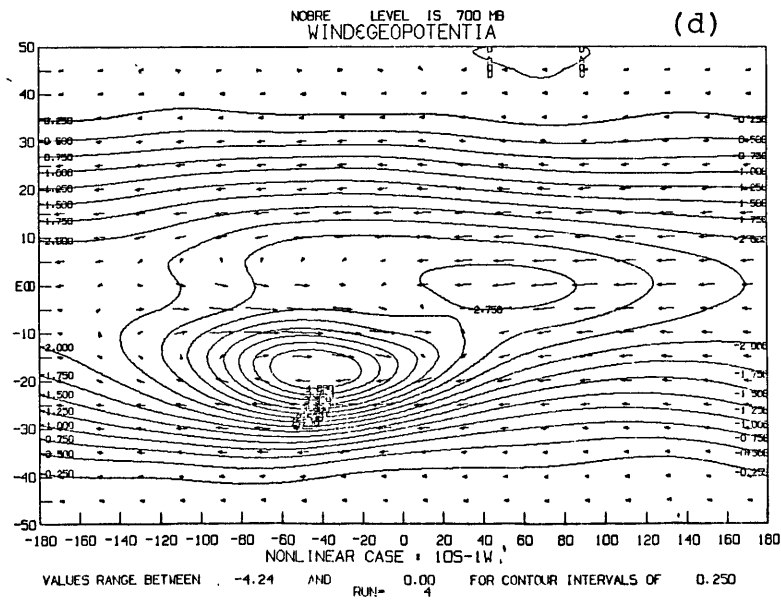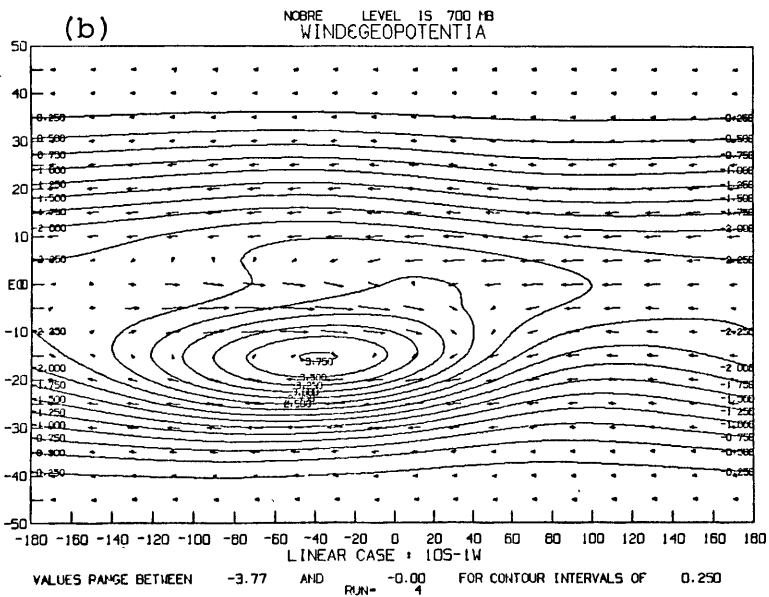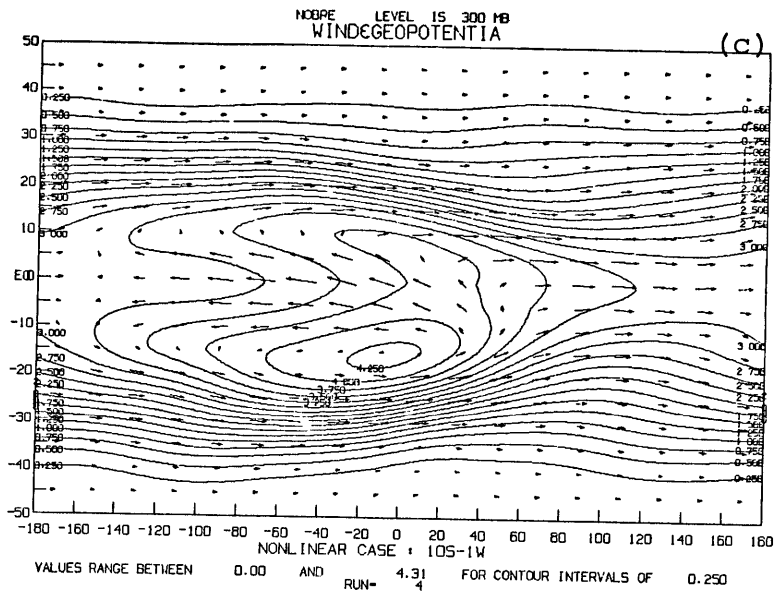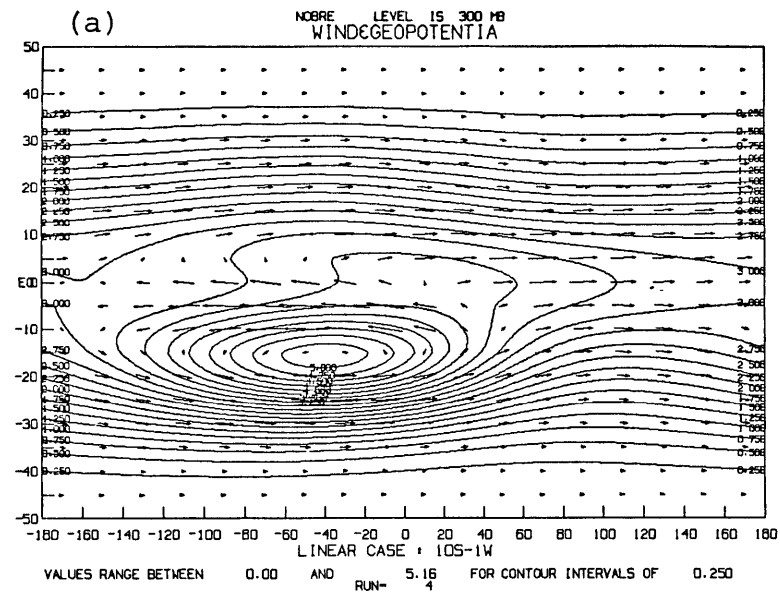Figure 5.25 Same as figure 5.22 but for geopotential and wind vectors.

5.2.1 COMPARISON OF CASES I, II, AND III

The linear response is simply proportional to the intensity of forcing, and its structure, of course, does not change with the amplitude of heating. The linear solutions are very similar to the linear solutions of Chapter 3. The difference is that here we have added a positive mean heating so that the axially symmetric response to this mean heating adds linearly to the solutions with no mean heating as obtained in Chapter 3.

We see, for this linear solution at the lower level, easterlies throughout most of the domain except near the equator where a westerly jet exists to the west of the heat source (Figure 5.2b). For the upper levels (Figure 5.2a) the picture is reversed, with mostly westerlies and an easterly jet to the west of the heat source. The geopotential field (Figure 5.5a and b) presents a wavenumber (wn) 1 structure of small amplitude with the ridge to the west of the heat source. The zonal wind is in geostrophic balance even at equatorial latitudes. We observe that centers of cyclonic (anticyclonic) circulation are found symmetrically about the equator to the west of the heat source for the lower (upper) level. This solution is very similar to the solutions obtained by Matsuno (1966) and Gill (1980). Quantitatively and qualitatively the upper- and lower-level linear responses are very similar and that is caused by the constant vertical structure of our model (constant static stability and Rayleigh friction coefficient, no surface drag, etc.).

When the intensity of the heat source is increased, there is a noticeable change in the nonlinear response. For Case 1 (low heating), linear and nonlinear responses are very similar (Figure 5.2-5.5). As the intensity of the thermal forcing increases (Figures 5.6-5.13), upper-level easterlies to the west of the heat source weaken considerably; the upper-

level westerlies to the east of the heat source also decrease but not as much as the upper-level easterlies. The major change is seen in the position of the upper-level maximum winds. Linearly and nonlinearly for small heating, the position is found at the equator west of the heat source, and the winds are westerly . For medium and strong heating, the maximum winds are westerlies, and the band has shifted to the subtropics and shows a NW-SE tilt in the northern hemisphere (symmetric in the southern hemisphere). The geopotential field for cases II and III shows a large-amplitude wavenumber 1 response at the upper levels. This wn 1 geopotential response is seen also for the linear cases, but it is smaller in amplitude and presents a small latitudinal scale. For strong heating, its latitudinal scale is greater and the response is largest northeast and southeast of the heat source, corresponding to the position of the maximum winds. Reflecting the increased amplitude of the geopotential response away from the equator, the meridional wind distribution undergoes significant changes for moderate and strong heating. Its maximum magnitudes are 40% greater as compared to the linear case, and also it presents a NW-SE tilt in the northern hemisphere. The vertical wind, shown in Figure 5.12 for case III, shows an increase (decrease) at the upper (lower) levels for the nonlinear case of up to 80%.

For the lower level the equatorial westerly jet intensifies slightly ($\simeq$ 10%), but the westerlies occupy a narrower longitudinal band for the nonlinear case than for the linear case ($\simeq$ 50° of longitude shorter at the equator for strong heating) as shown in Table 5.4. The region of easterlies to the east of the heat source increases in size, and the magnitudes are smaller ($\simeq$ 10% smaller). Centers of cyclonic circulation are found in opposite sides of the equator at approximately 8°N and 8°S and 40° west of the longitude of maximum heating for the linear case. For

medium and strong heating, the cyclonic circulation becomes more intense around these centers and longitudinally more confined. Slack meridional geopotential gradients are seen in the equatorial area west of the heat source. The nonlinear solution for cases with strong heating are markedly more asymmetric in the zonal direction when compared with linear solutions and with the nonlinear solution for small heating. Lower-level meridional winds almost double in magnitude for strong heating and now attain higher magnitude to the west of the heat source and are very weak to the east of it (Figure 5.11d). The wn 1 geopotential response increases in amplitude but its latitudinal scale is not as large as for the upper-level response (compare Figures 5.13c and d).

5.2.2 COMPARISON OF CASES IV AND V

The general features of the solution for three heat sources centered at the equator and equally spaced along the x-direction show agreement with the solution for the cases with one heat source. Linearly, as the x-scale of the forcing decreases, the zonal wind speed decreases and the meridional wind speed remains about the same in accordance with the scale arguments in Chapter 3; so maximum zonal velocities are smaller for this case as compared with the case of one heat source of planetary scale (see Table 5.3). Easterlies (westerlies) are seen throughout the subtropics for the lower (upper) levels, and strongly convergent flow is seen in the equatorial latitudes with three centers of maximum vertical velocities coinciding with the position of the heat sources (Figures 5.14-5.21).

The nonlinear solution presents several differences which are qualitatively similar to the changes seen when linear and nonlinear solutions were compared for cases I and II. For the case with strong

heating (case V), the three wind speed maxima at 300 mb are now found away from the equator in the subtropics of each hemisphere and display a NW-SE tilt in the northern hemisphere. Also, the magnitude of the upper-level equatorial easterlies to the east of each heat source has become less than 1/2 of its former value (Figure 5.18c). The upper-level geopotential shown in Figure 5.21c shows a large-amplitude wn 3 structure with latitudinal scale much larger than that for the corresponding linear case (Figure 5.17a). Upper-level meridional wind speed is twice as large for the nonlinear case (see Table 5.3a), and maximum southerlies in the northern hemisphere are found further poleward and tilted horizontally (Figure 5.19c). The upper-level vertical wind increases in magnitude, and the geometry of areas of upward motions and downward motions changes considerably for the nonlinear solution with areas of subsidence appearing northeast and southeast of the heat source.

At the lower levels the changes between the linear and nonlinear solutions are qualitatively similar to the cases with one heat source. We see increased and longitudinally more confined equatorial westerlies (Figure 5.18d), increased meridional winds which are more confined to the west of the heat source (Figure 5.19d), decreased vertical winds (Figure 5.20d), and weaker meridional geopotential gradients in the equatorial area (Figure 5.21d).

5.2.3 CASE VI

Here, one heat source was placed away from the equator at 10°S, and we examined the case with medium intensity of heating. The linear response now shows non-zero meridional winds at the equator; a low is observed at 15°S and 40° to the west of the longitude of maximum heating, and its magnitude and the cyclonic circulation associated with it is more intense

than for the case with one heat source at the equator (compare Figures 5.25 and 5.9). Maximum meridional velocity are observed at that latitude of the heat source and east of it, in marked contrast with the cases for which the heat source was placed on the equator. Also, the upper- (lower-) level easterlies (westerlies) cover a broader longitudinal band as shown in Table 5.4. These major features of linear response to a heat source away from the equator were considered in Chapter 3.

The nonlinear response shows upper- level easterlies shifted northward and considerably weaker. The upper- level westerly maximum increases in magnitude and is found to the east and poleward of its former position (Figure 5.22). Upper- level southerlies become stronger ($\approx 40\%$ larger) and northerlies decrease in magnitude and cross-equatorial flow towards the northern hemisphere increases. The upper- level maximum meridional wind is now found at the equator (Figure 5.23c). The upper- level geopotential low center becomes weaker and is displaced about 30° to the east of its position for the linear case (compare Figures 5.25a and c), whereas the lower-level geopotential is slightly stronger and displaced to the west. Comparing Figures 5.25c and d, we observe that the geopotential presents an eastward tilt with height for the nonlinear solution. No such tilt is observed for the linear solution. The nonlinear response is observed to change significantly in the northern hemisphere; therefore, cross-equatorial flow is likely to play an important role.

5.3 LINEAR AND NONLINEAR BALANCES

As an aid to understanding the nature of nonlinear solutions, we calculate all the terms in the dynamical equations and show in Figures 2.26 - 2.33 their longitudinal profile for a set of selected longitudes at 300 mb and 700 mb and for linear and nonlinear solutions. We will concentrate on Case III (one strong heat source at the equator) because most of the aspects of the nonlinear response can be seen more clearly for that case.

In Figure 5.26a and b the terms of the zonal momentum equation are shown for Case III. The linear solution presented on top of Figure 5.26a and b shows that away from the equator the major balances in the zonal direction are among the Coriolis force and the zonal pressure gradient force, and near the equator friction becomes increasingly important, and at the equator there is a two-way balance between friction and the pressure gradient force. The balances for the nonlinear solution present a quite different behavior. At 300 mb (bottom of Figure 5.26a) we see that at the equator the major balances are between $-\partial\phi/\partial x$ and advection terms. In Figure 2.29 we break the advection terms in zonal, meridional, and vertical advections of zonal momentum. For the upper- level at the equator, vertical advection of zonal momentum is the largest advection term to the west of the heat source. The upper- level nonlinear response increases poleward as is evidenced from Figures 2.26a to d (bottom).
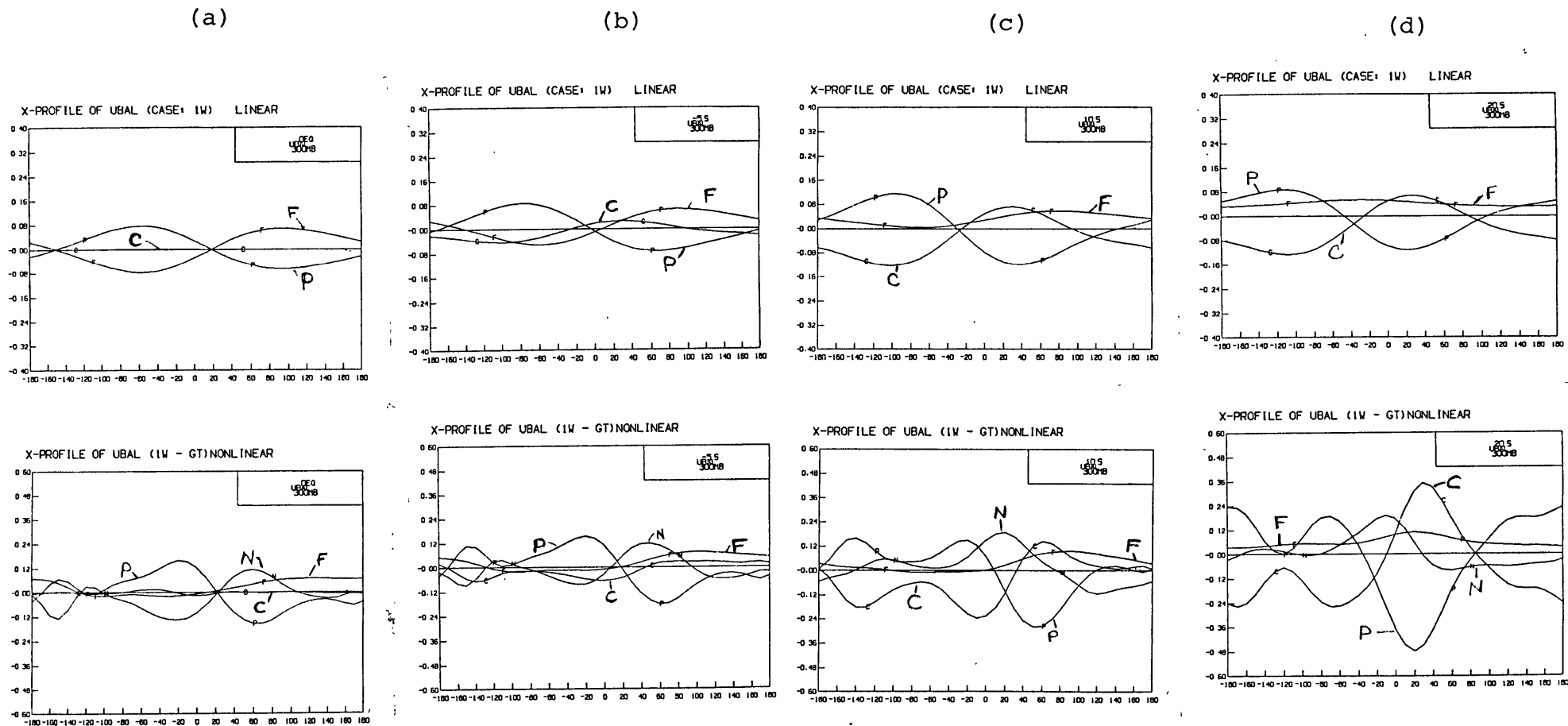
Figure 5.26a   Zonal momentum balances for Case III at 300 mb. Top: linear solution;
bottom: nonlinear solution. a) EQ, b) 5 S, c) 10 S and d) 20 S.   The
labels read as follows: C=Coriolis force, P=pressure gradient force,
F=friction, and N=sum of zonal, meridional and vertical advections.

(a)

(b)

(c)

(d)

X-PROFILE OF UBAL (CASE: 1W)   LINEAR

X-PROFILE OF UBAL (CASE: 1W)   LINEAR

X-PROFILE OF UBAL (CASE: 1W)   LINEAR

X-PROFILE OF UBAL (CASE: 1W)   LINEAR

X-PROFILE OF UBAL (1W - GT)NONLINEAR

X-PROFILE OF UBAL (1W - GT)NONLINEAR

X-PROFILE OF UBAL (1W - GT)NONLINEAR

X-PROFILE OF UBAL (1W - GT)NONLINEAR
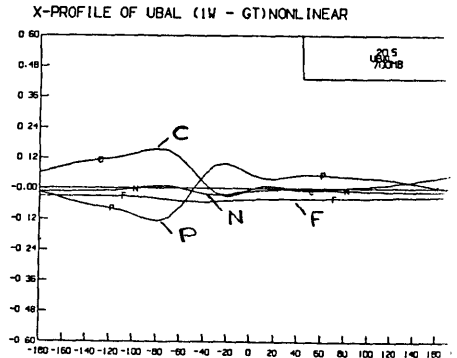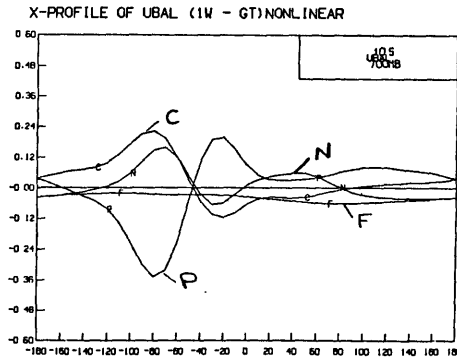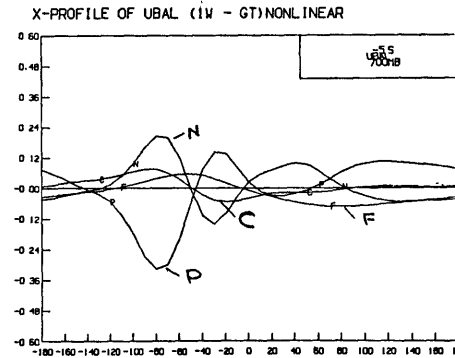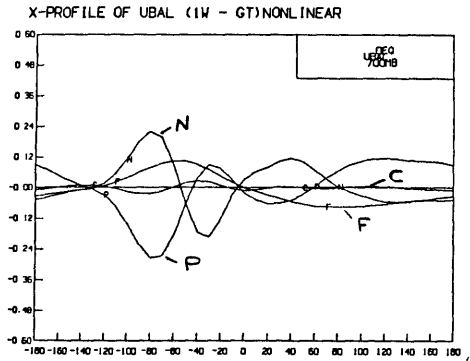
Figure 5.26b   Same as figure 5.26a but at 700 mb.

At 20°S the upper- level response is the largest, and for that latitude the main balances are between Coriolis and pressure gradient forces, but we remark that nonlinear terms still are important and zonal advection of momentum is the leading advection term (Figure 2.29d, top).

The nonlinear response at 700 mb also shows distinct differences as compared to the linear solution (Figure 2.26b, bottom). Here we see that the nonlinear solution is largest at 10°S and shows rapid poleward decrease. At the equator the major balances are between pressure gradient force and zonal advection of zonal momentum, and the latter is larger to the west of the heat source in the region of strong equatorial westerlies. At 10°S there is a three-way balance among Coriolis, pressure gradient, and meridional advection of zonal momentum.

Linear and nonlinear meridional momentum balances are shown in Figures 5.27a and b at 300 mb and 700 mb, respectively. The linear balance shows that the motions are mostly in geostrophic balance in the y-direction and the response peaks at 20°S and decrease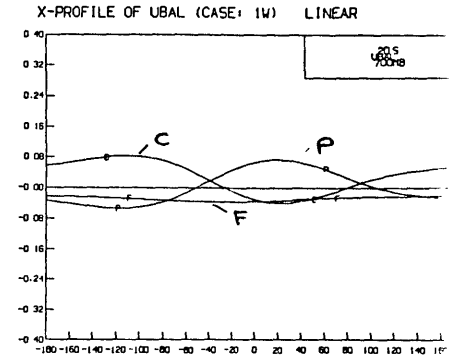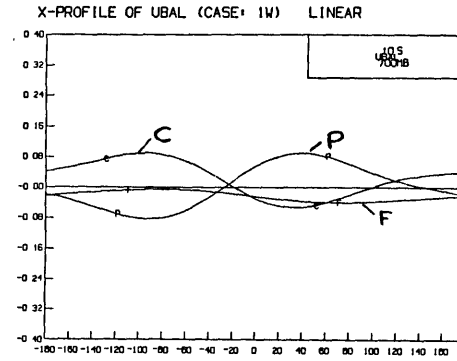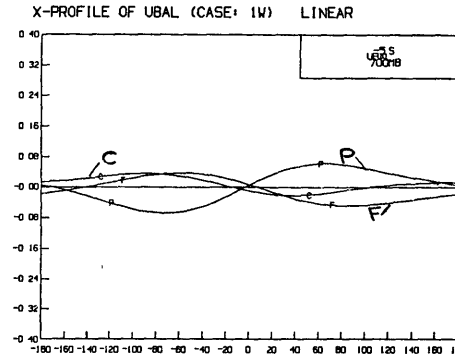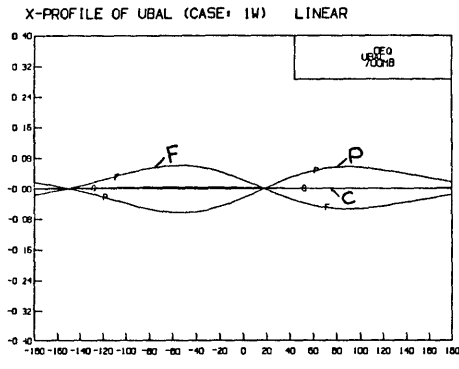s poleward (not shown) and equatorward of that latitude (at the equator v=0, for this forcing). The nonlinear solution also is largest at 20°S but shows a marked longitudinal variation with maximum response 20°E. The smallness of v compared to u makes the frictional and advection terms negligible. Note that the meridional balances are an order of magnitude larger than the zonal balances and that was seen to be related to the longitudinal and latitudinal scales of the forcing (Chapter 3, Section 3.2.2). At 700 mb (Figure 5.27b) we see that the response is not as large as for the upper levels and shows a maximum at 20°S and 40° to the west of the heat source.

(a)　　　　　　　　(b)　　　　　　　　(c)　　　　　　　　(d)

X-PROFILE OF VBAL (CASE: 1W)　LINEAR

X-PROFILE OF VBAL (CASE: 1W)　LINEAR

X-PROFILE OF VBAL (CASE: 1W)　LINEAR

X-PROFILE OF VBAL (CASE: 1W)　LINEAR

X-PROFILE OF VBAL (1W - GT)NONLINEAR

X-PROFILE OF VBAL (1W - GT)NONLINEAR

X-PROFILE OF VBAL (1W - GT)NONLINEAR
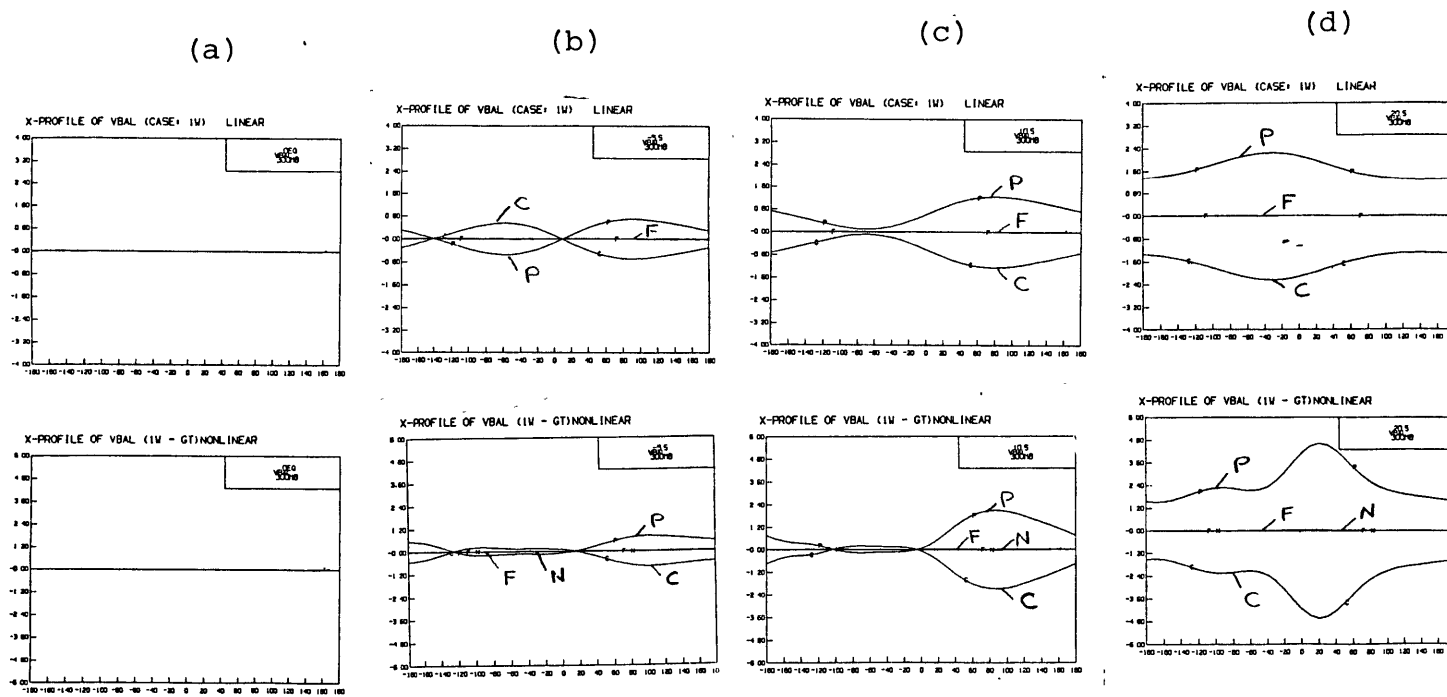
X-PROFILE OF VBAL (1W - GT)NONLINEAR

Figure 5.27a　Same as figure 5.26a but for the meridional momentum balances.
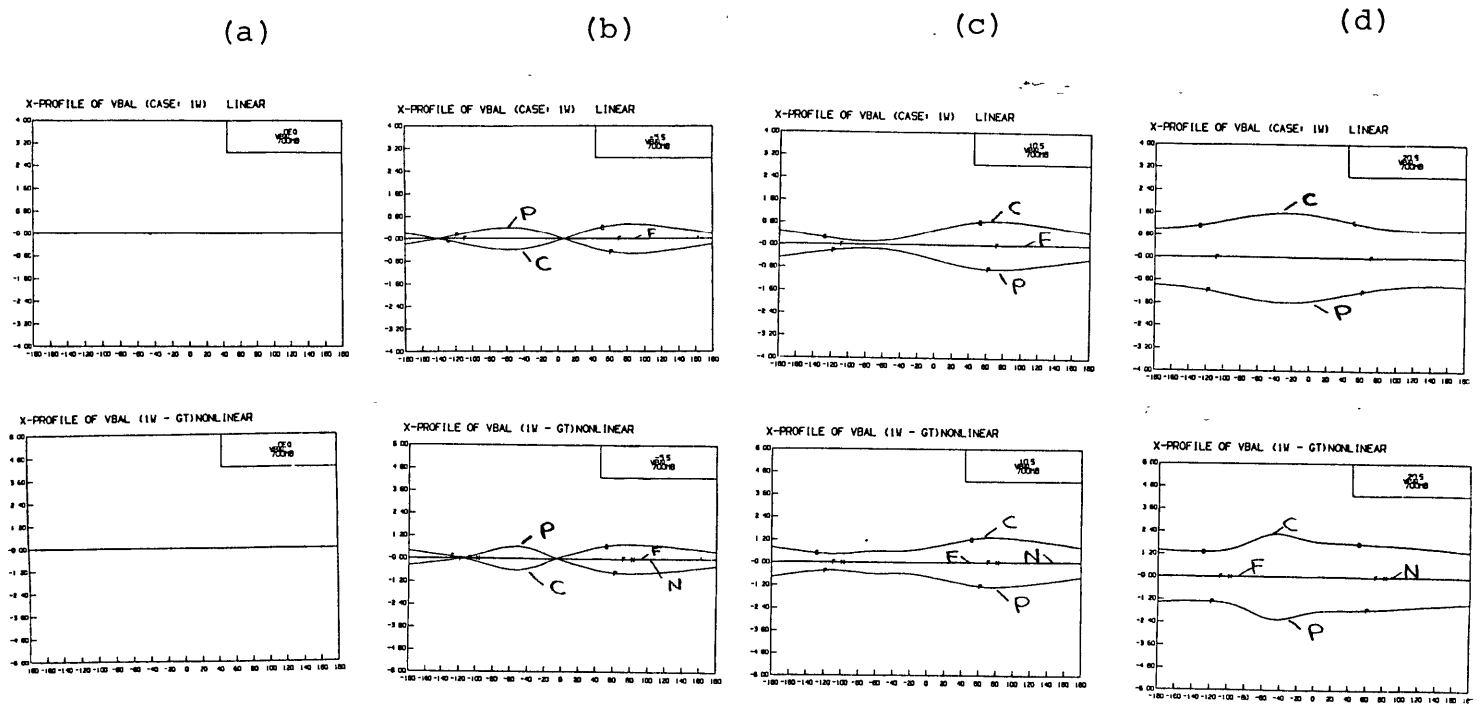
(a) (b) (c) (d)

Figure 5.27b Same as figure 5.27a but at 700 mb

The thermo-dynamic balances are shown in Equations 5.28a (300 mb) and b (700 mb). Throughout the heating region the major balance is $Sw \sim (Q_L/C_p)$, and it is $Sw \sim (T'/\tau_r)$ elsewhere for the linear case. The nonlinear solution shows that nonlinear advection becomes important where the heat source is strong, i.e., near the equator. Inspection of Figure 5.30 reveals that vertical advection is the largest advection. T' is maximum approximately at the level of maximum heating, so $\partial T'/\partial z < 0$ at the upper levels and $\partial T'/\partial z > 0$ at the lower levels; and since $w(S + \partial T'/\partial z) \sim (Q_L/C_p)$, we see that the vertical velocity increases (decreases) at the upper (lower) level. Linearly, the assumption $S w \sim (Q/C_p)$ seems to be a good approximation. However, for deep and intense heat sources as is the case for tropical convection, vertical advection of heat becomes important.

In Figures 5.31, 5.32, and 5.33, we compare the dynamical balances of zonal momentum, meridional momentum, and the advection of zonal momentum at 300 mb for Cases I, II, and III at selected latitudes. The ratio of the scales 1 : 2 : 3 for Cases I, II, III, respectively, is the same ratio as the intensity of heating so as to make comparisons easy. As seen before in Section 5.2, the nonlinear response to small heating (Case I) is very similar to the linear one, i.e., advection terms are small and there is no qualitative difference between the two solutions. For strong heating, nonlinear advection becomes important for the maintenance of the zonal wind, and the upper-level response is changed both qualitatively and quantitatively, and the maximum response is poleward of the region of maximum heating and to the west of it.
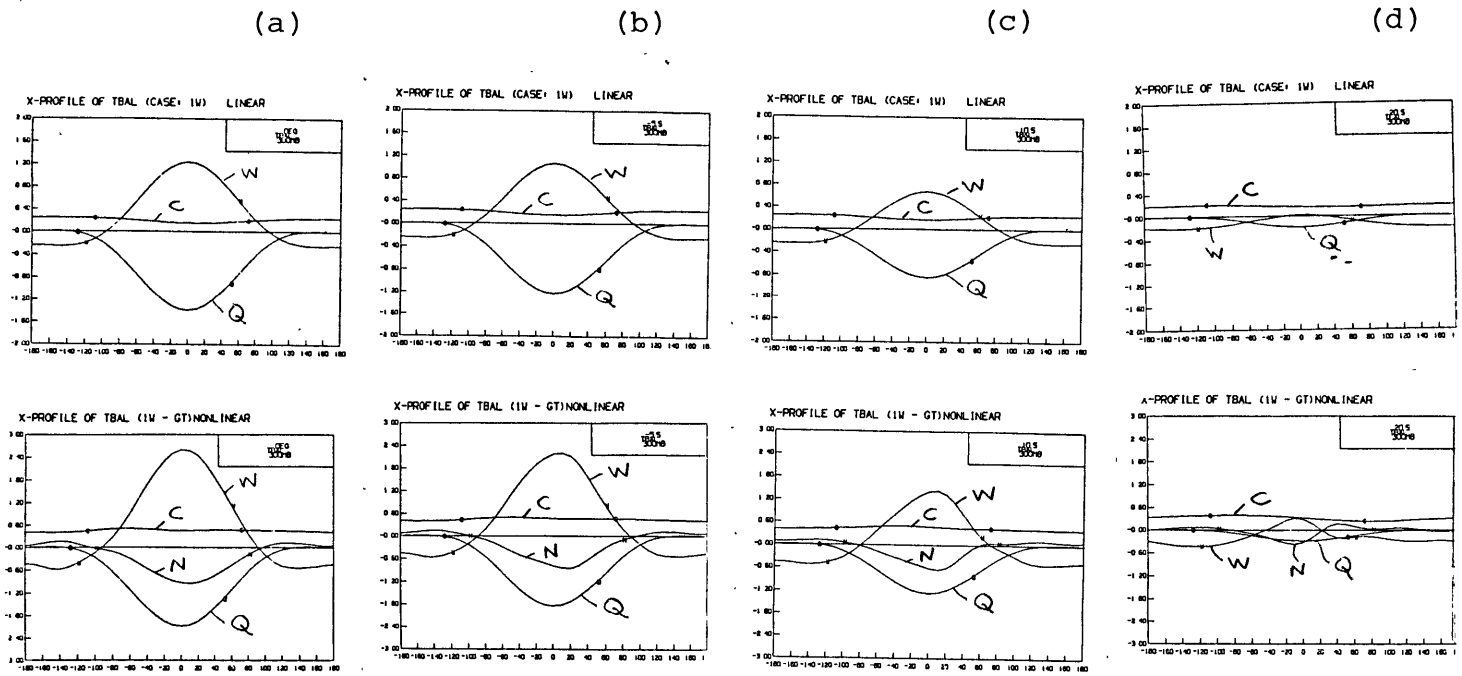
Figure 5.28a　Same as figure 5.26a but for the thermodynamical balances. The labels in the curves read as follows: Q = latent heating, C = Newtonian cooling, W = adiabatic ascent or descent and N = sum of advections.

...

X-PROFILE OF TBAL (CASE: 1W)   LINEAR

X-PROFILE OF TBAL (CASE: 1W)   LINEAR

X-PROFILE OF TBAL (CASE: 1W)   LINEAR

X-PROFILE OF TBAL (CASE: 1W)   LINEAR

X-PROFILE OF TBAL (1W - GT)NONLINEAR

X-PROFILE OF TBAL (1W - GT)NONLINEAR

X-PROFILE OF TBAL (1W - GT)NONLINEAR

X-PROFILE OF TBAL (1W - GT)NONLINEAR
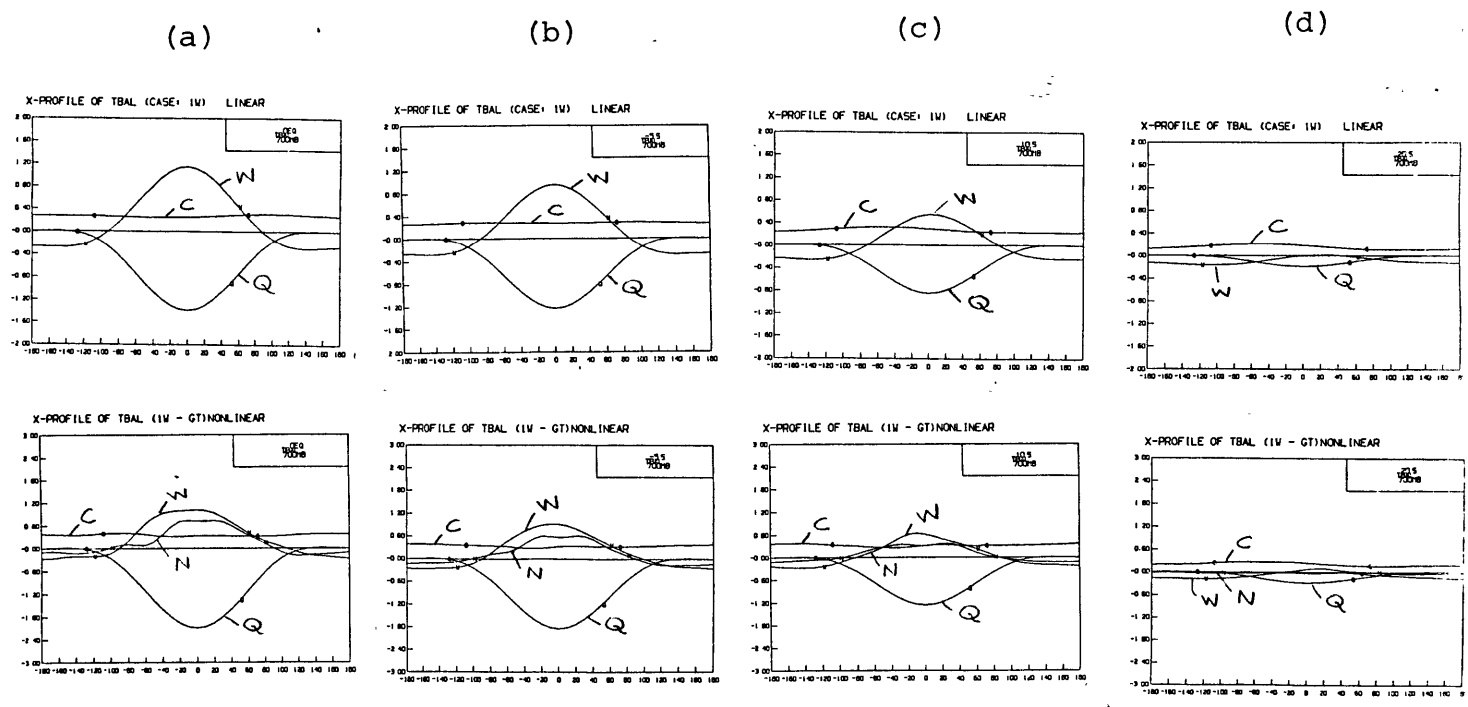
Figure 5.28b   Same as figure 5.28a but at 700 mb.

(a)   (b)   (c)   (d)

X-PROFILE OF UADV (IW - GT)NONLINEAR   X-PROFILE OF UADV (IW - GT)NONLINEAR   X-PROFILE OF UADV (IW - GT)NONLINEAR   X-PROFILE OF UADV (I_ - GT)NONLINEAR

X-PROFILE OF UADV (IW - GT)NONLINEAR   X-PROFILE OF UADV (IW - GT)NONLINEAR   X-PROFILE OF UADV (IW - GI)NONLINEAR   X-PROFILE OF UADV (IW - GT)NONLINEAR
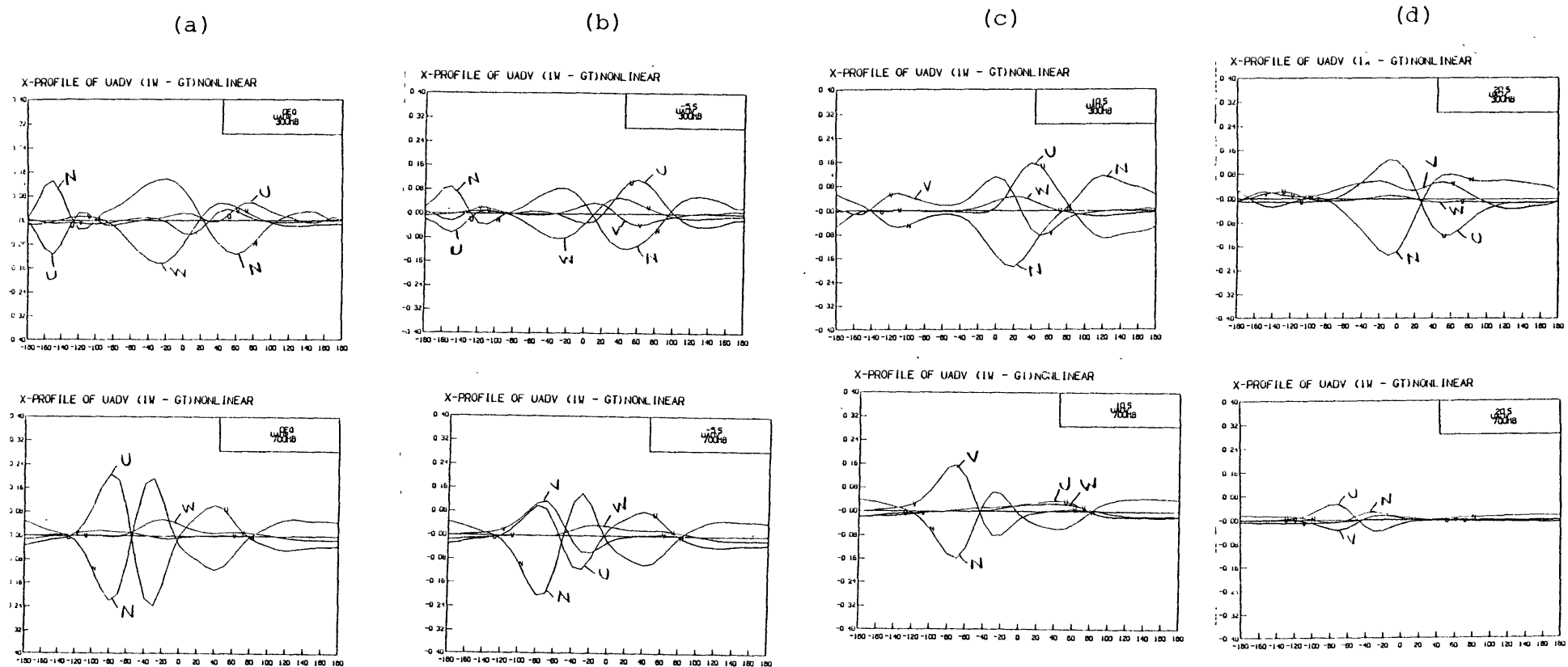
Fig.5.29 Advection of zonal momentum for Case III. Top: 300 mb; bottom: 700 mb. a) EQ, b) 5 S, c) 10 S and d) 20 S. Labels of curves read as follows: U = zonal advection, V = meridional advection, W = vertical advection and N = negative of the sum of the three advections.

(a)   (b)   (c)   (d)

X-PROFILE OF TADV (IW - GT)NONLINEAR

X-PROFILE OF TADV (IW - GT)NONLINEAR

X-PROFILE OF TADV (IW - GT)NONLINEAR

X-PROFILE OF TADV (IW - GT)NONLINEAR

X-PROFILE OF TADV (IW - GT)NONLINEAR

X-PROFILE OF TADV (IW - GT)NONLINEAR

X-PROFILE OF TADV (IW - GT)NONLINEAR

X-PROFILE OF TADV (IW - GT)NONLINEAR
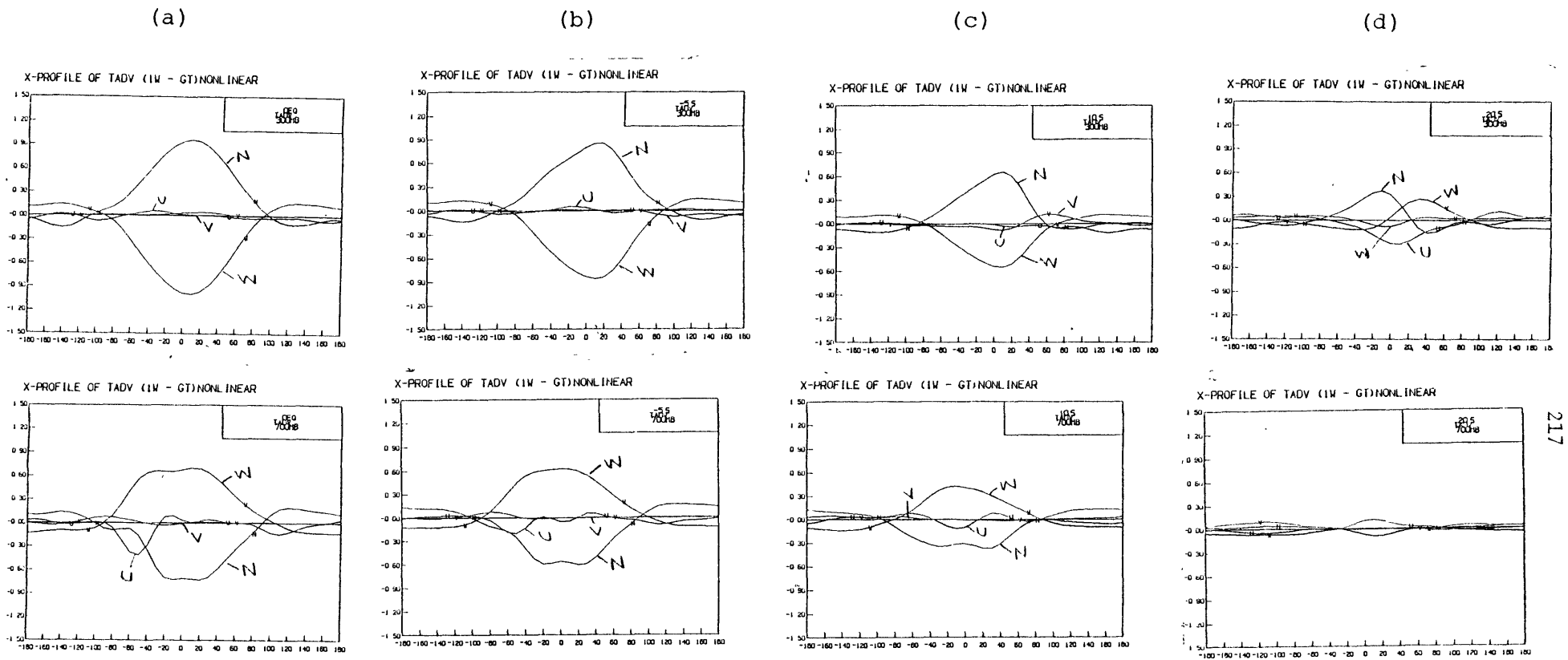
Figure 5.30   Same as figure 5.29 but for the advection of temperature.

(a)   (b)   (c)

CASE I

X-PROFILE OF UBAL (IW-HALF)NONLINEAR   X-PROFILE OF UBAL (IW-HALF)NONLINEAR   X-PROFILE OF UBAL (IW-HALF)NONLINEAR

CASE II

X-PROFILE OF UBAL (CASE: IW)NONLINEAR   X-PROFILE OF UBAL (CASE: IW)NONLINEAR   X-PROFILE OF UBAL (CASE: IW)NONLINEAR

CASE III

X-PROFILE OF UBAL (IW - GT)NONLINEAR   X-PROFILE OF UBAL (IW - GT)NONLINEAR   X-PROFILE OF UBAL (IW - GT)NONLINEAR
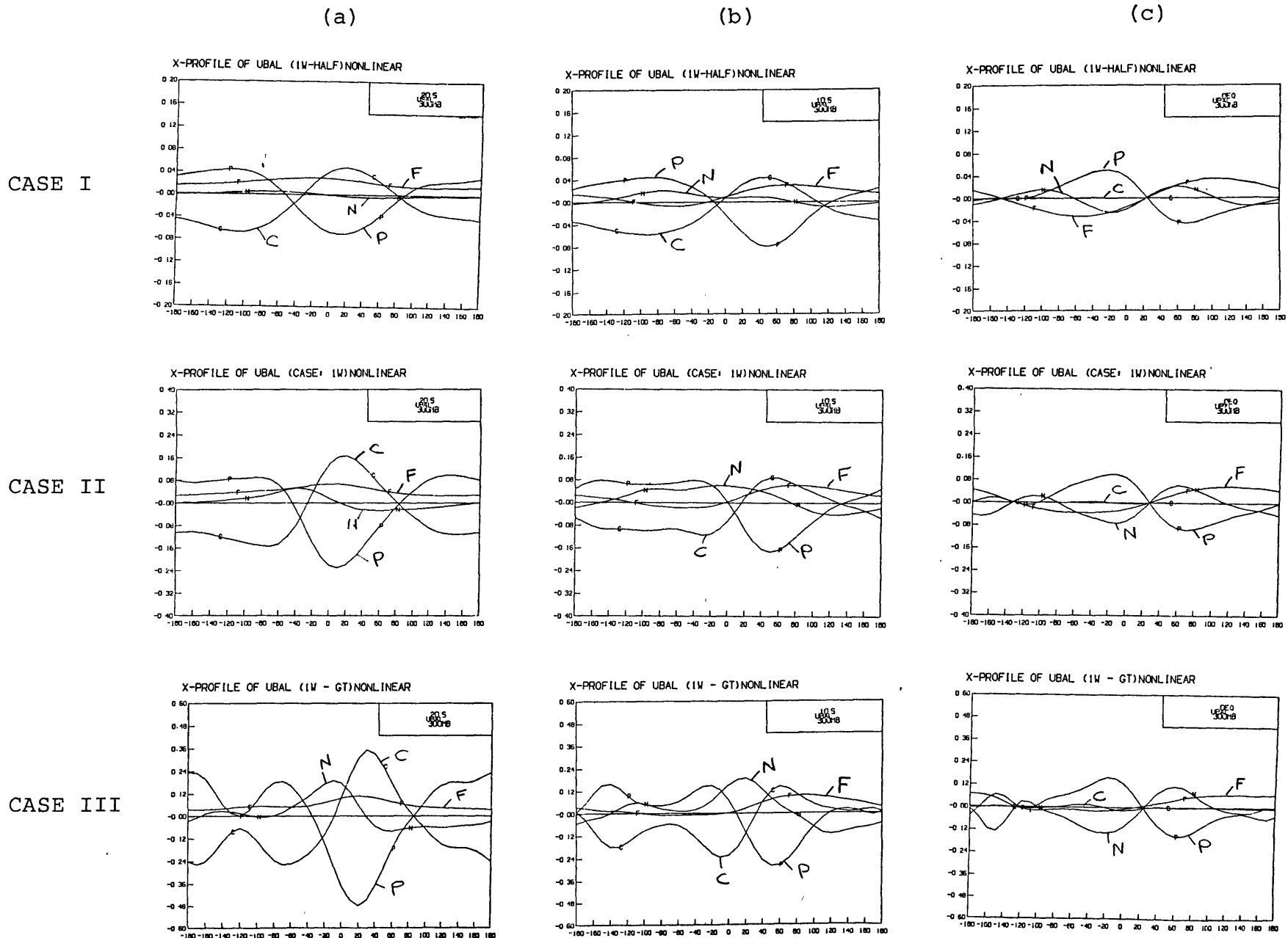
Figure 5.31   Zonal momentum balances for Case I (top), Case II (middle) and
Case III (bottom) at 300 mb. a) 20 S, b) 10 S and c) EQ. Lbels
in curves read as in figure 5.26a.

218

(a)

(b)

(c)

X-PROFILE OF VBAL (1W-HALF)NONLINEAR

X-PROFILE OF VBAL (1W-HALF)NONLINEAR

X-PROFILE OF VBAL (1W-HALF)NONLINEAR

CASE I

X-PROFILE OF VBAL (CASE: 1W)NONLINEAR

X-PROFILE OF VBAL (CASE: 1W)NONLINEAR

X-PROFILE OF VBAL (CASE: 1W)NONLINEAR

CASE II

X-PROFILE OF VBAL (1W - GT)NONLINEAR

X-PROFILE OF VBAL (1W - GT)NONLINEAR
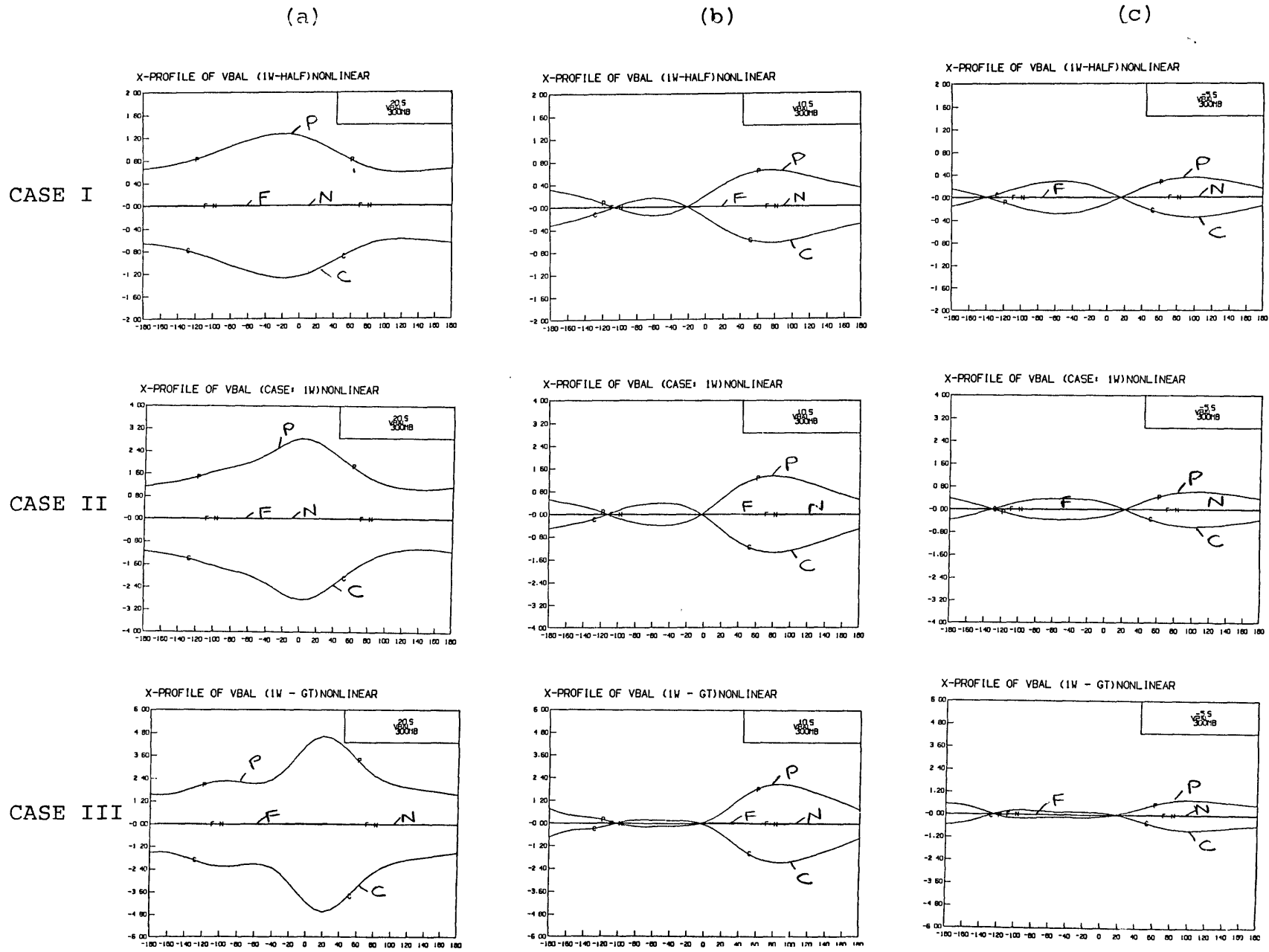
X-PROFILE OF VBAL (1W - GT)NONLINEAR

CASE III

Fig.5.32   Same as figure 5.31 but for the meridional momentum balances. a) 20 S, b) 10 S and c) 5 S. Labels in curves read as in figure 5.26a.

(a)   (b)   (c)

X-PROFILE OF UADV (IW-HALF)NONLINEAR   X-PROFILE OF UADV (IW-HALF)NONLINEAR   X-PROFILE OF UADV (IW-HALF)NONLINEAR

CASE I

X-PROFILE OF UADV (CASE) IW)NONLINEAR   X-PROFILE OF UADV (CASE) IW)NONLINEAR   X-PROFILE OF UADV (CASE) IW)NONLINEAR

CASE II

X-PROFILE OF UADV (IW - GT)NONLINEAR   X-PROFILE OF UADV (IW - GT)NONLINEAR   X-PROFILE OF UADV (IW - GT)NONLINEAR
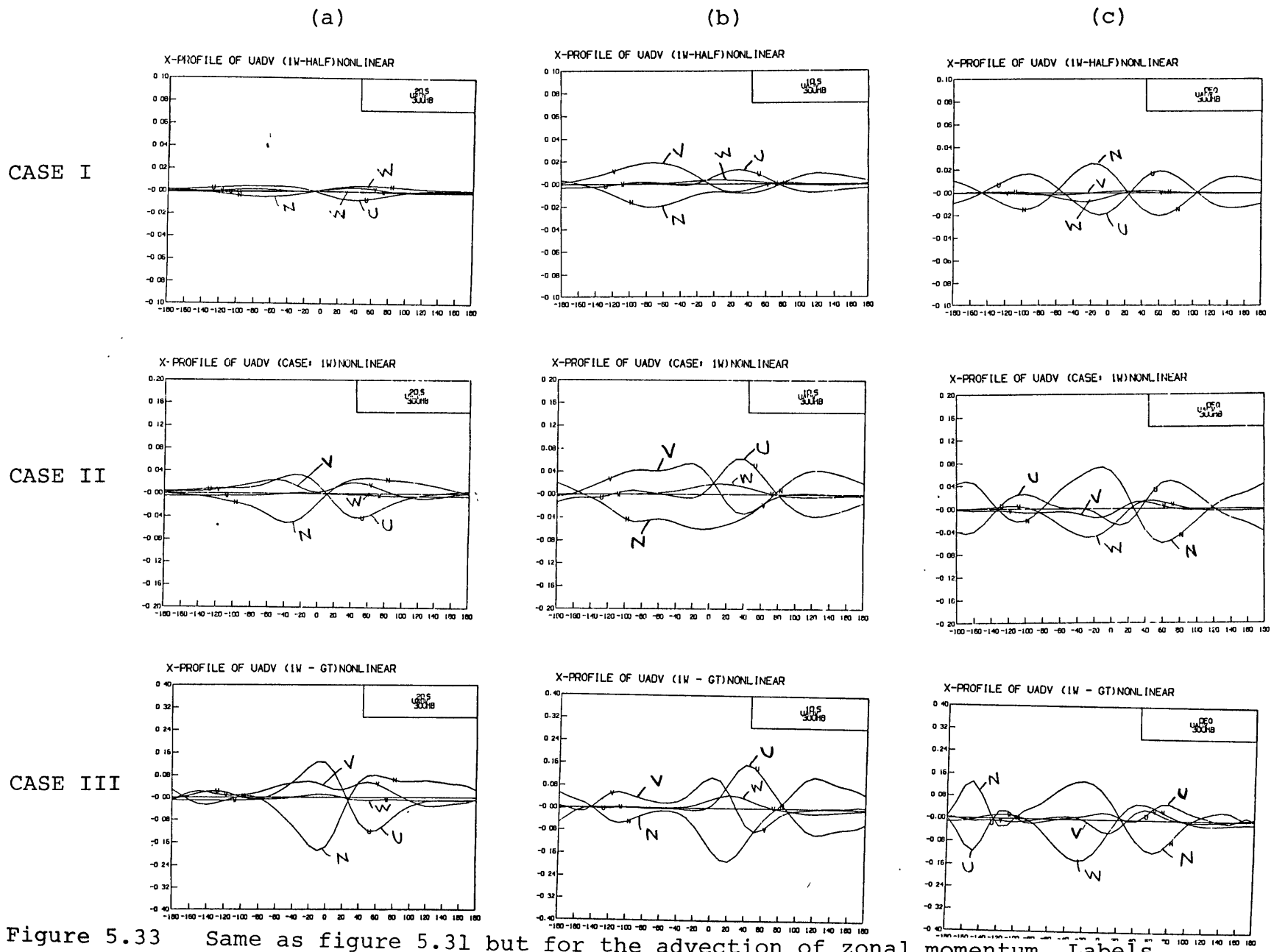
CASE III

Figure 5.33   Same as figure 5.31 but for the advection of zonal momentum. Labels in curves read as in figure 5.29.

For Cases IV and V (three heat sources at the equator), the nonlinear balances display a similar behavior as for the cases with one heat source. The leading balance near the equator in the zonal momentum equation is between advection terms and pressure gradient force. In the meridional momentum equation, the main balance is between pressure gradient and Coriolis forces; that is, the zonal wind is in geostrophic balance throughout most of the domain. Vertical advection of temperature $(w\partial T'/\partial z)$ is the most important nonlinear advection and is large only in the heating region, so the main thermodynamic balance in that region is $(Q_L/C_p) \sim w(S+\partial T'/\partial z)$. Since $\partial T'/\partial z > 0$ at the lower levels and $\partial T'/\partial z < 0$ at the upper levels, the stratifaction increases at the lower levels and decreases at the upper levels.

Also, as in Cases II and III, the upper-level maximum response is seen in the subtropics. In Figure 5.34 we show the meridional momentum equation balances at 20° of latitude away from the equator for Cases IV and V as a function of longitude. The wavenumber 3 response is observed for the linear solution but has small amplitude when compared with the nonlinear solution. Note that the stationary wave pattern becomes more asymmetric in the x-direction, i.e., there is a steeper gradient to the east of the crest than to the west. This seems to be a feature related to the behavior of nonlinear waves.

We now examine the linear and nonlinear balances for Case VI (one heat source at 10°S). In Figure 5.35 we show the zonal momentum equation balances for the linear and nonlinear solutions at 300 mb and 700 mb. Away from the equator in the southern hemisphere, the balances are primarily geostrophic. Frictional and nonlinear terms are small for both upper and lower levels. Near the equator and up to 10°N, the nonlinear terms are

X-PROFILE OF VBAL (CASE: 3W) LINEAR

a

X-PROFILE OF VBAL (CASE: 3WBIG) NONLINEAR

b

X-PROFILE OF VBAL (3W-GT-BIG) NONLINEAR
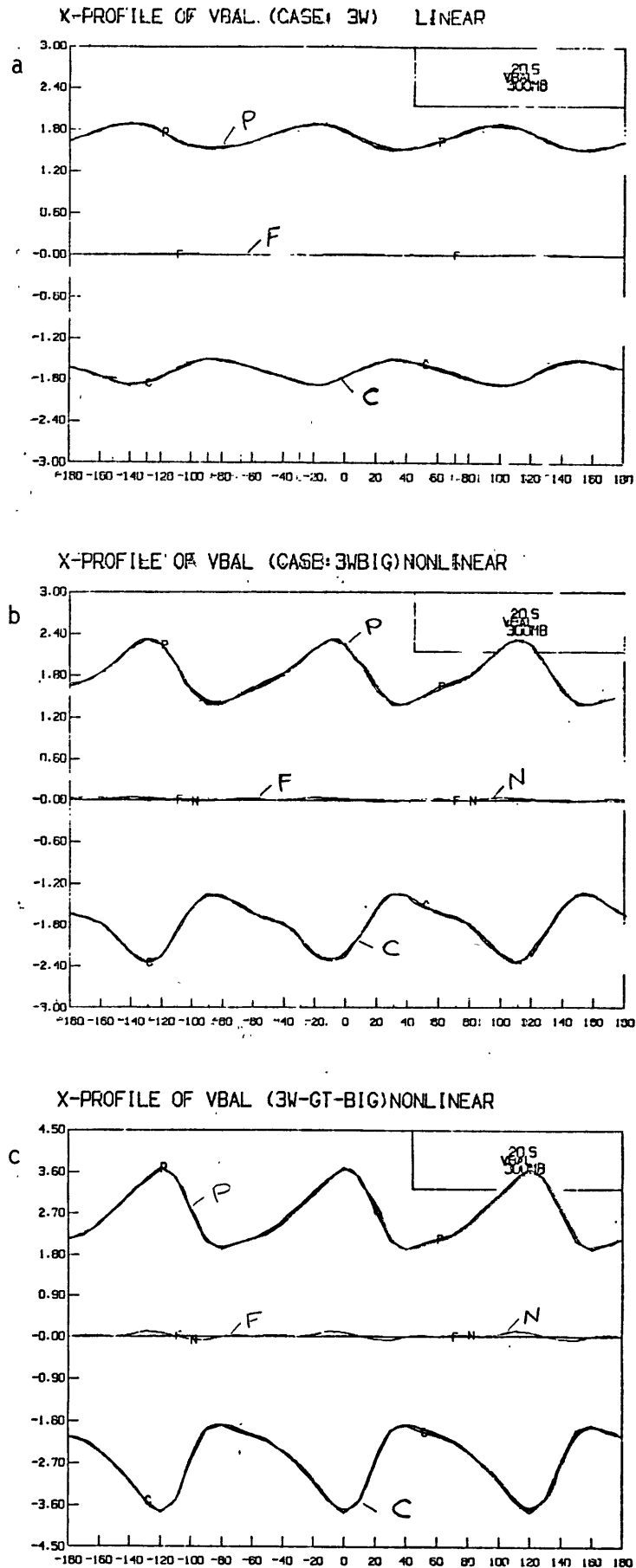
c

Figure 5.34   Meridional momentum balances for Case IV linear (a),
Case IV nonlinear at 20 S.   Labels in curves read
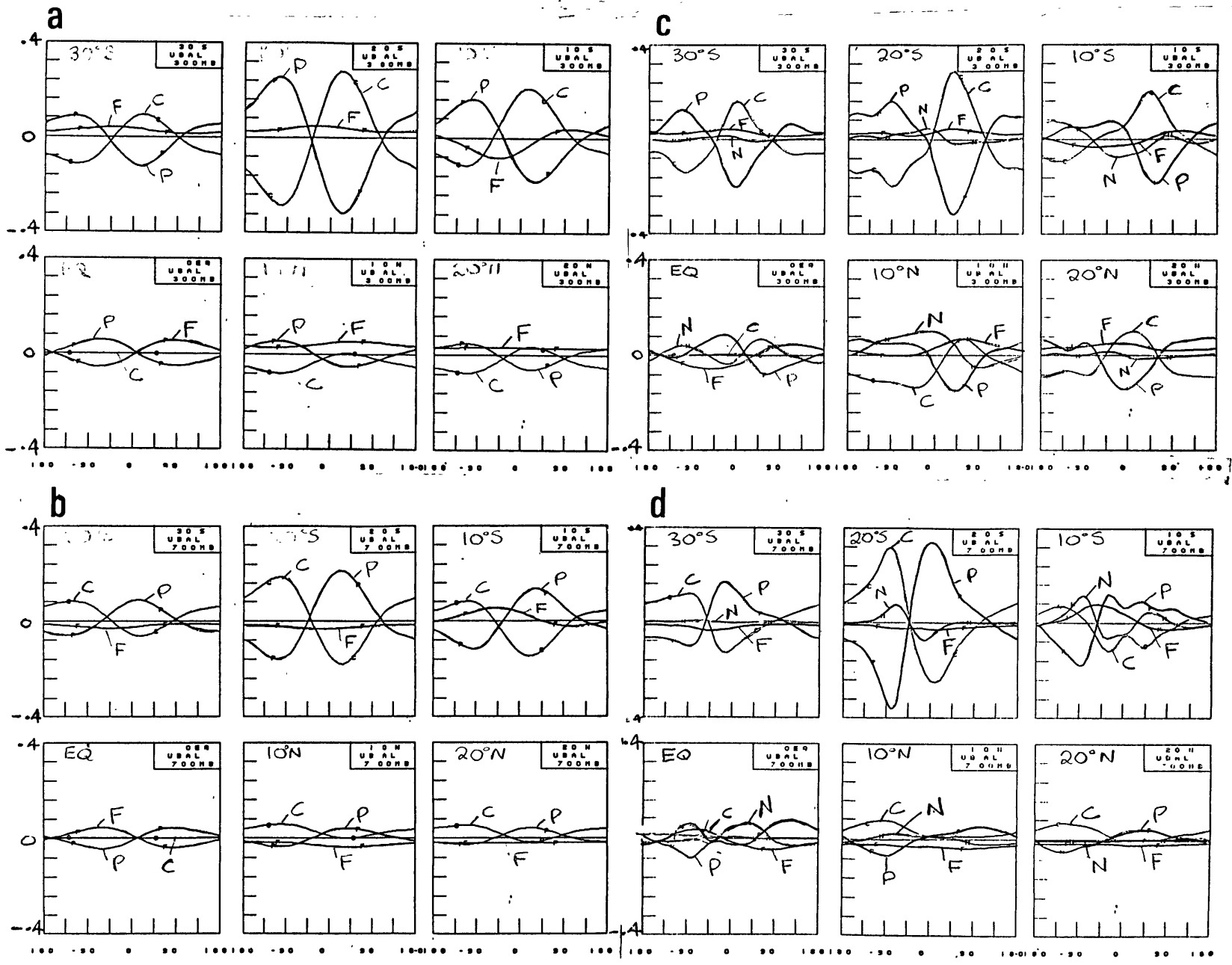as in Figure 5.26a.

Figure 5.35   Zonal momentum balances for Case VI, a) linear at 300 mb, b) linear at 700 mb, c) nonlinear at 300 mb, and d) nonlinear at 700 mb. Labels in curves read as in Figure 5.26a.

about the same magnitude as the other terms and the balances are between Coriolis (except at the equator), pressure gradient, frictional forces, and nonlinear advections. It is interesting to note that the advection terms are comparable to the other forces approximately from 10°S to 10°N (Figure 5.36a). At 10°N and 300 mb, the meridional advection of zonal momentum is the dominant advection term, and at the equator this advection is positive. In Figure 5.37 we show the meridional momentum balances. The balances are geostrophic throughout most of the domain. The nonlinear response, however, differs from the linear one in important respects. At southern latitudes, that is, near the heat source, the upper-level nonlinear response shows a larger wn 1 response. However, it is in the hemisphere opposite to the source that the maximum response is seen. The 300 mb response at 10°N and 20°N departs considerably from the linear solution (compare Figures 5.37a and c). The wn 1 response is significantly larger for the nonlinear case.

Near the equator where the Coriolis force is small, arguments in terms of advections can be invoked to interpret the results. The decrease of the upper-level equatorial easterlies to the west of the heat source, markedly for the cases of strong heating, can be understood in terms of vertical advection of zonal momentum. For Case III, Figure 5.29a (top) shows that the vertical advection of zonal momentum is the leading advection term in the neighborhood of the heat source at the equator. To the west of the heat source, there is strong deposition of westerly momentum; hence, there is weakening of the easterlies. This is mainly due to two factors. First, the vertical wind shear is large to the west of the heat source and second, the upper-level vertical velocity is larger. We recall that the upper-level vertical velocity is larger because vertical advection of heat

makes the temperature lapse-rate more stable for the upper levels. The deposition of easterly momentum in a region of westerlies will decrease the magnitude of the westerlies. The equatorial westerlies to the east of the heat source are decreased approximately 40% in the nonlinear solution when compared to the linear one. To the east of the heat source, there is deposition of easterly momentum which is brought about by vertical and zonal advections. The vertical advection is weaker than the vertical advection to the west of the heat source, which is consistent with the smaller vertical shear of the zonal wind to the east of the heat source.

For the lower levels near the equator, vertical advection of zonal momentum as seen in Figure 5.29a (bottom) is less important. We have seen that this is a result of the vertical velocity being smaller in the source region. The leading advection term is the zonal advection of zonal momentum. The longitudinal structure of this advection at the equator can be used to explain, in a qualitative sense, the narrowing of the region of westerlies to the west of the heat source and their intensification in the nonlinear solution. Figure 5.29a at 700 mb shows a region of strong negative advection of zonal momentum extending from ~ 125°W to ~ 60°W, followed by strong positive advection to ~ 5°E and then weaker negative advection to the east of 5°E. In a simple kinematic sense, we can say that the deposition of easterly momentum at both flanks of the region of westerlies contributes to making the region narrower, and the deposition of westerly momentum within it contributes to its intensification.

For the linear calculations the dynamical balances near the equator are primarily between frictional and pressure gradient forces,

so the nature of the response depends on the formulation of friction, as remarked by Webster (1972). The nonlinear solutions show near-equatorial balances primarily between pressure gradient forces and nonlinear advections, so the precise formulation of friction probably will not affect the results to a great extent, although one should recall that for the free atmosphere Rayleigh friction is too simplified an approximation for momentum dissipation processes. A logical follow-up for this type of study is to test the sensitivity of the response to the formulation of friction, i.e., to take a form of frictional dissipation which better simulates frictional dissipation processes in the real atmosphere, i.e., a formulation of the type $\partial/\partial z \; \nu \; \partial\vec{V}/\partial z$, where the turbulent diffusivity of momentum ν is a function of height and becomes small at the upper levels.
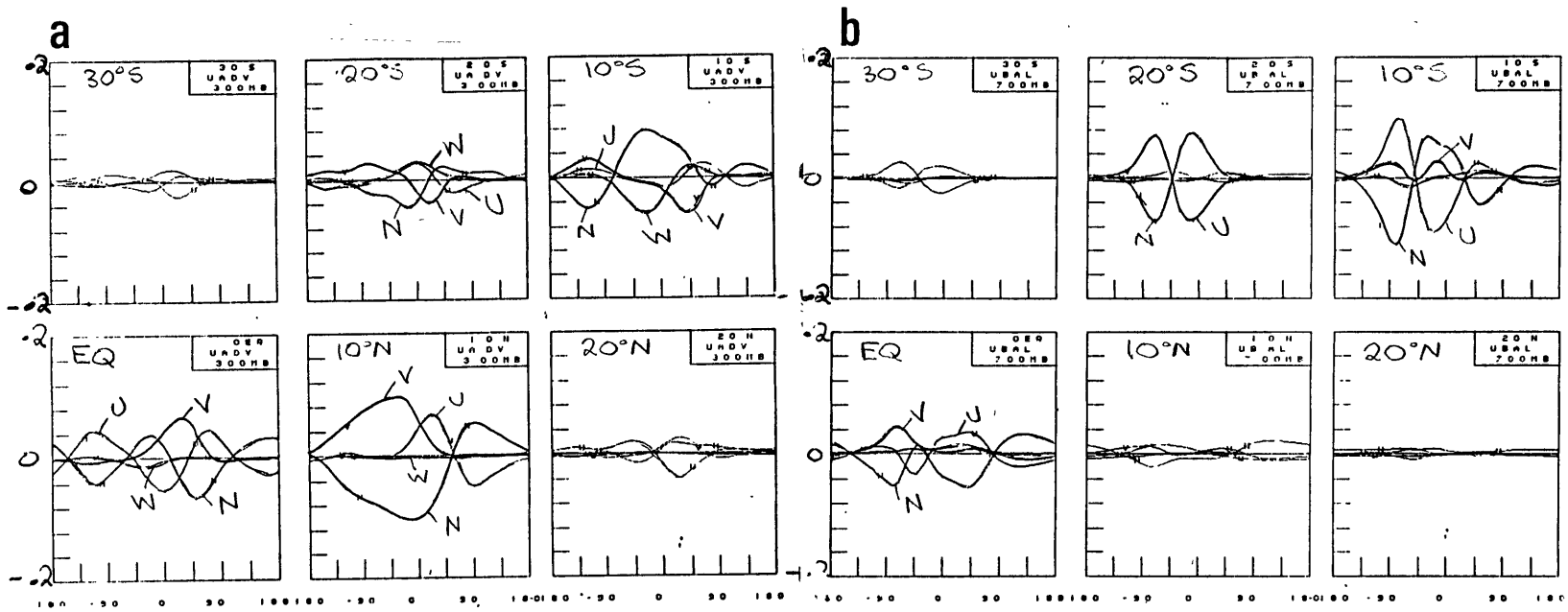
Figure 5.36 Advection of zonal momentum for Case IV, a) at 300 mb and
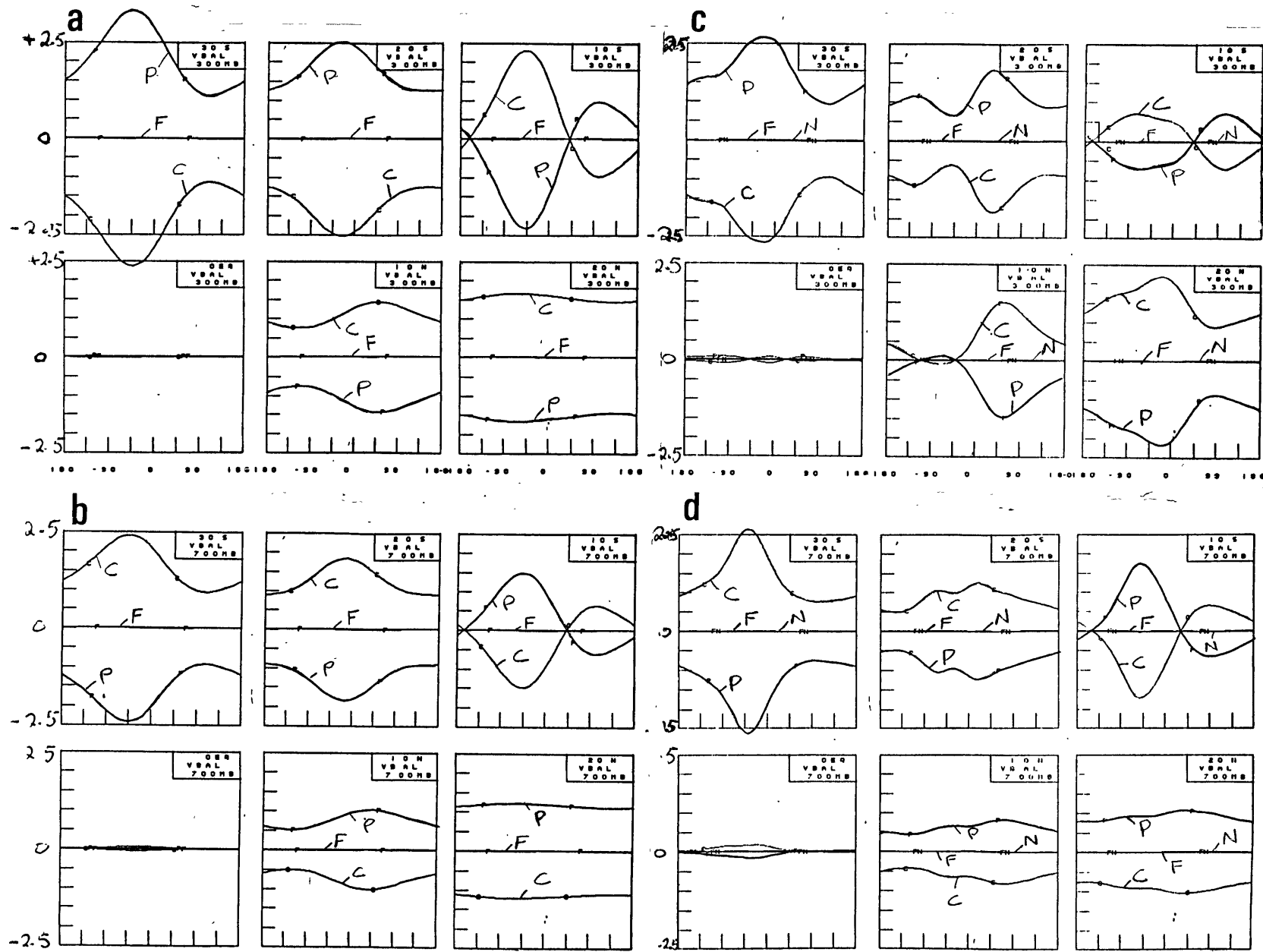b) at 700 mb. Labels in curves read as in Figure 5.29.

Figure 5.37 Meridional momentum balances for Case IV, a) linear at 300 mb, b) linear at 700 mb, c) nonlinear at 300 mb, d) nonlinear at 700 mb. Labels in curves read as in Fig. 5.26a.

228

5.4 COMPARISON OF ZONAL AVERAGES OF A 3-D MODEL WITH THE SOLUTION OF A 2-D MODEL

In this section we will briefly describe zonally averaged solutions for Case III (one intense heat source at the equator). Figure 5.38 shows latitudinal profiles of u, v, w, ϕ, and T' for the following cases: a) zonally averaged linear solution for Case III, b) zonally averaged nonlinear solution for Case III, c) nonlinear solution of a 2-dimensional (latitude × height) version of our model forced by the zonal mean diabatic heating of Case III. The main differences between cases b and c are seen in the fields of [u] and [T']. For case c the zonal winds are similar to the zonal winds for the linear case. Both lower- and upper-level zonal winds have larger magnitudes for case b. Moreover, the temperature departure field is larger at 300 mb for case b than it is for case c. We also point out that the latitudinal gradients of [u] are larger for case c as compared to case b.

The analysis of Figure 5.38 reveals that the zonally averaged 3-dimensional solutions generally resemble the solutions of the 2-dimensional model. However, that should not be taken as a justification for the validity of zonally asymmetric models in explaining the main atmospheric motions in the tropics since the fields from which the zonal averages were formed were highly zonally asymmetric (see Figures 5.10 - 5.13), although it is clear that v and w and consequently the mass transports by the MMC are well predicted by the 2-D model.

The main similarities and differences between the zonally averaged 3-D model solution and the 2-D model solution can be simply understood in terms of the role of the stationary eddies in the zonally averaged solutions of the 3-D model. If the zonally averaged flux divergences by the stationary eddies played no role, we would expect the zonally averaged 3-D model
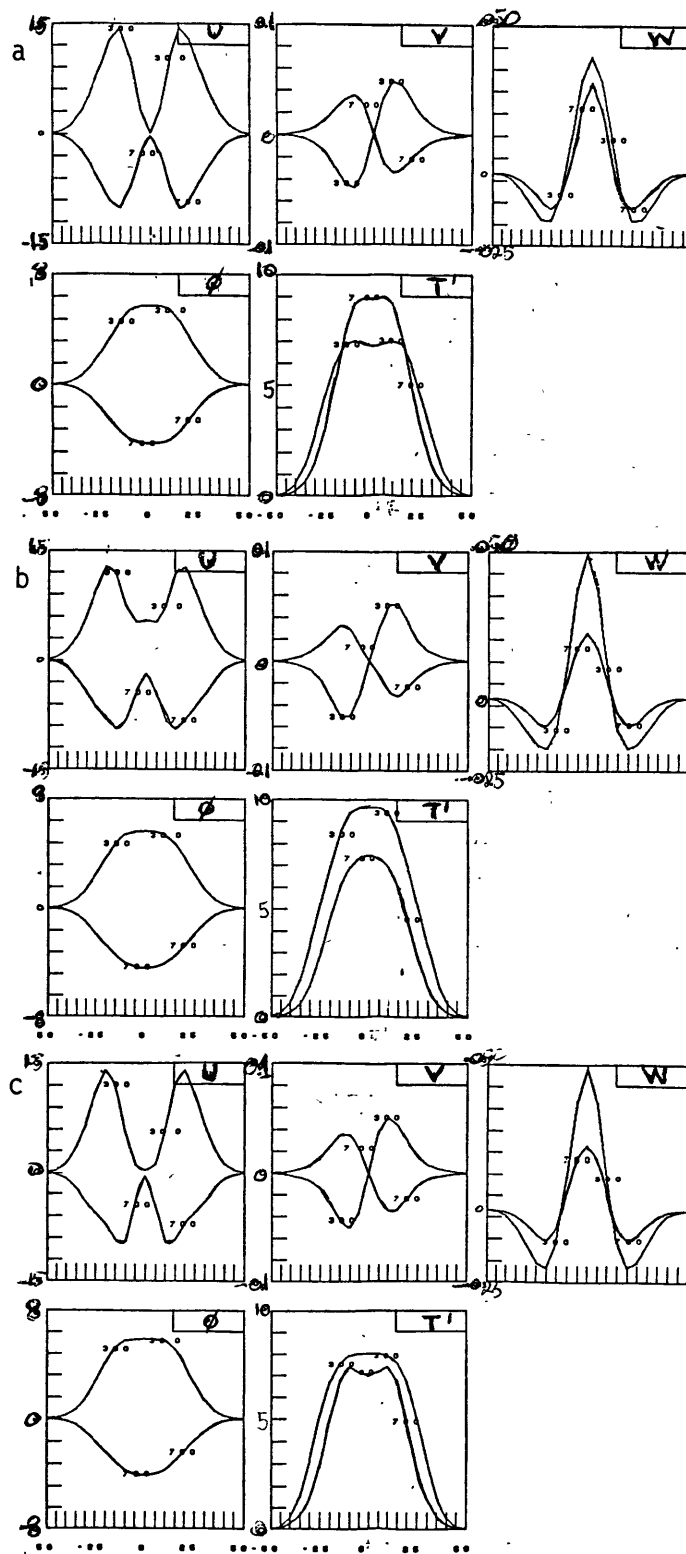
Figure 5.38   Latitudinal profiles of u,v,w,ϕ,and T' for a) zonally
averaged linear solution for Case III, b) zonally averaged
nonlinear solution for Case III, and c) nonlinear solution
of a 2-D version of the model forced by the zonal mean
latent heating of Case III.   Labels in curves read as
follows: 300 = solution at 300 mb, 700 = solution at 700 mb.

solution to be similar to the solution of the 2-D model forced by the zonal mean heating of the 3-D model. Accordingly, we will be looking at the zonally averaged divergences of the meridional and vertical transports of momentum and temperature by the stationary eddies. In the following discussion a square-bracketed quantity refers to the zonal average of the 3-D model solution and a quantity with the subscript 2D refers to the 2-D model solution.

We start by noticing the similarity of [w] and w_{2D} for both lower and upper levels. That can be explained by seeing that at steady-state the leading thermodynamic balances are between the diabatic heating term and adiabatic ascent or descent. To a good approximation the thermodynamic equation can be expressed as

$$S(z) \ w = Q_T/C_p \ .$$

Since this is a linear equation it immediately follows that [w] and w_{2D} will be similar, which is readily seen in Figure 5.38b and c. Using this conclusion and the linearity of the zonally averaged continuity equation, it also follows that [v] ~ v_{2D} as seen in Figures 5.38b and c for the meridional wind. These simple linear arguments cannot be applied to the zonal momentum equation because the 3-D model balances are nonlinear and terms of the type $\partial[v^*u^*]/\partial y$ and $\partial[w^*u^*]/\partial z$ may be different than zero. Hence, if one takes these flux divergences of zonal momentum as forcing terms in a 2-D model, then the generated zonal winds should be similar to the zonally averaged zonal winds of the 3-D model. From Figure 5.29 for the longitudinal profiles of the advection of zonal momentum we can estimate the magnitude of these fluxes. For the upper levels near the equator, Figure 5.29a (top) reveals that the zonal average of the vertical advection of zonal momentum will be nontrivial, seeing that wu_z is not

zonally symmetric; and it can be seen that $-[w^*u^*]_z$ will be positive so the stationary eddies are depositing westerly momentum; this explains why $[u]$ is westerly and larger than u_{2D} near the equator. Following the same type of analysis for Figure 5.29d (top) at 20°S (close to the latitude of maximum $[u]$), we conclude that $-[v^*u^*]_y$ is negative, which means deposition of easterly momentum at those latitudes; this would tend to decrease the magnitude of the maximum $[u]$. Indeed the maximum $[u]$ is 1.26 in nondimensional form, whereas the maximum u_{2D} is 1.39.

5.5 SCALE ANALYSIS

In this section we will use the FGGE data for Jan-Feb 1979 analyzed in Chapter 2 to estimate the magnitudes of the terms of the zonal and meridional momentum equations at upper tropospheric levels in order to obtain an idea about the predominant planetary-scale dynamical balances and assess the relative importance of nonlinear terms. We will perform this calculation at 2 different latitudes, at $\approx 5°$ of latitude within a typical region of tropical heating, and away from the equator at $\approx 20°N$.

5.5.1 ZONAL MOMENTUM EQUATION AT 200 mb

The following values taken from the FGGE data analysis will be used in estimating the magnitudes of terms of the zonal momentum equation.

A) Near equatorial balances ($\sim 5°$)   B) Balances away from the equator ($\sim 20°N$)

$u \approx 5 - 10$ m/s	$u \approx 20 - 25$ m/s
$v \approx 2 - 3$ m/s	$v \approx 5$ m/s
$w \approx 5\times10^{-4} - 10^{-3}$ mb/s	$w \approx 10^{-4}$ mb/s
$\Delta_h u \approx 10$ m/s	$\Delta_h u \approx 15$ m/s
$\Delta_z u \approx 5 - 10$ m/s	$\Delta_z u \approx 10$ m/s
$\Delta x \approx 4\times10^6$ m	$\Delta x \approx 4\times10^6$ m
$\Delta y \approx 1\times10^6$ m	$\Delta y \approx 1\times10^6$ m
$\Delta p \approx 300$ mb	$\Delta p \approx 300$ mb
$\Delta t \approx 3\times10^6$ s	$\Delta t \approx 3\times10^6$ s
$\Delta_x \phi \approx 20$ m	$\Delta_x \phi \approx 100$ m

where Δ_h, Δ_x and Δ_h represent typical horizontal, longitudinal, and vertical variations of a variable, respectively, and TE, given below, is a crude estimate of the flux divergences by the transient eddies obtained from Figures 2.26 ($\overline{u'v'}$) and 2.28 ($\partial[\overline{u'v'}]/\partial y$) and from maps of $\overline{u'}^2$ (not shown here).

Vertical derivatives are estimated for the layer from 500 mb to 200 mb. Friction is assumed to be small.

The results in 10^{-5} m/s^2 are as follows:

$$\frac{\partial \overline{u}}{\partial t} + \overline{u}\,\frac{\partial \overline{u}}{\partial x} + \overline{v}\,\frac{\partial \overline{u}}{\partial y} + \overline{\omega}\,\frac{\partial \overline{u}}{\partial p} = f\overline{v} - \frac{\partial \overline{\phi}}{\partial x} + \overline{F}_X + TE \qquad [5.1]$$

A ($\sim 5°$)   (0.25)   (2)   (2.5)   (3)   (3)   (5)   (small)   (1)

B ($\sim 20°$N)   (0.75)   (8.5)   (7.5)   (0.5)   (25)   (25)   (small)   (7)

5.5.2 MERIDIONAL MOMENTUM EQUATION AT 200 mb

The same procedure used for the zonal momentum equation is now utilized to estimate the magnitude of the terms of the meridional momentum equation. The following values are used:

A) Near equatorial balances ($\sim 5°$)   B) Balances away from the equator ($\sim 20°$N)

A) Near equatorial balances ($\sim 5°$)	B) Balances away from the equator ($\sim 20°$N)
$u \approx 5 - 10$ m/s	$u \approx 20 - 25$ m/s
$v \approx 2 - 3$ m/s	$v \approx 5$ m/s
$w \approx 5 \times 10^{-4} - 10^{-3}$ mb/s	$w \approx 10^{-4}$ mb/s
$\Delta_h v \approx 3 - 5$ m/s	$\Delta_h v \approx 5 - 10$ m/s
$\Delta_z v \approx 3$ m/s	$\Delta_z v \approx 5$ m/s
$\Delta x \approx 4 \times 10^{6}$ m	$\Delta x \approx 4 \times 10^{6}$ m
$\Delta y \approx 10^{6}$ m	$\Delta y \approx 1.5 \times 10^{6}$ m
$\Delta p \approx 300$ mb	$\Delta p \approx 300$ mb
$\Delta t \approx 3 \times 10^{6}$ s	$\Delta t \approx 3 \times 10^{6}$ s
$\Delta_y \phi \approx 15$ m	$\Delta_y \phi \approx 200$ m

where Δ_y is a typical latitudinal variation of a variable.

The results in 10^{-5} m/s^2 are as follows:

$$\frac{\partial \overline{v}}{\partial t} + \overline{u}\frac{\partial \overline{v}}{\partial x} + \overline{v}\frac{\partial \overline{v}}{\partial y} + \overline{\omega}\frac{\partial \overline{v}}{\partial p} = -\overline{fu} - \frac{\partial \overline{\phi}}{\partial y} + \overline{F}_y + TE \qquad [5.2]$$

A) (~5°) (0.08) (0.8) (1.0) (1.0) (10) (14) (small) (0.5)

B) (~20°N) (0.17) (2.5) (3.5) (0.2) (120) (130) (small) (5)

5.5.3 THERMODYNAMIC EQUATION AT EQUATORIAL LATITUDES

The results for the thermodynamical balances (not shown here) indicate that dominant balance is between diabatic heating and adiabatic expansion or contraction. This result is similar to the one obtained by Cornejo-Garrido and Stone (1977) studying the heat balance of the Walker circulation. This balance was already evident in Figure 2.14 (Chapter 2) in which the longitudinal profiles of diabatic heating and vertical velocity were shown.

5.5.4 COMPARISON OF THE SCALE ANALYSIS WITH THE MODEL'S RESULTS

We seek here only qualitative similarities and differences between typical balances in the real atmostphere and balances produced by the nonlinear model. Given the simplified nature of the model, accurate quantitative agreement is not expected.

The meridional momentum balances (Eq. [5.1]) show that the zonal wind is approximately in geostrophic balance even near the equator. This result is in very good agreement with the nonlinear model results (see Figure 5.27a). Estimates of the flux convergences by the transient eddies

indicate that these are at least one order of magnitude smaller than the main geostrophic balance. Advection of meridional momentum is one order to two orders of magnitude smaller than the Coriolis force.

Eq. [5.1] for the zonal momentum balances reveals that the nonlinear terms are comparable in magnitude to the other terms. Away from the equator, vertical advection is smaller but horizontal advections are of the same order of magnitude as the Coriolis and geopotential terms. This is in agreement with the model's results (for instance, compare with Figures 5.26a (bottom) and 5.29 (top)).

In terms of the magnitudes of the dynamical balances, the cases with intense heat sources (Cases III and V) bear a closer association with the magnitudes revealed by this scale analysis.

As mentioned before, the main thermodynamical balance between diabatic heating and adiabatic ascent or descent is well represented by the model, as can be seen in Figures 5.28 and 5.30.

CHAPTER 6

SUMMARY, DISCUSSION AND CONCLUDING REMARKS

To substantiate and emphasize the relevance of zonal asymmetries in the tropical forcing and circulation, we reviewed a selected set of observations and previous observational studies. We also analyzed a subset of FGGE data for SOP-1 (January 5 to March 5, 1979) attempting to identify zonal asymmetries in the thermal forcing and relate them to the observed asymmetries in the circulation. Precipitation and cloudiness asymmetries were seen to be linked to the continents straddling the equator and in the western Pacific, possibly related to warmer SST's. The degree of precipitation was shown to be greater for the tropical southern hemisphere during southern summer due to the larger longitudinal land-sea contrast. Also, it was seen that the position of the precipitation maximum within a tropical continent moves in a SE-NW orientation from southern summer to northern summer and vice-versa. It was suggested that such orientation is related to the establishment of the northern hemisphere summer monsoonal circulations or, in the last instance, to north-south land-sea contrasts, with a tropical continent lying north of an equatorial ocean.

The scale and intensity of the latent heat sources were seen to have considerable geographical dependence. The Indonesian-western Pacific heat source is broad and intense. The heat sources over South America and Africa are generally more localized, where the former is a strong heat source comparable in strength to the Indonesian heat source while the latter is somewhat weaker, except for West Africa during northern summer monsoon.

The atmospheric circulation in the tropics was observed to depart significantly from zonal symmetry. Lower and upper-level equatorial westerlies and easterlies at the same latitude are a persistent feature of the climatological tropical flow, as are the semi-permanent subtropical highs. The upper level centers of anticyclonic circulation over the tropical continents appear to be associated with the heat source and located to the west and polewards from where precipitation is maximum. It was also seen that the sea level isobars are more parallel to latitude circles in the winter hemisphere. We also remarked that the subtropical jet stream of the northern hemisphere upper troposphere shows a wavenumber 3 structure with three regions of maximum wind speed during northern winter contrasting with the southern hemisphere subtropical jet stream during southern winter which presents less zonal structure. It was suggested that this may be related to the tropical heat sources being more zonally asymmetric during northern winter than what they are during southern winter.

The velocity potential and streamfunction fields were analyzed. The divergent part of the wind provided a clear picture of thermally direct, large-scale mass overturnings in the tropics. The rotational and divergent components of the wind were seen to attain comparable magnitudes in the tropics. Major areas of divergent motions at the upper level were observed over South America and the Indonesian-western Pacific region during southern summer and a quite strong divergent circulation centered over the Southeast Asian monsoon region during northern summer. Convergent upper-level motions were observed over the subtropical oceans and deserts. North-south mass overturnings were seen to be confined to the longitudes of the heat source and comparable in strength to the east-west circulations.

The position of the upper air easterlies and lower-level westerlies in the tropics was seen to bear correspondence with the westward branch of the Walker-type circulation, i.e., divergent winds being easterlies at the upper levels and westerlies at the lower level. <u>The general level of agreement found seems to indicate that the planetary-scale, stationary asymmetric circulations in the tropics are predominantly forced by condensational heating.</u>

The main asymmetric heating of the tropical atmosphere is due to the latent heating of condensation in deep cumulus clouds, which can be locally quite intense. Seasonal precipitation rates higher than 10 mm/day are observed over broad areas in the tropical continents. The intensity and relative short scale of the tropical latent heat sources along with the increasingly ageostrophic balances near the equator are likely to make the effect of nonlinearities important. The highly asymmetric nature of thermal forcing and circulation in the tropics, which is related to the uneven distribution of land masses, suggests that one should try to examine the effects of such asymmetric forcing and its influence on the time-mean circulation, primarily when we recognize that the mechanisms that determine the long-term circulation in the tropics are not well-known. In this work we investigated the nonlinear response of the tropical atmosphere to large-scale, stationary, zonally asymmetric diabatic heating sources that arise primarily due to the localized character of precipitation over tropical continents. In previous theoretical studies of tropical circulations forced by isolated heat sources, the effects of advection of momentum and temperature were not taken into account except by considering, in some studies, the effects of zonal advection by a constant mean wind.

Although we cannot rule out the influence of the midlatitude baroclinic eddies on the tropical motions, it appears reasonable to examine the tropical atmosphere response to forcing which is located within the tropics and to separate it from midlatitude forcing. Therefore, the effects of the baroclinic eddies are suppressed. Also, we do not include the effects of topography although we recognize that the Andes and Tibetan Plateau are likely to exert a major influence on the tropical and extra-tropical circulations.

For the purpose of examining the tropical atmosphere's response to isolated heat sources, we developed two models. The first model is a simple semi-analytic linear model which is used to study the linear response to changes in the structure and position of the heat sources. The second model is a 5-layer, primitive equation nonlinear model used to assess the importance of nonlinearities. Equatorial β-plane geometry, used in both models, seems justifiable in view that the model's main forcing, i.e., cumulus heating, decays rapidly away from the equator in the subtropics and also that midlatitude baroclinic eddies were not considered.

The choice of structure and intensity of the distributions of diabatic heating was guided by observations. To a first approximation the horizontal scale of a diabatic heating source over a tropical continent is given by the continent's dimensions. This is probably true for the heating sources over South America, Africa and the Indonesian Archipelago. As mentioned above, the large precipitation rates over the western Pacific are likely related to large-scale convergence patterns associated with warmer SST's. In this respect it is probable that the heat sources over oceans are more dependent on the dynamics of the large-scale flow and on the

underlying surface conditions than are heat sources over continents. Tropical continental rainfall seems to be less dependent on large-scale convergence than does equatorial oceanic rainfall. Local evapotranspiration seems to provide an important moisture source for precipitation over forested surfaces, and several studies estimate that up to 65% of the tropical rainfall over continents originates from evapotranspiration. The latitudinal scale of the tropical heat sources over continents is not related only to its meridional dimensions. If a continent extends into middle and high latitudes, the high rainfall area associated with cumulus precipitation will not extend to those latitudes. The meridional scale of these heat sources is directly related to solar radiation forcing, thereby an appropriate scale is given by the solar declination, i.e., of the order of 23° of latitude.

In Chapter 3 we used simple arguments based on the linearized equations to explain certain features of the linear model solution, such as the changes in the position and intensity of lows and highs, and the relative magnitudes of the zonal and meridional winds when the latitudinal position and horizontal scale of the heat source were changed. Also, we studied the sensitivity of the response to changes in friction and mean winds. For mean easterly winds the solution is equatorially confined, whereas for mean westerly winds there is meridional propagation and the response away from the equator is large. This result is qualitatively similar to the results on meridional propagation of Rossby waves obtained by Hoskins and Karoly (1981), and Simmons (1982) using more sophisticated models.

Linear and nonlinear solutions were compared in Chapter 5 for a number of cases in which the forcing was changed. In some cases only the

intensity of the heat source was changed; in others, the number of heat sources and in one case the heat source was placed away from the equator. When the intensity of the heat sources was changed, the nature of the solution for the nonlinear cases changed considerably when compared to the linear case. For weak heating rates the linear and nonlinear response are very similar. When realistic heating rates were prescribed, the nonlinear model produced upper level maximum winds that not only were higher in magnitude as compared to the linear model winds but more importantly were found in the subtropics away from the latitude of maximum heating, whereas for the linear model maximum winds were found at the latitude of maximum heating. East-west asymmetry, a feature which was already seen in the linear model, becomes more pronounced in the nonlinear solution with stronger and more confined lower-level westerlies to the west of the heat source. The comparison of linear and nonlinear balances revealed that advection terms are important. Near the equator, zonal and meridional advection of zonal momentum is significant as well as vertical advection of temperature in the source region. Linearly, the standing wave pattern associated with the heat source is confined to the equatorial regions, whereas for the nonlinear case the influence of the heat source is clearly seen in the subtropics. The results of our model provide some indication that nonlinearities are necessary to simulate some features of the planetary-scale, time-mean atmospheric motions in the tropics which are not present in linear models.

We summarize the most important results of our model as follows:

● The linear model is able to simulate to the zeroth order some major features of the time-mean tropical circulation such as continental lows in association with heat sources and subtropical highs in association with

heat sinks. For a reasonable distribution of asymmetric heat sources representing typical southern hemisphere heating during the summer, there is some success in simulating the general distribution of easterlies and westerlies in the tropics.

● One of the most remarkable results of the nonlinear model is that for realistic heating rates it produces upper-level maximum zonal winds in subtropical latitudes and to the east and polewards of the heat source, a feature not seen in linear models, which produce maximum zonal winds at the latitude of maximum heating. This seems to provide a zeroth order explanation for the location and longitudinal structure of the subtropical jet stream. The model's position for the wind maxima does not agree well with the observed position of the wind maximum of the jet stream off the east coast of North America, which is found to the northwest of the tropical heat source over South America for northern winter. However, we are not taking into account in our model the effect of topography, which would tend to change the phase of the stationary wave and also the effect of transient disturbances forced by the strong midlatitude temperature gradient. The observed position of the other two wind speed maxima is to the north/northeast of the tropical heat sources over Africa and Indonesia.

● The nonlinear model's low-level zonal winds show considerable east-west asymmetry with confined westerlies to the west of the heat source and easterlies elsewhere. In the real atmosphere, low-level easterlies cover most of the tropics, and the regions of westerlies such as those over the Indian Ocean are more confined .

● Zonally averaged solutions of the nonlinear 3-D model are, in general, similar to solutions of a nonlinear 2-D (latitude × height) model

and the differences are due to the role of the stationary eddies. However, the fields we are zonally averaging are highly asymmetric so it is not justifiable to think of the tropical circulations as being mostly axially symmetric.

• Scale analysis of the dynamical and thermodynamical equations based on FGGE data showed good qualitative agreement with the nonlinear model's results indicating that the zonal wind is in geostrophic balance even near the equator, nonlinear terms are important in the zonal momentum equation, and the main thermodynamical balances are between diabatic heating and adiabatic ascent or descent.

We have neglected the effects of the transient eddies in our model. In Chapter 2 we have shown that the zonal momentum flux divergences associated with the transient eddies have magnitudes which are comparable to the magnitudes of the advections by the time-mean circulation. From the global distribution of $\overline{u'}^2$ (not shown here) for Jan-Feb 1979, one can see that there is significant convergence of the zonal transport of zonal momentum by the transient eddies to the west of the jet stream wind speed maxima off the east coast of North America, i.e., acceleration of the westerlies, and divergence of this flux to the east of the wind speed maximum and consequent deceleration of the westerlies. Thereby it appears that the transient eddies play a role in determining the longitudinal position of this jet stream wind speed maximum. Figure 2.28 for the zonally averaged meridional divergence of zonal momentum by the transient eddies at 200 mb indicates that in general the transient eddies are depositing easterly momentum throughout the tropics and subtropics, and since westerlies are predominant in this region, they are taking westerly momentum away. A rough estimate of a dissipation time scale is simply

given by the time it would take for the transient eddies to reduce the westerly wind to zero. At 20°N (approximate latitude of maximum meridional flux divergences by the transient eddies) the rate momentum is being dissipated by the transient eddies is $\approx 3.5 \times 10^{-5}$ m/s^2 and $[u] \approx 25$ m/s, giving a dissipation time scale of ≈ 8 days. At equatorial latitudes the flux divergences by the transient eddies are much smaller but so is the zonal wind. A typical value of the flux divergence is $\approx 0.50 \times 10^{-5}$ m/s^2 and $[u] \approx 3$ m/s, yielding a dissipation time scale of ≈ 7 days. In a very rudimentary way, one may think of Rayleigh friction in the model as a representation of the dissipative effects of the transient eddies at the upper levels. However, in this crude approximation we are not taking into account the detailed horizontal structure of the transient eddies flux divergences. Its longitudinal variations act as sinks and sources of westerly momentum at the upper levels whereas the Rayleigh friction acts only as a momentum sink. It would be interesting to see how the results of our nonlinear model would be modified by considering the transient eddies flux divergences as forcing terms of the momentum equations and also by considering a more realistic formulation of momentum dissipation processes.

Gill (1980) suggested that the observed east-west asymmetry in the Walker circulation may be due to the different propagation properties of equatorial waves with faster Kelvin waves to the east of the heat source and slower Rossby waves to the west, so the region of easterlies is larger than the region of westerlies. We have seen that nonlinearities make the east-west asymmetry even more pronounced. In Gill's linear model and in our nonlinear model, however, there was almost no zonal asymmetry in the heat sinks, which were given by a simple linear damping law. It is likely

that in the real atmosphere there are zonal variations in diabatic heating sinks such as radiative cooling and sensible heating. Associated with the heat sources there is upward motion and downward motion associated to heat sinks so that the east-west scale of the Walker-type circulations might be determined by the scale of the forcing. The eastern part of the subtropical ocean basins might provide just such a heat sink. For those regions precipitation and thus latent heating is very low, usually cloudless skies add to the radiative losses of the atmosphere, and the cold underlying ocean acts as a sensible heating sink for the atmosphere. Topography is another factor which is not taken into account in these simple models and which would almost certainly influence the east-west circulation. For instance, the high topographical barrier provided by the Andes, extending north-south to the west of the Amazonian heat source, would block the westerly return flow to the source region and thereby affect the east-west asymmetry.

Another important question that arises in connection with tropical heat sources is the relationship between tropical precipitation and the underlying surface, whether ocean, forested land, or bare land. Are forested surfaces more active in providing the conditions for the observed copious rainfall over tropical continents or are they just passively responding to high precipitation and consequently high soil moisture content that would be high even in the absence of the rainforest? There have been a number of attempts to assess the effects of changes in soil moisture and albedo using GCM's, but the results have been inconclusive probably due to imperfections in the physical parameterizations of ground hydrology and PBL processes (Shukla and Mintz, 1981; see Mintz, 1982, for a review on the subject). The question of whether tropical deforestation

would cause a change in tropical precipitation and in which direction is far from being settled. The soil-forest-atmosphere system is a complex interactive biological system which probably does not respond to the surface heat budget in simple ways. Lettau et al. (1979) have estimated that up to 60% of tropical rainfall over the Amazon region comes from local evapotranspiration; this would point to the need for better knowledge of the energy and moisture exchange over a tropical rainforest.

The interannual variability of tropical and extra-tropical large-scale circulations may be related to the interannual variability of the heat sources since the zonally asymmetric heat sources seem to be an important determinant of time-mean planetary circulations. Improved observations and better models will be needed in order to capture and understand the interannual variablity of the circulation.

REFERENCES

Abramowitz, M. and I. A., Stegan, 1965: Handbook of Mathematical Functions, Dover, 1046 pp.

Arakawa, A. and W. H. Schubert, 1974: Interaction of a cumulus cloud ensemble with the large scale environment, I, J. Atmos. Sci., 31, 674-701.

Baker, W. E., D. Edelmann, M. Iredell, D. Han, and S. Jakkempudi, 1981: Objective analysis of observational data from the FGGE observing systems, NASA Tech. Memo. 82062, 132 pp. NTIS N81226237.

Bjerknes, J., 1966: A possible response of the atmospheric Hadley circulation to equatorial anomalies of ocean temperature, Tellus, 18, 820-829.

_____, 1969: Atmospheric teleconnections from the equatorial Pacific, Mon. Wea. Rev., 97, 163-172.

Brenner, S., 1981: A study of the moving flame effect in three dimensions and its implications for the general circulation of the upper atmosphere of Venus, Ph.D. Thesis, M.I.T.

Bushbridge, I. W., 1948: Some integrals involving Hermite polynomials, J. London Math. Soc., 23, 135-141.

Charney, J. G. and A. Eliassen, 1949: A numerical method for predicting the perturbations of the middle latitudes westerlies, Tellus, 1, 38-54.

_____, 1971: Tropical cyclogenesis and the formation of the intertropical convergence zone. Mathematical Problems in Geophysical Fluid Dynamics, W. H. Reid, ed., Lectures in Applied Mathematics, vol. 13, Amer. Math. Soc., 355-368.

Cornejo-Garrido, A. G. and P. H. Stone, 1977: On the heat balance of the Walker circulation, J. Atmos. Sci., 34, 1155-1162.

Crawford, S. L. and T. Sasamori, 1981: A study of the sensitivity of the mean meridional circulation to sources of heat and momentum, Tellus, 33, 340-350.

Derome, J. and A. Wiin-Nielsen, 1971: The response of a middle-latitude model atmosphere to forcing by topography and stationary heat sources, Mon. Wea. Rev., 99, 564-576.

Dickinson, R. E., 1971a: Analytic model for zonal winds in the tropics: I. Details of the model and simulation of gross features of the zonal mean troposphere, Mon. Wea. Rev., 99, 501-510.

_____, 1971b: Analytic model for zonal winds in the tropics: II. Variations of the tropospheric mean structure with season and differences between hemispheres, Mon. Wea. Rev., 99, 511-523.

Egger, J., 1976a: The linear response of a hemispheric two-level primitive equation model to forcing by topography, Mon. Wea. Rev., 104, 351-364.

_____, 1976b: On the theory of steady perturbations in the troposphere, Tellus, 28, 381-389.

_____, 1977: On the linear theory of the atmospheric response to sea surface temperature anomalies, J. Atmos. Sci., 34, 603-614.

Eliassen, A., 1949: The quasi-static equations of motion with pressure as independent variable, Geofys. Publ., 17, No. 3, 44 pp.

Geisler, J. E., 1981: A linear model of the Walker circulation, Mon. Wea. Rev., 38, 1390-1400.

Gill, A. E., 1980: Some simple solutions for heat-induced tropical circulations, Quart. J. Roy. Meteor. Soc., 106, 447-462.

Godbole, R. V. and J Shukla, 1981: Global Analysis of January and July Sea Level Pressure, GSFC/NASA, Maryland.

Halem, M., E. Kalnay, W. E. Baker, and R. Atlas, 1982: An assessment of the FGGE satellite observing system during SOP-1, Bull. Amer. Meteor. Soc., 63, 407-426.

Held, I. M. and A. Y. Hou, 1980: Nonlinear axially symmetric circulations in a nearly inviscid atmosphere, J. Atmos. Sci., 37, 515-529.

Holton, J. R., 1978: The dynamic meteorology of the stratosphere and mesosphere, Am. Met. Soc., Boston, MA, 218 pp.

Horel, J. D. and J. M. Wallace, 1981: Planetary-scale atmospheric phenomena associated with the Southern Oscillation, Mon. Wea. Rev., 109, 813-829.

Hoskins, B. J. and D. J. Karoly, 1981: The steady linear response of a spherical atmosphere to thermal and orographic forcing, J. Atmos. Sci., 38, 1179-1196.

Houze, R. A., Jr., 1973: A climatological study of vertical transports by cumulus-scale convection, J. Atmos. Sci., 30, 1112-1123.

Isaacson, E. and H. B. Keller, 1966: Analysis of Numerical Methods, Wiley, 541 pp.

Jaeger, L., 1976: Monatskarten des Niederschlags fur die Ganze Erdie, Berichte des Deutschen Wetterdienstes 18 no. 139, Im Selbstverlag des Deutschen Welterdienstes, Offenbach, West Germany.

Johnson,, D. R. and R. D. Townsend, 1981: Diagnostics of the heat sources and sinks of the Asiatic monsoon and the thermally-forced planetary scale response, Proc. Int. Conf. on Preliminary FGGE Results, Bergen, Norway, WMO, 523-533.

Julian, P. R. and R. M. Chervin, 1978: A study of the Southern Oscillation and Walker circulation phenomenon, Mon. Wea. Rev., 106, 1433-1451.

Kalnay-Rivas, E. and M. E. Halem, 1981: Large amplitude stationary Rossby waves in the Southern Hemisphere. International Results on FGGE and its Monsoon Experiment, WMO, 3-5 to 3-15.

Katayama, A., 1964: On the heat budget of the troposphere over the Northern Hemisphere, Ph.D. thesis, Tohaku University, Japan.

Krishnamurti, T. N., 1961: The subtropical jet stream of winter, J. Meteor., 18, 172-191.

_____, 1971: Tropical east-west circulations during the northern summer, J. Atmos. Sci., 28, 1342-1347.

_____, N. Kanamitsu, W. J. Koss, and J. D. Lee, 1973: Tropical east-west circulations during the northern winter, J. Atmos. Sci., 30, 780-787.

Krueger, A. F. and J. S. Winston, 1974: A comparison of the flow over the tropics during two contrasting circulation regimes, J. Atmos. Sci., 31, 358-370.

Lau, K. and H. Linn, 1982: Thermally-driven motions in an equatorial β-plane: Hadley and Walker circulations during the winter monsoon, Mon. Wea. Rev., 110, 336-353.

Lettau, H., K. Lettau, and L. C. B. Molion, 1979: Amazonia's hydrological cycle and the role of atmospheric recycling in assessing deforestation effects, Mon. Wea. Rev., 107, 227-238.

Lindzen, R. S., E. S. Batten, and J.-W. Kim, 1968: Oscillations in atmospheres with tops, Mon. Wea. Rev., 96, 133 - 140.

Matsuno, T., 1966: Quasi-geostrophic motions in the equatorial area, J. Met. Soc. Japan, 44, 25-43.

Mintz, Y., 1982: The sensitivity of numerically simulated climates to land-surface boundary conditions, NASA Tech. Memo No. 83985, 81 pp.

Moura, A. D. and J. Shukla, 1981: On the dynamics of droughts in Northeast Brazil: Observations, theory and numerical experiments with a general circulation model, J. Atmos. Sci., 38, 2653-2675.

Newell, R. E., 1979: Climate and the ocean, Amer. Sci., 67, 405-416.

_____, J. W. Kidons, D. G. Vincent, and G. J. Boer, 1972: The General Circulation of the Tropical Atmosphere and Interaction with Extratropical Latitudes, Vols. I and II, M.I.T. Press, 258 pp. and 371 pp.

Oort, S. A., 1982: Global Atmospheric Circulation Statistics, 1958-1973, NOAA Professional Paper, U.S. Government Printing Office, Washington, DC (in preparation).

Orzag, S. A., 1980: Spectral methods for problems in complex geometries, J. Comp. Physics, 37, 70-92.

Otto-Bliesner, B. L. and D. R. Johnson, 1982: Thermally-forced mean mass circulations in the Northern Hemisphere, Mon. Wea. Rev., 110, 916-932.

Paegle, J. and W. E. Baker, 1982: Planetary-scale characteristics of the atmospheric circulation during January and February 1979, J. Atmos. Sci., 39, 2522-2538.

Pedlosky, J., 1979: Geophysical Fluid Dynamics, Springer-Verlag, 624 pp.

Puri, K. and W. Bourke, 1974: Implication of horizontal resolution in spectral model integrations, Mon. Wea. Rev., 102, 333-347.

Pushistov, P. Yu., 1973: Results of numerical modeling of the stationary zonal circulation of the atmosphere in the equatorial region, Izv., Atmospheric and Oceanic Physics, 9, 219-234.

Ramage, C. S., 1968: Role of a tropical "maritime continent" in the atmospheric circulation, Mon. Wea. Rev., 96, 365-370.

Riehl, H., 1979: Climate and Weather in the Tropics, Academic Press, 611 pp.

Sanders, F., 1975: Synoptic Meteorology, class notes, Dept. of Meteorology, M.I.T.

Schneider, E. K. and R. S. Lindzen, 1977: Axially symmetric steady-state models of the basic state for instability and climate studies. Part I: Linearized calculations, J. Atmos. Sci., 34, 262-279.

_____, 1977: Axially symmetric steady-state models of the basic state for instability and climate studies. Part II: Nonlinear calculations. J. Atmos. Sci., 34, 280-296.

Shapiro, R., 1970: Smoothing, filtering and boundary effects, Rev. Geophys. Space Physics, 8, 359-387.

Shukla, J. and Y. Mintz: The influence of land surface evapotranspiration on the Earth's climate, Science, 215, 1498-1501.

Shukla, J., D. Strauss, D. Randall, and Y. Sud, 1981: Winter and summer simulations with GLAS climate model, NASA Tech. Memo. No. 83866, 282 pp.

Simmons, A. J., 1982: The forcing of stationary wave motions by tropical diabatic heating. Quart. J. Roy. Met. Soc., 108, 503-534.

Smagorinsky, J., 1953: The dynamic influence of large-scale heat sources and sinks on the quasi-stationary mean motions of the atmosphere, Quart. J. Roy. Met. Soc., 79, 342-366.

Stockenius, T., 1981: Interannual variations of tropical precipitation patterns, Mon. Wea. Rev., 109, 1233-1247.

Susskind, J., J. Rosenfield, D. Reuter, and M. T. Chahine, 1982: The GLAS physical inversion method for analysis of HIRS 2/MSU sounding data, NASA Tech. Memo. No. 84936, 181 pp.

U. S. Department of Commerce and U. S. Air Force, 1971: Global atlas of relative cloud cover, 1967-1970 based on data from meteorological satellites, Washington, DC, 235 pp.

Van de Boogaard, H., 1977: The mean circulation of the tropical atmosphere - July, NCAR TN-118 + STR (41 pp), Boulder, CO.

Virji, H., 1979: Summer circulation over South America from satellite data, Ph.D. thesis, University of Wisconsin, Madison, WI.

Webster, P. J., 1972: Response of the tropical atmosphere to local steady forcing, Mon. Wea. Rev., 100, 518-541.

_____, 1981: Mechanisms determining the atmospheric response to sea surface temperature anomalies, J. Atmos. Sci., 38, 554-571.

_____, 1982: Seasonality in the local and remote atmospheric response to sea surface temperature anomalies, J. Atmos. Sci., 39, 41-52.

_____ and J. R. Holton, 1982: Low latitude and cross-equatorial response to middle-latitude forcing in a zonally varying basic state, J. Atmos. Sci., 39, 722-733.

Zebiak, S., 1982: A simple atmospheric model of relevance to El Nino, J. Atmos. Sci., 39, 2017-2027.

APPENDIX A

DECOMPOSITION OF THE FORCING OF CHAPTER 3 INTO FOURIER SERIES

In Chapter 3 we make use of idealized forcings whose basic x-structure is shown in Figure A.1. The resulting forcing will be a linear combination of such half-cosine functions given by

$$f(x) = A \cos \frac{\pi}{2d} (x-b)$$

[A.1]

where A is the amplitude 2d the width, and b is the displacement of the forcing from the center.
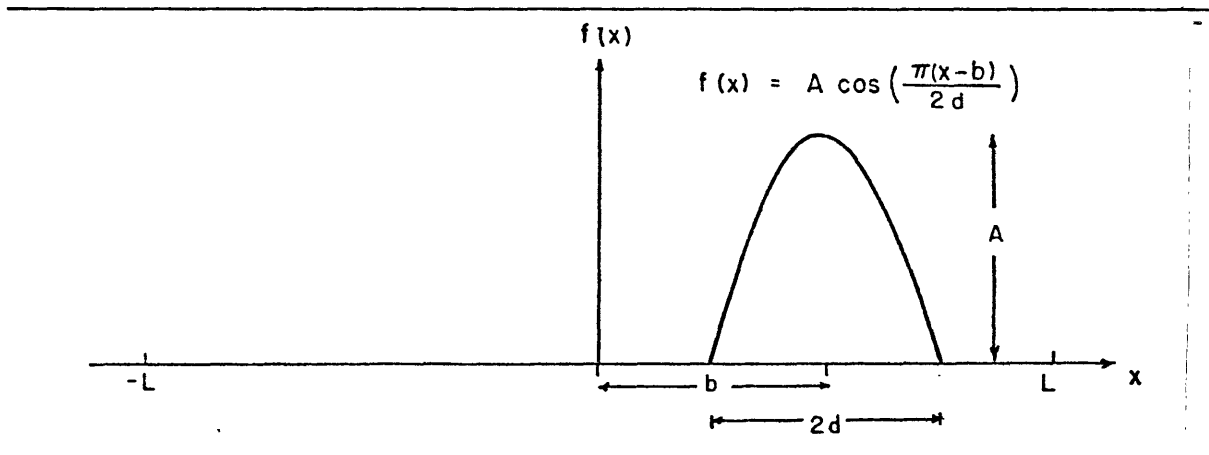
Figure A.1 Basic X-Structure of Idealized Forcing

We want to obtain the expansion in Fourier series of the function f(x), i.e.,

$$f(x) = \frac{Ao}{2} + \sum_{m=0}^{\infty} [A_n \cos(\frac{n\pi x}{L}) + B_n \sin(\frac{n\pi x}{L})]$$

[A.2]

where

$$A_n = \frac{1}{L} \int_{-L}^{L} f(x) \cos(\frac{n\pi x}{L}) \, dx$$

[A.3]

and

$$B_n = \frac{1}{L} \int_{-L}^{L} f(x) \sin(\frac{n\pi x}{L}) \, dx. \qquad\qquad [A.4]$$

After substitution of $f(x)$ in [A.3] and [A.4] and upon integration, we obtain the following expressions for the Fourier coefficients:

$$A_n = \frac{4Ad}{\pi L} \frac{1}{[1 - (n\frac{2d}{L})^2]} \cos(\frac{\pi bn}{L}) \cos(\frac{\pi dn}{L}) \qquad \text{if } n \neq \frac{L}{2d} \qquad [A.5]$$

$$A_n = \frac{Ad}{L} \cos(\frac{\pi d}{2d}) \qquad\qquad \text{if } n = \frac{L}{2d} \qquad\qquad [A.6]$$

$$B_n = -\frac{8A}{\pi} (\frac{d}{L})^2 \frac{n}{[1 - (n\frac{2d}{L})^2]} \sin(\frac{\pi bn}{L}) \cos(\frac{\pi dn}{L}) \qquad \text{if } n \neq \frac{L}{2d} \quad [A.7]$$

$$B_n = \frac{Ad}{L} \sin(\frac{\pi b}{2d}) \qquad \text{if } n = \frac{L}{2d} \qquad\qquad [A.8]$$

Table A.1 below presents the values of the Fourier coefficients for the x-structures of the forcing functions utilized in Chapter 3 corresponding to Figure A.2a, A.2b and A.2c. The series is truncated at N = 15.

TABLE A.1

Fourier Expansion Coefficients of Functions of Figure A.2

n	Figure A.2a		Figure A.2b		Figure A.2c	
	A_n	B_n	A_n	B_n	A_n	B_n
0	-	-	-	-	-	-
1	0.12263	-	-	-	-	-
2	0.11694	-	-0.18671	-	-	-
3	0.10931	-	-0.26009	-	0.48017	-
4	0.10000	-	-0.13086	-	-	-
5	0.08940	-	0.07558	-	-	-
6	0.07795	-	0.16667	-	0.25000	-
7	0.06603	-	0.08272	-	-	-
8	0.05406	-	-0.06114	-	-	-
9	0.04244	-	-0.11614	-	0.16837	-
10	0.03154	-	-0.05169	-	-	-
11	0.02164	-	0.04084	-	-	-
12	0.01300	-	0.06770	-	0.09701	-
13			0.02592	-	-	-
14			-0.02067	-	-	-
15			-0.02722	-	0.03880	-
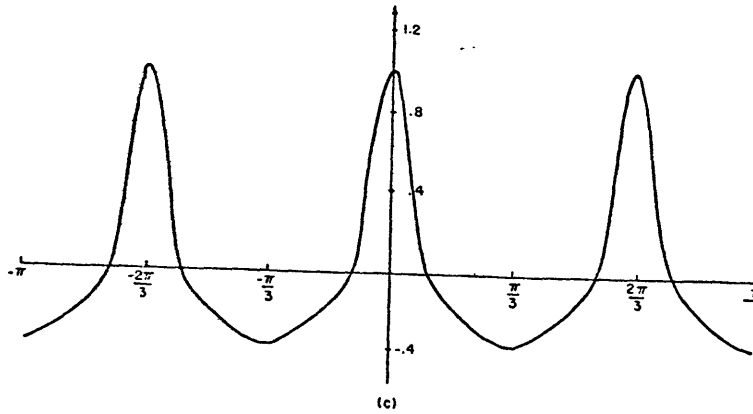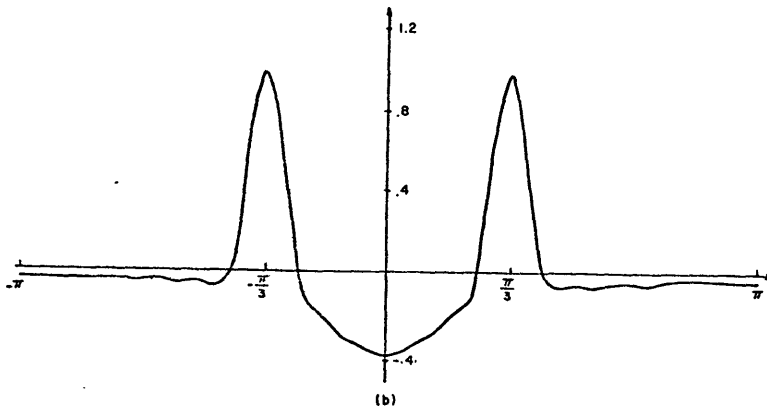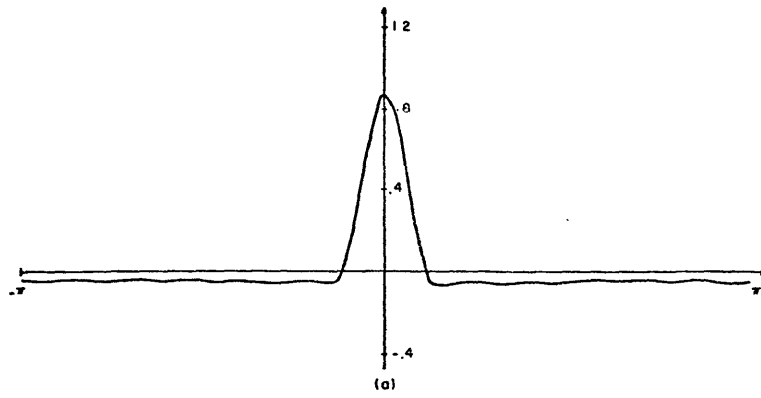
Figure A.2 X-Structures of Forcing. One Heat Source (a), 2 Heat Sources

(b), and 3 Heat Sources (c)

APPENDIX B

SUMMARY OF PROPERTIES OF HERMITE FUNCTIONS AND POLYNOMIALS

Definition of Normalized Hermite Function (see Abramowitz and Stegun, 1965):

$$\Psi_n(x) = \frac{H_n(x)\ e^{-x^2/2}}{(2^n\ n!\ \pi^{1/2})^{1/2}}$$ [B.1]

where $H_n(x)$ is the Hermite polynomial of order n. The first five normalized Hermite Functions are shown in Figure B.1.

Definition of Hermite Polynomial:

$$H_n(x) = (-1)^n\ e^{x^2}\ \frac{d^n}{dx^n}\ (e^{-x^2})$$ [B.2]

Hermite Polynomials H_0 through H_8

$H_0 = 1$

$H_1 = 2x$ $H_5 = 32x^5 - 160x^3 + 120x$

$H_2 = 4x^2 - 2$ $H_6 = 64x^6 - 48x^4 + 700x^2 - 120$

$H_3 = 8x^3 - 12x$ $H_7 = 128x^7 - 1344x^5 + 3360x^3 - 1680x$

$H_4 = 16x^4 - 48x^2 + 12$ $H_8 = 256x^8 - 3584x^6 + 13440x^4 - 13440x^2 + 1680$

[B.3]

Recursion Relations for Hermite Polynomials

$$xH_n = \frac{1}{2} H_{n+1} + nH_{n-1}$$ [B.4]

$$\frac{dH_n}{dx} = 2n\ H_{n-1}$$ [B.5]
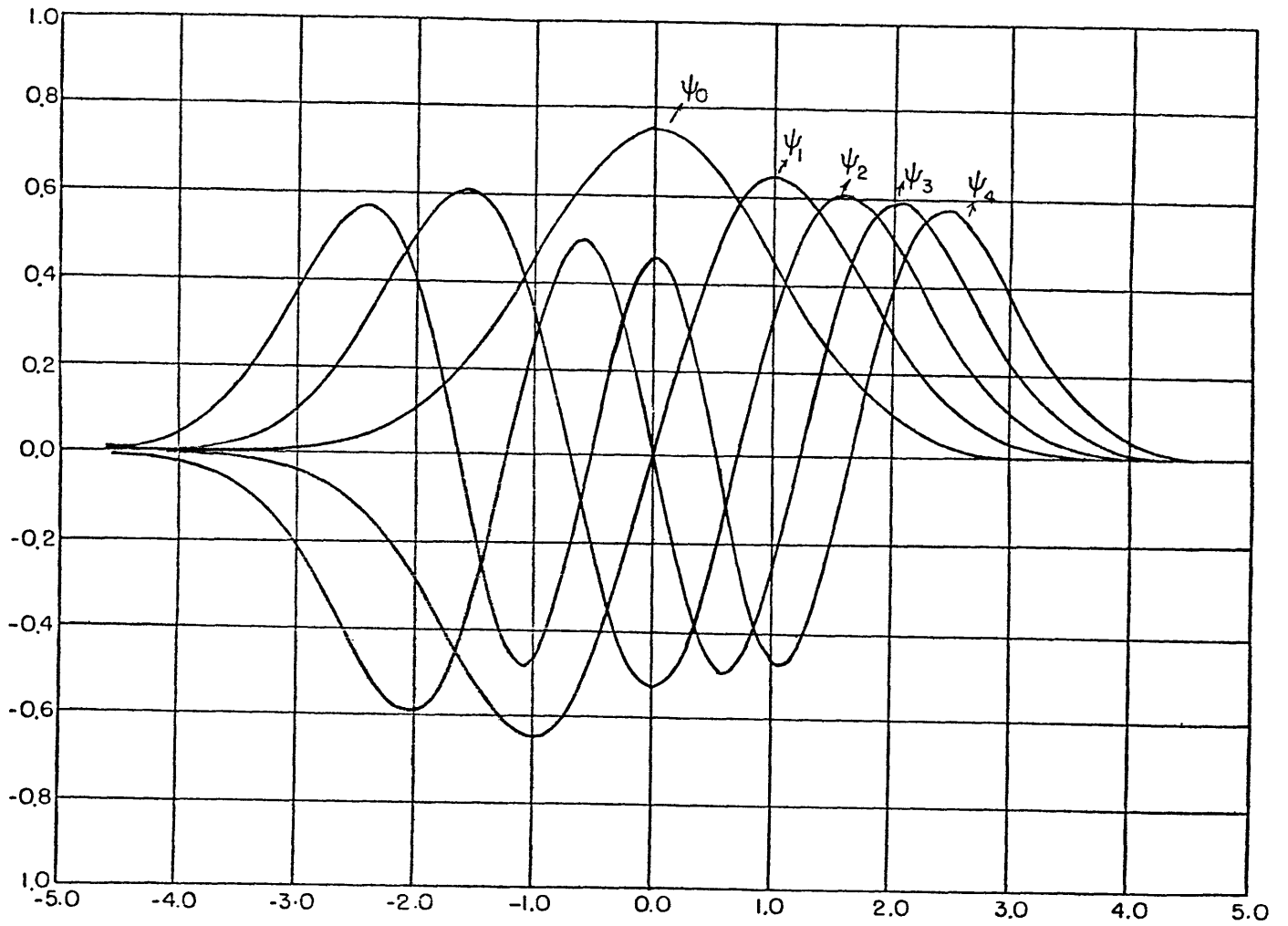
Figure B.1   First Four Normalized Hermite Functions Given By

$$\Psi_n(x) = \frac{H_n(x)\ e^{-x^2/2}}{(2^n n!\ \pi^{1/2})^{1/2}}$$

Recursion Relations for Normalized Hermite Functions

$$x\Psi_n = \left(\frac{n}{2}\right)^{1/2} \Psi_{n-1} + \left(\frac{n+1}{2}\right)^{1/2} \Psi_{n+1} \qquad \text{[B.6]}$$

$$\frac{d\Psi_n}{dx} = \left(\frac{n}{2}\right)^{1/2} \Psi_{n-1} - \left(\frac{n+1}{2}\right)^{1/2} \Psi_{n+1} \qquad \text{[B.7]}$$

$$\frac{d^2\Psi_n}{dx} = \frac{(n(n-1))^{1/2}}{2} \Psi_{n-2} + \left(n + \frac{1}{2}\right) \Psi_n + ((n+1)(n+2))^{1/2} \Psi_{n+2} \qquad \text{[B.8]}$$

$$\int_{-\infty}^{\infty} \Psi_{n+1}(x)dx = \left(\frac{n}{n+1}\right) \int_{-\infty}^{\infty} \Psi_{n-1}(x)dx \ , \qquad \text{[B.9]}$$

where,

$$\int_{-\infty}^{\infty} \Psi_0(x)dx = (2\pi^{1/2})^{1/2} = 1.88279253 \qquad \text{[B.10]}$$

Orthonormality Relation

$$\int_{-\infty}^{\infty} \Psi_m(x)\ \Psi_n(x)\ dx = \begin{cases} 1 & 1 \ m = n \\ 0 & 1 \ m \neq n \end{cases} \qquad \text{[B.11]}$$

Triple Integral (Bushbridge, 1948)

$$\int_{-\infty}^{\infty} \Psi_\ell(x)\ \Psi_m(x)\ \Psi_n(x)\ dx =$$

$$= \begin{cases} \left(\frac{2}{3}\right)^{1/2} \left(\frac{4}{3}\right)^K \Gamma(K + \frac{1}{2}) \sum_{r,s,t}^{K} \dfrac{(-\ell)_{s+t}(-m)_{t+r}(-m)_{r+s}}{r!\ s!\ t!\ (1/2 - K)_{r+s+t}} \left(\frac{3}{2}\right)^{r+s+t} \\ \qquad\qquad\qquad 0 < r+s+t < K \qquad\qquad\qquad\qquad \text{if } \ell+m+n \text{ is even} \\ \\ \\ 0 \quad \text{if } \ell+m+n \text{ is odd} \end{cases} \qquad \text{[B.12]}$$

where

$K = (\ell + m + n)/2$

$F(\alpha)$ is the Gamma Function

$(\alpha)_n = \alpha\ (\alpha + 1)(\alpha + 2) \ \text{----} \ (\alpha + n - 1)$ is the Pochammer Function.

Hermite Integration Formula

From Abramowitz and Stegun (1965, pp. 924), we present in Table B-1 below the zeroes and weights for the 20-point Hermite integration formula.

$$\int_{-\infty}^{\infty} e^{-x^2} f(x)\ dx = \sum_{i=1}^{n} w_i\ f(x_i) \qquad\qquad \text{[B.13]}$$

or

$$\int_{-\infty}^{\infty} g(x)\ dx = \sum_{i=1}^{n} w_i e^{x_i^2}\ g(x_i) \qquad\qquad \text{[B.14]}$$

TABLE B.1

Zeros of Hermite Polynomials and Weight Factors

$\pm x_i$	w_i	$w_i e^{x_i^2}$
0.24534	(-1) 4.62243	0.49092
0.73747	(-1) 2.86675	0.49384
1.23407	(-1) 1.09017	0.49992
1.73853	(-2) 2.48105	0.50967
2.25497	(-3) 3.24377	0.52408
2.78880	(-4) 2.28338	0.54485
3.34785	(-6) 7.80255	0.57526
3.94476	(-7) 1.08606	0.62227
4.60368	(-10) 4.39934	0.70433
5.38748	(-13) 2.22939	0.89859

APPENDIX C

SPECTRAL METHODS FOR CALCULATING NONLINEAR INTERACTION COEFFICIENTS

Assume A and B are variables expressed as spectral expansions of a set of orthogonal basis functions

$$A = \sum_{m=-M}^{M} \sum_{\ell=0}^{L} A_{m,\ell} \; \Psi_\ell(y) \; e^{-imx} \qquad \text{[C.1]}$$

$$B = \sum_{m=-M}^{M} \sum_{\ell=0}^{L} B_{m,\ell} \; \Psi_\ell(y) \; e^{-imx} \qquad \text{[C.2]}$$

where Ψ_ℓ is the Hermite function of order ℓ.

We want to calculate the spectral representation of the product AxB, i.e., the series of coefficients $C_{m,\ell}$ such that

$$AxB = \sum_{m=-M}^{M} \sum_{\ell=0}^{L} C_{m,\ell} \; \Psi_\ell(y) \; e^{-imx}. \qquad \text{[C.3]}$$

To obtain the nonlinear interaction coefficients $C_{m,\ell}$ two methods can be used: the direct method and the transform method.

Direct Method

The procedure to calculate the nonlinear interactions coefficients via the direct method is quite straight forward.

$$AxB = \sum_{m=-M}^{M} \sum_{\ell=0}^{L} C_{m,\ell} \; \Psi_\ell(y) \; e^{-imx}$$

$$= (\sum_{m=-M}^{M} \sum_{\ell=0}^{L} A_{m,\ell} \; \Psi_\ell \; e^{-imx}) \; (\sum_{n=-M}^{M} \sum_{k=0}^{L} B_{n,k} \; \Psi_k \; e^{-inx})$$

$$\text{[C.4]}$$

Multiply Eq. [C.4] through by $\Psi_p(y)e^{irx}$ and integrate in x from $-\pi$ to π and in y from $-\infty$ to ∞. We obtain

$$\sum_{e=-M}^{M} \sum_{j=0}^{L} C_{eij} \left(\int_{-\infty}^{\infty} \Psi_j(y)\, \Psi_p(y)\, dy \right) \left(\int_{-\pi}^{\pi} e^{-i(e-r)x}\, dx \right)$$

$$= \sum_{m=-M}^{M} \sum_{n=-M}^{M} \sum_{\ell=0}^{L} \sum_{k=0}^{L} A_{m,\ell}\, B_{n,k} \left(\int_{-\infty}^{\infty} \Psi_\ell\, \Psi_k\, \Psi_p\, dy \right)$$

$$\times \left(\int_{-\pi}^{\pi} e^{-i(m+n-r)x}\, dx \right) \qquad \text{[C.5]}$$

The orthogonality relations for Hermite functions and Fourier series are given by

$$\int_{-\infty}^{\infty} \Psi_m\, \Psi_n\, dy = \begin{cases} 1 & 1 \quad m = n \\ 0 & 1 \quad m \neq n \end{cases} \qquad \text{[C.6]}$$

$$\frac{1}{2\pi} \int_{-\pi}^{\pi} e^{-i(m-n)x}\, dx = \begin{cases} 1 & 1 \quad m = n \\ 0 & 1 \quad m \neq n \end{cases} \qquad \text{[C.7]}$$

Applying [C.6] and [C.7] in [C.5) results in

$$C_{r,p} = \sum_{m=-M}^{M} \sum_{\ell=0}^{L} \sum_{k=0}^{L} A_{r-m,\ell}\, B_{m,k}\, I\,(\ell,k,p) \qquad \text{[C.8]}$$

where $I(\ell,k,p)$ is the triple Hermite function integral

$$I(\ell,k,p) = \int_{-\infty}^{\infty} \Psi_\ell(y)\, \Psi_k(y)\, \Psi_p y)\, dy. \qquad \text{[C.9]}$$

Because $A_{m,\ell} = 0$ for $|m|>M$ and $A_{r-(-M)} = A_{r+M}$ we see that the summation can be started at $m = r-M$. Hence the expression for the

nonlinear interaction coefficients $C_{r,p}$ becomes

$$C_{r,p} = \sum_{m=r-M}^{M} \sum_{p=0}^{L} \sum_{q=0}^{L} A_{r-m,p} \, B_{m,q} \, I(p,q,\ell).$$

[C.10]

The integral $I(\ell,k,p)$ is calculated once and for all using relation [B.12] (Appendix B).

Although this is a straight-forward way of calculating the nonlinear interaction coefficients, it has a serious limitation. The number of operations goes as N^3 per calculation of nonlinear terms. Also N^3 *numbers* have to be stored for the integrals $I(p,q,\ell)$. For $N = 10$ (10 modes in Fourier and 10 modes in Hermite) there are 1,000 operations per calculation. For $N = 20$ the number of operations grows to 8,000 per nonlinear calculation. Spectral methods have historically been less attractive primarily because the number of operations goes as N^3. Only recently with the advent of alternative methods to calculate the interaction coefficients have spectral methods become widely used.

Transform Method

The idea of the transform method (see Orzag (1980) for a review on the subject) is to perform certain operations in the spectral domain and some others in the grid-point domain. Differentiation is performed in the spectral domain since higher accuracy is obtained when compared with finite-difference schemes. Calculation of nonlinear terms is executed in the grid-point domain where it is simply a multiplication.

Define the collocation points x_i and y_j. Any quantity A can be expressed as

$$A(x_i, y_j) = \sum_{m=-\infty}^{\infty} \sum_{\ell=0}^{\infty} A_{m,\ell} \, \Psi_\ell \, (y_j) \, e^{-imx_i} \quad .$$

[C.11]

The spectral representation of a nonlinear term of the form

$$A \, \frac{dB}{dx}$$

is evaluated as follows:

1) Evaluate the derivative dB/dx in the spectral domain, i.e., simply multiply by (-im).

2) Calculate the nonlinear product for each pair (x_i, y_j)

$$C(x_i, y_j) = \left(\sum_{m=-M}^{M} \sum_{\ell=0}^{L} A_{m,\ell} \, \Psi_\ell(y_j) e^{-imx_i} \right)$$

$$\times \left(\sum_{m=-M}^{M} \sum_{\ell=0}^{L} (-im) \, B_{m,\ell} \, \Psi_\ell(y_j) e^{-imx_i} \right) \qquad [C.12]$$

3) Find the spectral representation of $C(x,y)$

$$C(x_i, y_j) = \sum_{m=-M}^{M} \sum_{\ell=0}^{L} C_{m,\ell} \, \Psi_\ell(y_j) e^{-imx_i} \quad . \qquad [C.13]$$

$C_{m,\ell}$ is obtained by numerically evaluating the double integral

$$C_{m,\ell} = \int_{-\infty}^{\infty} \int_{-\pi}^{\pi} C(x,y) \Psi_\ell(y) \, e^{imx} \, dxdy. \qquad [C.14]$$

Each operation is carried out in the domain where it can be most accurately and efficiently implemented. Unlike the direct method where the number of operations grows as N^3, now it grows roughly as $2N^2$ for the transform method. For large N (N>10) the transform method is much more efficient.

To increase computational efficiency even further, the FFT (Fast Fourier Transform) algorithm is utilized in [C.12] and [C.14]. It is not of the author's knowledge that any "Fast Hermite Transform" to evaluate terms of the form

$$\sum_{\ell=0}^{L} A_\ell \Psi_\ell(y)$$

and integrals of the form

$$\int_{-\infty}^{\infty} A(y)\Psi_\ell(y)dy$$

exists. To calculate these integrals, we made use of the 20-point Hermite integration formula (see Appendix B).

APPENDIX D

MODIFIED MATSUNO TIME INTEGRATION SCHEME

The Matsuno (or Euler backward) time integration scheme is a two-step integration scheme. For the ordinary differential equation

$$\frac{dA}{dt} = F(A) \tag{D.1}$$

the scheme can be represented as

$$A^{t*} = A^t + \Delta t \; F^t$$

$$A^{t+1} = A^t + \Delta t \; F^{t*}. \tag{D.2}$$

First, a new value of A is calculated for the auxiliary time t*; then, the solution is advanced to the time t+1.

In the integration of the numerical model in Chapter 4, a slight modification of the scheme was necessary to keep errors from growing. The error growth arises in connection with truncation errors for the series of Hermite functions when y-derivatives are calculated.

Let

$$A = \sum_{n=0}^{N} A_n \; \Psi_n(y), \tag{D.3}$$

$$B = \sum_{n=0}^{N} B_n \; \Psi_n(y), \tag{D.4}$$

and,

$$B = \frac{dA}{dy} \; . \tag{D.4}$$

Using the recurrence relations of Appendix B, the Bn's can be written as a function of the An's

$$Bn = (\frac{n+1}{2})^{1/2} A_{n+1} - (\frac{n}{2})^{1/2} A_{n-1} .$$

[D.5]

For n = N (truncation value)

$$B_N = - (\frac{N}{2})^{1/2} A_{N-1}$$

since we assume $A_n = B_n = 0$ for n > N. For n sufficiently large, $B_n \rightarrow 0$, but in our expansion, N = 10, and we observed that for some instances the error in the calculation of B_N tends to accumulate. More precisely, error accumulation arises in the numerical integration of the prognostic equation for the meridional wind v due to the error in the calculation of the y-derivative of the geopotential ($d\phi_n/dy$). Because of this error accumulation problem, the Hermite spectral coefficients for v would start to diverge after a few dozen time steps.

The problem was corrected simply by not time-advancing the geopotential in the intermediate step of the Matsuno scheme. The prognostic equations for u and v can be symbolically written as

$$\frac{du}{dt} = - \frac{d\phi}{dx} + F_u$$

[D.6a]

and

$$\frac{dv}{dt} = - \frac{d\phi}{dy} + F_v$$

[D.6b]

where F_u and F_v represents the remaining terms of the u and v momentum equations, respectively.

Applying the modified Matsuno time integration scheme to Eqs. [D.6] yields for the first iteration t*

$$u^{t*} = u^t - \Delta t \; (\frac{d\phi}{dx})^t + \Delta t \; F_u{}^t \qquad \text{[D.7a]}$$

$$v^{t*} = v^t - \Delta t \; (\frac{d\phi}{dy})^t + \Delta t \; Fv^t \qquad \text{[D.7b]}$$

and for the final time step t + 1

$$u^{t+1} = u^t - \Delta t \; (\frac{d\phi}{dx})^t + \Delta t \; F_u{}^{t*} \qquad \text{[D.8a]}$$

$$v^{t+1} = v^t - \Delta t \; (\frac{d\phi}{dy})^t + \Delta t \; F_v{}^{t*} \qquad \text{[D.8b]}$$

We found that by using this scheme, the errors in the calculation of $(d\phi/dy)$ remain bounded and the series of Hermite coefficients for the variables converges.

In Table D.1 we present an example of a 15 time-step integration of a linear version of the model [Eqs. [4.43] through [4.48]] for the modified Matsuno scheme and for the Matsuno scheme. Hermite coefficients are shown for $(d\phi/dy)_n$ and for V_n for selected time steps.

From Table D.1 we see that for time step = 15, the errors in the calculation of $(d\phi/dy)_n$ for the Matsuno time integration scheme are already large, i.e., $|(d\phi/dy)_n|$ is increasing as n increases. After a few more time steps, these errors will show up in the V_n's and eventually, in all the remaining fields. For the modified Matsuno scheme, $|(d\phi/dy)_n|$ decreases as n increases and the series converges.

TABLE D.1

Coefficients $(d\phi/dy)_n$ and V_n for a 15 Time-Step Integration of Eq. [4.45]

Time Step	n	Matsuno Modified		Matsuno	
		$(d\phi/dy)_n$	V_n	$(d\phi/dy)_n$	V_n
1	1	(0.0, 0.0)	(0.0, 0.0)	(-0.12082, 0.0)	(0.0, 0.0)
2	1	(-0.12054, 0.0)	(0.0, 0.0)	(-0.12054, 0.0)	(0.60E-2, 0.0)
3	1	(-0.21958, 0.0)	(0.60E-2, -0.52E-4)	(-0.19879, 0.61E-4)	(0.17E-2, -0.52E-4)
				(-0.340E-1, -0.15E-3)	(0.83E-2, 0.0)
5	1	(-0.33182, -0.92E-2)	(0.03100, -0.52E-3)	(-0.29667, -0.47E-3)	(0.04510, -0.53E-3)
	3	(-0.07716, -0.13E-2)	(0.31E-2, -0.41E-4)	(-0.05928, -0.62E-3)	(0.72E-2, -0.31E-4)
	5	(-0.02929, 0.0)	(0.42E-3, -0.37E-5)	(-0.04927, -0.56E-3)	(0.32E-2, 0.75E-5)
10	1	(-0.44131, -0.01037)	(0.12128, -0.53E-2)	(-0.38997, -0.88E-2)	(0.13219, -0.53E-2)
	3	(-0.06302, -0.88E-2)	(-.01777, -0.13E-2)	(-0.13929, -0.01114)	(0.02349, -0.11E-2)
	5	(0.01140, -0.01145)	(0.49E-2, -0.63E-3)	(0.68E-2, -0.01039)	(-0.22E-2, -0.46E-3)
15	1	(0.46659, -0.04635)	(0.22501, -0.01781)	(-0.18023, -0.04965)	(0.23536, -0.01697)
	3	(-0.30108, -0.04184)	(0.04373, -0.37E-2)	(-1.64210, -0.06246)	(0.06602, -0.36E-2)
	5	(-0.07375, -0.04526)	(0.55E-2, -0.11E-2)	(1.76180, -0.01827)	(0.24E-2, -0.67E-4)

APPENDIX E

NUMERICAL INTEGRATION SCHEME FOR THE NONLINEAR MODEL OF CHAPTER 4

The numerical integration scheme for the nonlinear equations of Chapter 4 will be presented in this appendix in detail.

Equations [4.43] through [4.48] can be represented schematically as

$$\frac{dU^k_{m,\ell}}{dt} = A^k(U, V, W) + B^k(\phi) \qquad\qquad\qquad \text{[E.1]}$$

$$\frac{dV^k_{m,\ell}}{dt} = C^k(U, V, W) + D^k(\phi) \qquad\Bigg\} \; k \text{ even} \qquad \text{[E.2]}$$

$$\frac{dT^k_{m,\ell}}{dt} = E^k(U, V, W, T, Q) \qquad\qquad\qquad \text{[E.3]}$$

$$\frac{d\phi^k_{m,\ell}}{dt} = F^k(W), \; k = 1 \qquad\qquad\qquad \text{[E.4]}$$

$$\phi^{k+1}_{m,\ell} = G^{k-1}(\phi) + H^k(T) \qquad\qquad\qquad \text{[E.5]}$$

$$\Bigg\} k \text{ even}$$

$$W^{k-1}_{m,\ell} = I^{k+1}(W) + J(U, V) \qquad\qquad\qquad \text{[E.6]}$$

where we group the terms in the R.H.S. of [4.43] - [4.48] in two categories, terms containing the geopotential height and terms without it, as follows

$$A(U,V,W) = - R_0 \, C^k_{m,\ell}(U) + [(\frac{\ell+1}{2})^{1/2} V^k_{m,\,\ell+1} + (\frac{\ell}{2})^{1/2} V^k_{m,\,\ell-1}]$$

$$- r_0 \, U^k_{m,\ell} \qquad\qquad\qquad \text{[E.7]}$$

$$B^k(\phi) = + \, im\phi^k_{m,\ell} \qquad\qquad [E.8]$$

$$C^k(U,V,W) = - R_0 \, C^k_{m,\ell}(V) + [(\frac{\ell+1}{2})^{1/2} U^k_{m,\ell+1} + (\frac{\ell}{2})^{1/2} U^k_{m,\ell-1} \,]$$

$$- r_0 \, V^k_{m,\ell} \qquad\qquad [E.9]$$

$$D^k(\phi) = [(\frac{\ell+1}{2})^{1/2} \phi^k_{m,\ell+1} - (\frac{\ell}{2})^{1/2} \phi^k_{m,\ell-1} \,] \qquad\qquad [E.10]$$

$$E^k(U,V,W,T,\phi) = - R_0 \, C^k_{m,\ell}(T) - A_0 \, W^k_{m,\ell} + F_0 \, Q^k_{m,\ell} - \gamma_0 \, T^k_{m,\ell} \qquad [E.11]$$

$$F^k(W) = - N_0 \, W^k_{m,\ell} \qquad\qquad [E.12]$$

$$G^{k-1}(\phi) = \phi^{k-1}_{m,\ell} \qquad\qquad [E.13]$$

$$H^k(T) = \Delta z^k \, T^k_{m,\ell} \qquad\qquad [E.14]$$

$$I^{k-1}(W) = \frac{(1 - \Delta z^k)}{(1 + \Delta z^k)} W^{k+1}_{m,\ell} \qquad\qquad [E.15]$$

$$J^k(U,V) = \frac{\Delta z^k}{(1+\Delta z^k)} [-imU^k_{m,\ell} + (\frac{\ell+1}{2})^{1/2} V^k_{m,\ell+1} - (\frac{\ell}{2})^{1/2} V^k_{m,\ell-1} \,].$$
$$[E.16]$$

In the boundary condition [4.46] we are assuming flat topography, i.e., $h(x,y) = 0$ so

$$CH^1_{m,\ell}(h) = 0$$

and also we are making the additional assumption that

$$\left(u \frac{\partial \phi}{\partial x} + v \frac{\partial \phi}{\partial y}\right) \ll w \frac{\partial \phi_0}{\partial z}$$

at $z = 0$. We have carried out test runs with the horizontal advection term

$$\left(u \frac{\partial \phi}{\partial x} + v \frac{\partial \phi}{\partial y}\right)_{z = 0}$$

included and have concluded that eq. [E.12] is a very good approximation to the nonlinear boundary condition and that it saves us the computation of two nonlinear terms.

The integration starts at a given time, say, $t = \tau$. At this time we know all the initial fields, i.e., the coefficients

$$\{ U^{k,\tau}_{m,\ell}, V^{k,\tau}_{m,\ell}, W^{k,\tau}_{m,\ell}, \phi^{k,\tau}_{m,\ell}, T^{k,\tau}_{m,\ell} \} \text{ for} \begin{cases} 0 \leqslant m \leqslant M \\ 0 \leqslant \ell \leqslant L \\ 1 \leqslant k \leqslant K \end{cases} \quad [E.17]$$

are given.

We want to integrate numerically the set of equations [E.1] through [E.6] and find a new set of coefficients for time $t = \tau + \Delta t$ using the modified Matsuno time integration scheme. That will be accomplished through the following steps:

1) Advance the prognostic equations to an intermediate time step τ^*

$$U_{m,\ell}^{k,\tau^*} = U_{m,\ell}^{k,\tau} + \Delta t \left[A^{k,\tau} + B^{k,\tau}(\phi) \right] \qquad \left.\begin{array}{c} \\ \\ \\ \end{array}\right\}$$

[E.18]

$$V_{m,\ell}^{k,\tau^*} = V_{m,\ell}^{k,\tau} + \Delta t \left[C^{k,\tau} + D^{k,\tau}(\phi) \right] \qquad \left.\begin{array}{c} \\ \\ \end{array}\right\} \; k \; \text{even}$$

[E.19]

$$T_{m,\ell}^{k,\tau^*} = T_{m,\ell}^{k,\tau} + \Delta t \; E^{k,\tau} \qquad \left.\begin{array}{c} \\ \\ \end{array}\right\}$$

[E.20]

$$\phi_{m,\ell}^{k,\tau^*} = \phi_{m,\ell}^{k,\tau} + \Delta t \; F^{k,\tau} \qquad \left.\begin{array}{c} \\ \end{array}\right\} \quad k = 1$$

[E.21]

2) Integrate vertically the continuity and hydrostatic equations at
$t = \tau^*$

$$\phi_{m,\ell}^{k+1,\tau^*} = \phi_{m,\ell}^{k-1,\tau^*} + H^{k,\tau^*}$$

[E.22]

where $\qquad \phi_{m,\ell}^{1,\tau^*}$

is given by [E.21] and

$$W_{m,\ell}^{k-1,\tau^*} = I^{k+1,\tau^*} + J^{k,\tau^*}$$

[E.23]

with $I^{k,\tau^*} = 0$, i.e., $W(z_{top}) = 0$.

3) Now that all fields are known for $t = \tau^*$, advance the prognostic equations to the time $t = \tau + \Delta t$. Remember that the geopotential functions $B^k(\phi)$ and $D^k(\phi)$ will still have the values for $t = \tau$ (see Appendix D about this modification in the Matsuno scheme).

$$U_{m,\ell}^{k,\tau} = U_{m,\ell}^{k,\tau} + \Delta t \left[A^{k,\tau*} + B^{k,\tau}(\phi) \right] \qquad \text{[E.24]}$$

$$V_{m,\ell}^{k,\tau+\Delta t} = V_{m,\ell}^{k,\tau} + \Delta t \left[C^{k,\tau*} + D^{k,\tau}(\phi) \right] \qquad \left.\begin{array}{c}\\\\\end{array}\right\} k \text{ even} \qquad \text{[E.25]}$$

$$T_{m,\ell}^{k,\tau+\Delta t} = T_{m,\ell}^{k,\tau} + \Delta t E^{k,\tau*} \qquad \text{[E.26]}$$

$$\phi_{m,\ell}^{k,\tau+\Delta t} = \phi_{m,\ell}^{k,\tau} + \Delta t F^{k,\tau*} \qquad \left.\right\} \quad k = 1 \qquad \text{[E.27]}$$

4) Repeat step 2 and find the geopotential and vertical velocity for $t = \tau + \Delta t$.

5) Apply Shapiro filter to all fields to avoid the cascading of energy to small scales (see Appendix F).

6) Calculate the time derivatives of u, v and t for time $t = \tau + \Delta t$.

$$\frac{dU_{m,\ell}^{k,\tau+\Delta t}}{dt} = A^{k,\tau+\Delta t} + B^{k,\tau+\Delta t} \qquad \text{[E.28]}$$

$$\frac{dV_{m,\ell}^{k,\tau+\Delta t}}{dt} = C^{k,\tau+\Delta t} + D^{k,\tau+\Delta t} \qquad \left.\begin{array}{c}\\\\\end{array}\right\} k \text{ even} \qquad \text{[E.29]}$$

$$\frac{dT_{m,\ell}^{k,\tau+\Delta t}}{dt} = E^{k,\tau+\Delta t} \qquad \text{[E.30]}$$

and find

$$\text{MAX} \left(\left|\frac{dU_{m,\ell}^{k,\tau+\Delta t}}{dt}\right|\right), \quad \text{MAX} \left(\left|\frac{dV_{m,\ell}^{k,\tau+\Delta t}}{dt}\right|\right) \quad \text{and} \quad \text{MAX} \left(\left|\frac{dT_{m,\ell}^{k,\tau+\Delta t}}{dt}\right|\right) \quad \text{for} \begin{cases} 0 \leqslant m \leqslant M \\ 0 \leqslant \ell \leqslant L \\ k \text{ even} \end{cases}$$

7) Compute the value of u, v, w, ϕ and T for selected grid-points at t = τ + Δt.

8) Repeat steps 1 through 7 until the imbalances become very small, i.e., at least an error of magnitude smaller than the leading terms in the prognostic equations. That will provide a crude indication that a steady-state is being approached. Verify that the time evolution fields computed in 7 have met the defined criteria of less than 2% variation over 10 days of integration.

APPENDIX F

SHAPIRO FILTER

This description of the Shapiro filter closely follows Brenner (1981, pp. 166-168).

The Shapiro filter (Shapiro, 1970) is an ideal filter in that it operates only on the amplitudes and the phases are kept unchanged.

Let A be an arbitrary field represented by a truncated Fourier series.

$$A(x) = \sum_{m=-M}^{M} A_m e^{-imx} . \qquad [F.1]$$

The response function of the pth-order filter is defined by

$$R_p(m) = 1 - \sin^{2p} \left(\frac{m\pi}{2M}\right) , \qquad [F.2]$$

and the filtered field is simply given by

$$\overline{A}(x) = \sum_{m=-M}^{M} \overline{A}_m e^{-imx} \qquad [F.3]$$

with

$$\overline{A}_m = A_m R_p(m) . \qquad [F.4]$$

One of the main advantages of the Shapiro filter is that it can be made as selective as desired simply by choosing the order of the filter. This is illustrated in Figure F.1 which shows the filter response of an 11th order filter for various spectral truncations. The response function is flat, is close to one for long and medium wave numbers, and drops off sharply only near the truncation wavenumber. The longer waves are not

significantly damped while the shortest resolved waves are effectively

eliminated.
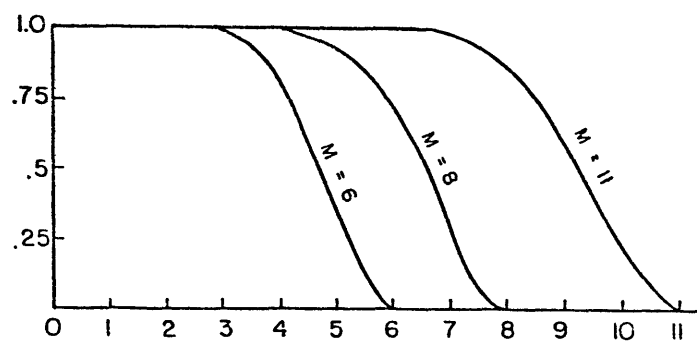
Figure F. 1   Shapiro Filter Response Function for Various Spectral
              Truncations

APPENDIX G

RESULTS OF A NONLINEAR INTEGRATION FOR   WAVENUMBER 1 SINUSOIDAL FORCING

We include in this appendix the results of a nonlinear integration of

the model of Chapter 4 for the wavenumber 1 sinusoidal forcing shown in

Figure G.1. We did not include this case with the other six analyses in

Chapter 5 mainly because the forcing's mean heating is zero for the former,

i.e., the prescribed diabatic heating sinks are equal and opposite to the

sources, and non-zero and positive for the latter. This would have

rendered comparisons difficult to make. Nevertheless, we find it is worth

describing briefly, in this appendix, the results for that case.

In Figures G.2 through G.7, we show the upper-level (300 mb) and lower-

level (700 mb) fields of u, v, w, ϕ, D, and ξ for both the linear and

nonlinear cases. Table G.1 below lists the minimum and maximum values of

all variables at 300 mb and 700 mb.

TABLE G.1 MINIMUM AND MAXIMUM VALUES OF ALL VARIABLES FOR THE
SINUSOIDAL FORCING CASE   (see Figure G.1)

| | u | | v | | w | | ϕ | | T' | | D | | ξ | |
	MIN	MAX	MIN	MAX	MIN	MAX	MIN	MAX	MIN	MAX	MIN	MAX	MIN	MAX
							300 mb							
L	-3.00	3.00	-0.17	0.17	-0.14	0.14	-1.32	1.32	-1.97	1.97	-0.31	0.31	-2.72	2.72
NL	-1.96	2.65	-0.21	0.21	-0.13	0.15	-2.06	1.13	-1.58	1.52	-0.29	0.40	-3.13	3.13
							700 mb							
L	-2.32	2.32	-0.12	0.12	-0.13	0.13	-0.88	0.88	-2.84	2.84	-0.29	0.29	-2.12	2.12
NL	-1.18	2.47	-0.22	0.22	-0.13	0.11	-1.09	0.44	-5.03	1.18	-0.31	0.30	-2.96	2.96

NOBRE   LEVEL IS 500 MB
LATENT HEATING

FORCING : COS(X)

VALUES RANGE BETWEEN   -1.00   AND   1.00   FOR CONTOUR INTERVALS OF   0.100
                                        RUN=   8
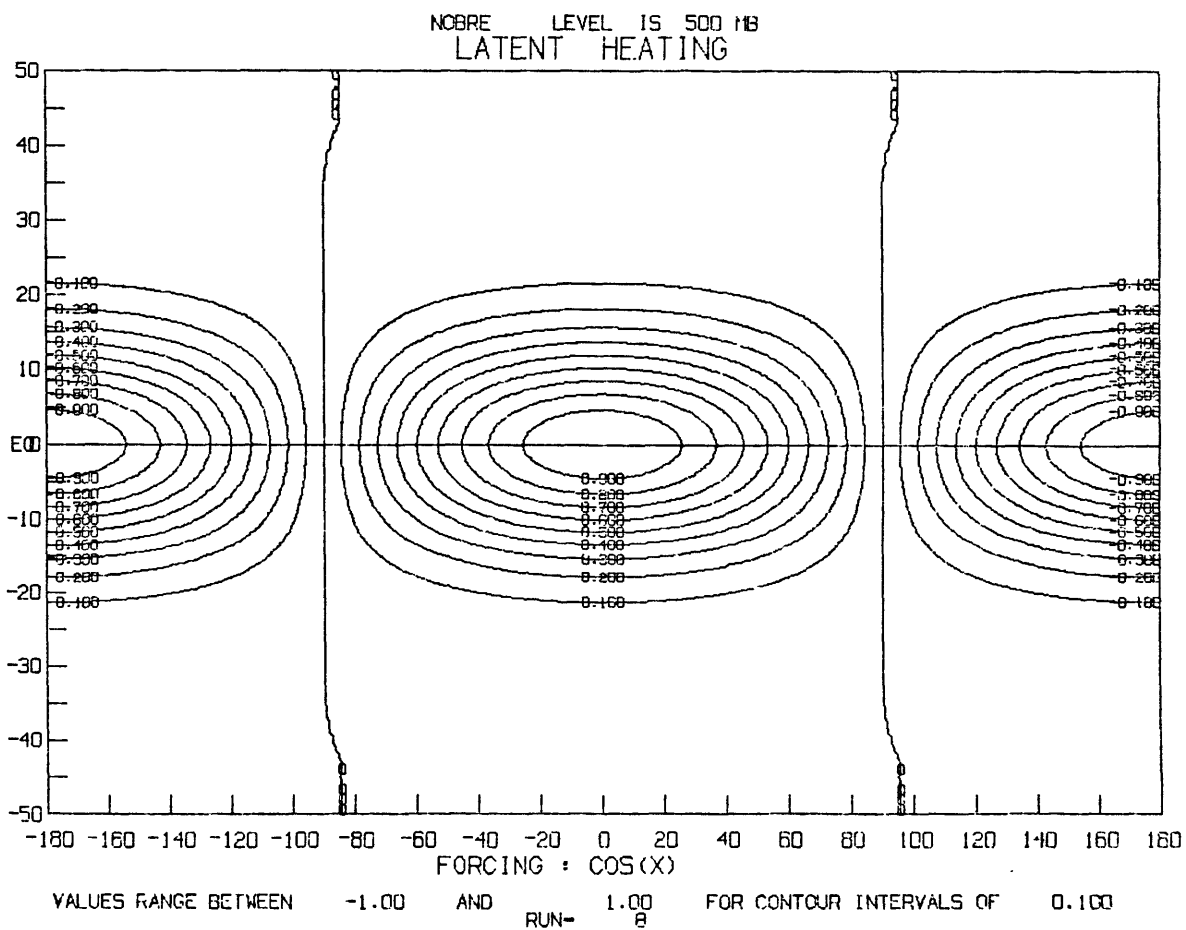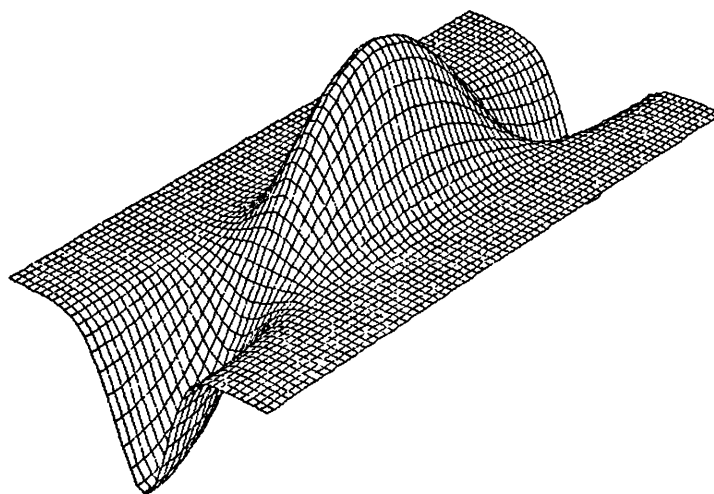
Figure G. 1   Wavenumber 1 sinusoidal latent heating forcing at 500 mb.
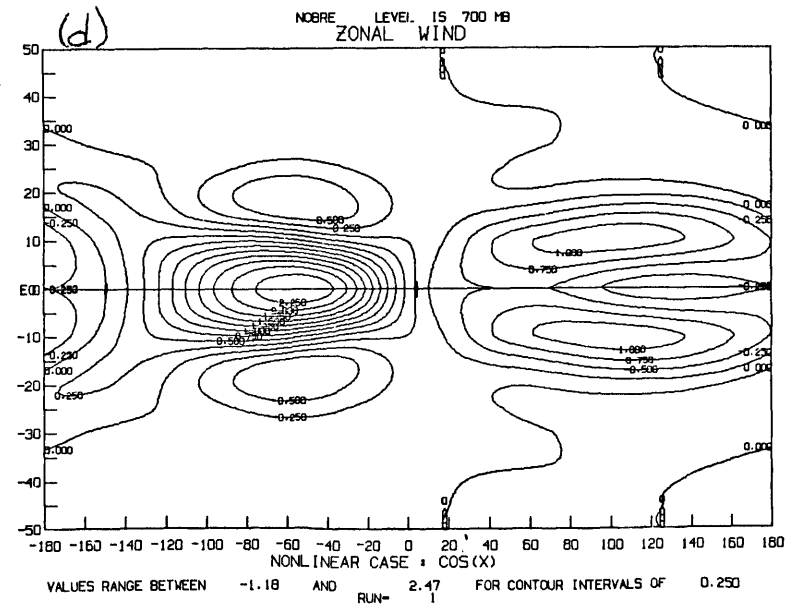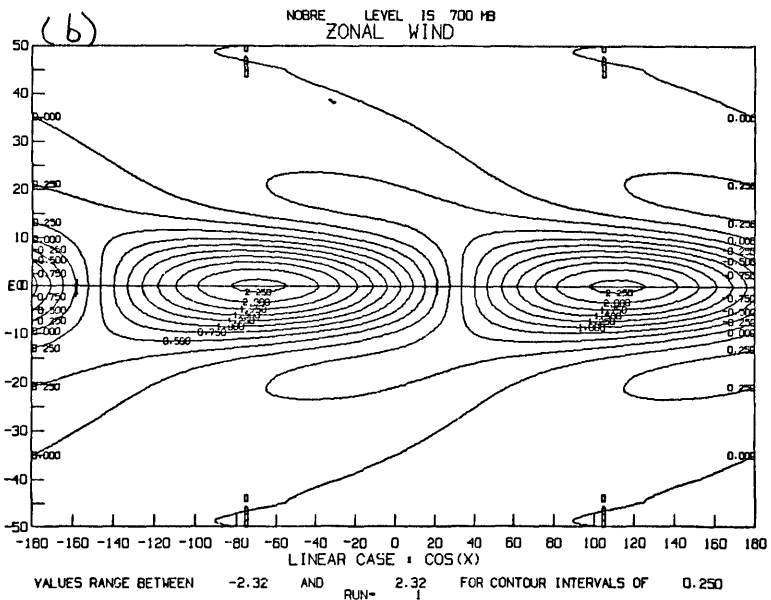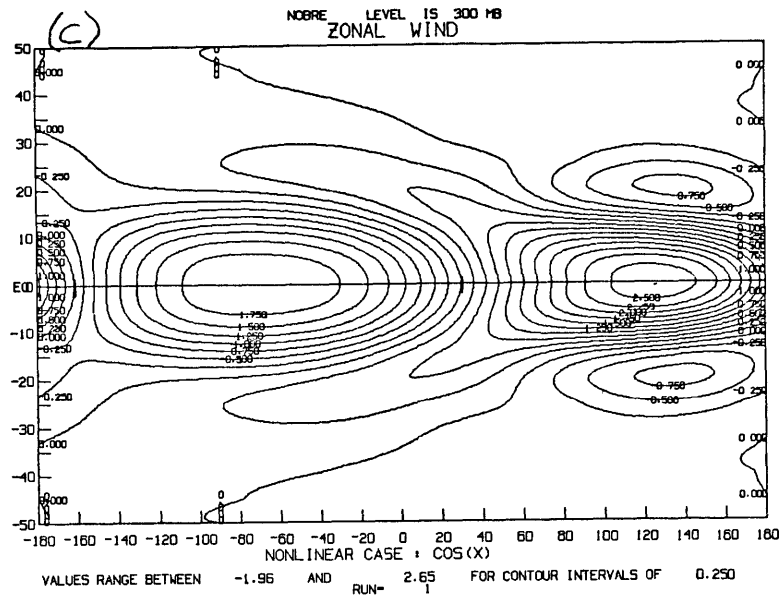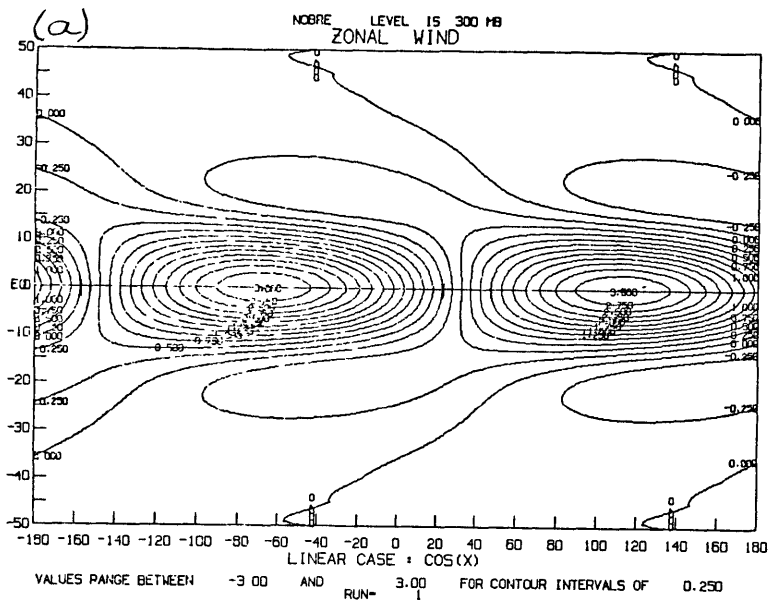
Figure G.2   Zonal wind (u) for the sinusoidal forcing case. Linear solution at 300 mb (a) and 700 mb (b), and nonlinear solution at 300 mb (c) and 700 mb (d).

(a)

NOBRE   LEVEL IS 300 MB
MERIDIONAL WIND

LINEAR CASE : COS(X)

VALUES RANGE BETWEEN   -0.17   AND   0.17   FOR CONTOUR INTERVALS OF   0.020
RUN= 2

(c)

NOBRE   LEVEL IS 300 MB
MERIDIONAL WIND

NONLINEAR CASE : COS(X)

VALUES RANGE BETWEEN   -0.21   AND   0.21   FOR CONTOUR INTERVALS OF   0.020
RUN= 2

(b)

NOBRE   LEVEL IS 700 MB
MERIDIONAL WIND

LINEAR CASE : COS(X)

VALUES RANGE BETWEEN   -0.12   AND   0.12   FOR CONTOUR INTERVALS OF   0.020
RUN= 2

(d)

NOBRE   LEVEL IS 700 MB
MERIDIONAL WIND

NONLINEAR CASE : COS(X)

VALUES RANGE BETWEEN   -0.22   AND   0.22   FOR CONTOUR INTERVALS OF   0.020

Figure G.3   Same as figure G.2 but for meridional wind (v).
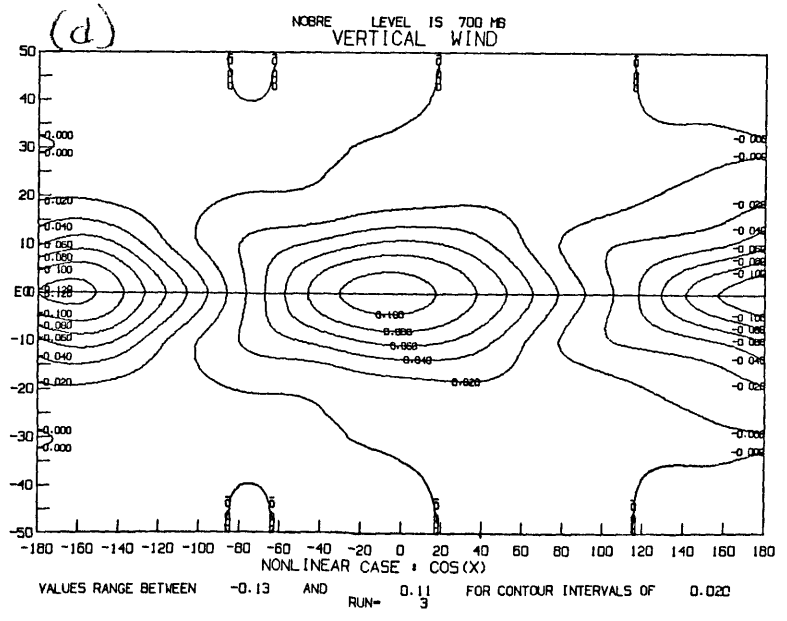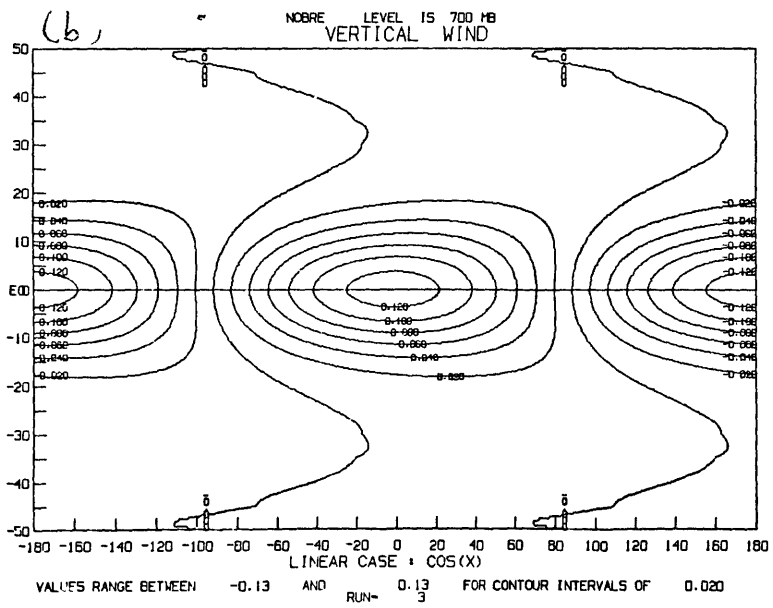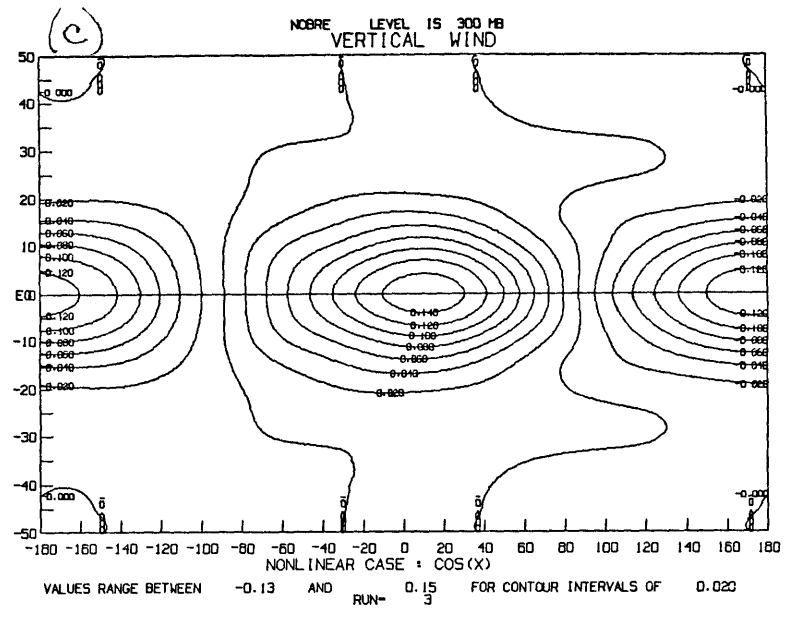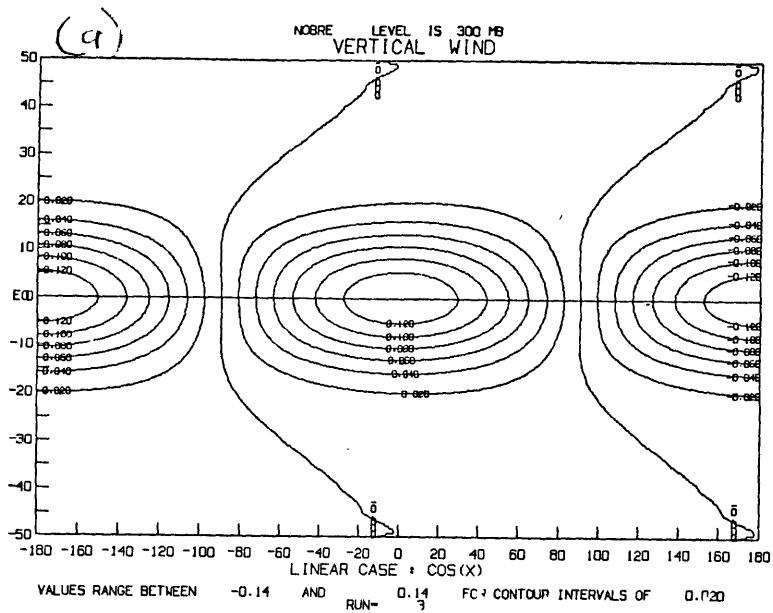
Figure G.4 Same as figure G.2 but for vertical wind (w).
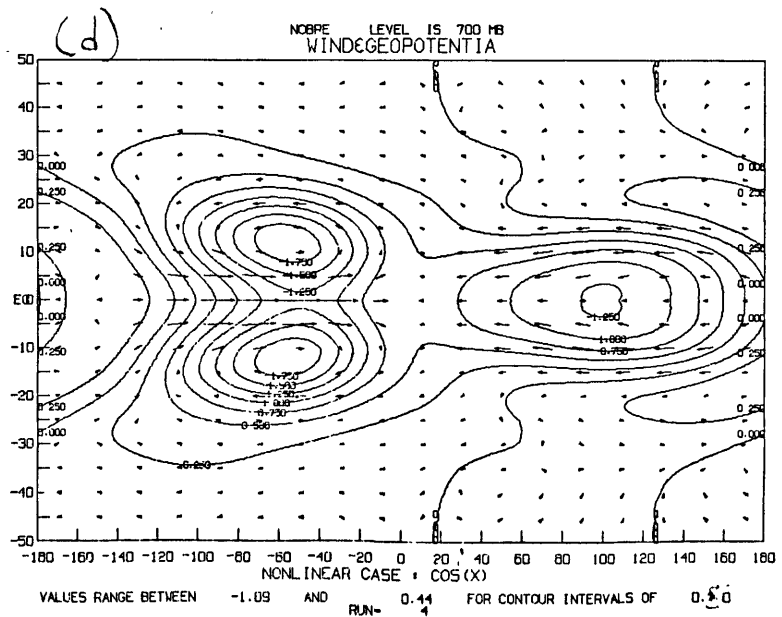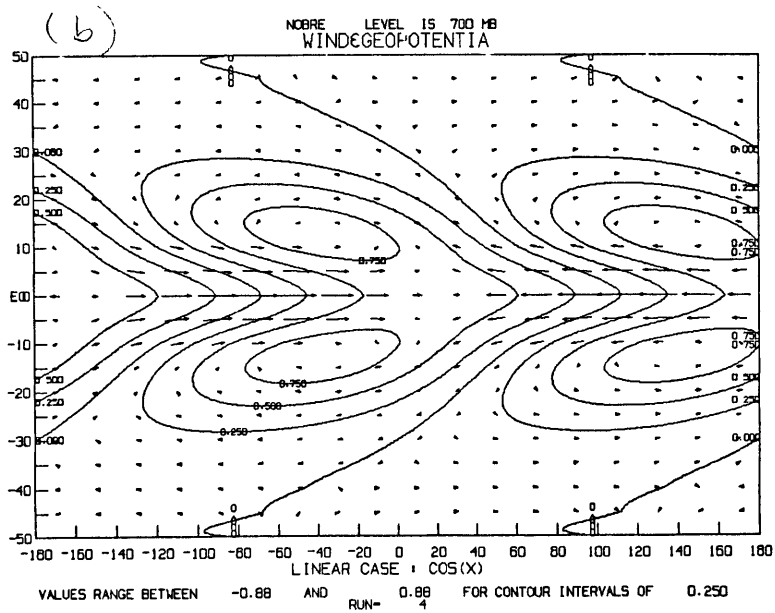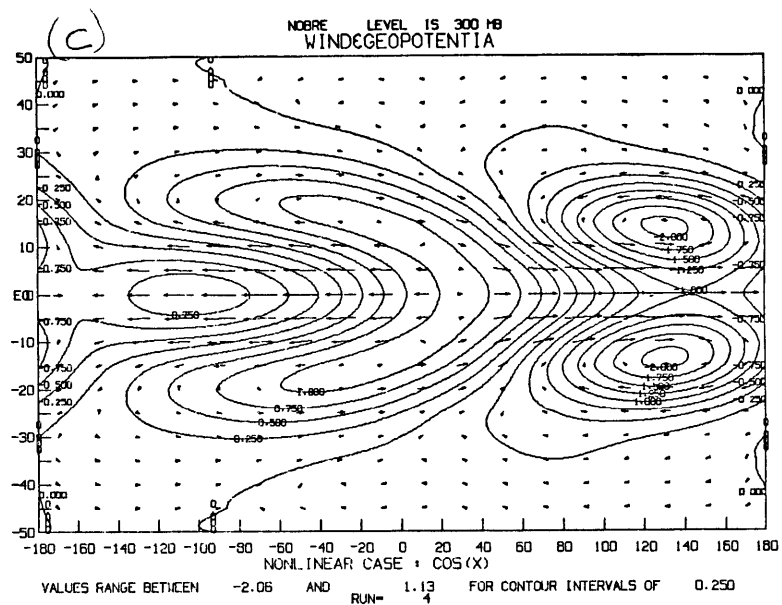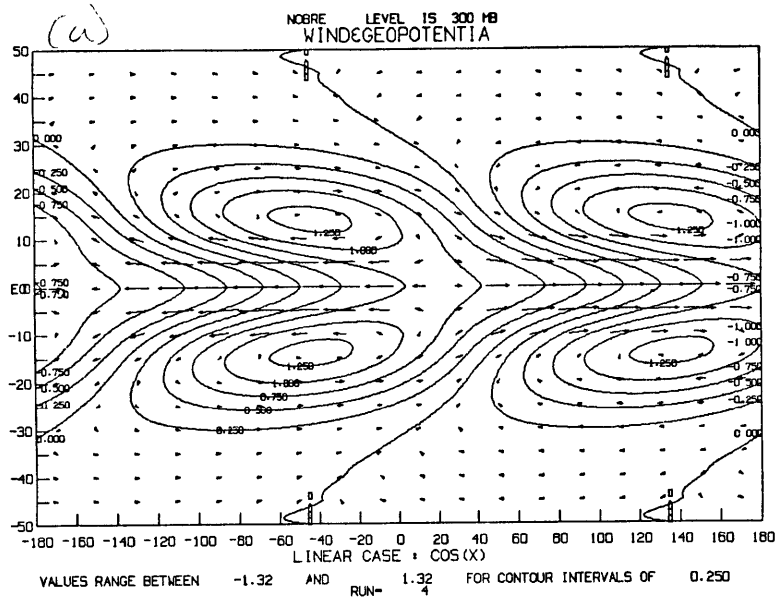
Figure G.5   Same as figure G.2 but for geopotential (ϕ) and horizontal wind ($\vec{v}$).
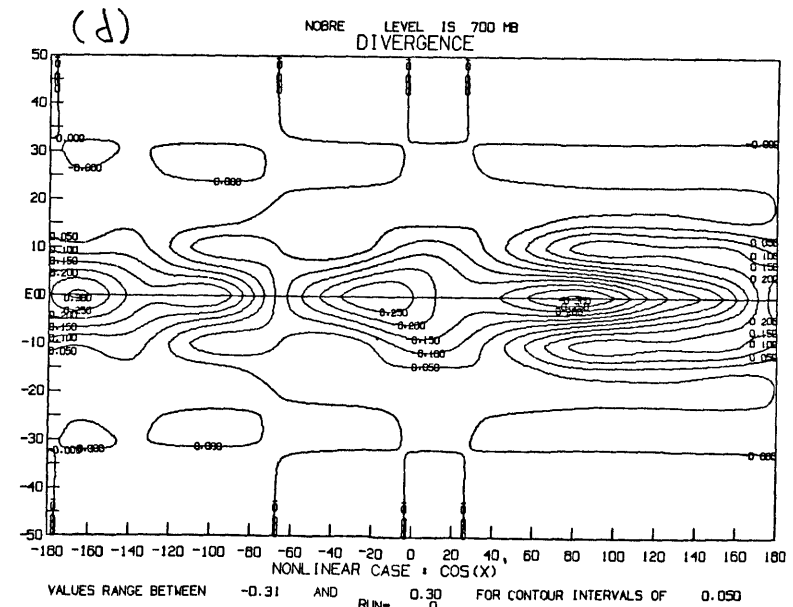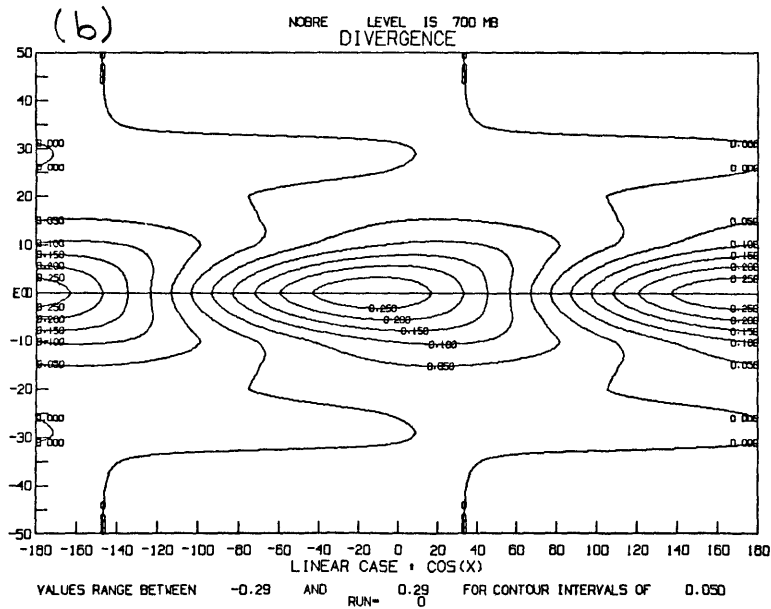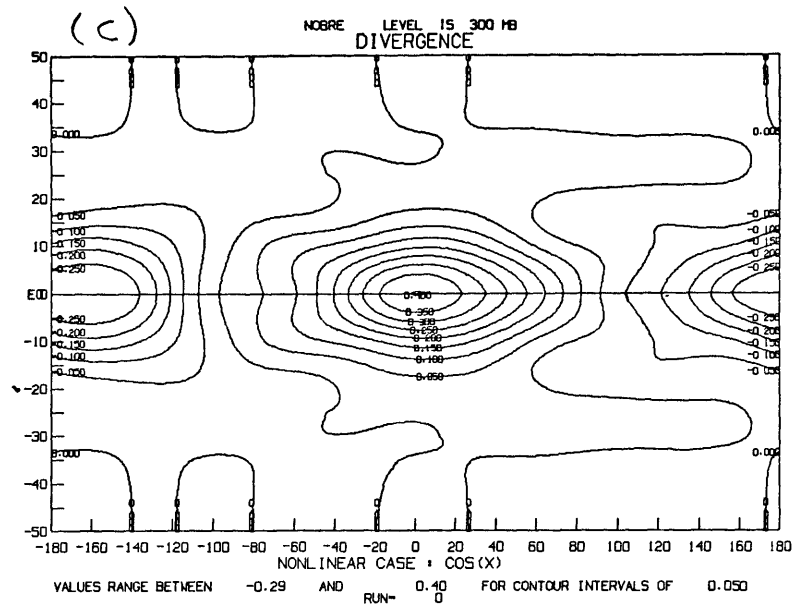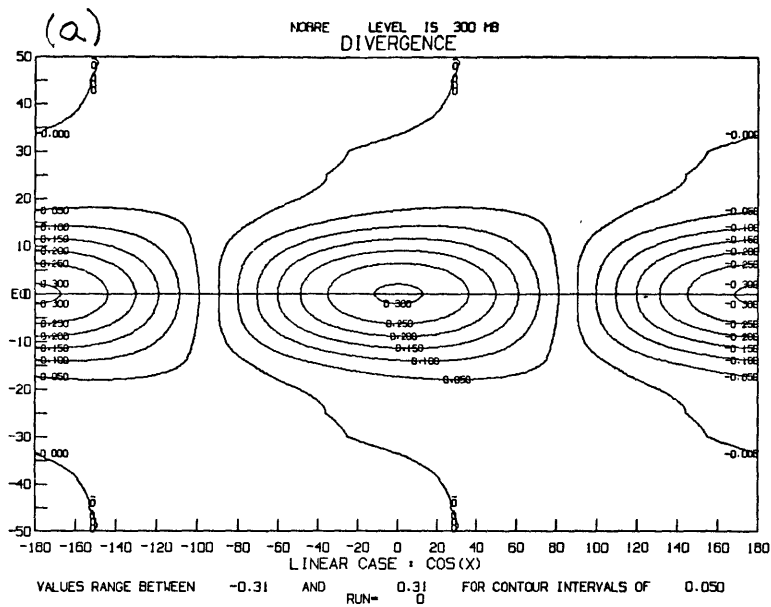
Figure G.6   Same as figure G.2 but for divergence (D).

(a)

NOBRE   LEVEL IS 300 MB
VORTICITY

LINEAR CASE : COS(X)

VALUES RANGE BETWEEN   -2.72   AND   2.72   FOR CONTOUR INTERVALS OF   0.500
RUN= 7

(c)

NOBRE   LEVEL IS 300 MB
VORTICITY

NONLINEAR CASE : COS(X)

VALUES RANGE BETWEEN   -3.13   AND   3.13   FOR CONTOUR INTERVALS OF   0.500
RUN= 7

(b)

NOBRE   LEVEL IS 700 MB
VORTICITY

LINEAR CASE : COS(X)

VALUES RANGE BETWEEN   -2.12   AND   2.12   FOR CONTOUR INTERVALS OF   0.500
RUN= 7

(d)

NOBRE   LEVEL IS 700 MB
VORTICITY

NONLINEAR CASE : COS(X)

VALUES RANGE BETWEEN   -2.96   AND   2.96   FOR CONTOUR INTERVALS OF   0.500
RUN= 7

Figure G.8   Same as figure G.2 but for vorticity (ξ).

The linear solution for this case is very similar to the stationary linear solution obtained by Matsuno (1966) using a simple shallow-water, equatorial β-plane model for a wavenumber 1 forcing, whereas in his model cooling and heating was interpreted as mass sinks and sources, periodic along the x-direction. At the lower level, lows with associated cyclonic circulation are found to the west of the heat source and highs with associated anticyclonic circulation to the west of the heat sink (Fig. G.5). The zonal wind presents maximum at the equator with westerlies to the west of the heat source and easterlies to the east of the heat source (Figure G.2). The upper-level linear solution is very similar to the lower-level one, but easterlies (westerlies) become westerlies (easterlies) and highs (lows) become lows (highs).

The upper-level zonal winds for the nonlinear solutions are smaller in magnitude ($\simeq$ 50% for easterlies and $\simeq$ 20% for the westerlies) as compared with the zonal winds of the linear solution (Figure G.2c). The lower-level westerlies slightly increase in magnitude and decrease considerably in longitudinal extent. Maximum easterlies decrease in magnitude and are found away from the equator and north of its former position (Figure G.3c). The geopotential for the nonlinear case undergoes a large degree of change, both qualitative and quantitative, as shown in Figures G.5c and d.

APPENDIX H

LIST OF SYMBOLS

Θ	latitude
x	distance in the eastward direction
y	distance in the northward direction
z	a measure of "height" $[\equiv -H \ln (p/p_S)]$
u	eastward velocity
v	northward velocity
w	a measure of "vertical velocity" $[\equiv dz/dt]$
w_{phys}	vertical velocity at the lower boundary
w_{topog}	vertical velocity due to topography
ω	omega "vertical velocity" $[\equiv dp/dt]$
$\vec{V}$	horizontal wind vector
$\vec{U}_S$	horizontal wind vector at the surface
$\vec{V}_\psi$	rotational part of the wind
$\vec{V}_\chi$	divergent part of the wind
U_0	basic-state zonal wind
ψ	streamfunction
χ	velocity potential
ξ	vorticity
D	divergence
p	pressure
p_S	a constant reference pressure $[\equiv 1000$ mb$]$
p_B	a variable surface pressure
Φ	geopotential
ϕ_0	a basic-state geopotential $[\equiv \phi_0(z)]$
ϕ	departure of local geopotential from $\phi_0(z)$

T	temperature
T_0	a basic-state temperature $[\equiv T_0(z)]$
T'	departure of local temperature from $\phi_0(z)$
$\overline{T}_0$	a constant tropospheric mean temperature
T_E	radiative equilibrium temperature
Ω	angular velocity of earth
a	radius of earth
β	y-derivative of Coriolis parameter at the equator $[\equiv 2\Omega/a]$
g	gravitational acceleration
R	gas constant for dry air
C_p	specific heat at constant pressure
κ	ratio of gas constant to specific heat at constant pressure
H	scale height $[\equiv R\,\overline{T}_0/g]$
h	height of topography
H_{top}	nondimensional height of model's top
H_Q	nondimensional heating scale height
F_x	friction in x-direction
F_y	friction in y-direction
τ_f	Rayleigh friction relaxation time
τ_r	Newtonian cooling relaxation time
S	static stability $[\equiv S(z)]$
$\dot{Q}$, $\dot{Q}_T$	total diabatic heating per unit mass
$\dot{Q}_L$	latent heating per unit mass
$\dot{Q}_R$	radiative heating per unit mass
$X(x)$	x-structure of diabatic heating
$Y(y)$	y-structure of diabatic heating
$Q_0(z)$	z-structure of diabatic heating

L   a constant length scale

S_0 a constant static stability scale

Q_0 a constant diabatic heating scale

R_0 Rossby number

m   wavenumber in the x-direction

m_s critical wavenumber $[\equiv (\beta/U_0)^{1/2}]$

ℓ order of Hermite function

k   vertical level

M   truncation wavenumber of Fourier series in x

L   truncation number of modes of Hermite function in y

Ψ_ℓ Hermite function of order ℓ

X   arbitrary independent variable

$X_{m,\ell}$ spectral coefficient of order m, ℓ

$X_{m,\ell}^{k}$ spectral coefficient of order m,ℓ at level k

$X_{m,\ell}^{k,\tau}$ spectral coefficient of order m,ℓ at level k and time τ

$\dfrac{d}{dt}$ total derivative $\left[\equiv \dfrac{\partial}{\partial t} + u\dfrac{\partial}{\partial x} + v\dfrac{\partial}{\partial y} + w\dfrac{\partial}{\partial z}\right]$

∇ horizontal gradient $\left[\equiv \dfrac{\partial}{\partial x}\vec{i} + \dfrac{\partial}{\partial y}\vec{j}\right]$

$\nabla\cdot$ horizontal divergence $\left[\equiv \dfrac{\partial}{\partial x} + \dfrac{\partial}{\partial y}\right]$

∇^2 horizontal Laplacian $\left[\equiv \dfrac{\partial^2}{\partial x^2} + \dfrac{\partial^2}{\partial y^2}\right]$

$C_{m,\ell}(X)$ spectral representation of tridimensional advection

$CH_{m,\ell}(X)$ spectral representation of horizontal advection

$\overline{X}$ time mean

$C_{m,\ell}(X)$ spectral representation of tridimensional advection

$CH_{m,\ell}(X)$ spectral representation of horizontal advection

$\overline{X}$ time mean

X' departure from time mean

$[X]$ zonal average

X^{*} departure from zonal average

APPENDIX I

LIST OF FIGURES

Figure 2.13 Vertically averaged diabatic heating distribution for Jan-Feb, 1979 (units: K/day, interval every unit).

Figure 2.14 Vertically and latitudinally averaged diabatic heating (thick line, units: K/day) and vertical omega velocity (thin line, units: 10^{-3} mbs^{-1}) for Jan-Feb, 1979; zonal averages of diabatic heating (thick straight line) and vertical omega velocity (thin straight line) are indicated.

Figure 2.15 Vertical omega velocity at 400 mb for Jan-Feb, 1979 (units 10^{-3} mbs^{-1}, interval every 0.50 units).

Figure 2.16 Average effective cloud top pressure, weighted by cloud fraction, retrieved by GLAS for January 1979. (After Susskind et al., 1982).

Figure 2.17a Geographical distributions of a) rawinsonde stations reporting at 0000 GMT 9 January 1979, b) satellite temperature soundings per day for the period 5-21 January 1979, and cloud-track winds per day for the period 5-21 January 1979, c) low-level (below 700 mb) winds, d) high-level (above 400 mb) winds (after Halem et al., 1982).

Figure 2.17 Zonal velocity at 200 mb (b) and 850 mb (c) for Jan-Feb, 1979 (units: ms^{-1}, interval every 5 units for (b) and every 2.5 units for (c)).

Figure 2.18 Meridional velocity at 200 mb (a) and 850 mb (b) for Jan-Feb, 1979 (units: ms^{-1}, interval every 2.5 units).

Figure 2.19 Geopotential height at 1000 mb (a) and 200 mb (b) for Jan-Feb, 1979 (units: ms^{-1}, interval every 25 units for (a) and every 50 units for (b)).

Figure 2.20 Temperature at 850 mb (a) and 300 mb (b) for Jan-Feb, 1979 (units: K, interval every 2 units for (a) and every 1 unit for (b)).

Figure 2.21 Vorticity at 850 mb (a) and 200 mb (b) for Jan-Feb, 1979 (units: 10^{-6}s^{-1}, interval every 5 units for (a) and every 10 units for (b)).

Figure 2.22 Streamfunction at 850 mb (a) and 200 mb (b) for Jan-Feb, 1979 (units: 4 x 10^3 m^{2}s^{-1}, interval every 0.10 units for (a) and every 0.01 units for (b)).

Figure 2.23 Divergence at 700 mb (a) and 200 mb (b) for Jan-Feb, 1979 (units: 10^{-6} s^{-1}, interval every 2.5 units).

Figure 2.24 Velocity potential at 700 mb (a) and 200 mb (b) for Jan-Feb, 1979 (units: 4 x 10^6 m^{2}s^{-1}, interval every 0.10 units for (a) and every 0.20 units for (b)).

Figure 2.25 Global distribution of $\overline{uv}$ at 200 mb for Jan-Feb, 1979 (units: m^{2}s^{-2}, interval every 50 units).

.

Figure B.1   First four normalized hermite fuctions given by

$$\Psi_n(x) = \frac{H_n(x) \, e^{-x^2/2}}{(2^n n! \, \pi^{1/2})^{1/2}}$$

Figure F.1   Shapiro filter response function for various spectral truncations.

Figure G.1   Wavenumber 1 sinusoidal latent heating forcing at 500 mb.

Figure G.2 through 6.7   Zonal wind, meridional wind, vertical wind, geopotential and wind vectors, divergence, and vorticity, respectively, for the sinusoidal forcing case at 300 mb and 700 mb.

APPENDIX J

LIST OF TABLES